POLITECNICO DI MILANO

DEPARTMENT OF ENERGY

DOCTORAL PROGRAMME IN

ENERGY AND NUCLEAR SCIENCE AND TECHNOLOGY

DEVELOPMENT OF A COMPREHENSIVE CFD MODEL FOR SPARK-IGNITION ENGINE COMBUSTION

Doctoral Dissertation of:

Lorenzo Sforza

Supervisor:

Prof. Tommaso Lucchini

Tutor:

Prof. Angelo Onorati

The Chair of the Doctoral Program:

Prof. Carlo Enrico Bottani

2018 - XXX Cycle

*Dedicated to **Cinzia**.*

"So, so you think you can tell

heaven from hell?

[...]

How I wish, how I wish you were here."

— Wish you were here, Pink Floyd —

Acknowledgements

First and foremost, I would like to express my sincere gratitude to my supervisor Prof. Tommaso Lucchini, for his suggestions, patience, kindness and for the incredible support during these years. His guidance helped me to grow up as a researcher and a teacher. I am very grateful to have had a mentor like him.

My gratitude goes also to my tutor Prof. Angelo Onorati, who always encouraged my work and supported me through important advices and suggestions.

I would like to thank Prof. Gianluca D'Errico, for his insightful comments and encouragements, Prof. Giancarlo Ferrari, who introduced me into this working environment, and all other people of the ICE research group.

My sincere gratitude goes also to Prof. Christian Hasse, who gave me the possibility to work in his research group and provided me constant support during my visiting period in Freiberg. I would like to thank Sebastian, for his help and the fruitful discussions, and all the NTFD guys for their hospitality. A special thanks is for Andrea: I'm glad I found a friend like him.

I would like to thank Dr. Pierre Brequigny and Prof. Fabriche Foucher, for the possibility to visit their research laboratory and to perform some combustion measurements. My visit in Orleans was comfortable also thanks to the hospitality of their PhD students.

I owe my gratitude to all my office mates that shared with me the ups and downs of

this PhD, for the stimulating discussions, the help and all the fun we had together. It is an honour to have been working with you side by side.

Thanks to all my friends who helped me in enjoying life out of the office. A special thanks goes to Emanuele and Martina, for their patience and care for me.

I would always be in debt to my family, especially to my parents and grandparents: their love and support motivated me every day.

Last and most importantly, I would like to thank Cecilia. Thanks for all. I love you.

Abstract

Objective of this work is the development of a Comprehensive CFD Model to predict Spark-Ignition (SI) engine combustion. To this end, a run-time coupled Eulerian-Lagrangian strategy was chosen to describe ignition and flame propagation, accounting for complex electrical circuit features, stretch effects and thermo-diffusive flame instabilities (Lewis number influence). In particular, the effects of energy transfer from electrical circuit and turbulent flame propagation were fully decoupled. The first ones are taken into account by Lagrangian particles whose main purpose is to generate an initial burned field in the computational domain. Turbulent flame development is instead considered only in the Eulerian gas phase for a better description of the local flow effects. Concerning the turbulent combustion modelling, two different approaches were investigated. The Flame Surface Density model was used to validate the Comprehensive Model in a RANS context. The Artificially Thickened Flame (ATF) model was analyzed for future LES investigations and improved in terms of flame front detection and treatment of the mixture fraction gradient thickening. For what concerns the Comprehensive Model validation, several steps were followed. A preliminary assessment of proposed flame stretch and electrical circuit models was performed over simplified configurations, in order to understand separately their predicting capabilities. Then, experiments carried out at Michigan Tech University in a pressurized, constant-volume vessel were used to validate the general approach. On the other hand, the Darmstadt

Turbulent Stratified Flame (TSF) burner was selected to provide a preliminary assessment of the ATF model implementation, because characterized by a three-pipes ejector where a stationary flame is generated over a *lean-lean* charge stratification. The final part of the work is dedicated to some first steps towards additional validations of the proposed modelling strategies. First, an heat losses analysis was carried out on the TSF burner, in preparation to future non-adiabatic investigations. Then, combustion tests were performed on the Orleans spherical constant-volume vessel, in which a nearly isotropic turbulence intensity can be controlled nearby the central ignition zone.

Contents

Nomenclature

Abbreviations

ATF	Artificially Thickened Flame
ATFM	Artificially Thickened Flame Model
CA	Camera
CCV	Cyclic Combustion Variability
CDI	Capacitor Discharge Ignition System
CFD	Computational Fluid Dynamics
CFM	Coherent Flamelet Model
CHT	Conjugated Heat Transfer
CMOS	Complementary Metal-Oxide Semiconductor
CT	Cell Thickening
DC	Direct Current
DENA	German Energy Agency
DNS	Direct Numerical Simulation

DP	Dot Point
ECFM	Extended Coherent Flame Model
EEA	European Environment Agency
EGR	Exhaust Gas Recirculation
ERTRAC	European Road Transport Research Advisory Council
EU	European Union
FGM	Flamelet Generated Manifolds
FPI	Flame Propagation of Intrinsic low-dimensional manifolds
FPV	Flamelet Progress Variable
GHG	Greenhouse Gas
HR-PIV	High Resolution Particle Image Velocimetry
IC	Internal Combustion
ICE	Internal Combustion Engine
L	LED
LDV	Laser Doppler Velocimetry
LE	Optical Lens
LED	Light Emitting Diode
LES	Large Eddy Simulation
LR-PIV	Low Resolution Particle Image Velocimetry
MRF	Moving Reference Frame
PFI	Port Fuel Injection
PIV	Particle Image Velocimetry
PM	Parabolic Mirror

R&D	Reserach and Development
RANS	Reynolds Averaged Navier-Stokes
SGS	Sub-Grid Scale
SGSC	Spary-Guided Stratified-Charge
SI	Spark-Ignition
TCI	Transistor Coil Ignition System
TSF	Turbulent Stratified Flame
Zcorr	Mixture Fraction Gradient Thickened only along $\vec{n}$
ZnoCorr	Non Thickened Mixture Fraction Gradient
ZoldCorr	Mixture Fraction Gradient Thickened according to its own direction

Greek Characters

α	Thermal diffusivity; Constant; Angle of Alignment; Air-Fuel Ratio
β	Constant; Charlette Model Exponent
Δ	Interval; Size; Filter Size
δ	Thickness
η	Efficiency
Γ	Numerical Fitting Function
γ	Expansion Ratio; Electrons Emitted from the Cathode Metal per Impacting Positive Ion
κ	Flame Stretch
λ	Taylor Microscale of Turbulence; Normalized Air-Fuel Ratio
μ	Dynamic Viscosity
ν	Kinematic Viscosity

Ω	Flame Sensor	
ω	Reaction Progress; Turbulence Kinetic Energy Specific Rate of Dissipation; Fan Speed	
ϕ	Equivalence Ratio; Function to be Filtered	
Φ_0	Electrodes Metal Work Function	
π	Mathematical constant	3.14 [-]
ρ	Density	
Σ	Flame Surface Density	
σ	Corrected Sample Standard Deviation	
τ	Time	
θ	Polar Coordinate of Cylindrical/Spherical Reference System	
ε	Turbulence Kinetic Energy Dissipation Rate	
φ	Polar Coordinate of Spherical Reference System	
Ξ	Wrinkling Factor	

Latin Characters

$1/R$	Flame Curvature
$\bar{\bar{T}}$	Rotational Tensor
$\vec{n}$	Flame Front Normal Direction
$\vec{U}$	Velocity Vector
$\vec{V}$	Flame Surface Velocity Vector
$\vec{X}$	Radial Direction
$\vec{x}$	Position Vector
$\vec{x}_1$, $\vec{x}_2$, $\vec{x}_3$	Generic Reference System Axis Directions with $\vec{x}_1$ Perpendicular to Flame Surface

$\vec{Y}$	Axial Direction
$\vec{y}$	Position Vector
A	Surface Area; Constant; Parameter
a	Voltage Parameter; Coefficient; Flow Field Strain Rate; Constant
B	Constant
b	Voltage Parameter; Constant
C	Constant; Efficiency Function; Correction Factor
c	Specific Heat; Coefficient; Voltage Parameter; Combustion Normalized Progress Variable; Flame Shape Parameter
c_{ms}	Constant
D	Destruction Term; Molecular Diffusivity; Computational Domain; Fan Diameter
d	Distance; Differential
Da	Damköhler number
E	Energy; Efficiency Function
F	Thickening Factor
f_0	Fan Speed Frequency
f_u, f_Δ, f_{Re}	Charlette Model Functions
G	Integral Function; Filter Kernel
H	Parameter; Heat Received
h	Convective Heat Transfer Coefficient
i	Current
I_0	Stretch Factor

j	Generic 1D Variable; Anode Current Density
K	Karlovitz Stretch Factor
k	Specific Heat Ratio; Turbulence Kinetic Energy; Thermal Conductivity
Ka	Karlovitz number
L	Equivalent Inductance; Wrinkling Lenght; Domain Length
l	Length Scale; Length
Le	Lewis Number
M	Filter Moment
m	Mass; Deficient Reactant Order of Reaction
Ma	Markstein Number
N	Number of Measurements
n	Number, Amount, Quantity; Abundant Reactant Order of Reaction
n_x, n_y, n_z	Components of $\vec{n}$
OP	Discrete Operator
P	Production Term
p	Pressure
PV	Combustion Non-Normalized Progress Variable
Q	Energy
q	Generic Quantity
R	Equivalent Resistance; Flame Radius
r	Radius; Vortex Size
Re	Reynolds Number

S	Surface Area; Effective Strain
s	Speed
Sc	Schmidt Number
T	Temperature
t	Time
U	Velocity Magnitude; Average Velocity of Lagrangian Particles; Velocity Component along X Orleans Vessel Axis
u'	Turbulence Intensity; Fluctuation of Orleans Vessel U Velocity
V	Volume; Voltage; Flame Surface Velocity; Velocity Component along Y Orleans Vessel Axis
v'	Vortex Velocity; Fluctuation of Orleans Vessel V Velocity
w	Flame Front Displacement Speed
X	Orleans Vessel Axis
x	Integration Variable; Parameter; Generic 1D Variable
Y	Orleans Vessel Axis
y	Parameter; Generic 1D Variable
Y_c	Combustion Non-Normalized Progress Variable
Z	Mixture Fraction; Axial Coordinate of Cylindrical Reference System; Orleans Vessel Axis
Ze	Zel'dovich Number

Superscripts

$'$	Available for Breakdown Stage; Modified After Thickening Procedure
0	Unthickened

1	Thickened

Subscripts

$//$	Parallel to $\vec{n}$
0	Energy Deposition under Quiescent Mixture; Fresh Mixture
1	First Sub-Grid Scale Turbulence Intensity Expression; Component along $\vec{x}_1$ of the $\vec{x}_1$, $\vec{x}_2$, $\vec{x}_3$ Reference System
2	Second Sub-Grid Scale Turbulence Intensity Expression; Component along $\vec{x}_2$ of the $\vec{x}_1$, $\vec{x}_2$, $\vec{x}_3$ Reference System
3	Component along $\vec{x}_3$ of the $\vec{x}_1$, $\vec{x}_2$, $\vec{x}_3$ Reference System
Δ	Filter Size Scale
∞	Energy Deposition under High Velocity Flow
$\perp$	Perpendicular to $\vec{n}$
θ	Component along θ of a Cylindrical/Spherical Reference System
φ	Component along φ of a Spherical Reference System
a	Anode
abu	Abundant Reactant
act	Activation
ad	Adiabatic Flame
af	Anode Fall
arc	Arc Stage
$ATFM$	Artificially Thickened Flame Model
b	Burned
bd	Breakdown
c	Chemical; Progress Variable

$cantera$	Cantera Code
$cell$	Computational Mesh Cell
$ceramic$	Ceramic Material
cf	Cathode Fall
ch	Charlette
co	Colin
$corr$	Corrected
def	Deficient Reactant
eff	Effective Energy Deposition; Effective Transmission
f	Triangular Face; Flame
FSD	Flame Surface Density
g	Gas
gap	Inter-Electrode
gc	Gas-Column Fall
$glow$	Glow Stage
gp	Mesh Grid Point (Cells)
i	*i-th* Lagrangian Particle; *i*-th Measurement
IE	Inter-Electrode
if	*i-th* Triangular Face
k	Kolmogorov; *k-th* Value
L	Laminar
l	Laminar Flame
lim	Maximum

$local$	Local
max	Maximum
$mesh$	Mesh
min	Minimum
MP	Meneveau Poinsot
n	Colin Angelberger
P	Primary Circuit
p	Constant Pressure
$particles$	Lagrangian Particles
$pilot$	Pilot Pipe
$plasma$	Plasma Channel
R	Component along R of a Cylindrical/Spherical Reference System
$ratio$	Ratio
$restrike$	Restrike Event
S	Secondary Circuit
s	Sub-Grid Scale
$schl$	Schlieren
sgs	Sub-Grid Scale
$slot1$	Slot 1 Pipe
$spark$	Spark Discharge
$spark - time$	First Discharge Time
spk	Spark Discharge
st	Stoichiometric

T	Total
t	Integral Scale; Turbulent (of the Integral Lenght Scale); Turbulent; Tangential To Flame Surface
tc	CFM Dimensional Consistency
$test$	Test-Filtering
$therm$	Thermal Support of the Electrical Circuit
tot	Total
u	Unburned; Actual (or Stretched) Laminar Flame
$u0$	Unstretched Laminar Flame
$wall$	Pipe Wall
y	TSF Burner Axial Direction
Y_c	Non-Normalized Progress Variable
Z	Component along Z of a Cylindrical Reference System

Symbols

$\|\vec{\psi}\|$	Vector Norm
$*$	Convolution
$\bar{\psi}$	Time Average; Spacial Filtering; Sample Mean
$\cdot$	Scalar Product
$:$	Scalar Product between Matrices
$\dot{\psi}$	Rate of change; Flux
$\hat{\psi}$	Favre Spacial Test-Filtering
$\langle\psi\rangle$	Average on Flame Surface; Volume Average
$(\psi)_x$	Evaluated at x Value

∇	Nabla Operator
∇^2	Laplacian Operator
$\overbrace{\psi}$	Spacial Test-Filtering
$\overline{\psi}$	Segment Length
∂	Partial Derivative
$\psi\,(\,)$	a Function of; with an Inner Cut-Off Lenght Scale of
$\tilde{\psi}$	Favre Spacial Filtering
$\times$	Vector Product
$\widehat{\psi}$	Angular Sector
$\widetilde{\psi}$	Favre Average

Introduction

Scenario and future trends of powertrain technologies

Mobility of people and transportation of goods are fundamental needs of modern society. Any approach to fulfill them must meet sustainability criteria and achieve customer's acceptance. Accordingly, solutions and services have to comply with safety, energy efficiency, security, environmental compatibility and affordability criteria. Therefore, the evolution of transportation system will advance by combining new improvements and changes in:

1. the powertrain and vehicle technologies,

2. fuels and the energy scenario.

The already ongoing electrification of the powertrain will continue progressing according to the different vehicle mission profiles, while the need to increase the energy security and to reduce the use of fossil and oil based fuels will push for a wider use of renewable energy sources. Based on a global need this process will be deployed at local level according to the availability of raw materials and local policies. Long term trends, which are related to the evolution of both personal mobility needs and goods transportation, will participate in shaping the market portfolio. More people are expected to live in large agglomerations, asking for increasingly "clean" and efficient solutions. This "clean" factor will be provided not only by vehicle technological improvements

but also by the optimization of their use, thanks to the increasing role of connectivity. Likewise, the long haul transportation system will benefit from connectivity that will enhance automated driving conditions especially on intercity and highway routes.

The research agenda of ERTRAC, which is the European Road Transport Research Advisory Council, expects that 60% or more of new passenger vehicles in Europe still will be powered with an Internal Combustion Engine (ICE) even in the long term horizon until 2050. In fact, powertrain applications will include Hybrids, Range Extender architectures (e.g. Plug-in Hybrid Electric Vehicles) as well as dedicated alternative fuels (e.g. Natural Gas) engines. Similarly, the Heavy Duty market is expected to be dominated by ICE for some time to come, given the need for an high energy density in propulsion of larger vehicles.

Both the mid-term (till 2030) and the long-term (up to 2050) trends will depend on several technical and political events that will drive:

1. the progress of current technologies,
2. the take-off of new solutions.

Concerning the first aspect:

- *New combustion processes and architectures* to make ICE even cleaner, efficient and cost competitive *are expected to be developed*, supporting the integration in new hybrid architectures. They shall as well take the maximum benefit from the use of clean and alternative fuels. In parallel, political measures taken to comply with air quality legislation for large cities could lead to acceleration towards "clean" powertrains based on electric propulsion and/or alternative fuels with a consequent limitation in the use of conventional ICEs.
- Nevertheless, considering and targeting a larger use of electric driven powertrains in the future (e.g. by car sharing services), this transition process still requires:

  1. improvements in battery energy density,
  2. the development of appropriate grid and charging infrastructure.

  These are crucial elements for an effective market penetration of electric vehicles, including improvements in cost effectiveness as well as technology.

- In a longer term view, the development stage of a European hydrogen infrastructure and the costs of technologies will prevent Fuel Cell electric vehicles from moving out of few niche applications for a relatively long period. With a few exceptions, they still result in a very early stage of development with limited opportunities. New vehicle concepts, better suited for future integrated mobility systems and urban-mobility, need to be established.
- Drastic cost reductions, together with the production of renewable hydrogen and the build-up of an European wide hydrogen infrastructure, are needed to support fuel cells to market success.

In general, it is clear that new alternative powertrain solutions will find the right environment to penetrate the market only if an integrated approach is ensured at the political level by:

- continuing support for further strategic R&D,
- providing conditions to generate fuel/energy distribution infrastructures,
- leveraging progressive fleet renewal conditions,
- supporting customer acceptance through educational actions.

At the same time, automotive industries should continue to respect their societal responsibilities for sustainable solutions, emphasizing the need for pragmatic, cost-effective and user-friendly approaches. This will ensure true sustainability for environment, economy and society, maintaining EU industry competitiveness.

The European Union (EU) strategy for low-emission mobility

Transport represents almost *a quarter* of Europe's greenhouse gas (GHG) emissions and is the main cause of air pollution in cities. The transport sector did not experience the same gradual emissions reduction as other sectors. In fact, as shown by Figure 1, emissions only started to decrease in 2007 and today they remain still higher than in 1990. Within this sector, road transport is by far the biggest emitter, accounting for more than 70% of all GHG emissions from transport in 2014 (see Figure 2), and contributing for approximately *one-fifth* to the EU's total emissions of carbon dioxide

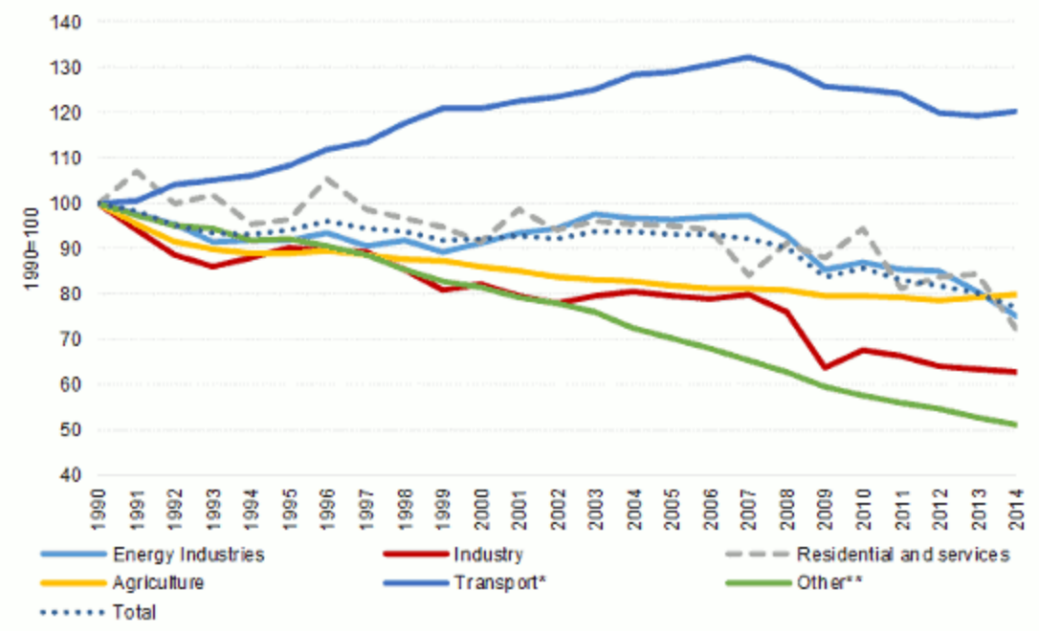

Figure 1: *Total GHG emissions since 1990, divided by sectors. Notes: [*]* transport *includes aviation but excludes maritime sector; [**]* other *include fugitive emissions from fuels, waste management and indirect CO_2 emissions. Source: European Environment Agency (EEA).*

(CO_2), the main greenhouse gas. Although these emissions fell by 3.3% in 2012, they are still 20.5% higher than in 1990.

In the context of an already underway global shift towards a low-carbon and circular economy, the EU's low-emission mobility strategy, adopted in July 2016, aims to ensure Europe competitiveness and its capability to answer to increasing mobility needs of people and goods. In this policy, by mid-century, the GHG emissions from transport will need to be at least 60% lower than in 1990 and firmly on the pathway towards zero. The clear target is to drastically reduce with no further delay the transport sector emissions of air pollutants, which harm people's health.

The EU strategy, by integrating a broader set of measures to support the transition to a low-carbon economy, will provide benefits to European citizens and consumers by:

- supporting jobs, growth, investments and innovation;
- improving air quality, infrastructures for alternative fuels, links between different modes of transport and safety;
- reducing noise, congestion levels and cars energy consumption.

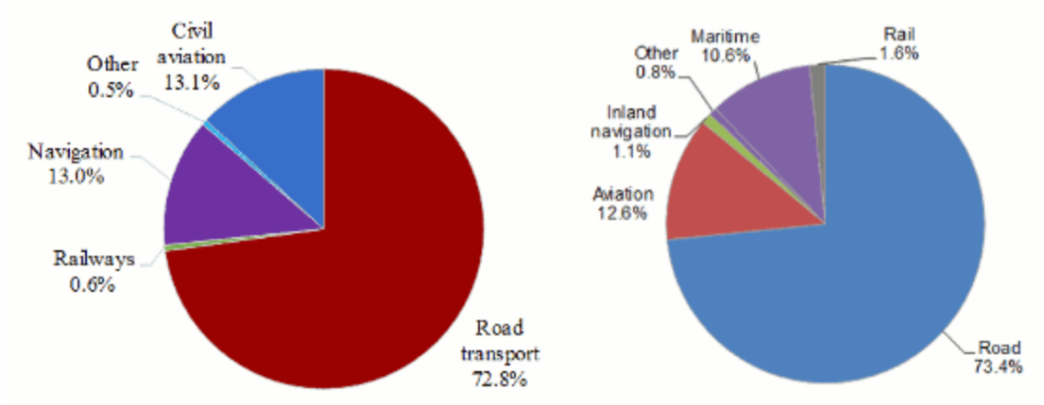

Figure 2: *For* Transport *sector in 2014: greenhouse gas emissions by mode (left) and share of energy demand by mode (right). Source: European Environment Agency (EEA).*

Three priority areas are identified for actions:

1. *Increasing the efficiency of the transport system*. Digital technologies and smart pricing will be exploited as much as possible, while the shift to lower emission transport modes will be further encouraged.

2. *Speeding up the deployment of low-emission alternative energy for transport*, such as advanced biofuels, electricity, hydrogen, less carbon intense (often gaseous) fossil fuels and renewable fuels of non-biological origin (e.g. e-fuels), removing obstacles to the electrification of transport.

3. *Moving towards zero-emission vehicles*. Further improvements to the IC engine will be needed, to take the maximum benefit from the use of clean and alternative fuels, supporting the integration in new hybrid architectures.

Cities and local authorities are considered fundamental in delivering this strategy, thanks to their capability to:

- implement incentives for low-emission alternative energies and vehicles;

- encourage active travel (cycling and walking), public transport, bike and car-sharing/pooling schemes.

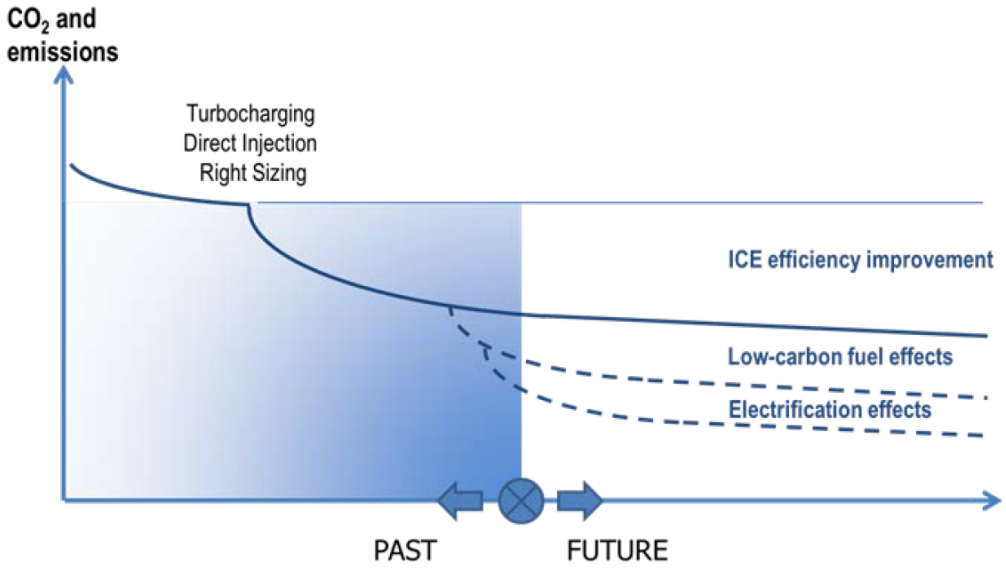

Figure 3: *Trend of CO_2 and emissions caused by ICEs for on road vehicles along with accompanying measures of low-carbon fuels and electrification of powertrains. Source: European Road Transport Research Advisory Council (ERTRAC).*

The future of IC engines

As a consequence of what discussed so far, it seems clear that high efficient and ultra clean IC engines using renewable low carbon fuel are a key element of an electrified/hybridised powertrain and represent the future of this technology.

Looking back into the history of IC engines, the development was primarily determined by continuous improvements instead of revolutionary technologies. The introduction of direct fuel injection in combination with turbo-charging (also known as *downsizing*) was one of the rare and visible exceptions to this trend, leading to a significant efficiency increase (in the order of 15%). Figure 3 shows ERTRAC's proposal for ICEs roadmap that supports the idea of an *high efficient and ultra clean IC engine, using sustainable fuel as an integral element of an electrified powertrain*.

Therefore, ICE technologies will continue to play a major role for the next decades mainly due to the energy and power density capability provided by liquid and gaseous fuels, together with the widespread existing infrastructure. The energy density of hydro-carbon based fuels will always be greater than electro-chemical storage, such as batteries (current difference: 2 orders of magnitude). Also from the recharging/refilling

time standpoint, liquid and gaseous fuels offer the best performance and flexibility in use. In this context, synthetic fuels produced in chemical plants based on renewable energy sources (the e-fuels) can lead to a net carbon free energy-cycle with high power density.

From a study of the German Energy Agency (DENA) completed in 2017, e-fuels are necessary to meet the EU climate targets within the transport sector. Even in a battery electric drive dominated scenario, DENA estimated that the final energy demand of all transport modes in the EU will be met with more than 70% of e-fuels in 2050. Here are reported some advantages and disadvantages of this solution:

- E-fuels have an high energy density. Therefore they can be transported conveniently over long distances and kept in large scale stationary storage over extended periods, allowing them to compensate even seasonal energy supply fluctuations.
- The entire petrol/diesel/kerosene/gas infrastructure (pipelines and gas stations) can continue to be used.
- E-fuels can be used by the existing stock of passenger, utility vehicles and by transport modes that are hard to electrify (aviation and shipping).
- The overall energy efficiency of electricity use in battery electric vehicles is 4-6 times, and via hydrogen in fuel cell vehicles about 2 times higher than e-fuels in combustion engines including grid integration.

The technological potential in Europe for renewable electricity generation is enough to cover the future demand of transport energy and e-fuels generation. However, a significant increase in electricity production from renewable energies will be necessary, because aforementioned demand in 2050 is estimated to be ten times bigger than the current annual renewable electricity generation in the EU. In particular, over 80% of this future demand is caused by the production of e-fuels. Some automotive manufacturers started to pursue e-fuels strategy, investigating their applicability; as an example, in March 2018 AUDI produced a sufficient quantity of this synthetic fuels for initial engine tests [1] (Figure 4). At the moment, e-fuels costs are high (up to 4.50 € per liter

[1] `https://www.volkswagenag.com/en/news/2018/03/Audi_e-fuels.html`, accessed: 2018-06-11

Figure 4: *Partial view of the AUDI e-fuel plant.*

diesel equivalent). Target costs, including CO_2 extraction from ambient air, of approximately 1 € per liter diesel equivalent appear possible with imports from regions with very good solar and wind power conditions. Nevertheless, future fuel cost are expected to also increase for all other clean transport variants based on the high share of renewable energy required, leading to a reduction of the clean fuels cost difference when comparing combustion engines and electric powertrains.

As previously mentioned, the progress to further improve the IC engine system and, thus, the powertrain can be divided in three steps (compare with Figure 3):

1. improvement of the engine efficiency itself, particularly regarding the properties of low-carbon fuels;

2. the use of low carbon/near net zero carbon fuels;

3. electrification including hybridization.

Concerning the first one, Figure 5, taken from ERTRAC's report, shows how the overall efficiency improvements in the order of 15 % points are possible for spark ignition engines, particularly in the case of highly knock resistant gas combustion systems, and $\approx$ 10-12 % points for compression ignition engines. This improvement potential is nearly equally distributed in the areas of volumetric, thermal as well as mechanical ef-

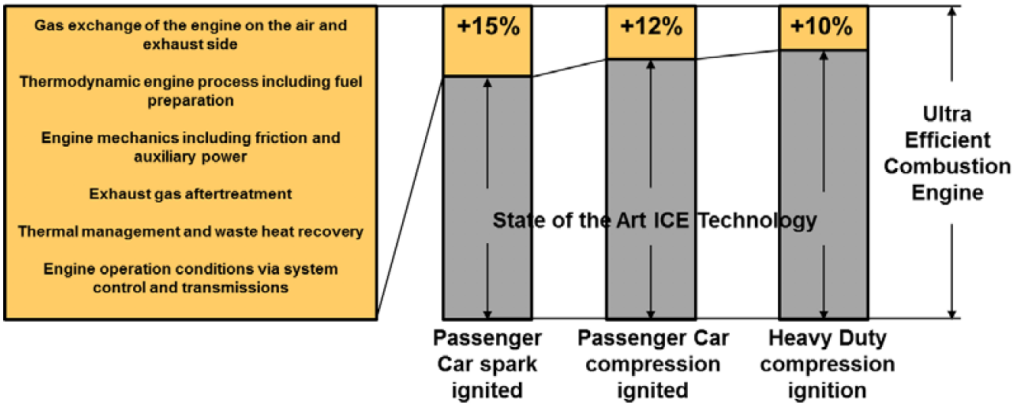

Figure 5: *Efficiency improvement potentials for spark and compression ignited engines. Source: European Road Transport Research Advisory Council (ERTRAC).*

ficiency. Massive downsizing should be mentioned since it increases efficiency first of all by reducing relative impact of heat and friction losses (just by increasing the specific power of smaller engine). Looking at remaining opportunities, a large number of technologies need to be developed and implemented. On a high level these technologies can be grouped in the following categories addressing the root cause of inefficiency:

- Gas exchange of the engine on the intake and exhaust side, together with the influence of (turbo)charging system efficiency.
- Dedicated thermodynamic engine process, including fuel preparation, in particular for low-carbon fuels.
- Engine mechanics, including friction and auxiliary power
- Exhaust gas aftertreatment.
- Thermal management and waste heat recovery, including on-board fuel reforming.
- Engine operation conditions via system control and transmissions.

To solve in future these competing challenges, the further research needs can be summarized as follows with an emphasis on affordability of all new developments:

- Further development on components and systems, based on existing engine technologies and application of advanced materials

- New combustion processes and new engine concepts, new combustion sensing methodology & control; with special focus on gas and other low-carbon fuels
- Radical approach to highly efficient, dedicated and robust combustion engines for the usage of alternative/ low carbon and high knock resistant fuels
- Development of dedicated ICEs for electrified powertrains including dedicated transmissions
- Solutions for recovery of engine heat losses including on-board chemical reforming of fuels.

Spark-Ignition (SI) engines

In the context depicted by previous Sections, the Spark-Ignition (SI) engine plays a key role in future powertrain technologies. In fact, as the name implies, in SI engines a mixture of *fuel* and *air* is ignited with a spark; therefore alternative fuels, such as hydrogen, natural gas, biofuels and renewable fuels of non-biological origin, can be easily used with limited modifications. This implies that SI engines represent the fastest and easiest solution for ultra clean ICEs embedded into an electrified/hybridised powertrain scenario.

Four-stroke spark-ignition engines cover a wide range of applications. They are installed in motorcycles, cars, small boats and electric generators.

Spark-ignition engines can be subdivided into *premixed* and *non-premixed* engines. In *premixed* engines the fuel is injected into the intake ports as a fine spray of droplets whose typical diameter ranges between 20-100 μm [55]. Fuel evaporation starts in the manifolds and continues after the mixtures is drawn into the cylinder. This afford to achieve a better control of the engine operation and to reduce the fuel consumption and pollutant emissions. In *non-premixed* engines the fuel is injected within the combustion chamber. This solution presents several advantages with respect to the conventional premixed solution:

- An increase of the volumetric efficiency can be achieved thanks to the absence of wall-wetting at intake ducts.

- Two different kinds of combustions can be performed by a suitable choice of the injection strategy:

  1. an *homogeneous combustion* with rich or stoichiometric mixtures, when the engine is running at full load,
  2. a *stratified combustion* at part load.

  In this last case, the mixture is rich close to the spark, so it can be easily ignited, while it becomes leaner with the increasing distance from the ignition zone. This strategy allows to work with an engine at overall lean equivalence ratios, increasing the thermal efficiency and reducing the catalyst heating.

This thesis work deals with the modelling of combustion in *premixed* SI engines, because the physical processes involved are simpler and better understood than in non-premixed ones; hence, more details about this topic are provided in next paragraphs. However, a working mathematical framework suitable for simulating premixed engines can be extended without prohibitive efforts to stratified combustion investigations. Therefore, this work can be considered a first step towards a comprehensive tool for predicting combustion in any SI engine type.

Premixed SI engine combustion Although more than a century ago it was recognized that the turbulence affects burning velocities [74], scientific studies of turbulent combustion did not begin until the works of Damköhler [35] and Schelkin [103] in early 1940's. At the same time, the theoretical foundations of turbulence were laid by Kolmogorov [63, 64]. These studies pointed out that:

1. the propagation velocity of the turbulent flame is (nearly) proportional to turbulence intensity;
2. the turbulent length scales affect the flame in different ways, according to their relative dimension with respect to the flame thickness.

A further step in the understanding of premixed combustion was accomplished in 1953 by Karlovitz [59], who introduced the concept of flame stretch and its effects.

In *laminar* premixed flames, combustion propagation requires thermal conduction and diffusion of species from the hot burned region to the unburned one.

In *turbulent* premixed flames, previous molecular processes are enhanced by:

- turbulent mixing, if the laminar flame thickness δ_l is greater than the Kolmogorov length scale l_k;
- distortion of the flame surface, leading to an increase of the interface area between burned and unburned gases [114].

As a consequence, the mass consumption rate is greatly enhanced by turbulence and in some circumstances the mean heat release rate is generally more influenced by turbulence than by chemical kinetics [114]. Therefore, premixed turbulent combustion can be regarded as primarily a fluid-dynamics problem, except for:

- mixtures near flammability limits,
- ignition,
- flame quenching,

in which both chemical kinetics and fluid mechanics are important [68].

Although many authors have proposed the existence of various regimes of premixed turbulent flames [14, 86, 97, 114], it is generally agreed that in most practical combustion systems, as SI engines, chemical reactions occur inside a *thin reaction zone*, often referred to as "(laminar) flamelet" [11, 56, 86]. In this context, *thin* means that the reaction zone is thinner than the smallest scale of turbulence (namely $\delta_l < l_k$). However, this condition is probably not satisfied in very lean mixtures, where arguably the combustion is of "distributed reaction" type. In fact, this regime is characterized by a fast turbulent mixing compared to chemistry time-scales, causing the combustion to occur in a thickened reaction zone with heat release occurring more or less homogeneously throughout the turbulent flame brush [114].

Traditionally, the flamelet regime is associated with the fast chemistry condition, usually characterized by a Damköhler number $Da \gg 1$ and a Karlovitz number $Ka < 1$. These two dimensionless numbers can be defined as follows:

$$Da = Da\left(l_t\right) = \frac{\tau_t}{\tau_c} = \frac{l_t / u'\left(l_t\right)}{\delta_l / s_{u0}} \tag{1}$$

$$Ka = \frac{1}{Da\left(l_k\right)} = \frac{\tau_c}{\tau_k} = \frac{\delta_l / s_{u0}}{l_k / u'\left(l_k\right)} \tag{2}$$

where l_t is the integral length scale, s_{u0} the unstretched laminar flame speed (namely, the local normal propagation velocity into the unburnt gas), $u'\left(l_t\right)$ and $u'\left(l_k\right)$ the turbulence intensities associated to integral and Kolmogorov length scales, respectively. In particular, the Damköhler number Da of (1) is the ratio between the large-scale turbulence time scale (or "eddy turnover" time) τ_t and the chemical time scale τ_c. On the other hand, the Karlovitz number Ka of (2) is the reciprocal of Damköhler number, defined with respect to Kolmogorov length scale.

The first condition above, $Da \gg 1$, implies that the reactions are much faster than the fluid motion processes, hence it is often assumed that a flamelet behaves locally like a laminar flame (i.e. it propagates normal to itself with the laminar burning velocity). However, because of the turbulent fluid motion, the flamelets are convoluted and their surface is wrinkled. The result of these distortions is that the reaction zone is strained in the tangential plane.

The second condition ($Ka < 1$), known as the Klimov-Williams criterion [86], suggests that the boundary between the flamelet and distributed reaction regimes is defined by $Ka = 1$. This implies that laminar flamelets cannot exist if the Kolmogorov scale of turbulence is smaller than the laminar flame thickness. Another interpretation of this criterion is that flamelets cannot exist at $Ka > 1$ because under this condition their internal structure is altered by stretching and quenching [93]. However, by means of DNS, Poinsot [92, 93] showed that laminar flamelets are more resilient to flame stretch than the Klimov-Williams criterion suggests. It was found that a local flame quenching can be observed in presence of rather large eddies, in particular orders of magnitudes larger than l_k.

Therefore, Poinsot [92,93] proposed a new diagram of burning regimes for premixed combustion, which is illustrated in Figure 6. According to this diagram, for example, a turbulent field of type *B* is able to corrugate the flame but not to quench it, hence it belongs to the flamelet regime. On the other hand, case *A* conditions characterize a pseudo-laminar flame type, because even the integral length scale eddies do not convey enough energy to interact with the flame. Type *C* turbulence, instead, may locally

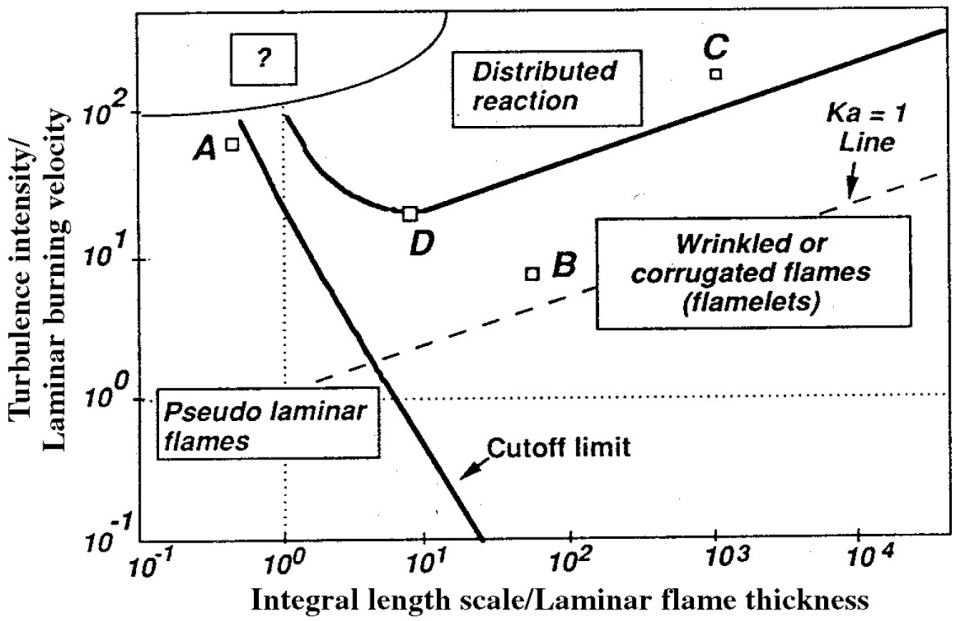

Figure 6: *Turbulent combustion diagram proposed by Poinsot: regimes of premixed combustion identified in terms of length (l_t/δ_l) and velocity ($u'\left(l_t\right)/s_{u0}$) ratios using a log-log scale, [93].*

quench the flame, therefore this case corresponds to the distributed reaction regime, while turbulent field *D* indicates the minimum turbulence intensity for quenching. Despite some criticism, particularly regarding the (in)ability of the Kolmogorov scales to quench the flame [15], Figure 6 diagram has been qualitatively confirmed by experiments of Roberts, Bédat and Cheng [23, 96]. However, quantitative differences were noted and can be attributed to certain simplifications in the DNS simulations, such as reduced one-step chemical kinetics, two-dimensional geometry and assumed high heat losses, among others.

State of the art of premixed SI engine combustion modelling The numerical modelling of SI premixed combustion is a primary issue in developing more efficient and less pollutant automotive and heavy-duty engines. In fact, a detailed numerical description of the combustion process that takes into account all the involved effects (the properties of the ignition system, the local flow conditions and the combustible mixture features) allows to improve engines design and development with greater effectiveness.

Over the years, increasingly detailed numerical approaches were proposed, accord-

ing to enhanced computational and experimental tools but also to more and more stringent engine design requirements. In the early nineties of the last century, Herweg and Maly [54] proposed the first idea of comprehensive model for SI engine combustion. In their work the development of a one-dimensional time-dependent single flame kernel is described considering, through different sub-models, the supplied electrical energy form the spark, the heat lost at the electrodes, the mean flow/turbulence effects (including the stretch phenomenon) and the contribution of chemical reactions (Figure 7a).

Later, in the first decade of the twenty-first century, improved comprehensive models where proposed by Reitz [107], Colin [37] and Bianchi [39]. The first one exploits a Lagrangian approach to track the early flame kernel, where particle markers are placed on the initial flame surface (assumed spherical) and moved in the radial direction with velocities that depend on heat transfer from the electrical circuit, laminar flame speed and local turbulence (Figure 7b). The second one introduces a detailed model for the electrical circuit, where also the restrike phenomenon is considered, and takes advantage of a cloud of Lagrangian particles, each one representing a possible ignited flame kernel, for the plasma channel description (Figure 7c). The third one uses improvements for the electrical circuit modelling similar to Colin's ones adopting, instead, a 1D single-particle approach for the early flame kernel evolution (Figure 7d). A limitation for this expansion is introduced when the kernel radius reaches the value of 2 mm in order simulate the fully turbulent flame only with the main Eulerian combustion model. In fact Bianchi's model, as Reitz and Colin's ones, exploits the coupling *Lagrangian particles – Eulerian flame model* only to improve the ignition stage description, leaving the prediction of the further flame propagation to the main Eulerian model (for example the Extended Coherent Flame Model – ECFM [30], used with success by all described models).

At the beginning of the 2010s, Dahms [32–34] and Lucchini [72, 118] used similar techniques to manage the ignition stage in their comprehensive models for SI combustion, confirming the strength of the coupled Lagrangian-Eulerian approach. Both models exploit a linear path of particles, positioned along the spark-gap centerline, to simulate in more detail the shape of the plasma channel (Figure 7e). In this way, the modeling of spark channel motion and elongation considers properly the local effects of

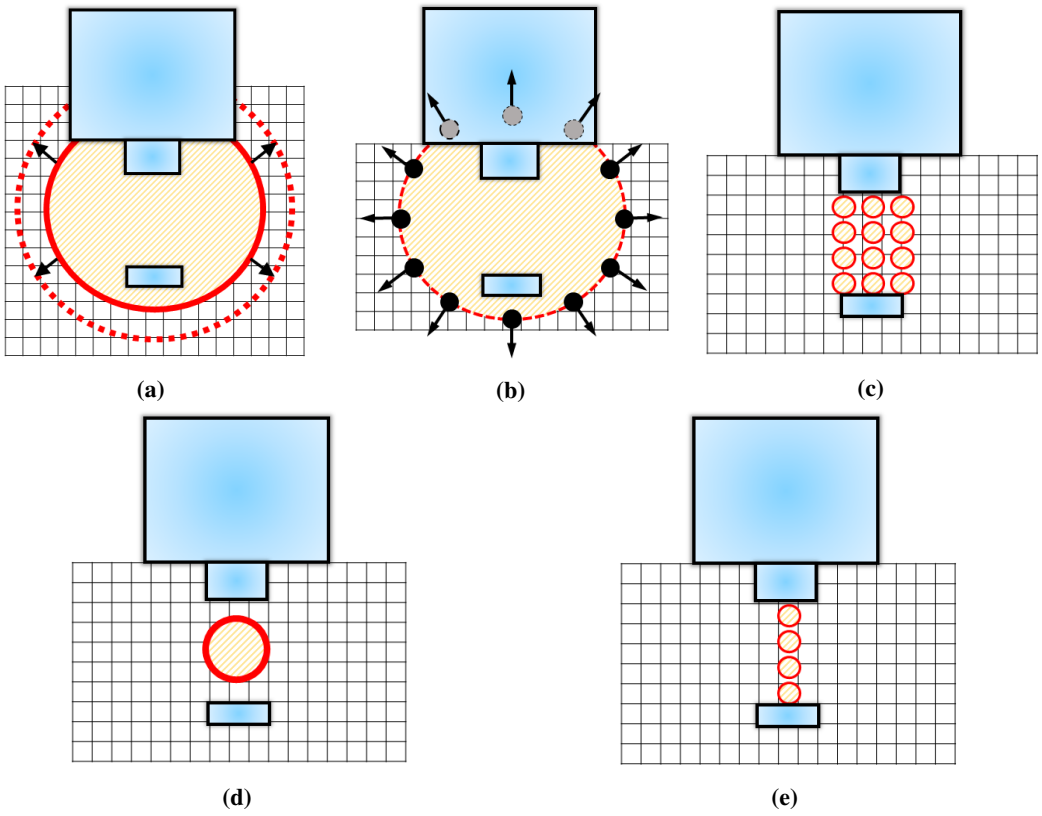

Figure 7: *Available comprehensive models for Spark-Ignition engine combustion: Herweg and Maly (a), Reitz (b), Colin (c), Bianchi (d), Dahms and Lucchini (e).*

flow and turbulence, improving the prediction of restrikes and local ignition events due to possible stratifications of mixture properties. The flame stretch effect, namely the strain rate introduced by turbulence and curvature effects on the flame, is considered in the early Lagrangian flame kernel development by both models. In this context, Dahms includes also non-unity Lewis number effects through the computation of an effective Lewis number for the mixture. Differently from the former proposed comprehensive SI models, Dahms and Lucchini implemented for the Eulerian turbulent flame description the G-equation model [88] and the Coherent Flame Model (CFM) [28], respectively.

Finally, Fansler [40] recently analyzed how advanced and detailed comprehensive models for SI combustion can be used not only to describe the ignition and the further flame development in the context of a Port Fuel Injection (PFI) strategy, but also with more recent configurations like Spary-Guided Stratified-Charge (SGSC) engines operated at part load with highly stratified fuel-air-residual mixtures.

Objective, approach and structure of the thesis

Despite different modeling strategies, all previously presented comprehensive models show good results when compared to experimental findings. However, under highly inhomogeneous flow condition at the spark-plug, the strain effects that turbulent eddies and curvature radius generate on the flame, namely the flame stretch effects, cannot be properly considered if included in a Lagrangian kernel growth approach coupled with a relatively coarse mesh. As well known, flow and turbulence stratifications at the ignition zone can be fully detected only if the local mesh is sufficiently refined. This condition leads to problems when chemical contribution, with flame stretch effects, are included in the Lagrangian particles evolution. In fact, when a particle becomes larger than a few cells the strain effects due to turbulence and curvature over a relatively large portion of the flame front are computed with respect to not only the same cell (where the particle center is positioned) but also considering values far from the actual flame front position. Moreover, recent DNS studies [50] about premixed flames propagation underline that the flame speed in presence of multidimensional and unsteady flows is a local property, and consequently the related stretch effects, which take a role in its computation, should be evaluated at the flame front position.

The main target of this thesis work is the development of a Comprehensive CFD Model for premixed combustion of SI engines. An improved version of the Artificially Thickened Flame Model (ATFM) is also developed, in order to get additional insight in available turbulent combustion models and to provide an alternative to the one used in this thesis work (i.e. the Coherent Flamelet Model - CFM).

The thesis is divided into three parts. The first part includes all proposed numerical approaches to model premixed SI combustion, in particular:

- *Chapter 1* describes in detail the developed Comprehensive CFD Model. The proposed approach accounts properly for the influence of:

  1. the electrical circuit features,
  2. possible laminar flame instabilities,
  3. *flame-turbulence* interaction

  on the ignition and the further combustion process. The Lagrangian and Eulerian

frameworks, characterizing the model structure, are schematically investigated. The role and features of each used sub-model is clarified, emphasizing main novelties as:

  - the effective Lewis number prediction of a premixed mixture;
  - the implementation of different strategies to model the arc and glow phases of the spark-discharge;
  - the modified strategy to consider flame stretch effects into ignition and premixed combustion prediction.

- *Chapter 2* proposes an improved version of the Artificially Thickened Flame Model (ATFM). The Artificially Thickened Flame concept is firstly described, together with the basic concepts of thickening factor F and efficiency function E. Then, the tabulation strategy to reproduce chemical kinetics is briefly reported, together with a flame sensor proposal, used to modify the diffusion terms of conservation equations only at the reacting region. Finally, the model fundamental transport equations, in which the main improvement of the $\vec{\nabla}\widetilde{Z}$ *directional thickening* is embedded, are analyzed in detail. As a supplement for the ATFM application, information on numerical strategies to filter LES fields and evaluate the sub-grid scale turbulence intensity are also reported.

The second part of this thesis deals with the validation of proposed numerical strategies, carried out on the open-source platform *OpenFOAM®*, which involves a 3-D finite volume discretization, and the additional use of suitable libraries (*Lib-ICE*) developed for combustion modeling. In particular:

- *Chapter 3* deals with a preliminary assessment of the proposed flame stretch and electrical circuit models (included into the Comprehensive model of Chapter 1) over simplified configurations. This analysis is carried out to understand separately their predicting capabilities, allowing to focus the investigation on single and specific phenomena.

- *Chapter 4* addresses the validation of the Comprehensive CFD Model described in Chapter 1. The experimental rig of Michigan Tech University (USA), characterized by a pressurized constant-volume combustion vessel, is chosen for this

purpose. First, an experimental campaign on the combustion process of lean and diluted *Propane-Air* mixtures is described. Then, after a numerical non-reacting flow analysis, combustion simulations are carried out to assess Chapter 1 model behaviour under variations of turbulence, air/fuel ratio and pressure conditions.

- *Chapter 5* includes the first assessment of the improved ATFM version, proposed in Chapter 2. For this purpose, the Turbulent Stratified Flame (TSF) burner of Darmstadt Technical University (Germany) is used. Consisting in a three concentric pipes ejector where different conditions of mixture stratification and flow shear can be investigated over a nearly steady-state flame, the ATFM first assessment is carried out only in presence an air/fuel ratio variation (no shear) and under adiabatic assumptions.

The third part of this thesis describes in detail some first steps towards additional validations of all proposed numerical approaches.

- *Chapter 6* analyzes the heat-losses experienced at TSF burner Pilot tube exit, where fully burnt products are in contact with the pipe. For this purpose, *Conjugated Heat Transfer* (CHT) simulations are carried out in the aforementioned heat-losses region. This analysis can be considered as preliminary to future non-adiabatic investigations with the ATFM of Chapter 2.

- *Chapter 7* reports the experimental investigation campaign carried out in Orleans University (France) over a spherical closed-volume vessel, in which high-pressure and high-temperature mixtures can be employed for both laminar and turbulent premixed flame investigations. In particular, suitable reacting conditions are investigated to understand the influence of an:

  1. equivalence ratio,
  2. turbulence intensity,
  3. pressure,
  4. Lewis number

  variation. This work represents not only the starting point of an additional validation of Chapter 1 comprehensive model, but it also provides the possibility to

further improve the actual modeling status of SI engine combustion.

Part

Numerical modelling strategy

CHAPTER 1

The Comprehensive CFD Model

The SI premixed combustion is a process affected by several phenomena, like the electrical circuit type and features, the local flow conditions, and the mixture properties. In particular, the ignition event and the overall initial stage of combustion need strong modeling efforts because all the aforementioned contributions compete together for the possible generation of a self-sustained fully turbulent flame or produce a misfire event.

Therefore, the comprehensive model proposed in [72,118] was chosen as basic strategy to model combustion. This decision was taken because its Eulerian-Lagrangian approach, joint with several sub-models, allows to consider correctly all the involved effects and to model the plasma arc as close as possible to its original geometry. In fact, especially under highly inhomogeneous flow conditions at the spark-gap, a correct representation of the electric arc is fundamental to properly simulate both its elongation and corrugation.

In this context, a novel approach to consider the flame stretch effects was intro-

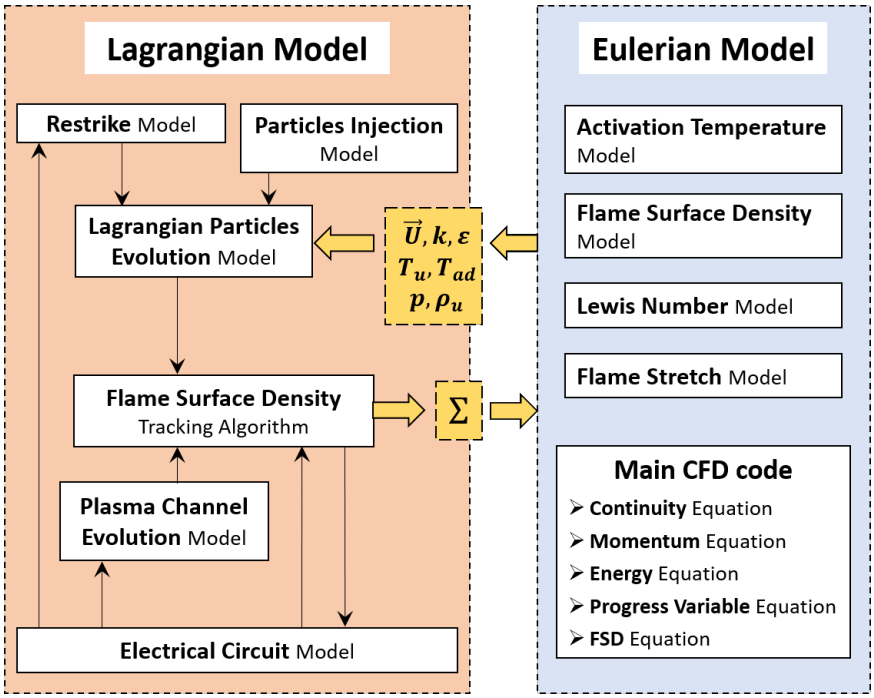

Figure 1.1: *Scheme of the modified Eulerian-Lagrangian model.*

duced. The Lagrangian particles, whose role is to simulate the spark evolution, were no more considered as possible ignited flame kernels but only as portions of the electric arc where the introduced thermal energy should be deposited. On the other hand, the laminar/turbulent flame evolution, including flame-turbulence interactions, curvature effects and chemical contributions, was modeled only by the main Eulerian CFD code. At this level, a suitable model considers the flame stretch effects as function of the local flame front conditions of curvature, flow velocity, turbulence and Lewis number. The Lagrangian and Eulerian approaches are still coupled at each time-step, because:

1. The particles must be affected by the local distribution of flow velocity, turbulence and pressure.

2. The Eulerian combustion code needs to be initialized by a burnt field, created by the transferred thermal energy and function of the electrical circuit properties.

Finally, modifications with respect to the original implementation concerned also:

1. The effective Lewis number prediction, in order to take into account possible non-unity Lewis number effects as thermal-diffusive instabilities of the laminar flame.

2. The electrical circuit modeling, to improve the prediction of possible restrike events and the achievement of proper current and voltage trends.

The result is the comprehensive model described schematically by Figure 1.1.

In next sub-sections all the sub-models used by both Lagrangian and Eulerian approaches (Figure 1.1) will be described in detail, focusing in particular on performed modifications.

1.1 Lagrangian Model

In the original and basic version [72], the Lagrangian model evolves particles considering not only the thermal effects of the electrical circuit but also the contribution of chemical reactions. In the following modified version, this last aspect was fully transferred to the Eulerian model removing from the Lagrangian particles evolution any influence of the laminar/turbulent flame speed parameter. The use of sub-models for:

1. Particles injection
2. Particles evolution
3. Plasma channel evolution
4. Electrical circuit
5. Restrike
6. Flame surface density tracking

was maintained (Figure 1.1) and improvements were carried out for the electrical circuit model. The Lagrangian model was coupled at each time-step with the Eulerian model to allow mutual influence.

1.1.1 Particles Injection Model

As in previous implementations [72, 118], among the three characteristic stages of ignition in SI engines, namely breakdown, arc and glow discharge, only the last two were modeled because of the negligible duration of the first one. At spark time, and after any possible restrike event, a set of 10 Lagrangian particles were introduced along the

spark-gap centerline, with the purpose to model properly the spark-channel geometry and its interaction with the local flow conditions. The particles were initialized in terms of temperature T_i and diameter d_i using the following relations [95, 105]

$$T_i = \left[\frac{1}{k}\left(\frac{T_{bd}}{T_u} - 1\right) + 1\right] T_u \tag{1.1}$$

$$d_i = 2\left[\frac{k-1}{k}\frac{E_{bd}}{p\, d_{gap}\left(1 - \frac{T_u}{T_i}\right)\pi}\right]^{\frac{1}{2}} \tag{1.2}$$

which exploit the breakdown stage features to provide an initialization of the arc stage. In particular, T_{bd} is the breakdown temperature (chosen equal to 60000 K, as suggested by Refael [95]), $k = 1.66$ is the plasma channel specific heat ratio, T_u the unburned gas temperature, d_{gap} the inter-electrode distance, p the gas pressure and E_{bd} the breakdown energy. This last value is computed by the electrical circuit model and assumes different values depending on the ignition event type (if first ignition or restrike), as it will be explained further in detail.

1.1.2 Lagrangian Particles Evolution Model

The particles introduced in the computational domain at spark time, or after any restrike event, were evolved considering the following three phenomena:

1. The convection imposed by the flow field distribution at the spark-gap.
2. The heat transferred by the hot plasma channel, generated during the breakdown stage, to the fresh surrounding mixture.
3. The heat released by the ignition system.

To take the convection from the gas flow into account, the equation [72]:

$$\frac{d\vec{x}_i}{dt} = \vec{U}_g \tag{1.3}$$

was solved for each particle, where $\vec{x}_i$ is the particle position vector and $\vec{U}_g$ is the local gas velocity. This last parameter was interpolated at the particle position adopting the cell-point-face technique [82], with the purpose to reduce the dependency of the

computed channel motion from the adopted mesh size. On the other hand, additional random contribution of local turbulence intensity were neglected from (1.3) to ensure a reasonable spark channel behaviour.

The initial hot plasma channel evolution and the further effect of the heat transfer from the electrical circuit were modelled by solving the mass conservation

$$\frac{dm_i}{dt} = 4\pi r_i^2 \, \rho_i \, s_{plasma} \tag{1.4}$$

and the radius variation

$$\frac{dr_i}{dt} = s_{plasma} + s_{therm} \tag{1.5}$$

equations, where m_i, r_i and ρ_i are the particle mass, radius and density, respectively. The equations (1.4) and (1.5) include no more the effects of the chemical reactions, as in the original model version [72, 118], but only the following contributions are considered:

1. Generation of an initial burnt field by the plasma channel fast expansion towards the surrounding fresh mixture (s_{plasma}).

2. Thermal support of the created spark-channel (s_{therm}).

The treatment of these different phenomena, and the consequently computation of s_{plasma} and s_{therm}, was carried out considering that:

1. The plasma channel expansion is experienced only at very high temperature conditions and under non-uniform temperature distribution inside the channel.

2. The thermal support available from the electrical circuit becomes important only when the spark channel temperature decreases and the plasma expansion tends to disappear. With such conditions inside the channel, the temperature can be assumed uniform and the composition at chemical equilibrium.

Therefore, these two mechanisms were modelled according to different approaches and a temperature threshold value of $3T_{ad}$ [39, 72, 113, 118], where T_{ad} is the adiabatic flame temperature, was used to switch from the first to the second one. Hence when the particle temperature T_i is:

1. $T_i > 3T_{ad}$, the plasma channel fast expansion governs the particle evolution and a suitable model (the plasma channel evolution model) computes the heat conduction inside the channel and the growth velocity s_{plasma}.

2. $T_i < 3T_{ad}$, the thermal support of the spark channel from the electrical circuit becomes relevant and the plasma expansion contribution (s_{plasma}) can be neglected. Consequently, the s_{therm} value for each particle is achieved by the resolution of an energy conservation equation under the hypothesis of uniform temperature and chemical equilibrium composition inside the channel.

For what concerns the s_{therm} computation, the following equation was used [72]

$$s_{therm} = \frac{V_i}{A_i}\left(\frac{1}{T_i}\frac{dT_i}{dt} - \frac{1}{p}\frac{dp}{dt}\right) \tag{1.6}$$

in which V_i and A_i are the particle volume and surface, while p is the pressure. The particle temperature variation $\frac{dT_i}{dt}$ was obtained solving the energy conservation equation

$$\frac{dT_i}{dt} = -\frac{\dot{m}_i}{m_i}\left(T_i - T_{ad}\right) + \frac{\dot{Q}_{spk_i}}{m_i c_p} + \frac{1}{\rho_i c_p}\frac{dp}{dt} \tag{1.7}$$

with c_p being the specific heat and $\dot{Q}_{spk_i}$ the energy deposition rate from the electrical circuit to the particle, reduced of the heat losses. This last term was computed as follows

$$\dot{Q}_{spk_i} = \frac{Q_{spk}\ \eta_{eff}}{n_{particles}} \tag{1.8}$$

where Q_{spk} and η_{eff} are the total heat transfer rate from the electrical circuit to the gas phase and the efficiency of this energy deposition, respectively, while $n_{particles}$ is the number the Lagrangian particles introduced along the spark gap and on which the thermal energy is distributed.

Finally, the Lagrangian particles evolution was interrupted upon the occurrence of one of the following possibilities:

1. Restrike event, because a new conductive path is generated between the electrodes, with the consequent introduction and evolution of a new set of particles.

2. Electrical circuit energy complete consumption, because no more energy is available for creation and/or support of any spark channel.

This modelling strategy, strictly coupled with the Eulerian flame evolution, allows also to take account of possible misfire events in case the electrical circuit is not able to generate a self-sustained flame kernel: this possibility could be verified in case of too low available energy at the secondary circuit or unfavourable flow conditions at the spark-gap.

1.1.3 Plasma Channel Evolution Model

Until the evolved Lagrangian particles satisfy the condition $T_i > 3T_{ad}$, the heat conduction from the hot plasma channel to the surrounding fresh mixture, which allows the creation of an initial fully burnt field, cannot be neglected. Therefore, the non-uniform temperature distribution inside the channel and its consequent growth rate (s_{plasma}) need to be modelled in detail, taking into account for actual plasma properties.

As performed in [72], all the tracked particles satisfying the condition $T_i > 3T_{ad}$ were assumed to have the same temperature distribution, computed by solving with a sub-cycle procedure the heat conduction equation for the space-dependent plasma temperature T_{plasma}

$$\frac{dT_{plasma}}{dt} = \alpha_{plasma}\,\nabla^2 T_{plasma} + \frac{\dot{Q}_{spk}\,\eta_{eff}}{\rho_{plasma}\,c_{p,plasma}\,V_{plasma}} \tag{1.9}$$

over a 1D axisymmetric mesh, representing a wedge of the gas region around the spark-gap centerline. In (1.9), α_{plasma}, ρ_{plasma}, $c_{p,plasma}$ and V_{plasma} are the thermal diffusivity, density, heat capacity and volume of the plasma channel, respectively. These properties were estimated employing the functions provided in [36] and assuming chemical equilibrium conditions [72], in order to take into account dissociation of molecules and atom ionization effects. Then, as suggested by Herweg and Maly [54], at each time step the plasma channel radius r_{plasma}, namely the end of the burnt field imposed over the 3D computational domain by the channel, is identified by the location on the 1D wedge mesh where the adiabatic flame temperature T_{ad} is detected. Hence, the s_{plasma} was computed as [72]

$$s_{plasma} = \frac{r_{plasma}\,(t + \Delta t) - r_{plasma}\,(t)}{\Delta t} \tag{1.10}$$

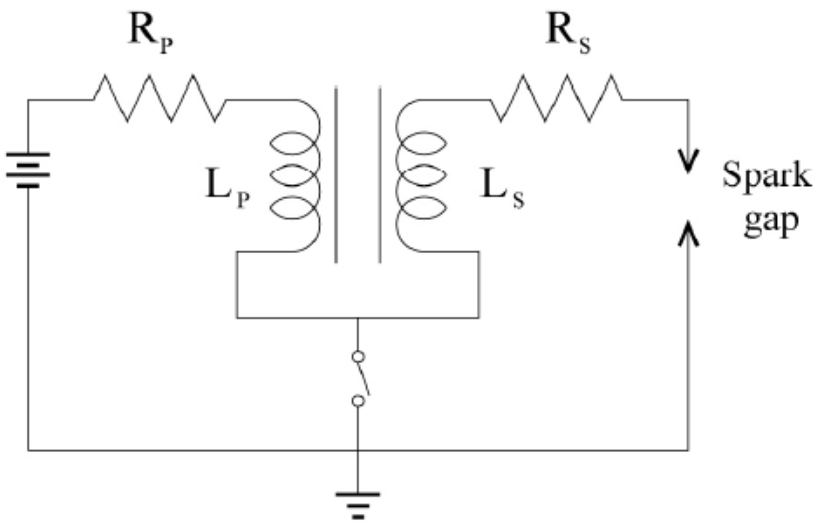

Figure 1.2: *Simplified scheme of a classical inductive ignition system characterized by a primary (subscript* P*) and a secondary (subscript* S*) circuit. The parameters R and L represent the equivalent resistance and inductance of both circuits, respectively [72].*

with Δt being the CFD simulation time-step.

1.1.4 Electrical Circuit Model

The capability to estimate the evolution of the main parameters of the adopted electrical circuit, since the spark time until the complete consumption of the stored energy, allows a detailed description of the energy transfer process to the fresh mixture through the generated spark channel. This is fundamental for a correct initialization of the burnt field in the Eulerian computational domain, especially under highly inhomogeneous flow conditions, lean mixtures and high turbulence/laminar flame speed ratios, in order to predict the propagation of fully turbulent flame or a misfire event.

The usual behavior of a generic inductive ignition system for SI engines, characterized by a primary and a secondary circuit as shown by Figure 1.2, can be summarized schematically as follows:

1. When the primary circuit is closed, a battery generates a primary current i_P allowing the storage of energy inside the primary inductance L_P.

2. At spark time, the primary circuit is opened and the energy stored in L_P is transferred to the secondary circuit.

3. The secondary circuit dissipates by Joule effect through both the spark-gap ($V_{IE}\,(t)\;i_S\,(t)$, where V_{IE} is the inter-electrode voltage fall and i_S the secondary current) and its other dissipative devices ($R_S\;i_S^2\,(t)$, with R_S being the secondary resistance) the whole received energy.

Therefore, taking example from already used approaches [37, 72], a suitable model was implemented. The presence of a primary and a secondary circuit was considered (Figure 1.2), although only the last one was modeled in detail. In fact, once known the amount of energy stored in the primary circuit at spark time E_P (which depends on the charging time), the energy transferred to the secondary circuit E'_S and available for the breakdown stage was simply computed as

$$E'_S = c_{eff} E_P \tag{1.11}$$

Here, $c_{eff} = 0.6$ is the transmission coefficient, which models the secondary inductance L_S dissipations during the energy transfer from primary to secondary circuit and whose value is estimated by [37]. According to the performed Lagrangian particles injection and evolution, only arc and glow stages were modelled. Therefore, the breakdown stage effects were considered only as initial condition for the available energy at the beginning of arc stage by the computation of the breakdown energy E_{bd} as carried out in [37, 39]

$$E_{bd} = \frac{V_{bd}^2}{C_{bd}^2\, d_{gap}} \tag{1.12}$$

Here, C_{bd} is the breakdown constant, a parameter expressed in $kV/(mJ^{1/2}mm^{1/2})$ and that needs to be calibrated, d_{gap} the inter-electrode distance in mm and V_{bd} the breakdown voltage in kV. This last parameter was computed as follows

$$V_{bd} = a + b\,\frac{p}{T_u} + c\,\frac{p}{T_u}\,d_{gap} \tag{1.13}$$

according to [39, 85]. The parameters a, b and c of (1.13) can assume different values depending if the modelled spark channel belongs to the first discharge (performed at the spark-time) or to any possible restrike phenomenon. The necessity of a variation for (1.13) parameters value can be deduced by:

- comparing typical experimental values of V_{bd} for the first discharge ($V_{bd} \approx 5 \div 20\ kV$, [61]) and for possible restrike events ($V_{bd} \approx 1.5 \div 4\ kV$, [54,61]), and
- considering that during the ignition process T_u and d_{gap} are constant, while p could also increase.

For the first discharge, as reported in [39,85], the parameters of (1.13) are the following: $a = 4.3\ kV$, $b = 136\ (kV\ K)\ /\ bar$ and $c = 324\ (kV\ K)\ /\ (bar\ mm)$.

Consequently, the available secondary circuit energy at the beginning of the arc stage was obtained from (1.11) and (1.12) as

$$\begin{cases} E_S\left(t = t_{spark-time}\right) = E'_S - E_{bd} \\ E_S\left(t = t_{restrike}\right) = E_S\left(t = t_{restrike}\right) - E_{bd} \end{cases} \tag{1.14}$$

where (1.14)a is valid for the first discharge and (1.14)b for any restrike, while the secondary circuit energy time variation was estimated as in [37]

$$\frac{dE_S\left(t\right)}{dt} = -R_S\ i_S^2\left(t\right) - V_{IE}\left(t\right)\ i_S\left(t\right) \tag{1.15}$$

Here, R_S assumes a constant value depending on the adopted electrical circuit type, while i_S and V_{IE} are time-dependent parameters computed at each time-step as

$$i_S\left(t\right) = \sqrt{\frac{2E_S\left(t\right)}{L_S}} \tag{1.16}$$

and

$$V_{IE}\left(t\right) = V_{cf} + V_{af} + V_{gc}\left(t\right) \tag{1.17}$$

The parameter L_S of (1.16) is a constant feature of the circuit, similarly to R_S, while V_{cf}, V_{af} and V_{gc} of (1.17) are the cathode, anode and gas-column voltage falls, respectively, whose modelling strategy is described in detail in Appendix A.

Concerning the possibility to experience heat losses at the electrodes during the spark-discharge, the approach used in [54,72] was followed. Hence, the computation of the parameter η_{eff}, already considered in (1.8) and (1.9) and representing the efficiency of the energy transfer process from the electrical circuit to the gaseous mixture, was

carried out according to

$$\eta_{eff} = \eta_0 + \frac{(\eta_\infty - \eta_0)\, U^3}{A + U^3} \tag{1.18}$$

The parameters η_0 and η_∞ represent the energy transfer efficiency under conditions of quiescent mixture and high velocity flow at the spark-gap ($> 15\ m/s$), respectively; together with the constant A, they assume different values depending on the discharge stage (see Table 1.1). On the other hand, U is simply the average velocity of the introduced Lagrangian particles, computed as in [72].

Table 1.1: *Parameters for η_{eff} computation. The parameters η_0 and η_∞ are in $\%$, while A is in m^3/s^3, [72].*

Parameter	Arc stage	Glow stage
η_0	36	8
η_∞	50	30
A	500	700

The proposed electrical circuit model was tested on the experimental data provided by Herweg and Maly [54] regarding two different electrical circuit systems:

1. the *Transistor Coil Ignition System* (TCI)
2. the *Capacitor Discharge Ignition System* (CDI)

The results were almost satisfactory, as it will be shown in Section 3.2.

1.1.5 Restrike Model

The restrike is a phenomenon that takes place when the inter-electrode voltage V_{IE} (1.17) becomes higher than a threshold value, which can be called restrike breakdown voltage V_{bd} ((1.13) with suitable parameters a, b and c), and a new spark channel is created along the spark-gap centerline. This can usually be experienced when, after the first discharge, a local high value of flow velocity elongates the spark channel, increasing the gas-column voltage fall V_{gc} ((1.17) and (A.2)) until the condition $V_{IE} > V_{bd}$ is reached (Figure 1.3). This phenomenon was observed by experimental tests [61] and its correct prediction is fundamental, because the sequential creation of several spark channel under local high flow conditions significantly influences the flame kernel development of engines with organized charge motion (e.g.: tumble or swirl) into the cylinder.

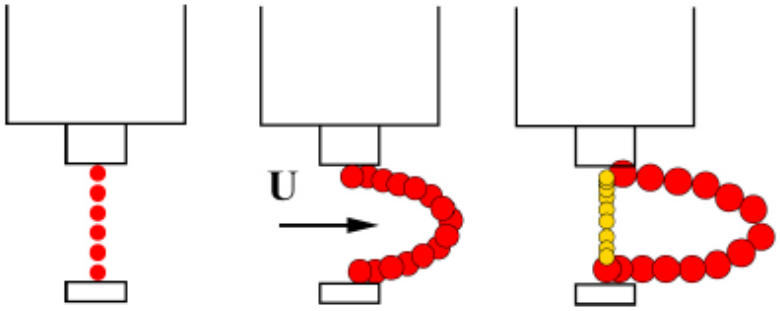

Figure 1.3: *The restrike phenomenon, [72].*

The implemented model allowed the restrike prediction thanks to the combined use of (1.13) and (1.17): when the condition $V_{IE} > V_{bd}$ was satisfied, a new set of Lagrangian particles was introduced between the electrodes. The particles representing the former spark channel were completely removed, in order to simulate the transition of the total heat transfer rate $\dot{Q}_{spk}$ to a new channel.

1.1.6 Flame Surface Density Tracking Algorithm

Following the approach proposed in [72] with the addition of some modifications, all the effects of the electrical circuit were introduced into the Eulerian domain through:

1. The computation of the flame surface density Σ.

2. The imposition of a fully burnt mixture inside the spark channel.

In fact, being Σ computed at each time-step, the flame kernel initialization performed on the Eulerian mesh by the ignition system was ensured. In particular, the Σ computation was carried out doing the following steps:

1. Placement of a spherical triangulated sphere at each particle position.

2. Variation of each triangulated sphere radius in order to match the related particle dimension.

3. Definition of flame surface as the total area of the non-intersecting triangular faces of the placed spheres (Figure 1.4).

4. Definition of the number of non-intersecting triangular faces $n_{f,cell}$ inside each cell of the computational mesh.
5. Computation of Σ for each cell as $\Sigma_{cell} = \left(\sum_{if=1}^{n_{f,cell}} A_{if} \right) / V_{cell}$, where A_{if} is the area of the i-*th* triangular face.

At the same time, a completely burnt mixture was imposed into the mesh cells located inside the evolved Lagrangian particles, in order to simulate the initial burned field generated by the spark channel. In case of particles smaller than the cell size only a fraction of burnt mixture was imposed to each involved cell, namely only the actual volume inside the particles was considered fully burnt.

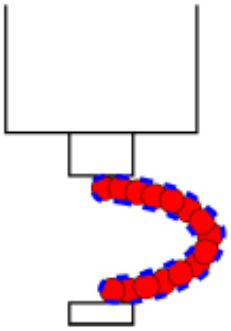

Figure 1.4: *The flame surface tracking technique, [72].*

When a restrike event happened, or at the end of the electrical circuit energy, the particles evolved since that time were removed and their contribution in terms of both Σ and burnt field were no more updated on the computational mesh with Lagrangian model information. This allows to leave the prediction of possible misfire events to the Eulerian model, in particular because of stretch, in case the electrical circuit will not be able to sufficiently sustain the early flame kernel growth.

1.2 Eulerian Model

The *Eulerian Model* definition was used to group together all that modelling strategies implemented to work into an Eulerian framework, as the 3D computational mesh. Consequently, it was possible to define five "environments" interacting together and in which different operations were carried out (Figure 1.1):

1. The main CFD code
2. The flame surface density model
3. The flame stretch model
4. The Lewis number model
5. The activation temperature model

This Eulerian framework was coupled at each time-step to the Lagrangian model:

- to provide the flow field ($\vec{U}$, k, ε and p, with k, ε being the turbulence kinetic energy and its dissipation rate) and mixture (T_u, T_{ad} and ρ_u) quantities necessary for the evolution of the spark channel particles,
- to receive information regarding the initial burnt field created by the spark discharge (Σ and the burnt mixture inside the channel).

A detailed description of the listed parts of the Eulerian model is provided in the following sub-sections.

1.2.1 Main CFD Code

The main CFD code is the environment that connects together all the implemented Eulerian sub-models. Its task is to manage the resolution of the flow field governing equations, namely the:

1. continuity,
2. momentum,
3. energy,
4. chemical species

ones, and the equations necessary for the laminar/turbulent flame modelling.

For this last topic, the Coherent Flamelet Model (CFM) proposed by Choi and Huh [28] was adopted, according to [72]. The model application was carried out by solving two transport equations:

1. the combustion normalized progress variable c,

2. the flame surface density Σ.

The source terms for the aforementioned equations were computed, respectively, as function of:

1. The unstretched laminar flame speed s_{u0}, the flame surface density Σ, and the stretch factor I_0, all suitable calculated for each cell of the computational domain.

2. The flame surface density Σ_{cell}, computed by the Lagrangian model during the spark discharge, and the flame surface density production P_{FSD} and destruction D_{FSD} terms, provided by the related model.

1.2.2 Flame Surface Density Model

The implemented flame surface density model provides the values of the production P_{FSD} and destruction D_{FSD} terms for the Σ equation resolution. Because the CFM model was used, these terms were computed as follows [28, 72]:

$$P_{FSD} = \alpha_{FSD} \frac{u'}{l_{tc}} \tag{1.19}$$

and

$$D_{FSD} = \beta_{FSD}\, s_{u0} \frac{\Sigma^2}{c\,(1-c)} \tag{1.20}$$

where α_{FSD} and β_{FSD} are model constants that need a suitable calibration, u' is the turbulence intensity and l_{tc} is a length scale introduced for dimensional reasons and set according to [28].

1.2.3 Flame Stretch Model

The unstretched laminar flame velocity s_{u0} can be computed by several correlations [78, 79], like the Gülder one [52] which was used in this work, as function of the fuel type, the local equivalence ratio, the temperature and the pressure. However, the calculated value does not take into account of:

- Curvature effects due to the flame front geometry (e.g.: a curved expanding flame).

- Strain effects due to the *flame front/flow field* interaction.

These effects are grouped in a single physical process, called flame stretch, which has to be modelled for a correct laminar flame speed estimation.

Hereafter, two different approaches for the flame stretch phenomenon modelling are proposed, both function of the same parameters:

- flame curvature,
- turbulence intensity,
- Lewis number,
- activation energy of the overall combustion reaction and
- flame thickness.

The first flame stretch model was obtained starting from the equations and assumptions of Bradley, Lau and Lawes [13, 102], while the second one was proposed by Herweg and Maly [54, 102].

The behaviour of aforementioned models was investigated over a simplified combustion chamber at different equivalence ratios and turbulence intensities, as it will be described in Section 3.1.2. Although no comparisons with experimental findings were performed, the achieved results show a good response of both stretch models with respect to theoretical considerations.

Bradley, Lau and Lawes stretch model Following the approach proposed in [118], the actual laminar flame speed s_u was computed according to Bradley, Lau and Lawes [102]:

$$s_u \approx s_{u0} \frac{1 - K\ Ma}{1 + \frac{c}{R}\ \delta_l\ Ma} \tag{1.21}$$

with δ_l being the laminar flame thickness and $c = 1$ the parameter to fit (1.21) for cylindrical flame shapes. This choice was justified by the well-known knowledge that the flame stretch effects are predominant during the initial kernel growth stage, where the local curvature effects are high. Hence, during this initial expansion, the flame has a similar shape to the modelled spark channel geometry, which is cylindrical. For more details about the validity of (1.21), please refer to Section 3.1.1.

The dimensionless Karlovitz stretch factor K was computed as in [13]

$$K = 0.157 \left(\frac{u'}{s_{u0}} \right)^2 Re_t^{-0.5} \tag{1.22}$$

where $Re_t = (u' l_t) / \nu$ is the turbulent Reynolds number, with l_t being the integral length scale of turbulence and ν the kinematic viscosity. The parameter $1/R$, known as the local flame curvature, was obtained on the Eulerian domain using the following relation

$$\frac{1}{R} = \left| \nabla \cdot \left(\frac{\nabla c}{\|\nabla c\|} \right) \right| \tag{1.23}$$

where $\nabla c / \|\nabla c\|$ is the flame front perpendicular direction.

Recent DNS studies [50] figured out that the flame speed is a local property when flows are multi-dimensional and unsteady, because the mass flow rate through the combustion region is not constant and varies through the flame. Consequently, its prediction under such conditions has to be completely carried out into an Eulerian framework, in order to avoid possible errors derived by a non-local approach. Moreover, in [50], the flame stretch formulation described by (1.21)-(1.23) and obtained through an asymptotic analysis was tested against DNS results. The conclusions showed how the Bradley, Lau and Lawes approach must be applied using fields values evaluated over an isotherm sufficiently close to the flame burnt side. Therefore, considering that this work adopted a RANS turbulence modelling and the inner flame front is not resolved, fields value of fully burnt products in the flame brush region were used.

Hence, the Markstein number Ma of (1.21) was evaluated into fully burnt products according to [50]:

$$Ma = \left[\frac{1}{\gamma} \ln \left(\frac{1}{1-\gamma} \right) + \frac{1}{2} Ze \left(Le - 1 \right) \frac{1-\gamma}{\gamma} \int_0^{\frac{1}{1-\gamma}} \frac{\ln (1+x)}{x} dx \right] - \ln \left(\frac{1}{1-\gamma} \right) \tag{1.24}$$

where $\gamma = (\rho_u - \rho_b) / \rho_u$ is the expansion ratio, being ρ_b and ρ_u the burned and unburned density, respectively, x is a dummy variable of integration, and Ze is the Zel'dovich number, computed as [10]

$$Ze = \frac{T_{act} \left(T_{ad} - T_u \right)}{T_{ad}^2} \tag{1.25}$$

Both the Lewis number Le in (1.24) and the activation temperature T_{act} in (1.25) were evaluated by suitable models.

Herweg and Maly stretch model Herweg and Maly, for their spherical flame kernel model, computed the actual laminar flame speed s_u through the following expression [54, 102]:

$$s_u = s_{u0} \left\{ 1 - \left[\left(\frac{\delta_l}{15\, l_t} \right)^{\frac{1}{2}} \left(\frac{u'}{s_{u0}} \right)^{\frac{3}{2}} + c\, \frac{\delta_l}{s_{u0}} \frac{1}{R} \frac{dR}{dt} \right] \left[\frac{1}{Le} + \left(\frac{Le - 1}{Le} \right) \frac{T_{act}}{2\, T_{ad}} \right] \right\} \tag{1.26}$$

in which $c = 1$ allows to fit cylindrical flame shapes, as previously discussed for (1.21). Similarly to conclusions drawn in Section 3.1.1 for Bradley, Lau and Lawes' laminar flame speed correction (3.15), the c parameter assumes the value of

- $c = 1$ if the initial flame shape is *cylindrical*,
- $c = 2$ if the initial flame shape is *spherical*.

1.2.4 Lewis Number Model

In the context of premixed combustion, various instability modes can affect the flame front. One of these is the thermo-diffusive instability, which is controlled by the relative importance of the heat diffusion with respect to the deficient reactant one [91], namely by the Lewis number, defined as the ratio of these magnitudes. However, this definition of the Lewis number shows problems in presence of a stoichiometric mixture, where the deficient reactant cannot be clearly defined. Moreover, the Lewis number of a common hydrocarbon (like propane) can experience a steep variation of its value when computed following this approach for a mixture with equivalence ratio 0.9 or 1.1.

Joulin and Mitani [58] noticed from experiments that the flame behaviour gradually changes as the equivalence ratio varies across the stoichiometric condition. This means that the combustion process is controlled not only by the deficient component of the mixture, but also by the abundant one; consequently, also the effect on the flame stability of this last component should be considered.

Accordingly, the implemented strategy for the prediction of the Lewis number of a

premixed mixture was that proposed in [58]:

$$Le = Le_{def} + H\left(Le_{abu} - Le_{def}\right) \tag{1.27}$$

where Le_{def} and Le_{abu} are the Lewis number defined with respect to the deficient and abundant reactant diffusivity, respectively. The parameter H is evaluated as

$$H = n\,\frac{G\left(m, n-1, A\right)}{G\left(m, n, A\right)} \tag{1.28}$$

with

$$G\left(m, n, A\right) = \int_0^\infty x^m \left(x + A\right)^n e^{-x} dx \tag{1.29}$$

Equations (1.28) and (1.29) are both function of m and n, which are the order of reaction of the deficient and abundant reactant. The value of A can be computed with the following expression

$$A = Ze\,\frac{y}{Le_{abu}} \tag{1.30}$$

in which $y = (\phi - 1)$ if $\phi > 1$, otherwise $y = \left(\frac{1}{\phi} - 1\right)$, being ϕ the equivalence ratio. The Zel'dovich number Ze is that of (1.25).

As can be noticed from (1.27), the Lewis number of a premixed mixture defined according to Joulin and Mitani [58] can be considered a weighted average of the Lewis number values computed only with respect to the deficient and abundant reactant.

1.2.5 Activation Temperature Model

The activation temperature of a premixed mixture was estimated by using the slope coefficient of the modified Arrhenius-type equation proposed in [19]

$$\ln s_{u0} = c - \frac{T_{act}}{2}\,\frac{1}{\bar{T_f}} \tag{1.31}$$

where T_f is the average flame temperature defined as

$$\bar{T_f} = T_u + 0.74\left(T_{ad} - T_u\right) \tag{1.32}$$

In other words, (1.31) is equivalent to a line equation $y = c+ax$ which is comparable to the least-square regression line of several values of $\ln s_{u0}$ obtained at different unburned mixture temperatures T_u. In fact, $\bar{T}_f$ is only function of T_u, because at fixed mixture composition $T_{ad} = f(T_u)$.

Values of T_{act} were computed before running any numerical simulation and written into a look-up table as function of pressure (p), equivalence ratio (ϕ) and exhaust gas recirculation (EGR).

1.3 Summary

The proposed CFD model, developed for premixed SI engines combustion, is characterized by a *comprehensive* structure with an *Eulerian-Lagrangian* run-time coupling. The Lagrangian framework allows to account for the electrical circuit effects with the minimum computational effort. The final objective was to simulate in detail the spark-discharge evolution and the further turbulent flame propagation.

Specific sub-models are included to properly consider each phenomenon affecting the combustion process. This methodology has a twofold advantage: it allows to handle the interplay between different and complex phenomena with a clear and schematic work-flow, providing at the same time unlimited and smooth extendibility of current modelling capabilities.

The developed approach accounts properly for the influence of:

1. the electrical circuit features,
2. possible laminar flame instabilities,
3. *flame-turbulence* interaction

on the ignition and the further combustion process. In particular:

- Specific improvements concerned the first two aforementioned phenomena, such as the effective Lewis number prediction of a premixed mixture and different strategies to model the arc and glow phases of the spark-discharge.
- On the other hand, the third phenomenon was improved thanks to a modified strategy to consider flame stretch effects into ignition and premixed combustion prediction. In particular, the thermal effects of the electrical circuit (modelled by a set

of Lagrangian particles, introduced to mimic the plasma channel shape) were fully decoupled from the chemical contribution of the laminar/turbulent flame speed. This last aspect was completely carried out by the Eulerian CFD solver, where a flame stretch model, recently verified by DNS studies, was adopted.

The validation of the proposed methodology will be carried out in Chapters 3 and 4.

CHAPTER 2

The Artificially Thickened Flame Model

Large Eddy Simulations (LES) are widely considered an helpful methodology to address the analysis of unsteady reacting flows. In fact, turbulent combustion phenomena like blow-off, flashback and general instabilities [75, 89] cannot be detected by a RANS turbulence modelling, because only time-averaged quantities are solved. Hence, for such problems, LES technique appears more suitable because it computes explicitly the flow field largest structures, which dominate and control reacting flows affected by instabilities [24, 90]. A practical example is the Cyclic Combustion Variability (CCV) analysis of an IC engine, where the explicit computation of *largest eddies - flame* interaction is fundamental for a correct estimation of this phenomenon.

In this context of LES turbulence modelling, numerical simulations of turbulent premixed reacting flows are not able to resolve the inner structure of the flame front on common computational grids, because the reaction zone is typically thin (premixed flame thickness: $\delta_l^0 \approx 0.1 \div 1\ mm$) and generally smaller than the LES mesh size

Δ_{mesh}.

To overcome this difficulty the Artificially Thickened Flame Model (ATFM) seems a promising solution: it increases artificially the flame thickness to allow the reaction layer resolution on usual computational grids, solving the aforementioned difficulty. However, the artificial thickening procedure affects the LES-resolved flame/turbulence interaction, hence additional modelling efforts are required.

In this chapter, the Artificially Thickened Flame (ATF) concept is firstly analyzed to deeply understand the ATFM theoretical basis. Then a detailed description of the main sub-models involved in the ATFM application is performed, as:

- the Thickening Factor *F* and Efficiency Function *E* computational strategies,
- the Flamelet Progress Variable (FPV) approach to tabulate the chemical kinetics and the flame sensor.

Therefore, as a result of the ATFM coupling with a chemical kinetics tabulation strategy, the transport equations of the Progress Variable Y_c and Mixture Fraction Z are introduced. Finally, additional numerical strategies used by the ATFM to evaluate the Sub-Grid Scale (SGS) turbulence intensity and to filter the LES fields are presented.

2.1 The Artificially Thickened Flame concept

The basic idea of the ATFM is to consider a flame thicker than the actual one, in order to allow its resolution on commonly used mesh grids, but keeping constant its laminar flame speed s_l^0 [22, 84]. In fact, from simple theories of laminar premixed flames [68, 114] it is possible to consider:

$$\begin{cases} s_l^0 \propto \sqrt{D\,\bar{\omega}} \\ \delta_l^0 \propto \frac{D}{s_l^0} \propto \sqrt{\frac{D}{\bar{\omega}}} \end{cases} \tag{2.1}$$

where s_l^0 and δ_l^0 are the laminar flame speed and thickness, respectively, while D is the molecular diffusivity and $\bar{\omega}$ is the mean reaction rate. Hence, an increase of δ_l^0 by a factor F, called *thickening factor*, keeping constant s_l^0 can be achieved by replacing at the same time:

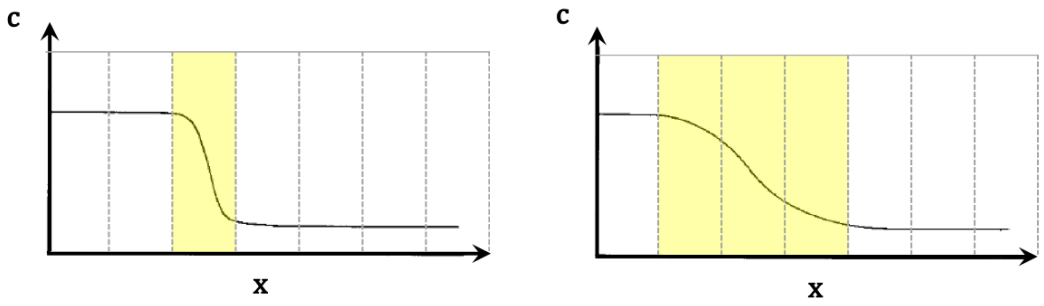

Figure 2.1: *Normalized progress variable* c *distribution of a premixed 1D flame: original unthickened flame (a) and artificially thickened flame (b). Grey vertical dashed lines represent the mesh spacing while yellow regions highlight flames mesh resolution.*

- the diffusivity D with $F\ D$
- the mean reaction rate $\bar{\omega}$ with $\bar{\omega}/F$

in (2.1). As a consequence, the following modified relations are obtained:

$$\begin{cases} s_l^0 \propto \sqrt{\frac{F\ D\ \bar{\omega}}{F}} \propto \sqrt{D\ \bar{\omega}} \\ \delta_l^0 \propto \sqrt{\frac{F^2\ D}{\bar{\omega}}} \propto F\ \sqrt{\frac{D}{\bar{\omega}}} \end{cases} \tag{2.2}$$

where the thickening factor F allows to adapt the flame thickness to a generic computational mesh without modifications of the s_l^0.

From a practical point of view, the artificial thickening of a flame can be achieved by performing a coordinates transformation (in terms of both time and space) along the flame front normal direction. This operation will affect all simulated fields, because the change of coordinates involves the computational domain. Taking as example a 1D flame (Figure 2.1a), if its progress variable balance equation

$$\frac{\partial \rho Y_c}{\partial t} + \frac{\partial \rho U Y_c}{\partial x} = \frac{\partial}{\partial x}\left[\rho D \frac{\partial Y_c}{\partial x}\right] + \dot{\omega}_c \tag{2.3}$$

is modified by replacing x with $x' = F\ x$ and t with $t' = F\ t$, the following expression is achieved

$$\frac{\partial \rho Y_c}{\partial t'} + \frac{\partial \rho U Y_c}{\partial x'} = \frac{\partial}{\partial x'}\left[\rho\,(F\ D)\,\frac{\partial Y_c}{\partial x'}\right] + \frac{\dot{\omega}_c}{F} \tag{2.4}$$

where U is the fresh gases velocity. Then, considering a steady-state propagating lam-

inar flame (in which $\partial/\partial t = \partial/\partial t' = 0$ and $\rho U = \rho_0 s_l^0$, being ρ_0 the fresh gases density), (2.4) has the same solution of (2.3) but thickened by a factor F, as shown in Figure 2.1, [22, 31].

In the light of what observed so far, the artificially thickened flame approach seems very attractive, because:

1. No restricting assumptions regarding the flame topology are contained in its theoretical derivation, therefore it can be applied to premixed flames [100], lifted flames [70] or ignition sequences [8].

2. The chemical reactions happening inside the flame front can be described, from a numerical point of view, as in a Direct Numerical Simulation (DNS) on a computational grid generated for LES. In fact, by choosing an appropriate F value, the inner flame structure can be modelled also on rather coarse meshes.

3. The reaction rate term of (2.4) can be expressed by using the Arrhenius law, hence different phenomena could be taken into account without requiring specific submodels (e.g.: *flame-wall* interaction, ignition, flame stabilization, etc.).

However, the flame thickening procedure generates also some drawbacks that must be faced carefully:

1. When the flame is thickened from δ_l^0 to $\delta_l^1 = F\delta_l^0$, the chemical time estimated as $\tau_c = \delta_l^0/s_l^0$ becomes $F\tau_c$. Accordingly, the *flame-turbulence* interaction is modified because the Damköhler number

$$Da = \frac{\tau_t}{\tau_c} = \frac{l_t}{u'}\frac{s_l^0}{\delta_l^0} \tag{2.5}$$

   which compares the turbulent time τ_t to chemical one, is decreased by a factor F, becoming Da/F. This has a twofold effect on the *flame-turbulence* interaction [4, 5, 26, 27, 31]:

   - Eddies smaller than the thickened flame thickness $\delta_l^1 = F\delta_l^0$ have no more interactions with the flame; consequently, their effects have to be included in a sub-grid scale model.

- Eddies larger than the thickened flame thickness $\delta_l^1 = F\delta_l^0$ still interact with the flame front, but their efficiency may be affected.

2. Theoretically, the thickening approach can be used to face complex chemistry problems, because (2.3) and (2.4) are valid for any species as long as molecular fluxes can be described by Fick's law. However, all chemical species have to be resolved on the computational grid, inducing a prohibitive thickening compared to flow motion or system size if radicals or intermediate species have to be solved [31].

3. In case of generic stratified mixtures, if concentration gradients occur without combustion (e.g. a mixing zone not overlapped to flame front) a modification of the diffusion term would dissipate gradients un-physically, altering a correct pure mixing simulation. This could negatively impact on the flame propagation prediction because the reaction layer may not experience the real mixture stratification.

The aforementioned drawbacks are faced and solved in the following Subsections as here briefly described, respectively:

1. An *efficiency function* E, derived from a DNS analysis of the flame-vortex interplay, is introduced as a sub-grid scale model to compensate the modified *flame-turbulence* interaction (Section 2.3).

2. The ATF concept is coupled with a *tabulation strategy* to include detailed chemistry effects into an LES framework without a prohibitive thickening of the flame. This approach allows a rather accurate description of the flame structure and propagation. In fact, if a reasonable number of grid cells is allocated inside the flame thickness, a correct reaction rate prediction is achieved (Section 2.4).

3. A *flame sensor* is used to detect the flame front position and modify the diffusion term accordingly, without affecting the pure mixing regions (Section 2.4.1).

2.2 The Thickening Factor *F*

Following the flame thickening concept [26,27,31,66,67], to achieve a proper representation of the flame structure on LES typical meshes, a thickening factor F is introduced into the transport equation of:

- *species mass fractions*, if the resolution of each chemical species is carried out on the computational mesh;
- *progress variable*, in case a chemical kinetics tabulation strategy is adopted;
- *mixture fraction* and *enthalpy*, for consistency with the change of coordinate system performed on the flame by the ATF strategy.

In the following subsections two different modelling strategies for the thickening factor are described: the adoption of a constant F value on the whole mesh domain, or the use of an adaptive F value changing in accordance with the local mesh cell size.

2.2.1 Constant thickening

The most conservative and simple approach for the thickening factor computation is to define a global F value which is valid for the whole CFD mesh domain.

Remembering the role of the thickening factor and considering that a generic LES mesh could be characterized by a large range of different grid sizes, a single global F value can be defined with respect to the coarsest mesh cell as

$$F = n_{gp} \frac{\sqrt[3]{V_{cell,max}}}{\delta_l^0} \tag{2.6}$$

where n_{gp} is the user-defined number of grid points (or cells) for the flame structure resolution, $V_{cell,max}$ the volume of the coarsest mesh cell and δ_l^0 the original (laminar) flame thickness. Here the side of the coarsest mesh cell is computed from its equivalent cubic volume. Concerning the n_{gp} value, its computation is usually carried out by running simple simulations of a steady-state 1D laminar flame. With such technique, different flame resolution are quickly tested and the minimum n_{gp} ensuring the correct laminar flame speed reconstruction is selected.

The choice of (2.6) definition is the result of a conservative approach which allows to guarantee the minimum number of desired cells (n_{gp}) for the flame front resolution, whatever cell dimension is encountered by the propagation of the reaction zone. In fact, in case the flame reaches a mesh region characterized by finer cells, the reaction zone will be thickened over more cells than the user-defined n_{gp} ones, with a consequent higher flame thickness resolution.

The error introduced by an F definition based on an average cell volume will be shown in next Section 2.2.2.

2.2.2 Grid adaptive thickening

As previously mentioned, generic LES meshes are usually featured by a large range of different grid sizes. As example, if the combustion chamber of a SI engine has to be investigated, a local high level of mesh refinement is required to reproduce its geometrical details (e.g. spark-plug electrodes, piston side crevices). On the other hand, a coarser mesh could be adopted at the combustion chamber center, in order to reduce the global computational effort.

In this context, the definition of a unique and global thickening factor as defined by (2.6) could be rather limiting because it introduces an high level of flame thickening where cells are refined. Indeed, if for example 5 grid points are enough to reproduce the laminar flame speed ($n_{gp} = 5$):

- in the coarsest mesh region the reaction layer will be solved with the minimum required resolution,

- in a local mesh region where the cell size is halved with respect to the coarsest one, the flame thickness resolution will be of 10 grid points.

According to the ATF concept, no error will be introduced. However, in the fine mesh region the *flame-turbulence* interaction will be stronger influenced by the thickening procedure because the *thickened flame thickness-local mesh size* ratio $\delta_l^1/\Delta_{cell,local} = (F\delta_l^0)/\Delta_{cell,local}$ will be doubled than in the coarse region. Hence, considering that $\Delta_{cell,local}$ is usually the LES fields filter and it is related to the smallest solved turbulence scale, the adoption of a constant thickening approach will introduce a not necessary modelling effort of the *flame-turbulence* interaction where the mesh refinement is high.

Therefore, a thickening factor definition based on the local mesh resolution is desirable in order to minimize the modelling effort, namely the turbulent flame speed uncertainty.

As first step, it is comfortable to define the maximum grid size $\Delta_{cell,lim}$ that allows

a correct resolution of the flame front

$$\Delta_{cell,lim} = \frac{\delta_l^0}{n_{gp}} \tag{2.7}$$

where n_{gp} is the minimum number of grid points inside the laminar flame front δ_l^0 which ensures a correct laminar flame speed reconstruction. As for the constant thickening approach (see Section 2.2.1) the n_{gp} value is user-defined and it is generally determined by running simple simulations of a steady-state 1D laminar flame.

Then, the local grid-adaptive thickening factor F can be evaluated as follows [67]

$$F = max\left(1, \frac{\sqrt[3]{V_{cell}}}{\Delta_{cell,lim}}\right) \tag{2.8}$$

being $\sqrt[3]{V_{cell}}$ the cell side computed from its equivalent cubic volume. Here, if the cell size is comparable to the coarsest mesh spacing allowing a correct flame reconstruction then $F \approx 1$ (very high level of refinement), otherwise the thickening factor increases with the grid coarsening.

Finally, the thickening factor value computed on each cell from (2.8) can be locally volume-averaged on the cell itself and its neighbors. This technique allows an additional spatial smoothing of the F value, avoiding strong discontinuities within the flame [67].

A simple test of the grid adaptive technique was performed by Kuenne [67] and shown in Figure 2.2. Kuenne analyzed a 1D flame propagating over a mesh characterized by a cell size variation (Figure 2.2, bottom). In particular, the flame was initialized at the mesh right end to propagate against the fresh mixture towards the left through the central coarse grid region. Three different techniques for the F computation were investigated, in particular the *grid adaptive* strategy was compared to:

- a constant thickening based on the *coarsest cell* size,
- a constant thickening based on an *average cell* size.

The achieved results in terms of CO_2 mass fraction distribution are shown in Figure 2.2 with a red, blue and black line, respectively.

As it is possible to notice (Figure 2.2), taken as a reference the constant thickening

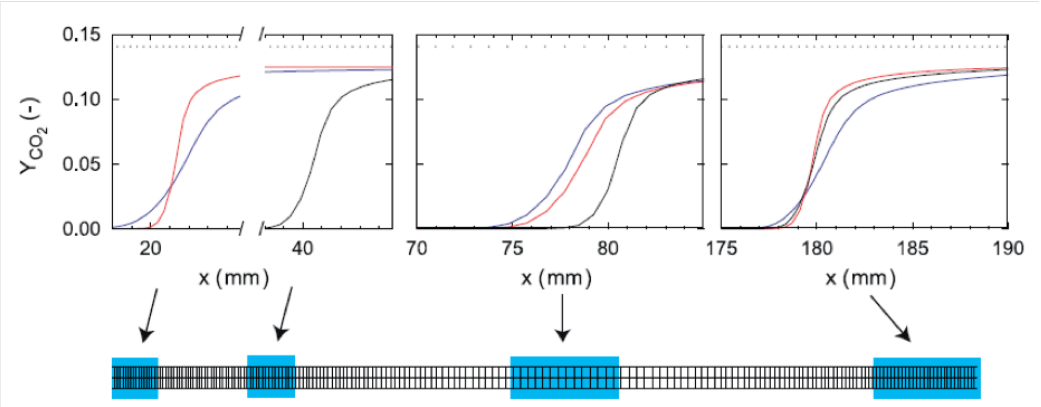

Figure 2.2: *1D simulation of a flame propagating from right to left using different thickening strategies: spatial CO_2 mass fraction distribution at three different time steps (top) showing the flame position at the marked regions on the computational domain (bottom). The F values of displayed Y_{CO_2} trends are computed with: a grid adaptive thickening (*red*), a constant thickening based on the coarsest cell (*blue*), a constant thickening based on an average cell size (*black*), [67].*

approach (Section 2.2.1), the grid adaptive technique is able to adapt the flame thickening with respect to the local grid size ensuring, at the same time, a correct laminar flame speed reconstruction.

On the other hand, it is clarified how the strategy to define a constant thickening factor over an average cell size introduces considerable errors in the laminar flame speed simulation. In fact, as shown in Figure 2.2, when the flame approaches the central coarse grid region this strategy (black line) is not able to thicken the flame over an adequate number of grid points and the correct flame resolution is lost.

2.3 The Efficiency Function *E*

One of the ATF concept drawbacks is the modified interaction between the flame front and the turbulence field generated by the flame thickening procedure (Section 2.1).

Therefore, in order to compensate the lost *flame-turbulence* interaction in terms of total flame surface reduction (namely, the lost wrinkling effect), an *efficiency function* E was proposed to increase the flame speed with no additional modification to its thickness. Starting form (2.2), which represents the basic idea of the ATF concept, if the diffusivity D as well as the mean reaction rate $\bar{\omega}$ are multiplied by E the following

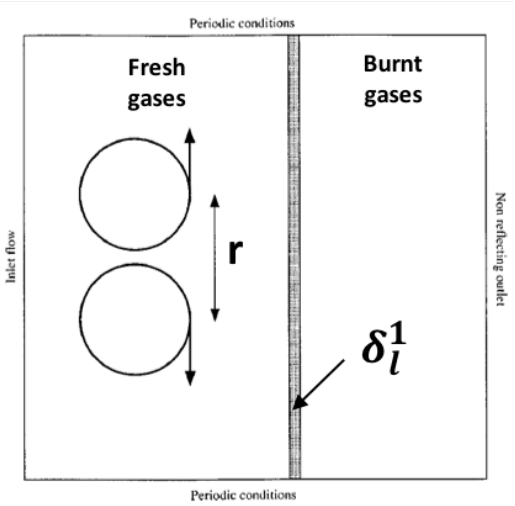

Figure 2.3: *DNS configuration for the* flame-vortex *interaction analysis: a pair of counter-rotating eddies (size* r*) interacts with an initially planar laminar premixed flame, whose flame thickness is* $\delta_l^1 = F\delta_l^0$*, [31].*

relationships are achieved

$$\begin{cases} s_l^0 \propto \sqrt{E^2\ D\ \bar{\omega}} \propto E\ \sqrt{D\ \bar{\omega}} \\ \delta_l^0 \propto F\ \sqrt{\frac{E\ D}{E\ \bar{\omega}}} \propto F\ \sqrt{\frac{D}{\bar{\omega}}} \end{cases} \tag{2.9}$$

where a thickened flame of thickness $\delta_l^1 = F\delta_l^0$ is propagated with a corrected local flame speed of $s_l^1 = Es_l^0$. This last s_l^1 value includes the contribution of:

1. the occurring chemical reactions (s_l^0) and of
2. the lost wrinkling effect ($E > 1$) in terms of flame surface, due to the artificially flame thickening procedure,

hence $s_l^1 \geq s_l^0$. In other words, s_l^1 is the laminar flame speed increased of the fraction of turbulent combustion velocity which needs to be modeled.

As a consequence, the efficiency function E modelling became an important topic for dealing with a correct application of the ATFM. This problem was firstly addressed by Colin and Angelberger [5,31] (Section 2.3.1), then also by Charlette (Section 2.3.2), but all of them based their modelling effort on DNS results of elementary *flame-vortex* interactions. In fact, the first common target was to get more insight on how the *flame-turbulence* interaction is affected by the flame front thickening procedure in order to

Table 2.1: *Analyzed conditions with DNS of* flame-vortex *interactions, [5, 31]. The vortex size r is estimated from the distance between the two vortex cores (see Figure 2.3); v' is the vortex velocity, the computational domain is $l_x \times l_y$ and the grid mesh contains $n_x \times n_y$ points.*

Test type	Test $[n.]$	r/δ_l^0	v'/s_l^0	F	r/δ_l^1	l_x/l	l_y/l	n_x	n_y
A	A1	30	8	1.0	30	3	3	1025	1025
	A2	30	8	2.5	12	6	3	801	401
	A3	30	8	5.0	6	3	3	201	201
	A4	30	8	10.0	3	3	3	129	129
	A5	30	8	25.0	1.2	10	3	257	129
B	B1	30	4	1.0	30	3	3	1025	1025
	B2	30	4	2.5	12	6	3	801	401
	B3	30	4	5.0	6	3	3	201	201
	B4	30	4	10.0	3	3	3	129	129
	B5	30	4	25.0	1.2	10	3	257	129
C	C1	30	0.8	1.0	30	3	3	1025	1025
	C2	30	0.8	2.5	12	6	3	801	401
	C3	30	0.8	5.0	6	3	3	201	201
	C4	30	0.8	10.0	3	3	3	129	129
	C5	30	0.8	25.0	1.2	10	3	257	129
D	D1	60	8	10.0	6	6	6	257	257
	D2	60	1.6	10.0	6	6	6	257	257

propose a suitable SGS model to take into account these lost effects.

In particular, DNS results concerning the effect of a pair of counter-rotating vortexes interacting with an initially planar laminar flame were used, as shown in Figure 2.3, [5, 31, 93]. By keeping constant the *vortex size-initial laminar flame thickness* ratio r/δ_l^0:

- three different values of vortex to laminar flame speed ratios v'/s_l^0 (*Tests A*, *B* and *C*),
- five values of thickening factor F ($F = 1.0$, 2.5, 5.0, 10.0 and 25.0),
- one additional value of r/δ_l^0 (*Tests D1* and *D2*)

were investigated. The parameters of performed DNS tests are summarized in Table 2.1, while the main results are shown by Figures 2.4 and 2.5.

First of all, in Figure 2.4a, it is clarified how in presence of a vortex to laminar flame speed ratio of $v'/s_l^0 = 0.8$ (see *Tests C* of Table 2.1) an increase of the thickening factor F produces a contemporary reduction of the total reaction rate $\dot{\omega}_T$ and of related total flame surface $S_{f,T}$. This result demonstrates how the artificial thickening of a flame does not affect the local reaction rate but influences the global flame behaviour in terms of a reduced wrinkling effect.

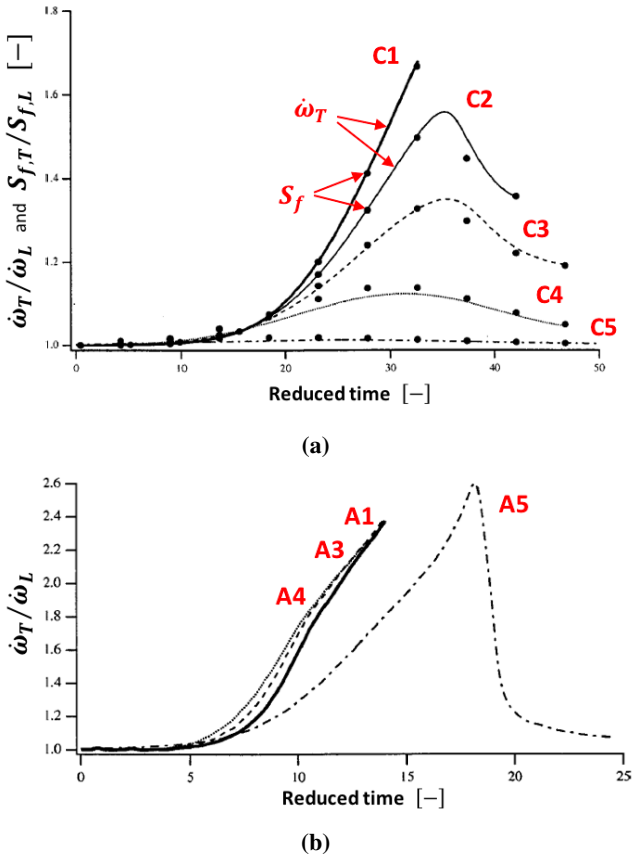

Figure 2.4: *Time evolution of the total reaction rate $\dot{\omega}_T$ during the DNS* flame-vortex *interaction for* Tests C *(a) and* Tests A *(b) of Table 2.1 at the following thickening factors: $F = 1$ (—, C1 and A1), $F = 2.5$ (—, C2), $F = 5$ (----, C3 and A3), $F = 10$ (· · ·, C4 and A4) $F = 25$ (–·–, C5 and A5). In Figure (a) also the related total flame surfaces $S_{f,T}$ are plotted (•). Total reaction rate and total flame surface values are made non-dimensional by the corresponding planar laminar flame quantities ($\dot{\omega}_L$ and $S_{f,L}$, respectively). Times are reduced using the characteristic laminar flame time δ_l^0/s_l^0.*

Then, Figure 2.4b shows how the same thickening factor variation performed on ten times stronger eddies ($v'/s_l^0 = 8$, see *Tests A* of Table 2.1) does not affect too much the global flame behaviour; the wrinkling is influenced only if prohibitive F values are applied (*Test A5*).

Finally, an analysis of the mean flame stretch (Figure 2.5) demonstrates how at each investigated vortex intensity v'/s_l^0 (*Tests A*, *B* or *C*, Table 2.1) the vortex to flame relative dimension r/δ_l^0 influences the eddies capability in making strain on the flame. This numerical results confirms how eddies larger than the thickened flame thickness $\delta_l^1 = F\delta_l^0$ still interact with the flame front, but their efficiency is affected (Section 2.1). With the purpose to numerically reproduce the mean flame stretch trends observed in

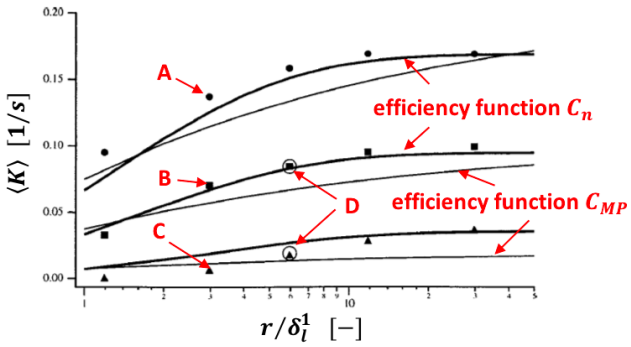

Figure 2.5: *Flame stretch $\langle\kappa\rangle$, induced by a pair of vortexes during the DNS* flame-vortex *interaction, as function of the length scale ratio r/δ_l^1 (see Figure 2.3). The following results of Table 2.1 are reported:* Tests A *(●),* Tests B *(■),* Tests C *(▲),* Tests D *(◯). The bold solid line (—) represents the efficiency function C_n of* (2.10) *proposed by Angelberger and Colin [5, 31], while the solid line (—) depicts the behaviour of Meneveau and Poinsot's efficiency function C_{MP} [77].*

Figure 2.5, Meneveau and Poinsot introduced the efficiency function C_{MP} to fit these DNS results [77]. Later, Colin and Angelberger proposed a new efficiency function C_n, characterized by the following expression

$$C_n\left(\frac{r}{\delta_l^1}, \frac{v'}{s_l^0}\right) = \frac{1}{2}\left\{1 + erf\left[0.6\ \ln\left(\frac{r}{\delta_l^1}\right) - \frac{0.6}{\sqrt{v'/s_l^0}}\right]\right\} \tag{2.10}$$

which improves Meneveau's one. A comparison between C_{MP} and C_n efficiency functions is shown in Figure 2.5.

As final result of the described DNS analysis, Colin [31] modeled the effective strain rate $\dot{S}$ induced by a pair of vortexes (size r and velocity v') with the following relation:

$$\dot{S} = C_n\left(\frac{r}{\delta_l^1}, \frac{v'}{s_l^0}\right)\left(\frac{v'}{r}\right) \tag{2.11}$$

In next sub-sections, Colin and Charlette strategies for the efficiency function E modelling are described.

2.3.1 Colin formulation

As described in detail in [31], Colin based the creation of an efficiency function E model on the comparison between real and thickened flame wrinkling. Starting from

the instantaneous flame surface density balance equation [25, 108, 111]

$$\frac{\partial \Sigma}{\partial t} + \nabla \cdot \left[\left(\vec{U} + w\, \vec{n} \right) \Sigma \right] = \left(\nabla \cdot \vec{U} - \vec{n}\, \vec{n} \colon \nabla \vec{U} \right) \Sigma + w\, \nabla \cdot \vec{n}\, \Sigma = \kappa\, \Sigma \qquad (2.12)$$

where Σ is the flame surface density (namely, the flame surface per unit volume), $\vec{U}$ the flow velocity, w the flame front displacement and $\vec{n}$ the unit vector normal to the flame front and pointing towards fresh gases, it is possible to point out that:

- the first RHS term of (2.12), which can also be called $a_T = \left(\nabla \cdot \vec{U} - \vec{n}\, \vec{n} \colon \nabla \vec{U} \right)$, corresponds to the strain rate induced by the flow field on the flame;
- the second RHS term of (2.12), namely $w\, \nabla \cdot \vec{n}$, represents the curvature contribution to the flame strain rate, because $\nabla \cdot \vec{n}$ denotes the flame surface curvature;
- the sum of the two previous contribution, κ, is the total flame stretch.

Therefore, by filtering (2.12) in an LES context, the following equation is obtained

$$\frac{\partial \bar{\Sigma}}{\partial t} + \nabla \cdot \left[\langle \vec{U} \rangle_s \bar{\Sigma} \right] + \nabla \cdot \left[\langle w\, \vec{n} \rangle_s \bar{\Sigma} \right] = \langle a_T \rangle_s \bar{\Sigma} + \langle w\, \nabla \cdot \vec{n} \rangle_s \bar{\Sigma} = \langle \kappa \rangle_s \bar{\Sigma} \qquad (2.13)$$

where $\bar{\Sigma}$ corresponds to the flame area per unit volume at the sub-grid scale level, while $\langle \cdot \rangle_s$ denotes an averaging along the sub-grid scale flame surface.

If a simplified approach is followed [31], the hypothesis here summarized

$$\begin{cases} w = s_l^0 = const \\ \langle \kappa \rangle_s \approx 0 \\ \langle \nabla \cdot \vec{n} \rangle_s \approx \frac{1}{L_s} \approx \frac{1}{\alpha} \frac{\Xi_\Delta - 1}{\Delta} \end{cases} \qquad (2.14)$$

can be adopted, where L_s is the sub-grid scale wrinkling length, Δ the filter size, α a model constant and $\Xi_\Delta = A_{f,sgs}/\Delta^2$ the sub-grid scale wrinkling factor (i.e. the ratio between the sub-grid scale flame surface $A_{f,sgs}$ and its projection in the propagating direction).

As a consequence, the integration of the effective strain rate induced by a pair of vortexes (see (2.11)) over all turbulence length scales that are:

- smaller than the filter size Δ (also called *outer* cut-off length scale)

- greater than an *inner* cut-off length scale, which can be assumed equal to the laminar flame thickness δ_l^0 because smaller eddies generate no wrinkling on the flame,

allows to formulate the following model for the sub-grid scale wrinkling factor $\Xi_\Delta\left(\delta_l^0\right)$:

$$\begin{cases} \Xi_\Delta\left(\delta_l^0\right) = 1 + \alpha\,\Gamma_{co}\,\frac{u'_\Delta}{s_l^0} \\ \alpha = \beta \frac{2\ln 2}{3c_{ms}\left(Re_t^{0.5}-1\right)} \\ \Gamma_{co} = \Gamma_{co}\left(\frac{\Delta}{\delta_l^0}, \frac{u'_\Delta}{s_l^0}\right) = 0.75\ \exp\left[-\frac{1.2}{\left(u'_\Delta/s_l^0\right)^{0.3}}\right]\left(\frac{\Delta}{\delta_l^0}\right)^{\frac{2}{3}} \end{cases} \tag{2.15}$$

Here, u'_Δ is the sub-grid scale turbulence velocity whose computation will be described in Section 2.6.2, β is a model constant of the order of unity which has to be calibrated, $c_{ms} = 0.28$ is a model constant determined by using Yeung's DNS results [115], Γ_{co} is the numerical fitting proposed by Colin for the "total" efficiency function of the considered eddies length scale spectrum, while Re_t is the turbulent Reynolds number. This last parameter can be computed as

$$Re_t = \frac{u' l_t}{\nu} = 4\,\frac{l_t}{\delta_l^0}\frac{u'}{s_l^0} \tag{2.16}$$

because for a laminar flame $\delta_l^0 s_l^0/\nu = 4$ (see [31, 60]).

Finally, after the evaluation of the sub-grid scale wrinkling factor for both the unthickened (inner cut-off length scale equal to δ_l^0) and thickened flame (whose inner cut-off length scale is the thickened flame thickness δ_l^1), for a general filter size value Δ

$$\begin{cases} \Xi_\Delta\left(\delta_l^0\right) = 1 + \alpha\,\Gamma_{co}\left(\frac{\Delta}{\delta_l^0}, \frac{u'_\Delta}{s_l^0}\right)\frac{u'_\Delta}{s_l^0} \\ \Xi_\Delta\left(\delta_l^1\right) = 1 + \alpha\,\Gamma_{co}\left(\frac{\Delta}{\delta_l^1}, \frac{u'_\Delta}{s_l^0}\right)\frac{u'_\Delta}{s_l^0} \end{cases} \tag{2.17}$$

the efficiency function E can be modelled as follows

$$E = \frac{\Xi_\Delta\left(\delta_l^0\right)}{\Xi_\Delta\left(\delta_l^1\right)} \tag{2.18}$$

where the underestimation of the flame front wrinkling by the ATF strategy can be corrected by increasing the flame speed by the E factor. For further details, please refer

to [31].

2.3.2 Charlette formulation

Charlette approach for the formulation of an efficiency function E model was very similar to Colin's one (Section 2.3.1): in fact, expression (2.12) as well as (2.13) were used as a starting point and similar observations were performed.

However, the simplified approach used in [31] was followed by Charlette with little modifications, as it can be evinced by the hypothesis here summarized

$$\begin{cases} w = s_l^0 = const \\ \langle \kappa \rangle_s \approx 0 \\ \langle a_T \rangle_s \approx \frac{u'_\Delta}{\Delta} \, \Gamma_{ch} \left(\frac{\Delta}{\delta_l^0}, \frac{u'_\Delta}{s_l^0}, Re_\Delta \right) \end{cases} \tag{2.19}$$

and adopted for the model generation. Here $\langle a_T \rangle_s$ is the strain rate induced by the flow field on the flame and averaged along the sub-grid scale flame surface, while Γ_{ch} is the numerical fitting proposed by Charlette for the "total" efficiency function of the considered eddies energy spectrum.

Concerning Γ_{ch} parameter, its role is the same of Γ_{co} one in (2.15), but its formulation comes from the integration of the effective strain rate induced by a pair of vortexes (see (2.11)) over the *energy spectrum* of all turbulence length scales:

- smaller than the filter size Δ (the *outer* cut-off length scale) and
- greater than the laminar flame thickness δ_l^0 (the *inner* cut-off length scale).

This approach, together with assumptions summarized in (2.19), allows to formulate the following model for the sub-grid scale wrinkling factor $\Xi_\Delta \left(\delta_l^0 \right)$

$$\begin{cases} \Xi_\Delta \left(\delta_l^0 \right) = \left(1 + min \left[\frac{\Delta}{\delta_l^0}, \Gamma_{ch} \frac{u'_\Delta}{s_l^0} \right] \right)^\beta \\ \Gamma_{ch} = \Gamma_{ch} \left(\frac{\Delta}{\delta_l^0}, \frac{u'_\Delta}{s_l^0} \right) = \left\{ \left[\left(f_u^{-a} + f_\Delta^{-a} \right)^{-\frac{1}{a}} \right]^{-b} + f_{Re}^{-b} \right\}^{-\frac{1}{b}} \end{cases} \tag{2.20}$$

where

$$\begin{cases} a = 0.6 + 0.2\ \exp\left[-0.1\left(\frac{u'_\Delta}{s_l^0}\right)\right] - 0.2\ \exp\left[-0.01\left(\frac{\Delta}{\delta_l^0}\right)\right] \\ b = 1.4 \end{cases} \tag{2.21}$$

In (2.20) the model exponent β can be determined alternatively by either a non-dynamic or a dynamic formulation (as described in the following Paragraphs of the present Section), while the complete Γ_{ch} expression can be written as

$$\begin{cases} f_u = f_u\left(\frac{u'_\Delta}{s_l^0}\right) = 4\left(\frac{27C_k}{110}\right)^{\frac{1}{2}}\left(\frac{18C_k}{55}\right)\left(\frac{u'_\Delta}{s_l^0}\right)^2 \\ f_\Delta = f_\Delta\left(\frac{\Delta}{\delta_l^0}\right) = \left\{\frac{27C_k\pi^{\frac{4}{3}}}{110}\left[\left(\frac{\Delta}{\delta_l^0}\right)^{\frac{4}{3}} - 1\right]\right\}^{\frac{1}{2}} \\ f_{Re} = f_{Re}\left(\frac{\Delta}{\delta_l^0}, \frac{u'_\Delta}{s_l^0}\right) = \left[\frac{9}{55}\ \exp\left(-\frac{3}{2}\frac{C_k\pi^{\frac{4}{3}}}{Re_\Delta\left(\frac{\Delta}{\delta_l^0}, \frac{u'_\Delta}{s_l^0}\right)}\right)\right]^{\frac{1}{2}}\left[Re_\Delta\left(\frac{\Delta}{\delta_l^0}, \frac{u'_\Delta}{s_l^0}\right)\right]^{\frac{1}{2}} \end{cases} \tag{2.22}$$

being $C_k = 1.5$ the universal Kolmogorov constant [26] and Re_Δ the sub-grid scale Reynolds number defined as [26, 31, 60]

$$Re_\Delta = \frac{u'_\Delta \Delta}{\nu} = 4\,\frac{\Delta}{\delta_l^0}\frac{u'_\Delta}{s_l^0} \tag{2.23}$$

Finally, similarly to Section 2.3.1, after the evaluation for a general filter size value Δ of the sub-grid scale wrinkling factor for both the unthickened (inner cut-off length scale equal to δ_l^0) and thickened flame (inner cut-off length scale equal to δ_l^1)

$$\begin{cases} \Xi_\Delta\left(\delta_l^0\right) = \left(1 + min\left[\frac{\Delta}{\delta_l^0}, \Gamma_{ch}\left(\frac{\Delta}{\delta_l^0}, \frac{u'_\Delta}{s_l^0}\right)\frac{u'_\Delta}{s_l^0}\right]\right)^\beta \\ \Xi_\Delta\left(\delta_l^1\right) = \left(1 + min\left[\frac{\Delta}{\delta_l^1}, \Gamma_{ch}\left(\frac{\Delta}{\delta_l^1}, \frac{u'_\Delta}{s_l^0}\right)\frac{u'_\Delta}{s_l^0}\right]\right)^\beta \end{cases} \tag{2.24}$$

the efficiency function E can be modelled as follows

$$E = \frac{\Xi_\Delta\left(\delta_l^0\right)}{\Xi_\Delta\left(\delta_l^1\right)} = \frac{\Xi_\Delta\left(\delta_l^0\right)}{\Xi_\Delta\left(F\delta_l^0\right)} = \frac{\Xi_\Delta\left(\delta_l^0\right)}{\Xi_\Delta\left(\Delta\right)} = \Xi_\Delta\left(\delta_l^0\right) \tag{2.25}$$

where the underestimation of the flame front wrinkling by the ATF strategy can be corrected by increasing the flame speed by the E factor. As suggested in [26, 31], because in practical applications the filter size is assumed equal to the thickened flame

thickness $\Delta = F\delta_l^0 = \delta_l^1$, this implies $f_\Delta = 0$ and $\Gamma_{ch} = 0$, therefore $\Xi_\Delta\left(\delta_l^1\right)$ becomes equal to 1, as shown in (2.25). For further details, please refer to [26, 27].

Non-dynamic formulation As described by Charlette in [26], the first step for estimating the β value of (2.20) power-law is to carry out an empirical choice where, assuming a $\beta = const$, a rather satisfactory estimation of the E value is obtained. In [26] is proposed the value

$$\beta = 0.5 \tag{2.26}$$

considered as the best compromise between excessively high or low turbulent flame speeds.

Dynamic formulation An improvement of the (2.20) power-law formulation can be achieved through a dynamic computation of the β exponent. In practice, if some resolved flame wrinkling is analyzed the β value can be consequently deduced with the purpose to match the modelled sub-grid scale wrinkling trend with the computed one. As proposed by Charlette in [27] and assessed by Hosseinzadeh [57], the β exponent of (2.20) is computed "on the fly" thanks to a *Germano-like* procedure, based on filtered resolved flow fields.

To apply the dynamic formulation, a test-filtering operation has to be carried out at a larger scale Δ_{test} with respect to the basic filter size Δ. Assuming that, for a generic quantity q, the regular filter operation is denoted:

- by a *bar* $\bar{q}$ at the Δ scale and
- by an *over-brace* $\overbrace{q}$ at the Δ_{test} scale (regular test-filtering),

while the Favre filter operation is indicated:

- by a *tilde* $\tilde{q}$ at the Δ scale and
- by a *hat* $\hat{q}$ at the Δ_{test} scale (Favre test-filtering),

the Germano identity for the reaction rate can be expressed as follows

$$\overbrace{\bar{\dot{\omega}}_c} = \overbrace{\dot{\omega}_c} \tag{2.27}$$

Here, $\widehat{\bar{\dot{\omega}}_c}$ represents the test-filtered resolved reaction rate and $\widehat{\dot{\omega}_c}$ denotes the reaction rate of test-filtered magnitudes.

As first step, by considering $\Delta = F\delta_l^0$ and remembering (2.25), the resolved reaction rate (or, in other words, the LES filtered reaction rate) can be cast in the form:

$$\bar{\dot{\omega}}_c = \frac{E}{F}\,\dot{\omega}_{c,l}\left(\widetilde{Y}_c, \widetilde{Z}\right) = \frac{\Xi_\Delta\left(\delta_l^0\right)}{\Delta}\,\delta_l^0\,\dot{\omega}_{c,l}\left(\widetilde{Y}_c, \widetilde{Z}\right) = \frac{\Xi_\Delta\left(\delta_l^0\right)}{\Delta}\,W_{\Delta,c}\left(\widetilde{Y}_c, \widetilde{Z}\right) \tag{2.28}$$

where $\widetilde{Y}_c$ and $\widetilde{Z}$ are the progress variable and mixture fraction, respectively.

Then, after the definition of a suitable test-filter scale Δ_{test} as

$$\begin{cases} \Delta_{test} = \gamma\Delta = \gamma F\delta_l^0 \\ \gamma > 1 \end{cases} \tag{2.29}$$

the test-filtered resolved reaction rate can be obtained as

$$\widehat{\bar{\dot{\omega}}_c} = \overbrace{\frac{\Xi_\Delta\left(\delta_l^0\right)}{\Delta}\,W_{\Delta,c}\left(\widetilde{Y}_c, \widetilde{Z}\right)} \tag{2.30}$$

On the other hand, for computing $\widehat{\dot{\omega}_c}$, the test-filtered magnitudes have to be determined as follows

$$\begin{cases} \widehat{\bar{\rho}} \\ \widehat{Y}_c = \widehat{\bar{\rho}\widetilde{Y}_c} \,/\, \widehat{\bar{\rho}} \\ \widehat{Z} = \widehat{\bar{\rho}\widetilde{Z}} \,/\, \widehat{\bar{\rho}} \end{cases} \tag{2.31}$$

Hence, after the evaluation of the laminar reaction rate $\dot{\omega}_{c,l}\left(\widehat{Y}_c, \widehat{Z}\right)$ from the test-filtered progress variable and mixture fraction (e.g. by using a tabulated chemistry approach), the RHS term of (2.27) can be computed as

$$\begin{aligned} &\widehat{\dot{\omega}_c} = \tfrac{E}{F}\,\dot{\omega}_{c,l}\left(\widehat{Y}_c, \widehat{Z}\right) = \tfrac{\Xi_{\Delta_{test}}\left(\delta_l^0\right)}{\Delta_{test}}\,\gamma\,\delta_l^0\,\dot{\omega}_{c,l}\left(\widehat{Y}_c, \widehat{Z}\right) = \\ &= \tfrac{\Xi_{\Delta_{test}}\left(\delta_l^0\right)}{\Delta_{test}}\,W_{\Delta_{test},c}\left(\widehat{Y}_c, \widehat{Z}\right) = \tfrac{\Xi_{\gamma\Delta}\left(\delta_l^0\right)}{\gamma\Delta}\,W_{\gamma\Delta,c}\left(\widehat{Y}_c, \widehat{Z}\right) \end{aligned} \tag{2.32}$$

Replacing (2.30) and (2.32) into the initial Germano identity (2.27), it is found:

$$\overbrace{\frac{\Xi_{\Delta}\left(\delta_l^0\right)}{\Delta} W_{\Delta,c}\left(\widetilde{Y}_c, \widetilde{Z}\right)} = \frac{\Xi_{\gamma\Delta}\left(\delta_l^0\right)}{\gamma\Delta} W_{\gamma\Delta,c}\left(\widehat{Y}_c, \widehat{Z}\right) \tag{2.33}$$

Now, the identity is written as if it holds locally, at every cell grid and time. However, it has often been found useful to apply the dynamic model in an averaged sense rather than a point-wise one, in order to avoid strong discontinuities and local inaccuracies [27]. In this context, because the global reaction rate is the most important effect to capture, an average of (2.33) terms over a sufficiently large volume allows to remove unphysical fluctuations. In addition, if (2.24) is used, the following expression can be written

$$\begin{aligned} &\left\langle \overbrace{\left(1 + min\left[\frac{\Delta}{\delta_l^0}, \Gamma_{ch}\left(\frac{\Delta}{\delta_l^0}, \frac{u'_{\Delta}}{s_l^0}\right)\frac{u'_{\Delta}}{s_l^0}\right]\right)^{\beta} \frac{W_{\Delta,c}\left(\widetilde{Y}_c, \widetilde{Z}\right)}{\Delta}} \right\rangle = \\ &= \left\langle \left(1 + min\left[\frac{\gamma\Delta}{\delta_l^0}, \Gamma_{ch}\left(\frac{\gamma\Delta}{\delta_l^0}, \frac{u'_{\gamma\Delta}}{s_l^0}\right)\frac{u'_{\gamma\Delta}}{s_l^0}\right]\right)^{\beta} \frac{W_{\gamma\Delta,c}\left(\widehat{Y}_c, \widehat{Z}\right)}{\gamma\Delta} \right\rangle \end{aligned} \tag{2.34}$$

where $\langle\cdot\rangle$ indicates a volume averaging operation.

Next, to provide a practically convenient framework, the sub-grid scale turbulent velocity u'_{Δ} is assumed uncorrelated from the local values of $W_{\Delta,c}\left(\widetilde{Y}_c, \widetilde{Z}\right)$ within the averaging control volume. Therefore, (2.34) can be recast as

$$\begin{aligned} &\left(1 + min\left[\frac{\Delta}{\delta_l^0}, \Gamma_{ch}\left(\frac{\Delta}{\delta_l^0}, \frac{\langle u'_{\Delta}\rangle}{s_l^0}\right)\frac{\langle u'_{\Delta}\rangle}{s_l^0}\right]\right)^{\beta} \left\langle \overbrace{W_{\Delta,c}\left(\widetilde{Y}_c, \widetilde{Z}\right)} \right\rangle = \\ &= \frac{1}{\gamma}\left(1 + min\left[\frac{\gamma\Delta}{\delta_l^0}, \Gamma_{ch}\left(\frac{\gamma\Delta}{\delta_l^0}, \frac{\langle u'_{\gamma\Delta}\rangle}{s_l^0}\right)\frac{\langle u'_{\gamma\Delta}\rangle}{s_l^0}\right]\right)^{\beta} \left\langle W_{\gamma\Delta,c}\left(\widehat{Y}_c, \widehat{Z}\right) \right\rangle \end{aligned} \tag{2.35}$$

Finally, by solving (2.35) for the unknown exponent β the dynamic formulation of Charlette model is achieved:

$$\begin{cases} \beta = \dfrac{\log\left(\gamma \left\langle \overbrace{W_{\Delta,c}\left(\widetilde{Y}_c, \widetilde{Z}\right)} \right\rangle / \langle W_{\gamma\Delta,c}\left(\widehat{Y}_c, \widehat{Z}\right)\rangle\right)}{\log\left(\dfrac{\left(1+min\left[\frac{\gamma\Delta}{\delta_l^0}, \Gamma_{ch}\left(\frac{\gamma\Delta}{\delta_l^0}, \frac{\langle u'_{\gamma\Delta}\rangle}{s_l^0}\right)\frac{\langle u'_{\gamma\Delta}\rangle}{s_l^0}\right]\right)}{\left(1+min\left[\frac{\Delta}{\delta_l^0}, \Gamma_{ch}\left(\frac{\Delta}{\delta_l^0}, \frac{\langle u'_{\Delta}\rangle}{s_l^0}\right)\frac{\langle u'_{\Delta}\rangle}{s_l^0}\right]\right)}\right)} \\ W_{\Delta,c}\left(\widetilde{Y}_c, \widetilde{Z}\right) = \delta_l^0\, \dot{\omega}_{c,l}\left(\widetilde{Y}_c, \widetilde{Z}\right) \\ W_{\gamma\Delta,c}\left(\widehat{Y}_c, \widehat{Z}\right) = \gamma\, \delta_l^0\, \dot{\omega}_{c,l}\left(\widehat{Y}_c, \widehat{Z}\right) \end{cases} \tag{2.36}$$

2.4 The Flamelet Progress Variable approach

In the proposed ATF model, the thickening concept is coupled with a tabulation strategy to include detailed chemistry effects into an LES framework avoiding prohibitive flame thickening.

Concerning the premixed flames context, the *Flamelet Progress Variable* (FPV) approach was adopted. This tabulation methodology is very similar to FPI (Flame Propagation of Intrinsic low-dimensional manifolds) [41, 51, 73] and FGM (Flamelet Generated Manifolds) [109, 110] strategies, which proved to be well suited for an accurate description of the flame propagation.

The FPV approach was applied as described below:

1. For the table generation, a first 1D freely propagating laminar premixed flame at constant equivalence ratio (i.e. constant mixture fraction $Z = const$) was simulated. For this purpose, *Cantera* tool for simulating detailed chemistry 1D flames was used.

2. The previous computation was repeated at different equivalence ratios to span a 2D space parameterized by:

   - the *mixture fraction* Z to consider each possible *air-fuel* mixing and
   - the reaction *progress variable* Y_c for the flame evolution detection, which can be either a single specie mass fraction (e.g. $Y_c = CO_2$) or a combination of them (e.g. $Y_c = CO + CO_2 + H_2 + H_2O$).

3. The two table parameters (Z and Y_c) were evolved by suitable equations on the 3D computational domain (see Section 2.5) and used, at each time-step and on each grid cell, to reconstruct the distribution of all tabulated magnitudes (e.g. chemical specie, laminar flame speed and thickness, flame sensor, etc.).

As previously tested by Kuenne [66], the main advantage of the tabulation strategy is the capability to reproduce important flame characteristics over the whole range of equivalence ratios without a run-time 3D simulation of the chemical kinetics. Therefore, a prohibitive flame thickening can be avoided if the tabulation methodology is coupled with the ATFM (as it will be shown in Chapter 5). As a consequence, the need

of a sub-grid scale wrinkling modelling is minimized with a reduction of the flame reconstruction inaccuracy.

On the other hand, the use of a tabulation strategy for chemical kinetics requires more *a-priori* knowledge of the reaction. For example, if heat losses are not negligible they can be considered by including an additional table dimension (e.g. the enthalpy), while with Arrhenius law this problem is naturally solved.

2.4.1 The Flame Sensor based on Progress Variable Gradient and Source Term

Since a correct pure mixing simulation is important in case of a generic stratified mixture, when the ATFM is used the diffusion terms of conservation equations (see Section 2.5) have to be modified only at the reacting region. Hence, a *flame sensor* Ω, which is zero everywhere except within the flame where it approaches the unitary value ($0 \leq \Omega \leq 1$), has to be applied: to detect the flame front position and to modify the diffusion terms accordingly, without affecting the pure mixing zones.

Assuming c as the normalized reaction progress variable (namely, the *burnt gases-actual mixture* ratio, which is equal to $c = 0$ in cells with fresh reactants only and $c = 1$ in burnt mixture only ones), several formulations for the flame sensor can be used as listed here below:

1. The *Box sensor*, where Ω is equal to

$$\begin{cases} \Omega = 1, & \text{if } c_{min} < c < c_{max} \\ \Omega = 0, & \text{otherwise} \end{cases} \tag{2.37}$$

   represents the first idea to limit the ATF concept at the reaction zone, starting from the initial methodology in which the thickening was applied over the whole computational domain (no sensor application).

2. The *Gaussian sensor*, whose expression proposed by Durand [38] and used by Kuenne [67] is

$$\Omega = 16\left[c\left(1-c\right)\right]^2 \tag{2.38}$$

   computes the Ω value with a Gaussian shape determined as function of the normalized progress variable c distribution.

3. The *Progress Variable Gradient Based sensor*, which is computed according to Proch formulation [94]

$$\Omega = \frac{\nabla Y_c}{(\nabla Y_c)_{max}} \tag{2.39}$$

exploits the progress variable gradient for the flame detection, hence Ω value is computed accordingly.

4. The *Flame sensor based on Progress Variable Gradient and Source Term*, here proposed with the following formulation

$$\Omega = \frac{\nabla Y_c}{(\nabla Y_c)_{max}} + \frac{\dot{\omega}_c}{(\dot{\omega}_c)_{max}} \left[1 - \frac{\nabla Y_c}{(\nabla Y_c)_{max}}\right] \tag{2.40}$$

links the flame sensor value not only to the progress variable gradient ∇Y_c (as performed by Proch's sensor) but also to the progress variable source term $\dot{\omega}_c$.

As it will be demonstrated in Section 5.2.2, the application of last described sensor (2.40) for the flame detection represents the best solution between the aforementioned possibilities because:

- Although Ω value changes rather slowly from 0 to 1 within the flame, producing a slight flame front deformation, it allows to avoid the "cascade" thickening effect, namely an uncontrolled thickening of the flame. As shown in Section 5.2.2, this phenomenon is caused by sensors which are almost constant and nearby the unitary value along the whole flame front (as the *Box* one), because they are not able to smooth the thickening factor value F and limit the increase of flame thickness.

- The slight flame deformation performed by (2.40) does not affect the capability to correctly predict the laminar flame velocity, as also figured out by Kuenne [67] for the *Gaussian sensor* (2.38).

- Expression (2.40) is easy to tabulate and considers all relevant characteristics of a premixed flame, independently from the composition and progress variable definition. This is not true for *Gaussian* and *Progress Variable Gradient Based* sensors, because their accuracy is strongly dependent on the progress variable choice (see Section 5.2.2).

2.5 The ATFM fundamental transport equations

The application of the ATF model, as proposed in previous Sections, is made possible by the use of two fundamental transport equations:

1. one for the *progress variable* Y_c,
2. one for the *mixture fraction* Z.

The combined use of these equations, in which the ATF concept is modelled through

- the *thickening factor* F (Section 2.2),
- the *efficiency function* E (Section 2.3),

allows to simulate on LES typical meshes the structure and evolution of a generic premixed flame, exploiting:

- the *FPV* tabulation strategy (Section 2.4) for the chemical kinetics modelling,
- the *Flame sensor based on Progress Variable Gradient and Source Term* of (2.40) for the flame front detection.

From a theoretical point of view, the Y_c and Z transport equations are not enough for the ATFM application on a general problem. In fact, if important heat losses needed to be considered, an additional transport equation (the *enthalpy* one) has to be solved and its result used as a third entry dimension of the FPV tabulation strategy. However, in this thesis work, as a first step the assumption of adiabatic conditions is always adopted for the ATFM application; future investigations will address this topic.

In the following sub-sections, under the assumption of negligible heat losses, the detailed formulations of two aforementioned transport equations is presented.

2.5.1 Progress Variable Y_c transport equation

The description of a *progress variable* Y_c evolution is fundamental in the framework of a premixed combustion modelling, where a reacting region has to be handled. There-

fore, as proposed in literature [67], the following transport equation is considered

$$\begin{gathered}\frac{\partial \bar{\rho}\widetilde{Y}_c}{\partial t} + \nabla \cdot \left(\bar{\rho}\widetilde{\vec{U}}\widetilde{Y}_c\right) = \\ = \nabla \cdot \left\{\left[F\left(\Omega\right) E\left(\Omega\right) \frac{\bar{\mu}}{Sc} + \left(1-\Omega\right) \frac{\mu_{t,sgs}}{Sc_{t,sgs}}\right] \nabla \widetilde{Y}_c\right\} + \frac{E(\Omega)}{F(\Omega)} \dot{\omega}_{c,l}\left(\widetilde{Y}_c, \widetilde{Z}\right)\end{gathered} \tag{2.41}$$

being $\vec{U}$ the flow velocity, μ the dynamic viscosity in $kg/\left(m\ s\right)$, $Sc = \mu/\left(\rho D\right)$ the dimensionless Schmidt number in which D is the molecular diffusivity, while $\mu_{t,sgs}$ and $Sc_{t,sgs}$ the sub-grid scale turbulence dynamic viscosity and Schmidt number, respectively.

As it can be noticed, in (2.41) the F and E values, as well as the whole diffusivity term (first RHS one), are function of the flame sensor Ω. This dependency is justified by the advantage in modifying the diffusion term only at the flame front region in order to not affect pure mixing zones. In particular, the actual F and E values, which depend on the flame sensor ($0 \leq \Omega \leq 1$) and are equal to 1 outside the flame, can be computed as follows:

$$\begin{cases} F\left(\Omega\right) = 1 + \left(F_{max} - 1\right)\Omega \\ E\left(\Omega\right) = 1 + \left(E_{max} - 1\right)\Omega \end{cases} \tag{2.42}$$

Here, F_{max} and E_{max} correspond to the thickening factor and efficiency function values calculated from the models described in Sections 2.2 and 2.3, respectively. It can be also noticed that

$$E\ \frac{\bar{\mu}}{Sc} = E\ D = D + \left(E-1\right) D \tag{2.43}$$

where the term $\left(E-1\right) D$ is the turbulent sub-grid scale diffusivity [31]; therefore, when the efficiency function sub-grid scale model is active no additional model is needed for the unresolved scalar transport. As a consequence, when far from the flame $F = E = 1$, a classical LES model for the sub-gird scale diffusivity has to be re-activated: this explains the Ω dependency of (2.41) first RHS term.

Concerning the laminar reaction rate $\dot{\omega}_{c,l}\left(\widetilde{Y}_c, \widetilde{Z}\right)$ of (2.41), it is extracted from the FPV chemical kinetics tabulation (Section 2.4) by entering with the Y_c and Z distributions of previous time-step.

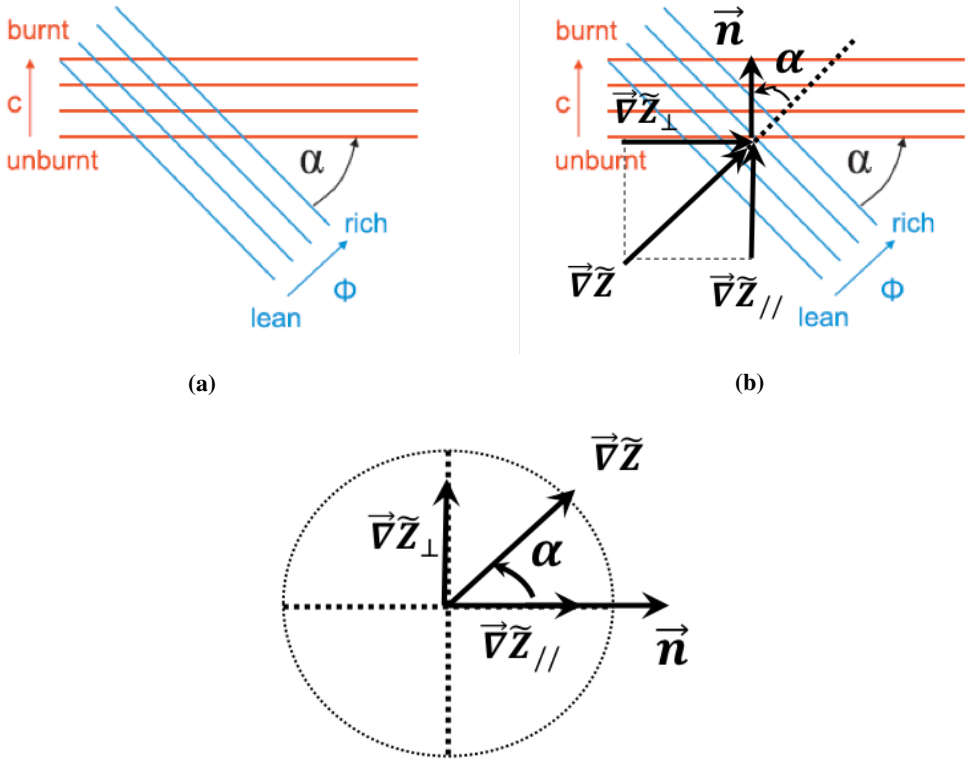

Figure 2.6: *Overlap between a mixture stratification (equivalence ratio ϕ and mixture fraction Z variation) and the flame front (progress variable Y_c and normalized progress variable c variation) with a generic alignment angle α, [67], (a); decomposition of $\nabla\widetilde{Z}$ into a parallel $\nabla\widetilde{Z}_{//}$ and perpendicular $\nabla\widetilde{Z}_{\perp}$ component to flame normal direction $\vec{n}$ (b); detail of $\nabla\widetilde{Z}$ decomposition (c).*

2.5.2 Mixture Fraction Z transport equation

A non-uniform mixture distribution, in other words a *stratification*, can often be observed in many industrial applications due to an incomplete mixing or an intentional efficiency improvement, as in direct-injection IC engines [106].

In general, a stratification can be characterized by two physical quantities [67]:

1. the *lenght scale* on which the equivalence ratio (or the mixture fraction) variations take place and

2. the *alignment* between mixing and reaction layers (the α angle of Figure 2.6a).

The first quantity allows to distinguish between small and large scale stratifications. When a small scale stratification is present, the local flame structure is significantly

affected compared to an homogeneous mixture flame, hence in the context of the ATFM application this topic has to be addressed. On the other hand, if large scale stratification are identified, the propagation of a quasi-homogeneous mixture flame can be observed and no significant modification to the reacting layer can be detected. Concerning the alignment between mixing and reaction layers, in case of a generic spherical flame shape propagating into a fresh mixture of a direct-injection IC engine, α (Figure 2.6a) can assume any value depending on space and time.

Therefore, if a small scale stratification is present and the reaction layer is overlapped to a not negligible mixing layer (with a generic α orientation), the flame inner structure detects a variation of the mixture composition. Consequently, if the ATF concept is followed, the thickening procedure should be applied not only on the progress variable gradient $\nabla\widetilde{Y}_c$ (namely on the flame front, see (2.41)) but also on the mixture fraction gradient component parallel to the flame normal direction $\nabla\widetilde{Z}_{//}$ (see Figures 2.6b and 2.6c). In fact, as previously discussed in Section 2.1, the artificial thickening of a flame is carried out by a coordinates transformation (in terms of both time and space) along the flame front normal direction $\vec{n}$. Hence, if $\nabla\widetilde{Z}$ is either not thickened or thickened in every other direction with except to $\vec{n}$, the consistency between the *reacting-mixing* layer overlapping cannot be guaranteed.

With the purpose to adapt for ATFM applications the original mixture fraction Z transport equation

$$\frac{\partial\bar{\rho}\widetilde{Z}}{\partial t}+\nabla\cdot\left(\bar{\rho}\widetilde{\vec{U}}\widetilde{Z}\right)=\nabla\cdot\left\{\left[\frac{\bar{\mu}}{Sc}+\frac{\mu_{t,sgs}}{Sc_{t,sgs}}\right]\nabla\widetilde{Z}\right\} \tag{2.44}$$

used in LES contexts with no flame thickening, the diffusion term (RHS) has to be modified as follows

$$\nabla\cdot\left\{\left[\frac{\bar{\mu}}{Sc}+\frac{\mu_{t,sgs}}{Sc_{t,sgs}}\right]\nabla\widetilde{Z}\right\}+\nabla\cdot\left\{\left[\frac{\mu}{Sc}\right]_{ATFM}\nabla\widetilde{Z}_{//}\right\} \tag{2.45}$$

where the term highlighted in red represents the directional thickening imposed by the ATF concept on mixture stratification. In (2.45), $\nabla\widetilde{Z}_{//}$ is the projection of $\nabla\widetilde{Z}$ along

the flame normal direction $\vec{n}$, which can be computed as

$$\vec{n} = \frac{\nabla \widetilde{Y}_c}{\left|\nabla \widetilde{Y}_c\right|} \tag{2.46}$$

However, a Z transport equation with the diffusion term characterized by (2.45) form cannot be easily resolved with implicit numerical techniques, as (2.44) equation. Therefore, if $\nabla \widetilde{Z}_{//}$ is re-casted as follows

$$\begin{aligned}
\nabla \widetilde{Z}_{//} = \left(\vec{n} \cdot \nabla \widetilde{Z}\right) \vec{n} = \left(n_x \frac{\partial \widetilde{Z}}{\partial x} + n_y \frac{\partial \widetilde{Z}}{\partial y} + n_z \frac{\partial \widetilde{Z}}{\partial z}\right) \begin{pmatrix} n_x \\ n_y \\ n_z \end{pmatrix} = \\
= \begin{pmatrix} n_x^2 \frac{\partial \widetilde{Z}}{\partial x} + n_x n_y \frac{\partial \widetilde{Z}}{\partial y} + n_x n_z \frac{\partial \widetilde{Z}}{\partial z} \\ n_y n_x \frac{\partial \widetilde{Z}}{\partial x} + n_y^2 \frac{\partial \widetilde{Z}}{\partial y} + n_y n_z \frac{\partial \widetilde{Z}}{\partial z} \\ n_z n_x \frac{\partial \widetilde{Z}}{\partial x} + n_z n_y \frac{\partial \widetilde{Z}}{\partial y} + n_z^2 \frac{\partial \widetilde{Z}}{\partial z} \end{pmatrix} = \begin{bmatrix} n_x^2 & n_x n_y & n_x n_z \\ n_y n_x & n_y^2 & n_y n_z \\ n_z n_x & n_z n_y & n_z^2 \end{bmatrix} \begin{pmatrix} \frac{\partial \widetilde{Z}}{\partial x} \\ \frac{\partial \widetilde{Z}}{\partial y} \\ \frac{\partial \widetilde{Z}}{\partial z} \end{pmatrix} = \bar{\bar{T}} \nabla \widetilde{Z}
\end{aligned} \tag{2.47}$$

where $\bar{\bar{T}}$ is the *rotational tensor* including all components of normal flame front direction, the diffusion term reported in (2.45) can be re-written as:

$$\begin{cases}
\nabla \cdot \left\{ \left[\frac{\bar{\mu}}{Sc} + \frac{\mu_{t,sgs}}{Sc_{t,sgs}} \right] \nabla \widetilde{Z} \right\} + \nabla \cdot \left\{ \left[\frac{\mu}{Sc} \right]_{ATFM} \bar{\bar{T}} \nabla \widetilde{Z} \right\} \\
\left[\frac{\mu}{Sc} \right]_{ATFM} = \left[F(\Omega) E(\Omega) \frac{\bar{\mu}}{Sc} + (1 - \Omega) \frac{\mu_{t,sgs}}{Sc_{t,sgs}} \right] - \left[\frac{\bar{\mu}}{Sc} + \frac{\mu_{t,sgs}}{Sc_{t,sgs}} \right]
\end{cases} \tag{2.48}$$

being $\left[\frac{\mu}{Sc}\right]_{ATFM}$ the resolved and sub-grid scale molecular diffusivity modified by the ATFM, similarly to (2.41). Finally, the modified version of mixture fraction Z transport equation for ATFM applications can be achieved by substituting the diffusion term of (2.48) in (2.44) one. The following expression is obtained

$$\begin{cases}
\frac{\partial \bar{\rho} \widetilde{Z}}{\partial t} + \nabla \cdot \left(\bar{\rho} \widetilde{\vec{U}} \widetilde{Z} \right) = \nabla \cdot \left\{ \left[\frac{\bar{\mu}}{Sc} + \frac{\mu_{t,sgs}}{Sc_{t,sgs}} \right] \nabla \widetilde{Z} \right\} + \nabla \cdot \left\{ \left[\frac{\mu}{Sc} \right]_{ATFM} \bar{\bar{T}} \nabla \widetilde{Z} \right\} = \\
= \nabla \cdot \left\{ \left[\frac{\bar{\mu}}{Sc} + \frac{\mu_{t,sgs}}{Sc_{t,sgs}} \right] \nabla \widetilde{Z} \right\} + \\
+ \nabla \cdot \left\{ \left[\left(F(\Omega) E(\Omega) \frac{\bar{\mu}}{Sc} + (1 - \Omega) \frac{\mu_{t,sgs}}{Sc_{t,sgs}} \right) - \left(\frac{\bar{\mu}}{Sc} + \frac{\mu_{t,sgs}}{Sc_{t,sgs}} \right) \right] \bar{\bar{T}} \nabla \widetilde{Z} \right\}
\end{cases} \tag{2.49}$$

where the pure mixing layers far from the flame front are preserved, thanks to flame

sensor Ω application.

2.6 Additional Numerical Strategies of the Model

To complete the proposed ATF model description and to allow the practical application of all equations presented so far, two techniques have to be introduced:

1. The methodology to carry out the *filtering of LES fields*, in order to dynamically compute the exponent of Charlette's efficiency function power-law (Section 2.3.2).

2. The *evaluation of the sub-grid scale turbulence intensity* u'_{Δ}, which is fundamental for the efficiency function computation (Section 2.3).

In the following sub-sections these techniques are described with the relative formulations.

2.6.1 Filtering of LES fields

The filtering procedure of an LES field, which by definition is already filtered, is usually carried out through a test-filter scale Δ_{test} greater than the basic LES filter size (e.g. the mesh grid Δ_{mesh}). This strategy is generally applied by dynamic procedures of sub-grid scale models, in order to adapt the unresolved field trends on resolved ones.

The only difference between a *test* and a *basic* filtering approach is the filter scale dimension, hence the theoretical basis and equations are the same. In general, a filtering procedure on a filter-size Δ is defined as the convolution between the filter kernel G and the function to be filtered ϕ on the computational domain D

$$\bar{\phi}\left(\vec{x}\right) = \int_{D} G\left(\vec{y} - \vec{x}\right) \phi\left(\vec{y}\right) d\vec{y} \tag{2.50}$$

However, if with structured grids the implementation of (2.50) filtering process is trivial, in case of unstructured grids it becomes far more complex [81].

Therefore, as demonstrated in [31, 81], a different approach based on the *truncation of filter moments* is more convenient to use. It basically consists in expanding any variable to be filtered into Taylor series before performing the convolution. Analyzing for

simplicity the 1D filtering and providing the definition of convolution between the filter kernel G and the function to be filtered ϕ (namely, the filtering procedure definition)

$$\bar{\phi}(x) = \int_{-\infty}^{\infty} G(y-x)\,\phi(y)\,dy = G * \phi \tag{2.51}$$

the Taylor expansion series for the function $\phi(y)$, after a more comfortable change of variable

$$\begin{cases} j = y - x \\ \bar{\phi}(x) = \int_{-\infty}^{\infty} G(j)\,\phi(j+x)\,dj \end{cases} \tag{2.52}$$

can be written as

$$\begin{aligned} \phi(j+x) &= \phi(x) + [(j+x)-x]\left(\frac{\partial\phi}{\partial j}\right)_x + \frac{[(j+x)-x]^2}{2}\left(\frac{\partial^2\phi}{\partial j^2}\right)_x + \ldots = \\ &= \phi(x) + j\left(\frac{\partial\phi}{\partial j}\right)_x + \frac{j^2}{2}\left(\frac{\partial^2\phi}{\partial j^2}\right)_x + \ldots = \sum_{k=0}^{\infty}\frac{1}{k!}j^k\left(\frac{\partial^k\phi}{\partial j^k}\right)_x \end{aligned} \tag{2.53}$$

If (2.53) is substituted in the convolution expression of (2.52), it can be obtained this alternative filtering formulation

$$\bar{\phi}(x) = \sum_{k=0}^{\infty}\frac{1}{k!}\left(\frac{\partial^k\phi}{\partial j^k}\right)_x \int_{-\infty}^{\infty} G(j)\,j^k dj = \sum_{k=0}^{\infty}\frac{1}{k!}M_k\left(\frac{\partial^k\phi}{\partial j^k}\right)_x \tag{2.54}$$

where the term highlighted in red represents the filter moments M_k. An example of M_k values computation (until the 4^{th} order) is here presented for the Box and Gaussian filters

Momentum n.	Value for Box Filter	Value for Gaussian Filter
M_0	$\int_{-\Delta/2}^{+\Delta/2}\frac{1}{\Delta}dj = \mathbf{1}$	$\mathbf{1}$
M_1	$\int_{-\Delta/2}^{+\Delta/2}\frac{1}{\Delta}j\,dj = \mathbf{0}$	$\mathbf{0}$
M_2	$\int_{-\Delta/2}^{+\Delta/2}\frac{1}{\Delta}j^2 dj = \mathbf{\frac{\Delta^2}{12}}$	$\mathbf{\frac{\Delta^2}{12}}$
M_3	$\int_{-\Delta/2}^{+\Delta/2}\frac{1}{\Delta}j^3 dj = \mathbf{0}$	$\mathbf{0}$
M_4	$\int_{-\Delta/2}^{+\Delta/2}\frac{1}{\Delta}j^4 dj = \mathbf{\frac{\Delta^4}{80}}$	$\mathbf{\frac{\Delta^4}{48}}$

being $1/\Delta$ at $-\Delta/2 \leq j \leq \Delta/2$ the Box filter kernel.

Afterwards, if the filter moments are truncated at the 2^{nd} order, (2.54) becomes

$$\bar{\phi}(x) = \phi(x) + \frac{\Delta^2}{24}\left(\frac{\partial^2\phi}{\partial x^2}\right)_x \tag{2.55}$$

for both aforementioned filters with the 2^{nd} derivative

$$\left(\frac{\partial^2\phi}{\partial x^2}\right)_x = \frac{\phi_{i+2} - 2\phi_i + \phi_{i-2}}{4\Delta^2} \tag{2.56}$$

discretized by using the central differencing technique (4Δ stencil).

As a consequence of the similarity between *test* and a *basic* filtering approaches, in case of a 3D test-filtering procedure carried out over the filter dimension defined in (2.29), expression (2.55) is simply rewritten as

$$\overbrace{\bar{\phi}}\,(\vec{x}) = \bar{\phi}\,(\vec{x}) + \frac{\Delta_{test}^2}{24}\,\nabla^2\left[\bar{\phi}\,(\vec{x})\right] \tag{2.57}$$

where $\bar{\phi}\,(\vec{x})$ is the basic-filtered 3D LES variable.

2.6.2 Evaluation of the Sub-Grid Scale Turbulence Intensity u'_Δ

As proposed by Colin [31], the basis for the sub-grid scale turbulence intensity u'_Δ computation comes form the similarity assumption here expressed

$$\begin{cases} \vec{u'} = c\left(\vec{\bar{U}} - \vec{\bar{\bar{U}}}\right) = OP\left(\vec{\bar{U}}\right) \\ u'_\Delta = \left|\vec{u'}\right| \end{cases} \tag{2.58}$$

where $\vec{\bar{U}}$ is the LES resolved velocity (i.e. the $\vec{U}$ filtered by the basic-filter size Δ_{mesh}), while $\vec{\bar{\bar{U}}}$ is a local average of $\vec{\bar{U}}$ (namely, $\vec{\bar{U}}$ filtered over a generic filter size $\Delta > \Delta_{mesh}$). Therefore, if Δ is assumed to be equal to the thickened flame thickness $\Delta = F\delta_l^0 = \delta_l^1$ the u'_Δ of (2.58) becomes the thickened flame sub-grid scale turbulence intensity, which is useful for the efficiency function E computation (see Section 2.3).

The flame characteristics impose two significant constraints on (2.58) discrete operator $OP\left(\vec{\bar{U}}\right)$, giving a $\vec{u'}$ approximation, [31]:

1. Because the proposed approach is based on the similarity properties of turbulent scales, the use of a local operator like the *Box filter* is mandatory.

2. Only the *rotational part* of the resolved velocity field has to be interpreted as a velocity fluctuation. This because its dilatational part, which is responsible for the velocity variation through a laminar flame, would create artificial velocity fluctu-

ations in presence of a planar laminar flame propagating with no turbulence.

Hence, by first applying on the LES resolved velocity $\vec{\tilde{U}}$ the filtering technique proposed in Section 2.6.1 it is possible to express the discrete operator $OP\left(\vec{\tilde{U}}\right)$ of (2.58) as

$$u'_{\Delta} = \left|\vec{u'}\right| = \left|c\left(\vec{\tilde{U}} - \vec{\bar{\tilde{U}}}\right)\right| = c_1\Delta^2 \left\|\nabla^2\vec{\tilde{U}}\right\| = OP_1\left(\vec{\tilde{U}}\right) \tag{2.59}$$

being $OP_1\left(\vec{\tilde{U}}\right)$ its first expression which includes both rotational and dilatational parts of the resolved velocity field. Then, a second and final expression of the operator $OP\left(\vec{\tilde{U}}\right)$ is derived by extracting only the rotational part of the first operator $OP_1\left(\vec{\tilde{U}}\right)$. The following relationship is achieved

$$u'_{\Delta} = \left|\vec{u'}\right| = \left|OP_2\left(\vec{\tilde{U}}\right)\right| = c_2\Delta^3 \left|\nabla \times \nabla^2\vec{\tilde{U}}\right| \tag{2.60}$$

where $c_2 = 2$ for all turbulent Reynolds number values.

Finally, an important consideration can be performed: if the sub-grid scale turbulence intensity u'_{Δ} is computed by assuming the test-filter size equal to the thickened flame thickness $\Delta = F\delta_l^0 = \delta_l^1$, the equation (2.60) becomes useful for the efficiency function E evaluation. In particular, the thickened flame sub-grid scale turbulence intensity is simply computed by a similarity assumption on the LES resolved velocity $\vec{\tilde{U}}$.

2.7 Summary

In the context of an LES turbulence description, numerical simulations of turbulent premixed reacting flows are not able to resolve the inner structure of the flame front on common computational grids. To overcome this difficulty the Artificially Thickened Flame Model (ATFM) can be adopted: it increases artificially the flame thickness to allow the reaction layer resolution on usual computational grids, solving the aforementioned difficulty.

The proposed ATFM version is characterized by the following features:

- The thickening factor F definition is based on the local mesh resolution (*grid adaptive*), in order to minimize the modelling effort (thicker flame fronts result in more modified *flame-turbulence* interactions).

- Several formulation of the efficiency function E are available to increase the flame speed with no additional modification to its thickness. This is necessary in order to compensate the lost *flame-turbulence* interaction in terms of total flame surface reduction (namely, the lost wrinkling effect), when the reaction layer is artificially thickened. In particular, also a dynamic formulation for E computation is available, where some resolved flame wrinkling is analyzed in order to match the modelled sub-grid scale wrinkling trend with the computed one.

- The thickening concept is coupled with a tabulation strategy to include detailed chemistry effects without prohibitive flame thickening.

- A flame sensor Ω is used to modify the diffusion terms of conservation equations only at the reacting region, to ensure a correct pure mixing simulation in case of a generic stratified mixture. In particular, the *Flame sensor based on Progress Variable Gradient and Source Term* is here proposed because it represents the best solution between the flame sensors available in literature (as it will be demonstrated in Section 5.2.2).

- In case a small scale stratification is present and the reaction layer is overlapped to a not negligible mixing layer (with a generic orientation), to correctly follow the ATF concept the thickening procedure should be applied not only on the progress variable gradient (flame thickening) but also on the mixture fraction gradient component parallel to the flame normal direction. This approach can be called *directional thickening* of the $\vec{\nabla}\widetilde{Z}$ and a strategy to apply this concept with a fully-implicit numerical formulation is here proposed.

As a supplement for the ATFM application, information on numerical strategies for:

- the filtering procedure of LES fields,

- the evaluation of the sub-grid scale turbulence intensity u'_{Δ},

are also reported.

The assessment of the proposed ATFM behaviour will be carried out in Chapter 5 under a *lean-lean* charge stratification.

Part

Model validation

CHAPTER 3

Flame stretch and electrical circuit models assessment

A preliminary assessment of the proposed flame stretch (Section 1.2.3) and electrical circuit (Section 1.1.4) models was carried out over simplified configurations, in order to understand separately their predicting capabilities. This strategy allowed to focus the investigation on single and specific phenomena, providing support to the further validation of the Comprehensive CFD Model reported in Chapter 4.

3.1 Flame stretch models assessment

The behaviour of stretch models proposed in Section 1.2.3, namely:

- Bradley, Lau and Lawes' one
- Herweg and Maly's one

is here investigated.

After a detailed mathematical explanation of Bradley, Lau and Lawes stretch model, numerical reacting simulations on a *Propane-Air* premixed mixture inside a simplified combustion chamber were performed at different

- equivalence ratios
- turbulence intensities

to carry out the assessment of both aforementioned models.

3.1.1 Mathematical explanation of Bradley, Lau and Lawes stretch model

As a consequence of flame stretch phenomenon, the unstretched laminar flame speed s_{u0} changes to a value of s_u through the following expression [13]:

$$\frac{s_{u0} - s_u}{s_{u0}} = \frac{1}{A_f}\frac{dA_f}{dt}\frac{\delta_l}{s_{u0}}Ma \tag{3.1}$$

where A_f is the flame surface area, t the time, δ_l the laminar flame thickness and Ma the Markstein number.

By analysing (3.1) the term $1/A_f\ dA_f/dt$, which represents the strain rate of a laminar flame, can be written as [13]

$$\frac{1}{A_f}\frac{dA_f}{dt} = \frac{1}{R}V_1 + \nabla_t \cdot \vec{V} \tag{3.2}$$

where R is the flame curvature total radius and $\vec{V} = (V_1; V_2; V_3)$ is the flame surface velocity vector. In particular, V_1 is the normal velocity component with respect to the flame surface, namely the flame speed, and $\nabla_t \cdot \vec{V}$ is the velocity gradient along the surface (for convenience, the flame surface lies on the $\vec{x}_2 - \vec{x}_3$ plane with $\vec{x}_1$ being its normal direction). The generality of this expression, which is suitable for any set of curvilinear coordinates, is fundamental for the strain rate estimation of a generic flame shape.

Then, Bradley, Lau and Lawes suggested to consider [13]:

1. The flame speed as the sum of the actual laminar burning velocity s_u and the fluid velocity along the flame surface normal direction.

2. The flow field contribution to strain rate as the flow field stretch ahead of the flame, which, for isotropic turbulence, is of about the same magnitude of the Eulerian mean strain rate [7].

The first suggestion allows to write:

$$\begin{cases} V_1 = s_u + U_1 \\ V_2 = U_2 \\ V_3 = U_3 \end{cases} \tag{3.3}$$

where $\vec{U} = (U_1; U_2; U_3)$ is the fluid velocity vector in the previously defined general coordinate system $\vec{x}_1 - \vec{x}_2 - \vec{x}_3$, reminding that $\vec{x}_1$ is the flame normal direction. Components V_2 and V_3 of the flame velocity $\vec{V}$ are equal to the corresponding components of fluid speed $\vec{U}$ because tangential velocities along the flame surface (identified by the $\vec{x}_2 - \vec{x}_3$ plane) are only those of the fluid. Hence, by substituting 3.3 in 3.2, the following expression was achieved

$$\frac{1}{A_f}\frac{dA_f}{dt} = \frac{s_u}{R} + \left(\frac{U_1}{R} + \nabla_t \cdot \vec{U}\right) \tag{3.4}$$

where s_u/R represents the contributions to strain rate due to both flame propagation and curvature, while the bracketed term $\left(U_1/R + \nabla_t \cdot \vec{U}\right)$ is the flow field contribution.

The second Bradley, Lau and Lawes' suggestion, which allows to consider $\left(U_1/R + \nabla_t \cdot \vec{U}\right)$ as the flow field stretch ahead of the flame, afford to write the following approximation

$$\left(\frac{U_1}{R} + \nabla_t \cdot \vec{U}\right) \approx \frac{u'}{\lambda} \tag{3.5}$$

where u'/λ is the Eulerian mean strain rate, computed as the ratio between the turbulence intensity u' and the Taylor microscale of turbulence λ. The validity of (3.5) in presence of isotropic turbulence is confirmed by Batchelor [7].

Let's consider, now, the possible shapes that a premixed SI engine flame can assume during the early propagation stage in a general CFD modelling strategy:

1. *cylindrical*, if the inter-electrodes plasma channel is modelled,

2. *spherical*, if a single-kernel model is adopted.

As suggested in [13], the general expression (3.2) can be rewritten as follows:

1. for a *cylindrical* flame

$$\frac{1}{A_f}\frac{dA_f}{dt} = \frac{1}{R}V_R + \left(\frac{\partial V_\theta}{R\,\partial\theta} + \frac{\partial V_Z}{\partial Z}\right) \tag{3.6}$$

where θ and Z are the polar and the axial coordinates of the system, respectively, in which:

$$\begin{cases} x_1 = R\ \cos\theta \\ x_2 = R\ \sin\theta \\ x_3 = Z \end{cases} \tag{3.7}$$

2. for a *spherical* flame

$$\frac{1}{A_f}\frac{dA_f}{dt} = \frac{2}{R}V_R + \left(\frac{\partial V_\theta}{R\,\partial\theta} + \frac{\cot\theta}{R}V_\theta + \frac{\partial V_\varphi}{R\ \sin\theta\,\partial\varphi}\right) \tag{3.8}$$

where θ and φ are the polar coordinates of the system in which:

$$\begin{cases} x_1 = R\ \sin\theta\ \cos\varphi \\ x_2 = R\ \sin\theta\ \sin\varphi \\ x_3 = R\ \cos\theta \end{cases} \tag{3.9}$$

Following the same considerations shown in (3.3) to rewrite (3.2) as (3.4), expressions (3.6) and (3.8) were rearranged to split the flame speed (V_R) in its two contributions (s_u and U_R). Thus, for a *cylindrical* flame shape was achieved

$$\frac{1}{A_f}\frac{dA_f}{dt} = \frac{s_u}{R} + \left(\frac{U_R}{R} + \frac{\partial U_\theta}{R\,\partial\theta} + \frac{\partial U_Z}{\partial Z}\right) \tag{3.10}$$

while for a *spherical* flame could be written

$$\frac{1}{A_f}\frac{dA_f}{dt} = \frac{2\ s_u}{R} + \left(\frac{2\ U_R}{R} + \frac{\partial U_\theta}{R\,\partial\theta} + \frac{\cot\theta}{R}U_\theta + \frac{\partial U_\varphi}{R\ \sin\theta\,\partial\varphi}\right) \tag{3.11}$$

It is worth to notice that the RHS bracketed term in (3.10) and (3.11) is the flow field

contribution to strain rate $\left(U_1/R + \nabla_t \cdot \vec{U}\right)$ expressed for a *cylindrical* and *spherical* flame shape, respectively. Therefore, thanks to (3.5) and to dimensionless Karlovitz stretch factor definition provided by Abdel-Gayed [2]

$$K = \frac{u'}{\lambda}\,\frac{\delta_l}{s_{u0}} \tag{3.12}$$

it is possible to obtain:

1. for a *cylindrical* flame

$$\frac{1}{A_f}\frac{dA_f}{dt} \approx \frac{s_u}{R} + \frac{u'}{\lambda} = \frac{s_u}{R} + K\,\frac{s_{u0}}{\delta_l} \tag{3.13}$$

2. for a *spherical* flame

$$\frac{1}{A_f}\frac{dA_f}{dt} \approx \frac{2\,s_u}{R} + \frac{u'}{\lambda} = \frac{2\,s_u}{R} + K\,\frac{s_{u0}}{\delta_l} \tag{3.14}$$

Finally, by substituting (3.13) and (3.14) in (3.1), after some mathematical manipulations the actual laminar flame speed s_u correction is achieved (as reported in Section 1.2.3):

$$s_u \approx s_{u0}\frac{1 - K\,Ma}{1 + \frac{c}{R}\,\delta_l\,Ma} \tag{3.15}$$

where c is the parameter that fits this formulation to the desired initial flame shape; in particular:

- $c = 1$ if *cylindrical*
- $c = 2$ if *spherical*

3.1.2 CFD investigation to assess models behaviour

In the context of CFD simulations, the two flame stretch models proposed in Section 1.2.3 were investigated. In particular, their behaviour was assessed under variations of the equivalence ratio and turbulence intensity, which are fundamental variables in a premixed charge SI engine.

With this purpose, numerical simulations of premixed combustion were carried out following the experimental investigation performed by Herweg and Maly [54]. There-

fore, the test conditions specified in Table 3.1 were analyzed. In particular, turbulence was described through the RANS approach and the $k-\varepsilon$ model was adopted. Moreover, all simulations were carried out:

1. Under the hypothesis of not decaying turbulence, because of the very small time-scales that characterize the early laminar flame kernel development.
2. Assuming a unitary Lewis number, to focus only on equivalence ratio and turbulence variations.
3. Neglecting the wrinkling effect (namely the surface increase) that turbulence generates on the flame, to understand if both flame stretch models consider correctly the strain produced by turbulence.
4. Inside a simplified combustion chamber.

Table 3.1: *Herweg and Maly experimental test conditions [54] used for stretch models assessment.*

Characteristic	Test conditions					
	1	2	3	4	5	6
Fuel	Propane	Propane	Propane	Propane	Propane	Propane
Mixture inlet temperature $[K]$	298	298	298	298	298	298
Pressure at ignition timing $[bar]$	5	5	5	5	5	5
Relative air-fuel ratio λ	1	1.5	1	1	1	1
Engine speed $[rpm]$	300	300	500	750	1000	1250

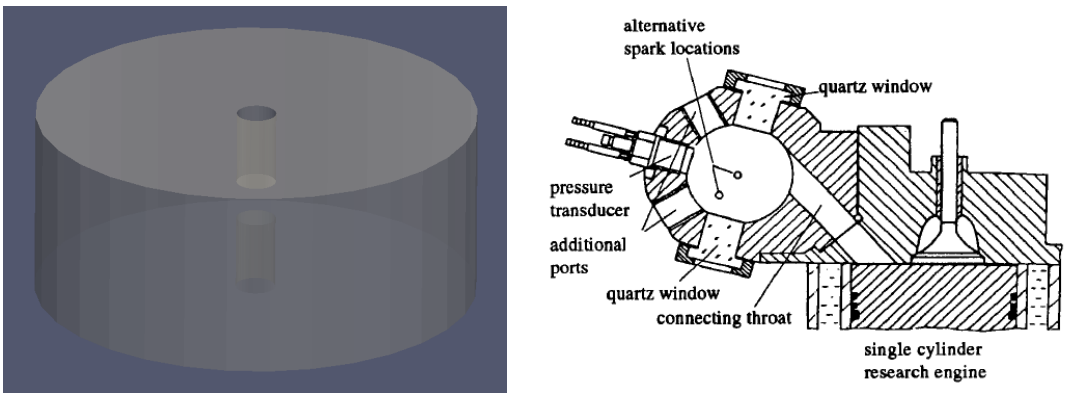

(a) **(b)**

Figure 3.1: *Simplified Herweg and Maly combustion side chamber around the centred spark-gap (a) and sectional view of the original one [54] (b).*

The investigated geometry (Figure 3.1a) is a cylindrical portion around the centred spark-gap of Herweg and Maly's side chamber [54] (Figure 3.1b). This choice was per-

formed to investigate the initial laminar flame kernel development with low computational costs and assuming a zero mean flow field velocity (because close to the ignition zone). On this combustion chamber volume, a structured hexahedral mesh was created with a $62.5\ \mu m$ cell size in the cylindrical spark-gap (Figure 3.2a). Then, the resolution was progressively reduced as the distance from the spark-plug increased (Figure 3.2b). Details on the combustion chamber geometry and the computational mesh are provided in Table 3.2.

Table 3.2: *Key features of the simplified geometry used for simulations and of the mesh realized on it.*

Characteristic	Value/Type
Spark-gap $[mm]$	1.0
Wire electrodes diameter $[mm]$	1.0
Chamber diameter $[mm]$	11.25
Chamber clearance $[mm]$	4.75
Spark location	central
Hexahedral cells $[n]$	$\approx 13'000$

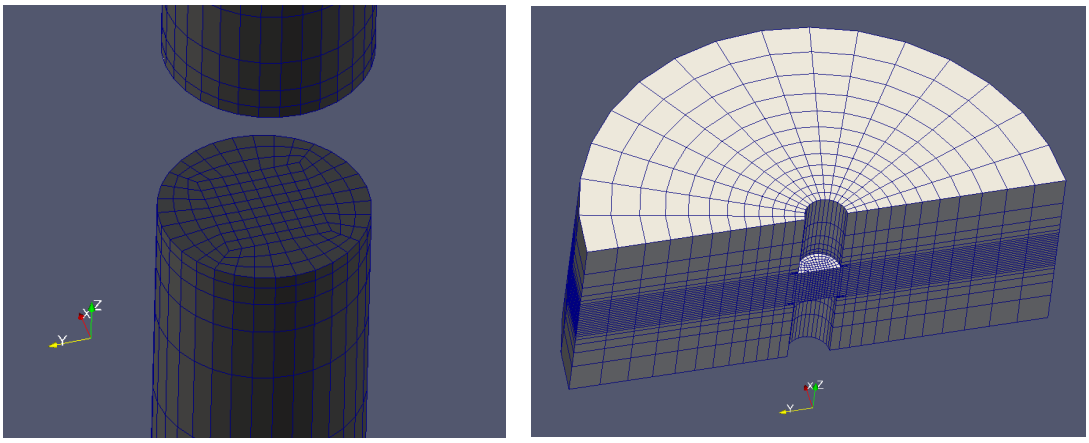

(a) **(b)**

Figure 3.2: *Simplified side chamber mesh details: cubic cells in the cylindrical spark-gap (a) and hexahedra of size increasing with chamber radius (b).*

The plasma channel was modelled through a set of Lagrangian particles placed along the spark-gap distance, as proposed in Section 1.1.1. However, the present investigation was carried out by following the simplified approach described in [72], where Lagrangian particles modelled not only the thermal effects from the electrical circuit, but also the chemical influence on kernel growth. This choice was performed in order to simplify drastically this preliminary analysis, avoiding the simulation of chemical reactions on the Eulerian framework.

Therefore, particles could be convected by the mean flow field velocity (here equal to zero in all test conditions, as previously mentioned) and grow in size because of:

- the flame speed,
- the thermal expansion generated by the heat transferred from the electrical circuit to the gaseous mixture.

The flame stretch phenomenon, quantified by the factor $I_0 = s_u/s_{u0}$, was considered by using (1.21) for the Bradley-Lau-Lawes model and (1.26) for the Herweg-Maly one. Both expressions were used with $c = 1$, because a cylindrical shape for the laminar flame kernel was assumed. From now on, the two models will be called with the names of the authors that proposed or suggested them.

Equivalence ratio variations The influence of flame stretch phenomenon on flame front development is strongly dependent on the air/fuel ratio of the investigated mixture.

For this reason, the equivalence ratio ϕ was the first analyzed parameter. It is defined as the ratio between the stoichiometric α_{st} and the actual α air/fuel ratio ($\phi = \alpha_{st}/\alpha = 1/\lambda$), where λ represents the inverse of ϕ; hence in presence of lean mixtures ($\phi < 1$) the value of λ is greater than one ($\lambda > 1$) and vice versa. Consequently, *Tests 1* and *2* were compared (see Table 3.1). Numerical simulations were performed using a $0.5\ \mu s$ time-step.

As Figures 3.3a and 3.3b show, at fixed turbulence (300 rpm engine speed) with both models the laminar flame kernel development is slower if the value of λ increases, namely the laminar flame speed is reduced as the mixture becomes leaner. Consequently, both models display the same trend to λ-variations, although that proposed by Bradley-Lau-Lawes is more sensitive. In fact, as Figure 3.3c shows, the laminar flame development predicted by this model is similar at stoichiometric mixtures ($\lambda = 1$) but slower at lean mixtures than Herweg-Maly's one.

Turbulence intensity variations Normal operating conditions of an actual IC engine are included in a certain crankshaft speed range: this generates variations on piston speed with consequences on mean (i.e. swirl or tumble) and turbulent flow field motion inside

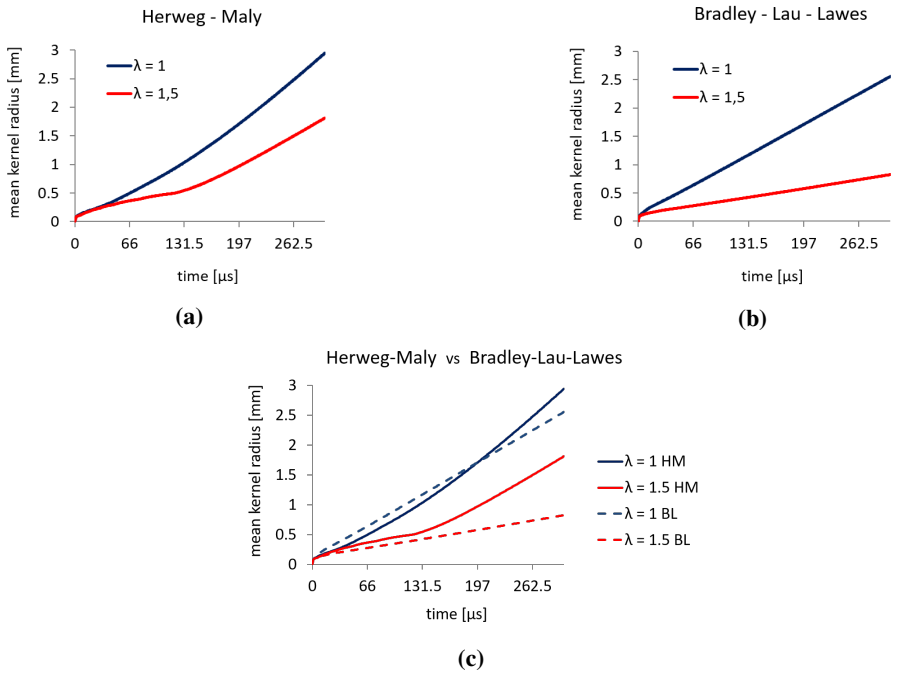

Figure 3.3: *Development of mean flame kernel radius in time at different λ values, using Herweg-Maly (HM) (a) and Bradley-Lau-Lawes (BL) (b) stretch model at constant turbulence (*Tests 1 *and* 2 *of Table 3.1). Image (c) compares the results estimated by the two models.*

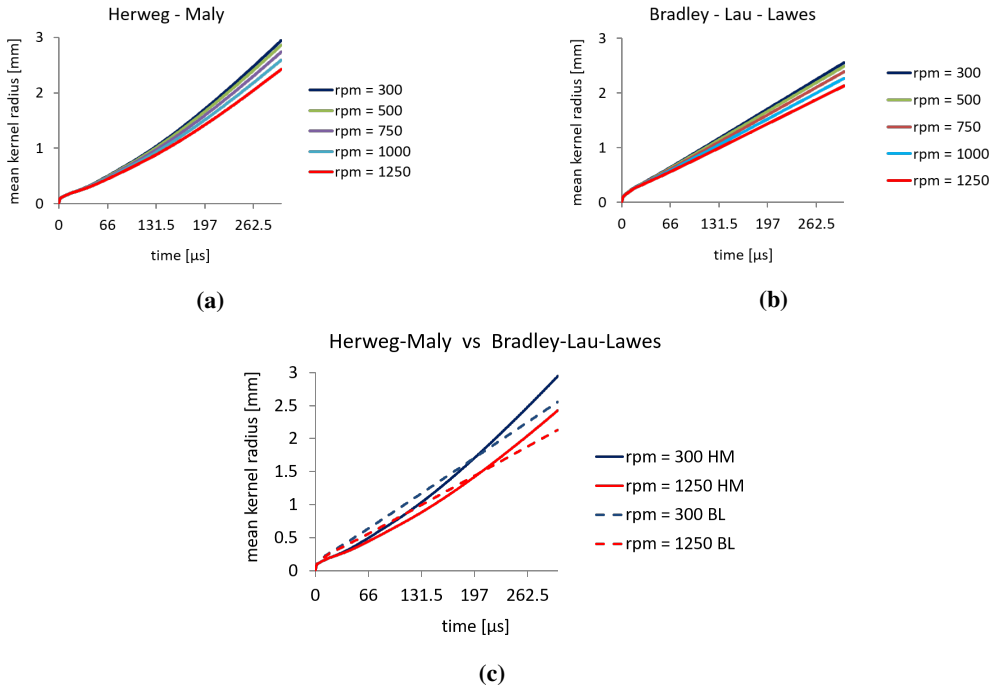

Figure 3.4: *Development of mean flame kernel radius in time at different engine speed values (rpm), using Herweg-Maly (HM) (a) and Bradley-Lau-Lawes (BL) (b) stretch model at constant equivalence ratio (*Tests 1, 3, 4, 5 *and* 6 *of Table 3.1). Image (c) compares the results estimated by the two models.*

the combustion chamber. Because flame stretch phenomenon is sensitive to turbulence intensity variations [13], this aspect was also investigated.

With this purpose, the mixture was ignited at the central point of the side chamber where the mean component of the flow field velocity can be neglected [54]; hence flow velocity was set to zero. Then the initial turbulence intensity u' was changed according to Herweg and Maly's test conditions at different engine speeds (300 rpm, 500 rpm, 750 rpm, 1000 rpm and 1250 rpm) [54]. Results from *Tests 1*, *3*, *4*, *5* and *6* (see Table 3.1) were compared. All numerical simulations were performed using a 0.5 μs time-step.

As Figures 3.4a and 3.4b show, at fixed equivalence ratio ($\phi = 1$) and with both models, a turbulence intensity increase causes a reduction of the laminar flame kernel development. This result is due to the increased flame stretch that a higher turbulence generates on the flame and that, in the context of this numerical investigation, is not counterbalanced by the wrinkling effect. In practice, turbulence affects a flame by two principal and opposing phenomena [13]:

1. The wrinkling effect, which increases the flame surface and consequently the flame speed.

2. The stretch effect, which strain the flame surface and causes a flame speed reduction.

However, in this work, first effect was removed and only the second one was considered. Another important aspect is that, as previously mentioned, for each test condition the hypothesis of not decaying turbulence was assumed because attention was focused on the very initial stage of combustion, whose characteristic time-scales are very small. Therefore, for these investigations, the turbulent flow field was not affected by the flame front propagation.

Finally, from Figure 3.4c, it is possible to notice how both stretch models exhibit an almost similar behaviour at both low and high turbulence intensities.

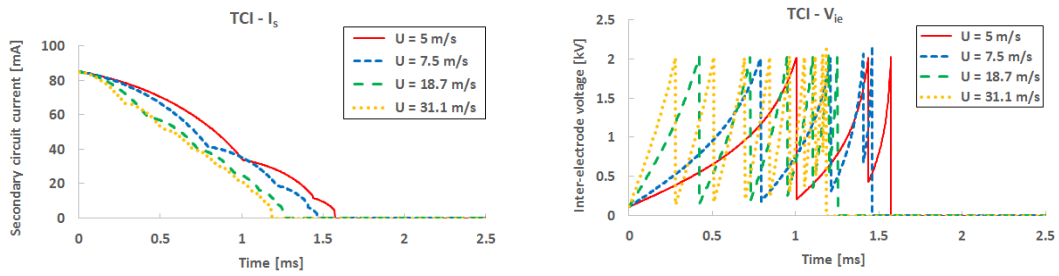

(a) **(b)**

Figure 3.5: *TCI ignition system numerical results with a variation of mean velocity at the spark-gap. Here are shown trends for the secondary circuit current i_S (a) and the inter-electrode voltage V_{IE} (b).*

3.2 Electrical circuit model validation

The validation of the proposed electrical circuit model was carried out over two different systems:

1. The *Transistor Coil Ignition System* (TCI), characterized by long discharge times (of the order of ms).

2. The *Capacitor Discharge Ignition System* (CDI), characterized by a short discharge duration (μs) because equipped with a lower inductance value with respect to TCI systems.

This allowed to assess the capability of the model to predict completely different spark events. In fact, the TCI ignition system provides the majority of the energy transfer during the glow discharge (long discharge duration), while the CDI system operates mainly during the arc stage, thanks to its short discharge time. Herweg and Maly [54] provided useful experimental data about the aforementioned ignition systems.

3.2.1 TCI system

The behaviour of the proposed electrical circuit model was tested with a variation of the spark-gap mean flow velocity (Figure 3.5) after being calibrated to fit the TCI system adopted by Herweg and Maly [54] (Figure 3.6).

The calibration of the model was carried out trying to obtain the best fit of the available trends for:

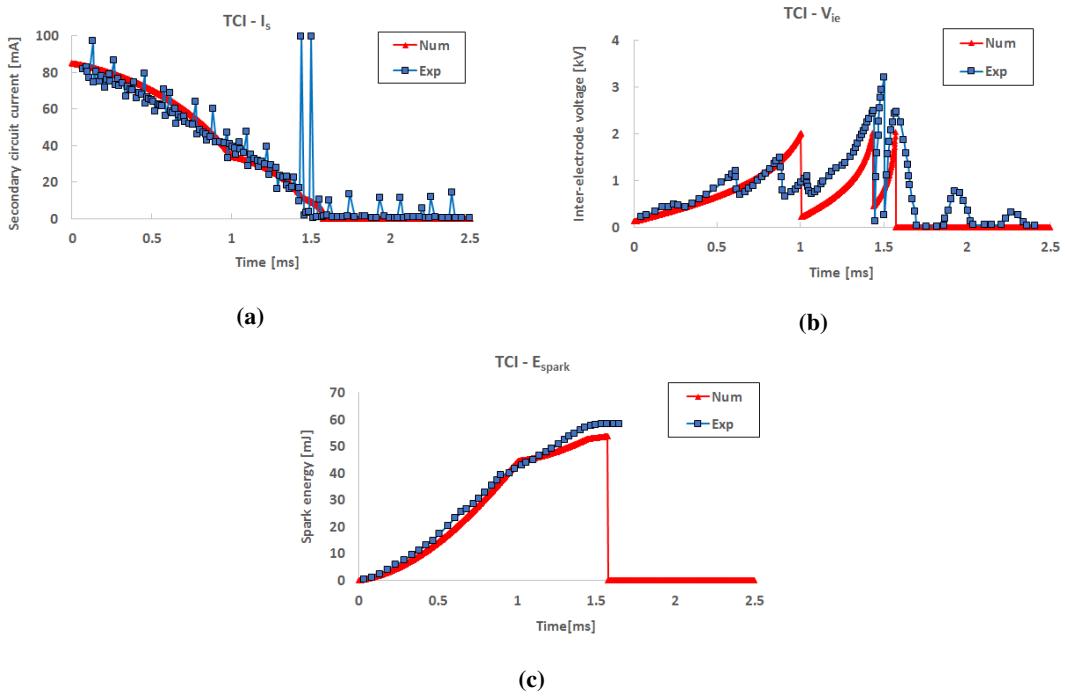

Figure 3.6: *Results of the calibration procedure carried out for the TCI ignition system. Comparison between experimental data from [54] and numerical results after model calibration for: the secondary circuit current i_S (a), the inter-electrode voltage V_{IE} (b) and the energy released to the mixture E_{spark} (c).*

- Secondary circuit current i_S
- Inter-electrode voltage V_{IE}
- Electrical energy supplied to the mixture E_{spark}

Figure 3.6 shows almost satisfactory results for all the investigated parameters; in particular, a mean flow velocity of $U = 5\ m/s$ was imposed at the spark-gap, in order to allow a correct fit.

Afterwards, the sensitivity of the model was tested under different flow velocities at the spark-gap. The results of Figure 3.5 allows to assert that, with an increase of the mean flow velocity:

1. The discharge duration is reduced
2. The number of restrike events is increased

This is in accordance to the experimental trend reported in Table 3.3, but also with other experimental findings [61].

Table 3.3: *Experimental and numerical discharge duration for a TCI system with different mean flow velocities at the spark-gap. The experimental data come form Herweg and Maly [54].*

Mean flow velocity at the spark-gap $[m/s]$	Discharge duration $[ms]$	
	Experimental	Numerical
7.5	1.2	1.5
18.7	0.9	1.3
31.1	0.7	1.2

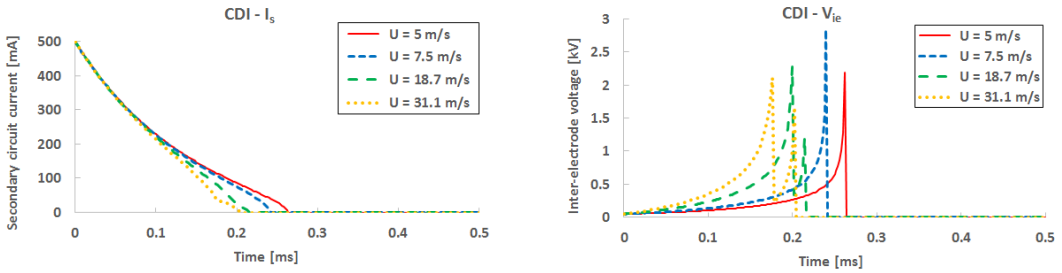

(a) **(b)**

Figure 3.7: *CDI ignition system numerical results with a variation of mean velocity at the spark-gap. Here are shown trends for the secondary circuit current i_S (a) and the inter-electrode voltage V_{IE} (b).*

3.2.2 CDI System

As performed for the TCI system, the implemented electrical circuit model was tested with different gas flow velocities at the spark-gap (Figure 3.7) after a calibration procedure (Figure 3.8), carried out to fit the Herweg and Maly [54] CDI system behavior.

As Figure 3.8 shows, after a suitable calibration which included the assumption of $U = 5\ m/s$ at the spark-gap, the experimental trends for secondary circuit current i_S, inter-electrode voltage V_{IE} and electrical energy supplied to the mixture E_{spark} were well captured by the proposed model.

Concerning the investigation on the model sensitivity to a flow velocity variation at the spark-gap, Figure 3.7 togheter with Table 3.4 allows to conclude that, in presence of an increase of the flow velocity, the:

- Reduction of discharge duration
- Increase of the restrike events number

are well captured. In particular, the first mentioned phenomenon was predicted with very good agreement also form a quantitative point of view (Table 3.4).

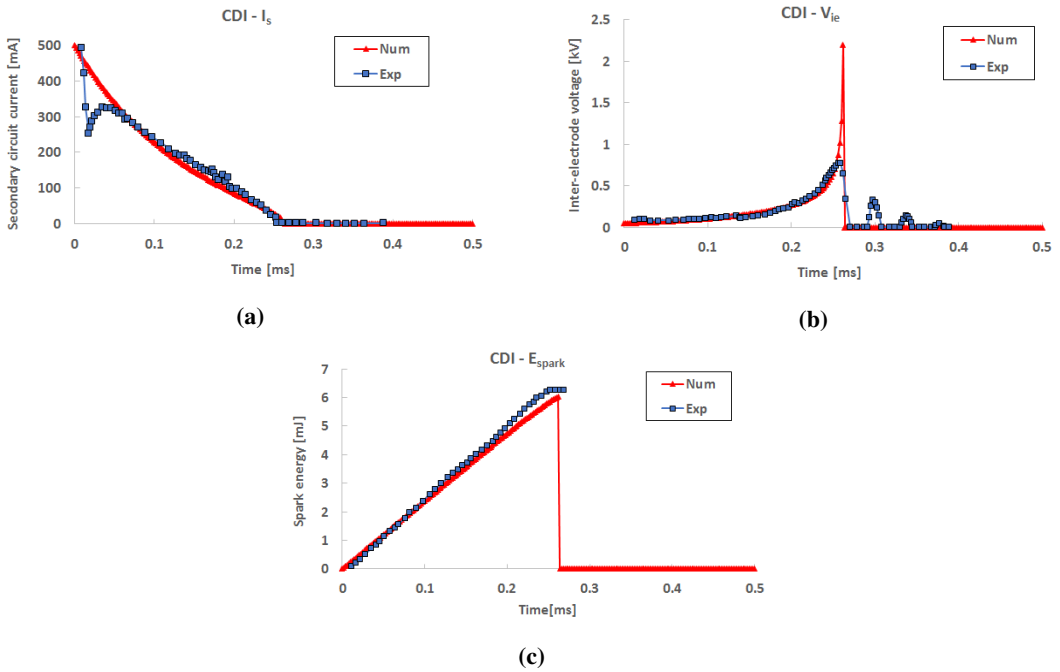

Figure 3.8: *Results of the calibration procedure carried out for the CDI ignition system. Comparison between experimental data from [54] and numerical results after model calibration for: the secondary circuit current i_S (a), the inter-electrode voltage V_{IE} (b) and the energy released to the mixture E_{spark} (c).*

Table 3.4: *Experimental and numerical discharge duration for a CDI system with different mean flow velocities at the spark-gap. The experimental data come form Herweg and Maly [54].*

Mean flow velocity at the spark-gap $[m/s]$	Discharge duration $[ms]$	
	Experimental	Numerical
7.5	0.24	0.24
18.7	0.22	0.22
31.1	0.20	0.20

3.3 Summary

The proposed flame stretch (Section 1.2.3) and electrical circuit (Section 1.1.4) models were preliminary assessed over simplified configurations, in order to understand separately their predicting capabilities.

In particular, the first target was to investigate how different flame stretch models affects the initial flame kernel development process in SI engines. To this end, numerical simulations were carried out using the proposed two different approaches:

- the Herweg and Maly
- the Bradley, Lau and Lawes

stretch models. From achieved results, both of them can fairly predict the flame stretch phenomenon. In fact, under the hypothesis of not decaying turbulence and unitary Lewis number, they are able to estimate a laminar flame speed reduction in case both of a leaner mixture and an increased turbulence intensity. This last result is true only if we neglect the wrinkling effect that turbulence generates on the flame in order to understand if the investigated stretch model considers correctly the strain produced by turbulence. Moreover, by comparison, both of them exhibit quite similar behaviours at λ and rpm variations; therefore, they can be considered almost interchangeable.

The second topic of the Chapter concerned the validation of the proposed electrical circuit model. It was carried out over two different systems:

- the TCI, characterized by long discharge times (of the order of ms),
- the CDI, characterized by short discharge durations (μs),

and testing a variation of the spark-gap mean flow velocity. The model was calibrated to fit Herweg and Maly experimental data at fixed conditions. The achieved results allow to assert that, with an increase of the mean flow velocity:

- The discharge duration is reduced.
- The number of restrike events is increased.

This is in accordance to available experimental findings on both ignition system types, demonstrating the capability of the model to predict completely different spark events.

CHAPTER 4

The Michigan Tech vessel

Different turbulence, air/fuel ratio and pressure conditions have a significant impact on a SI combustion process, as an highly inhomogeneous flow distribution nearby the ignition zone. Therefore, simplified experimental configurations are fundamental to clearly identify their influence on the reacting process, supporting the development of numerical models able to predict aforementioned phenomena.

With this purpose, at Michigan Tech University, experiments of SI combustion were performed in a pressurized, cubic, constant-volume vessel, featured by suitable optical accesses. In this configuration, a shrouded rotating fan coupled with a guide tube generates directly to the ignition zone a jet of fresh mixture with highly inhomogeneous flow and turbulence conditions. Combustion tests of premixed *Propane-Air* mixtures with 20 % mass-based EGR were performed under different levels of:

- air/fuel ratio,
- pressure,

- flow velocities at the spark-gap, with a consequent turbulence variation.

In this Chapter, a detailed description of the vessel set-up and the related experimental investigation is firstly reported. Then, the achieved findings were used to assess the numerical Comprehensive CFD Model proposed in Chapter 1.

4.1 Vessel set-up and experimental investigation

The Michigan Tech combustion vessel is characterized by a 1 l constant cubic volume. It is equipped with six windows, which can be either used as optical accesses (with a chamber coverage of over 95%) or for mounting experimental instruments (e.g. spark plugs, injectors and fans). The pressure transducer and the intake/exhaust valves are installed at the chamber corners, while a temperature control system allows to maintain the cubic body at a stable temperature up to 453 K. The vessel can withstand a maximum temperature of about 2100 K and pressures up to 345 bar, allowing combustion events inside its volume [116].

4.1.1 PIV tests

The *Particle Image Velocimetry* (PIV) is a non-intrusive technique used to characterize the flow field and measure the instantaneous velocity [3, 76]. To carry out PIV measurements the flow, illuminated by a laser, has to be filled with proper seeding particles, which need to be small enough to follow the fluid velocity [16].

The Diethylhexyl-Sebacate liquid, used as the particle seeding by [69], shows several advantages as:

- insolubility,
- lack of color,
- small and uniform size (below 1 μm),
- long life time,
- complete evaporation after the use.

Therefore, this seeding liquid together with a seeder tank, equipped with a Laskin nozzle inside, were used to create seeding particles, as shown in Figure 4.1. In partic-

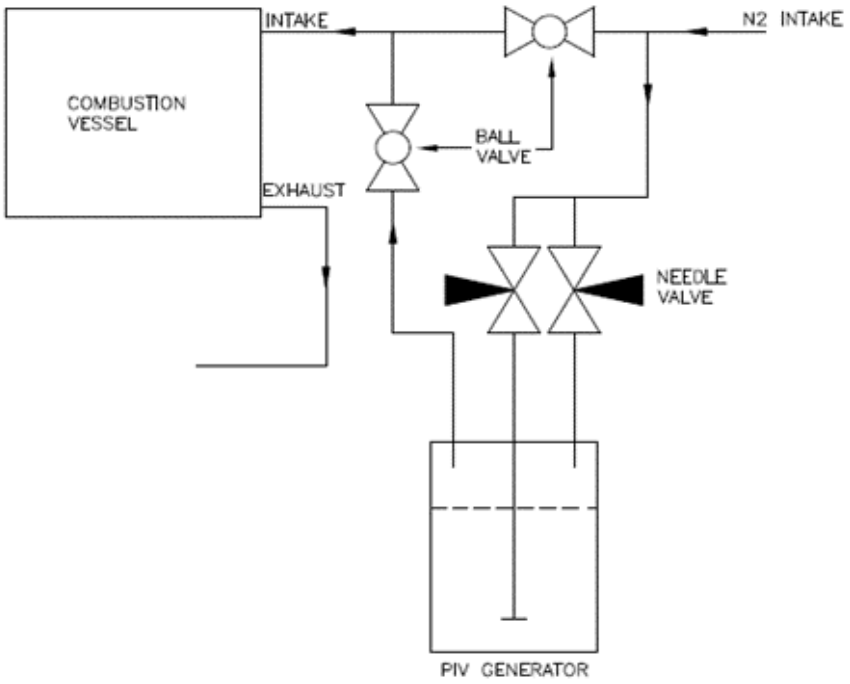

Figure 4.1: *Schematic diagram of the PIV seeding particle generator.*

ular, pressurized Nitrogen was pumped into the seeder tank, creating small droplets of Diethylhexyl-Sebacate of around 1 μm diameter; then, they were infused into the combustion vessel through the intake valve. Figure 4.2 shows the detailed schematic diagram of the adopted PIV system. Two *Nd-Yag* lasers of 532 nm were used to illuminate the seeding particles by generating continuously two laser sheets into the chamber; they were synchronized with a camera, which captured two consecutive images. The time interval between the two continuous laser pulses varied from 10 ms to 50 ms, according to different fan speeds. By comparing the two consecutive images, an instantaneous velocity profile was generated. Then, the *Insight 3G* software was used for:

1. synchronizing the laser and the camera,
2. processing the two consecutive images,
3. measuring the flow field velocity.

For each test condition, a series of 100 consecutive image pairs were collected and the average velocity profile over these 100 images was achieved.

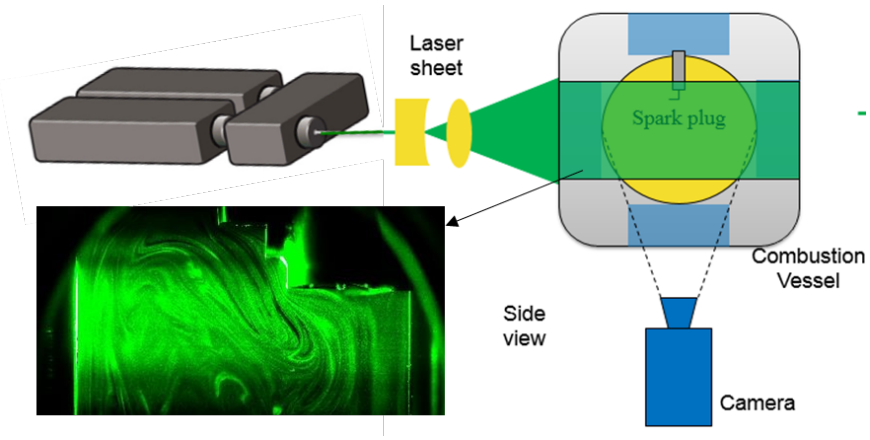

Figure 4.2: *The detailed schematic diagram of the PIV system and a sample image of laser sheet.*

A shrouded fan was designed to generate a turbulence flow field nearby the spark-plug, as shown in Figure 4.3. The fan is characterized by a 25.4 mm outer diameter and eight straight vanes with a 30° attack angle. It is connected to a 12 V brushed DC motor and it is driven by a closed-loop feedback system, which contains a control board, an optical encoder and a dedicated software. As a consequence, the fan speed can remain constant also in presence of pressure variations inside the combustion vessel.

As reported in Figure 4.3, the spark-plug centerline is positioned at 7.5 mm from the exit of the guide tube, whose centerline is located 4.25 mm above the y-axis origin. However, during PIV investigations a flat spark-plug adapter replaced the spark-plug at the same location to simplify the flow velocity measurements at the ignition zone.

From the performed PIV tests, the flow velocity corresponding to the fan speeds of 3000, 6000 and 9000 rpm were characterized. Pressure and temperature were modified to achieve similar values of fluid density with respect to the further ignition tests.

PIV experimental results Figure 4.4 shows the averaged velocity profile along the spark plug centerline for each tested condition, using 100 instantaneous images. During PIV tests, the chamber temperature was set at 423 K to avoid a too fast evaporation of the seeding particles, experienced at 453 K. The chamber pressures of Figures 4.4a, 4.4b, and 4.4c are 4, 8 and 16 bar, respectively.

By comparing the achieved results of Figure 4.4 and the PIV coordinate scheme of Figure 4.3, it can be observed that (going from bottom to top of the y-axis in Figure

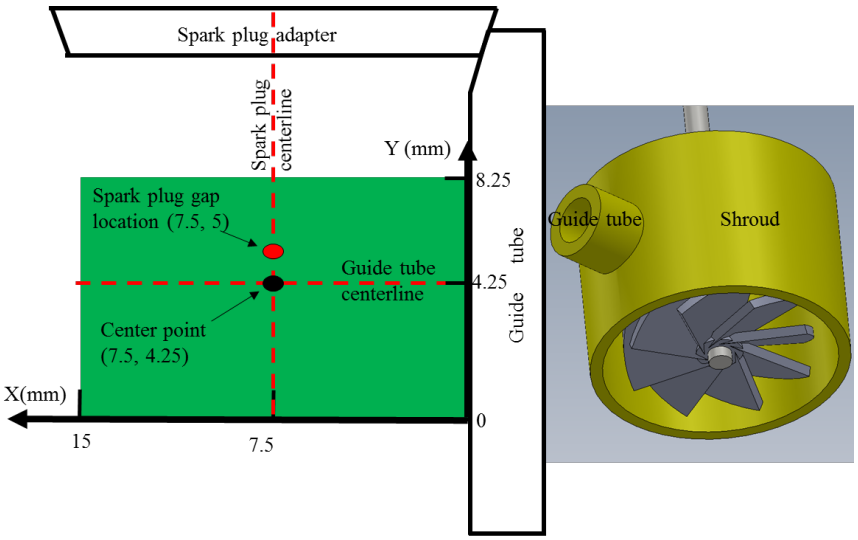

Figure 4.3: *Interested region of the PIV tests (left) and 3-D drawing of the shrouded fan (right). The spark-gap centre will be located at point* $(x = 7.5\ mm; y = 5\ mm)$.

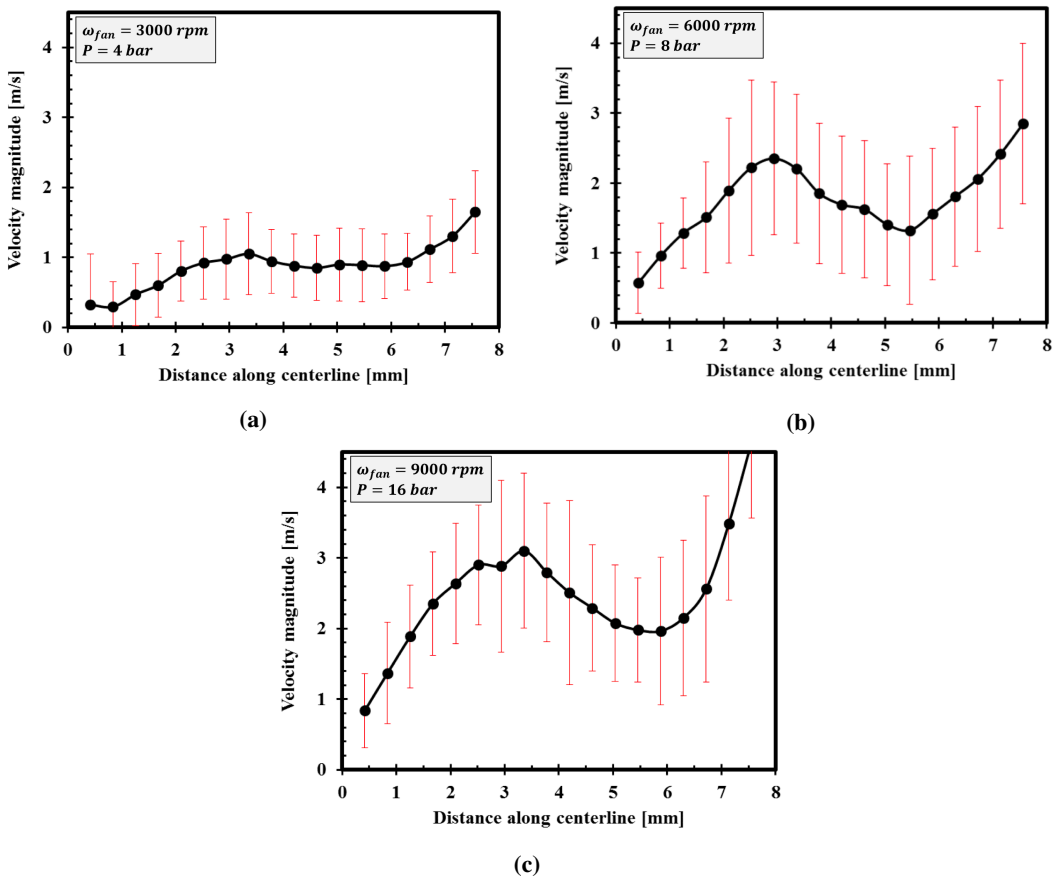

Figure 4.4: *Flow velocity profiles along the spark-gap centerline at chamber temperature of 432 K. Results at: 3000 rpm and 4 bar (a); 6000 rpm and 8 bar (b); 9000 rpm and 16 bar (c). For the adopted coordinate system please refer to Figure 4.3.*

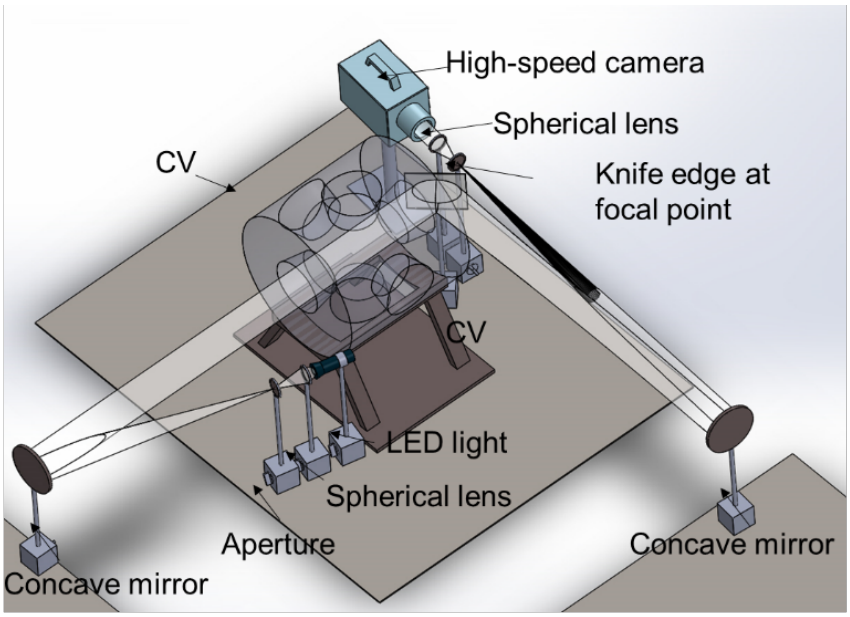

Figure 4.5: *Schematic of Z-shape high-speed Schlieren technique experimental setup.*

4.3) the flow velocity shows a first peak before the spark-gap centre (located around $y = 5\ mm$) and starts to increase again approaching the flat wall of the spark-plug adapter. This behaviour can be explained by an increased air flow coming out from the top part of the guide tube. Moreover, the velocity profile is similar for all analyzed conditions and the velocity value around the spark-gap centre is about:

- 1 m/s for 3000 rpm,
- 2 m/s for 6000 rpm,
- 3 m/s for 9000 rpm.

From the investigated conditions it can be concluded that:

1. The chamber temperature and pressure do not have strong effects on the flow velocity in terms of magnitude and shape (not present here).
2. The relationship between fan speed and flow velocity is fairly linear.

4.1.2 Ignition tests

A *Propane-Air* premixed mixture with a 20% of EGR was introduced inside the combustion chamber and ignited by a spark-plug, positioned after the guide tube exit, to

Table 4.1: *Test matrix for ignition tests.*

Propane with 20 % *EGR*					
Test $[n.]$	Φ	Pressure $[bar]$	Temperature $[K]$	Flow velocity $[m/s]$	Dwell time $[ms]$
1	0.7	8	453	0	6
2	0.7	8	453	1	6
3	0.7	8	453	2	6
4	0.7	8	453	3	6
5	0.7	16	453	0	6
6	0.7	16	453	1	6
7	0.7	16	453	2	6
8	0.7	16	453	3	2, 4, 6
9	0.9	8	453	2	4

carry out the ignition tests. Flame measurements were preformed according to the Z-shape high-speed Schlieren technique [101], whose schematic is shown in Figure 4.5. The pressure data is recorded at 100 kHz by a dynamic sensor located inside the combustion vessel and connected to a suitable acquisition system.

Because exact engine-like conditions cannot be replicated in the combustion vessel, as much as similar ones were used. In particular, the equivalence ratio (ϕ) values of 0.7 and 0.9 were tested, while the temperature was kept constant at 453 K. Four different levels of fan speeds were investigated: 0, 3000, 6000, and 9000 rpm. At quiescent conditions, no turbulence was detected inside the chamber. Three different levels of dwell time were also tested, while two different vessel pressures were used to explore the pressure effect on flame kernel development. The detailed test matrix, containing the investigated conditions, is shown in Table 4.1.

The schematic of the electrical circuit used during the ignition tests is shown in Figure 4.6. Probes for voltage and current measurements were added in the secondary circuit, because secondary current and voltage, together with the electrical circuit capacitance, were measured to calculate the discharge energy.

Flame kernel analysis After the discharge, a flame kernel is formed within the spark-plug electrodes, expanding and propagating towards the unburned mixture. At quiescent conditions, the flame front remains almost laminar and propagates similarly to a smoothed expanding sphere; hence, the flame front measurement is fairly straightforward. However, most of the tests were carried out under turbulent conditions, which are characterized by heavily wrinkled flame fronts, as it can be appreciated in Figure 4.7a.

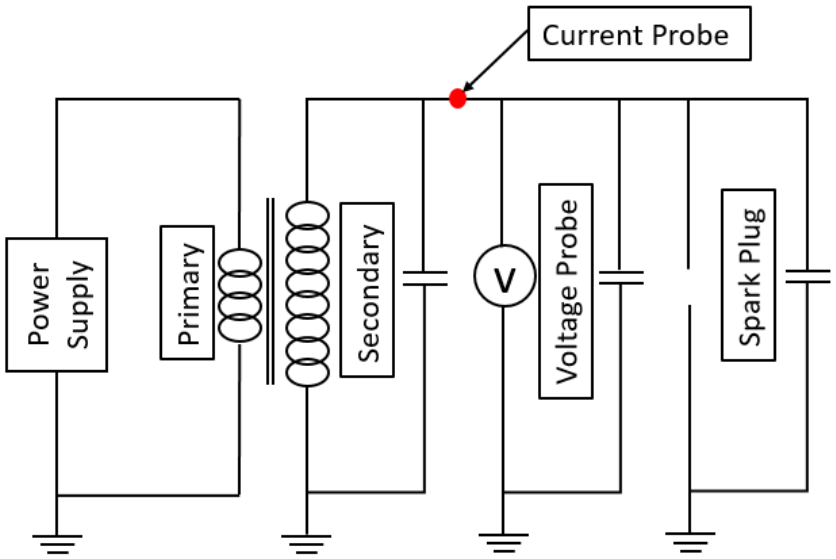

Figure 4.6: *Ignition coil circuit.*

Under these conditions, measuring the flame front propagation rate becomes more difficult, therefore the following method was developed to quantify the flame propagation trends.

Looking at Figure 4.7, the black-colored shadow contour represents the spark-plug in Schlieren images. Point *O* is located at the spark-gap centre and was taken as reference point. A sensitivity analysis was performed to choose the best span for the $\widehat{COD}$ angular sector. By varying this angle between 5 and 25° it was found that the 20° value provides the best results in terms of stability; therefore, this span was chosen as angle of interest. In fact, it was observed that the 5-15° interval included too small angles to extract enough flame front information, while for values larger than 25° portions of flame area affected by heat losses at the electrodes were considered.

In Figure 4.7a, the blue line represents the actual flame boundary, for which the propagation rate had to be quantified. Hence, the flame area within the *Area A* sector was measured and then used to extract the radius of its equivalent circular sector, called *Area B* (Figure 4.7b). The length of this sector, namely $\overline{OC}$ or $\overline{OD}$, was considered as the flame front location, thus the following equation was applied to compute the mean

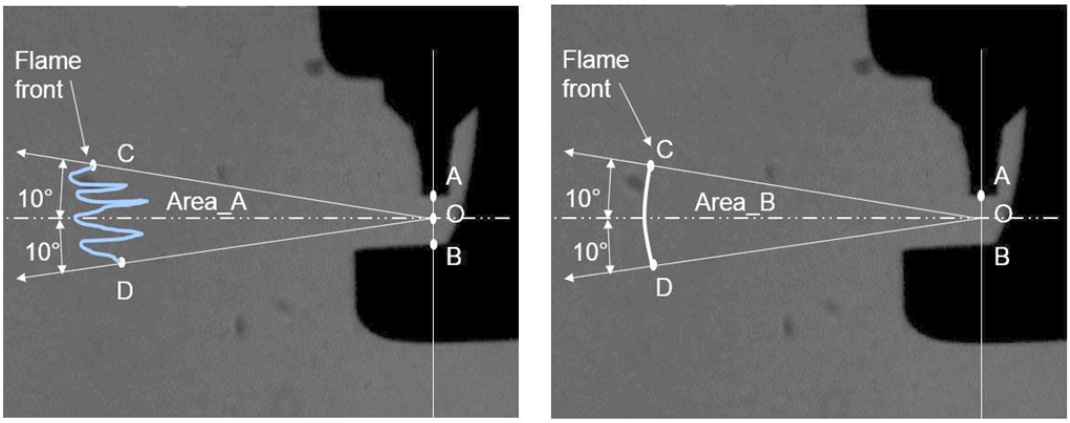

(a) **(b)**

Figure 4.7: *Methodology and interested region of flame kernel analysis: example of a real image (a) and of the corresponding sector shape (b).*

flame propagation rate $\bar{s}_f$

$$\bar{s}_f = \frac{d\overline{OC}}{dt} = \frac{d\overline{OD}}{dt} \tag{4.1}$$

considering that Schlieren images were sampled at 20'000 fps (two consecutive images have an interval of 0.05 ms). On the other hand, the flame front length ratio $l_{f,\,ratio}$ was computed as

$$l_{f,\,ratio} = \frac{l_{f,\,REAL}}{l_{f,\,SECTOR}} = \frac{\overline{CD}_{blue}}{\overline{CD}_{white}} \tag{4.2}$$

where $l_{f,\,REAL}$ and $l_{f,\,SECTOR}$ correspond to the Schlieren measured flame front ($\overline{CD}_{blue}$ of Figure 4.7a) and the corresponding circular sector shape ($\overline{CD}_{white}$ of Figure 4.7b), respectively.

Fan speed effect The fan speed effect was investigated by assuming the *no fan* condition (namely mixture at rest) as the baseline and then considering three different fan speeds: 3000, 6000 and 9000 rpm, with a fresh gases velocity nearby the spark-gap centre of approximately 1, 2 and 3 m/s, respectively.

Figure 4.8 shows the flame propagation rate computed from measured Schlieren images. As it can be noticed, a fan speed increase produces higher propagation rates of the flame front. In particular, values around 1, 4, 6 and 8 m/s were reached at fan speeds of 0, 3000, 6000 and 9000 rpm (no fan, 1, 2 and 3 m/s), respectively.

This result impacts also on the flame front position trend. In fact, the positive cor-

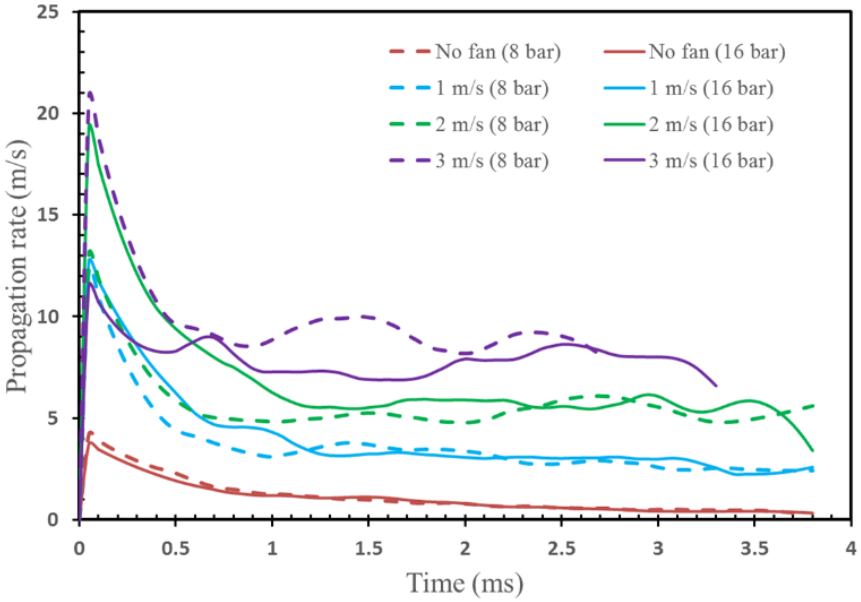

Figure 4.8: *Experimental flame propagation rates compared at different pressures (8 and 16 bar) and fan speeds (no fan, 1, 2 and 3 m/s, which correspond to 0, 3000, 6000 and 9000 rpm, respectively).*

relation observed in Figure 4.8 between the propagation rate and the fan speed can be appreciated also in Figure 4.9 where, at fixed time, the flame front position increases with the fan speed. However, an exception is represented by the solid purple line (3 m/s at 16 bar), which shows a lower propagation rate with respect to the solid green line (2 m/s at 16 bar) before 0.7 ms.

Pressure effect The pressure effect on the flame kernel propagation process was studied by comparing tests performed at 8 and 16 bar inside the combustion chamber, keeping constant the fan speed.

An analysis of Figure 4.8 allows to assert that pressure affects the flame kernel propagation rate only during a short period of time immediately after the discharge event (less than 2 ms), while, as time increases, the pressure influence tends to vanish. In particular, at quiescent conditions (*no fan*) and close to spark-timing, a pressure increase has a suppression effect on the flame kernel growth process. Similar results were observed also by Zhang during its experiment of combustion on a *Methane-Air* mixture with EGR, [117]. On the other hand, from both Figures 4.8 and 4.9, the results achieved at 1 and 2 m/s of flow velocity at the spark-gap (3000 and 6000 rpm fan

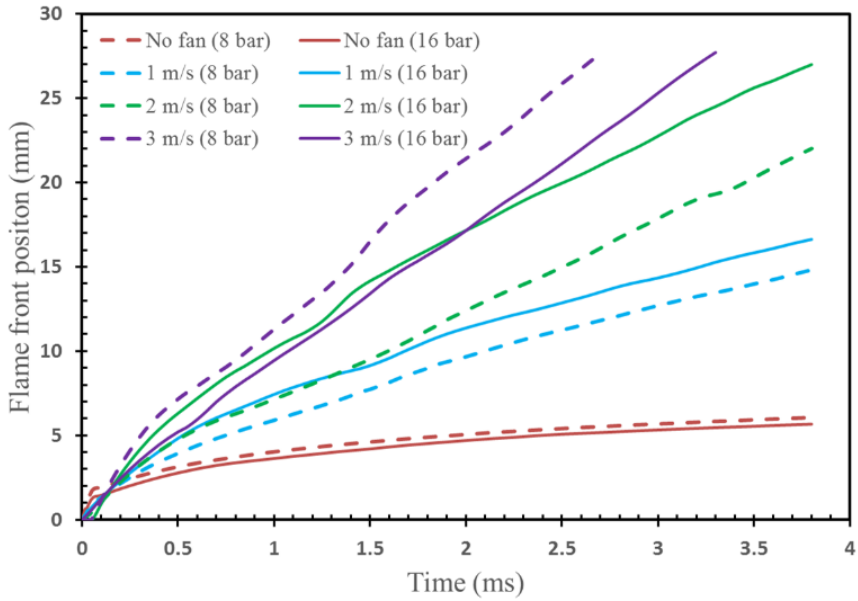

Figure 4.9: *Experimental flame front locations compared at different pressures (8 and 16 bar) and fan speeds (no fan, 1, 2 and 3 m/s, which correspond to 0, 3000, 6000 and 9000 rpm, respectively).*

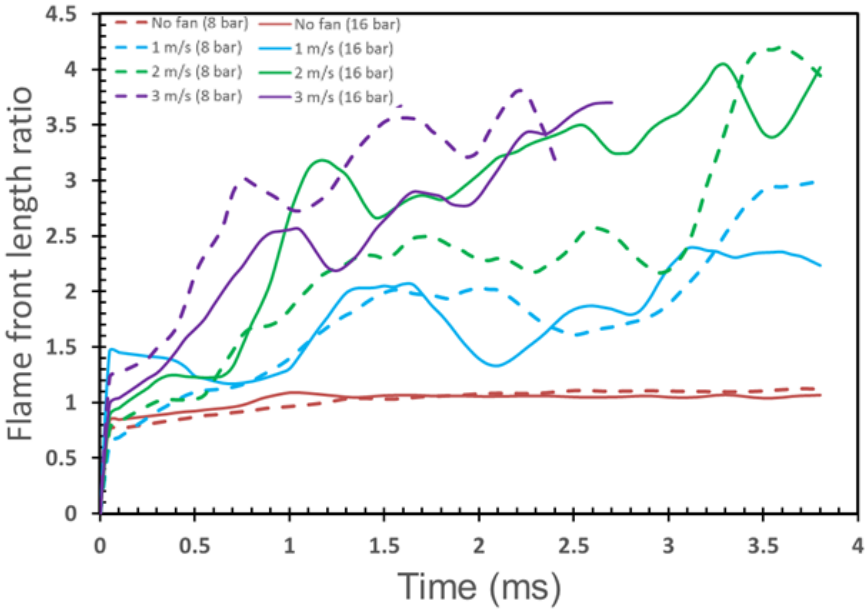

Figure 4.10: *Experimental flame front length ratios compared at different pressures (8 and 16 bar) and fan speeds (no fan, 1, 2 and 3 m/s, which correspond to 0, 3000, 6000 and 9000 rpm, respectively).*

speed, respectively) show that:

- higher the pressure, higher the propagation rate,
- a pressure increase has stronger effects at high flow velocities (e.g. 2 m/s condition).

In fact, moving from 8 to 16 bar, the flame propagation rate increase at 0.5 ms (see Figure 4.8) can be quantified as: $\approx 1\ m/s$ for the 1 m/s case, while of $\approx 4\ m/s$ for the 2 m/s condition. However, when the flow velocity at the ignition zone becomes 3 m/s, the suppression effect produced by pressure on the flame kernel propagation occurs again, similarly to what observed at *no fan* condition (Figures 4.8 and 4.9).

In order to get more insight in achieved results about pressure effect, the *flame front length ratio* (see (4.2)) was investigated. A comparison between Figures 4.8 and 4.10 points out that higher flame front length ratios correspond to higher flame propagation rates, at fixed time. In fact, an high value of length ratio means a longer flame front and a larger flame area, with a consequent increased amount of unburned mixture consumed by the reaction layer. In particular, from Figure 4.10 it can be observed that the pressure variation has different impacts on the analyzed flow velocity conditions. In fact, at quiescent mixture an almost constant length ratio of ≈ 1 can be observed. For the 1 m/s case small differences can be appreciated, while larger variations were detected at higher fan speeds: for example, at 2 m/s condition a larger length ratio was measured at 16 bar with respect to 8 bar pressure. However, at 3 m/s flow velocity the trend is opposite and a pressure increase generates a reduction of the flame front length ratio, according to the suppression effect observed in Figures 4.8 and 4.9.

To explain the opposing effects that pressure has on the flame kernel growth under variations of flow velocity and turbulence nearby the ignition position, the flame structure was analyzed. Figure 4.11 reports Schlieren images of the flame, measured at the investigated fan speeds and pressures. As it can be observed, under high pressure conditions the flame kernel shows smaller surface structures than the related low pressure cases. Moreover, at constant pressure, also an increase of the turbulence level results in the smaller flame structures.

This means that an increase of both pressure and turbulence intensity levels enhances

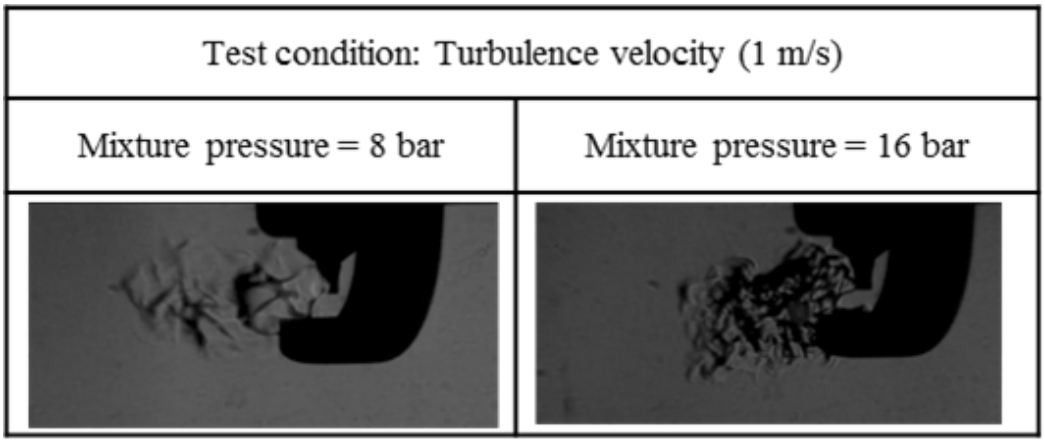

(a)

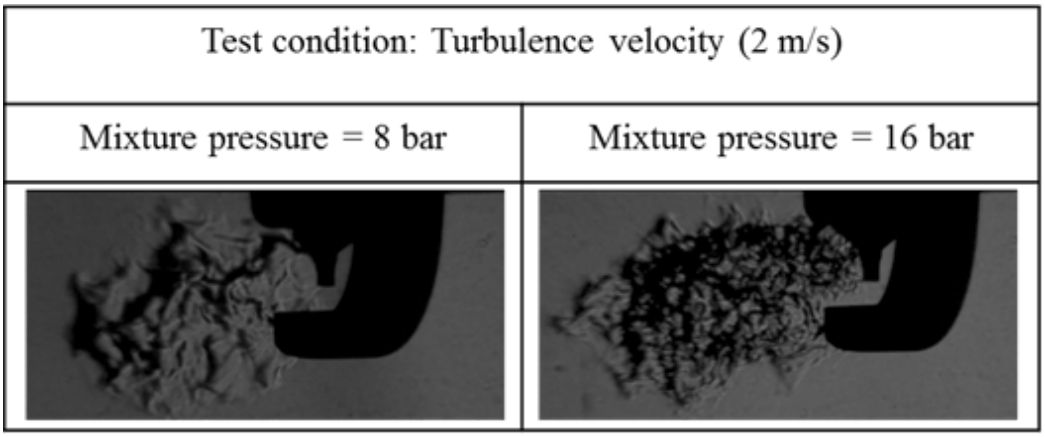

(b)

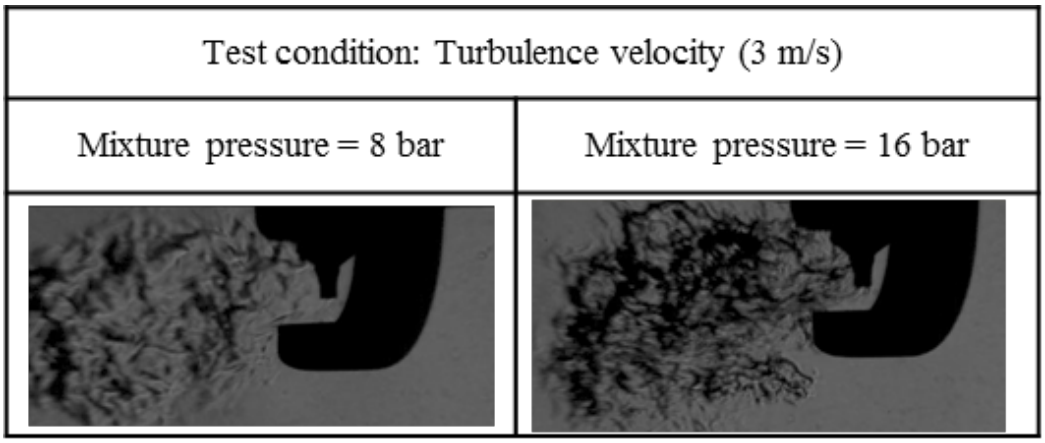

(c)

Figure 4.11: *Schlieren images of the flame front at 2.5 ms from spark onset for 8 and 16 bar: turbulence velocity of 1 m/s (a), turbulence velocity of 2 m/s (b), turbulence velocity of 3 m/s (c) at the spark-gap centre.*

the flame wrinkling by activating also the *smaller eddies/flame surface* interaction. An explanation of this phenomenon could be related to the higher energy amount introduced into the eddies spectrum, with a consequent extension of the Kolmogorov cascade. Therefore, in the light of previous observation, it can be concluded that at fixed turbulence intensity conditions:

- when the initial dimension of the flame surface structures are *larger* than a threshold value, a pressure increase (namely, more wrinkling caused by additional *small eddies/flame surface* interaction) enhances the propagation rate;

- when the initial dimension of the flame surface structures are lower than a threshold value (namely, already high wrinkling caused by small-scale eddies), a pressure increase suppresses the propagation rate.

The aforementioned threshold value is positioned in between turbulence initial conditions achieved at 2 m/s (Figure 4.11b) and 3 m/s (Figure 4.11c) of flow velocity at the spark-gap.

4.2 The *Comprehensive CFD Model*: numerical validation

The numerical investigation carried out on Michigan Tech vessel had the purpose to validate the *Comprehensive CFD Model* proposed in Chapter 1. In particular, the analysis was focused on the flame kernel formation processes of the experimentally investigated *Propane-Air* premixed mixture, whose features are described in Section 4.1.2. The governing equations were solved with the RANS approach and the $k - \omega$ SST model was used for turbulence.

In the following sub-sections, a description of the numerical approaches used for the analysis, as meshes and fan rotation simulation, will be first provided. Then, non-reacting flow conditions will be investigated in order to initialize the reacting test chosen for the validation and to understand the behaviour of the selected turbulence model. Finally, the computed results of the combustion process will be compared consistently with the available experimental findings about flame radius under different turbulence intensities, air/fuel ratios and pressures.

4.2.1 Numerical set-up: adopted meshes and fan rotation simulation

As previously described in 4.1, a close cubic volume of 1 l, in which a *Propane-Air* mixture is homogeneously pressurized with a suitable percentage of recycled exhaust gases (EGR), characterizes the experimental rig used by Michigan Tech University for premixed combustion tests.

Therefore, the adopted mesh considered the presence, inside the investigated vessel, of all the details that characterize the flow velocity and turbulence fields, namely (Figure 4.3):

1. the *spark-plug*, for the flame ignition;
2. the *cylindrical fan shell*, which provides a flow directed towards the ignition zone through a cylindrical guide tube;
3. the *fan-shaft coupling*.

On the resulting constant volume combustion chamber a structured mesh with cubic hexahedra of 10 mm side was first created. Then, starting from this basic mesh, 4 levels of mesh refinement were adopted to better describe the geometry of the three listed details inside the cubic volume. Moreover, additional refinements were performed over the edges of:

- fan-shaft coupling geometry, because of the high flow field velocity gradients expected on the rotating parts (especially blades);
- spark-plug geometry, because of the small curvature radius of electrodes details.

Finally a spark-gap centred refinement sphere, with a 8 mm radius and a refinement level similar to that adopted for spark-plug, fan shell and fan-shaft coupling description, was generated to describe more in detail the early stage of combustion where the Lagrangian/Eulerian models are coupled. The resulting constant volume combustion chamber mesh, characterized by about 200'000 cells, is shown in Figure 4.12, where the drawn triangles are not part of the real mesh but simply generated by the graphics display system.

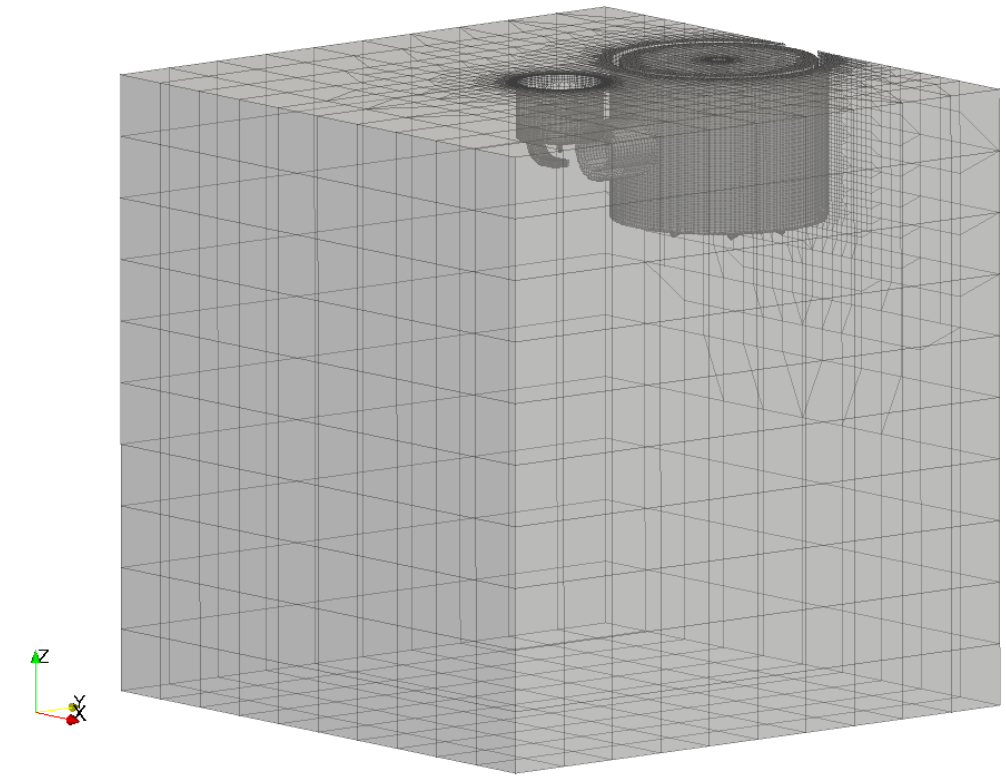

(a)

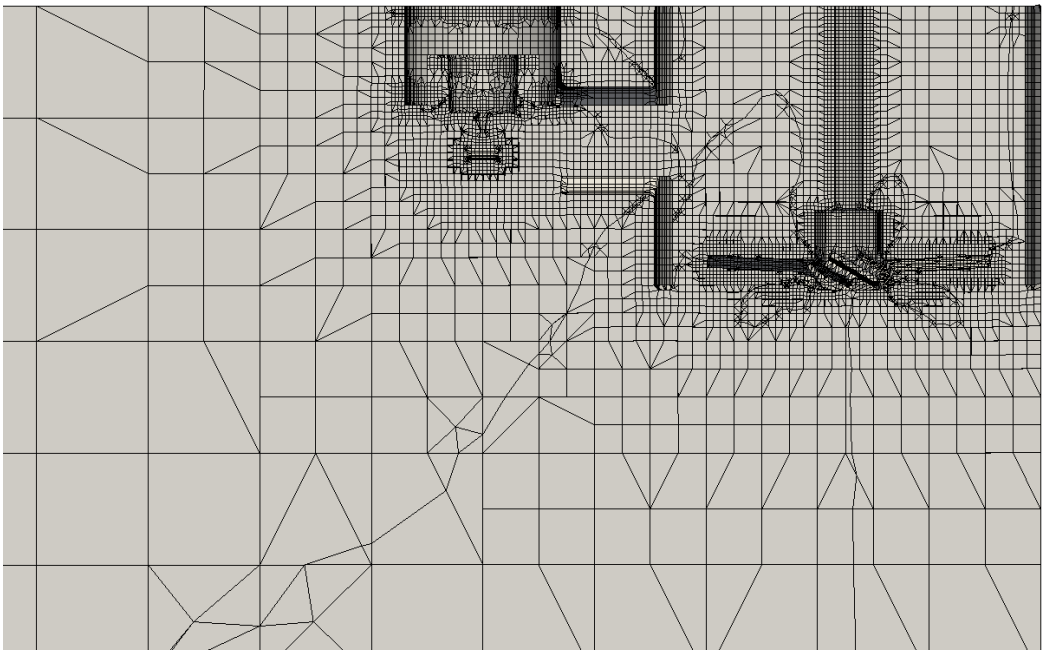

(b)

Figure 4.12: *Combustion chamber mesh: complete vessel transparency (a); sectional detailed view of the mesh nearby the internal geometrical details (b). The 4 refinement levels, the fan-shaft and spark-plug edge additional refinements, and the spark-gap centred refinement sphere can be noticed. The drawn triangles are not part of the real mesh but are simply generated by the graphics display system.*

However, with the purpose to understand the flow field distribution at the ignition zone, PIV measurements were performed nearby the spark-gap centerline with the presence of a flat cylindrical geometry (called spark-plug adapter) instead of the spark-plug (Figure 4.3); consequently a different chamber mesh was adopted to consider this configuration difference (Figure 4.13).

The followed steps for mesh realization were almost the same with respect to the ones performed for combustion chamber mesh with spark-plug inside, even if some differences where present, in particular:

- the basic grid was built with structured cubic hexahedra of 2.5 mm side, resulting in a globally more refined mesh;
- the edge additional refinement over the spark-plug was not performed because of the simpler spark-plug adapter geometry;
- the spark-gap centered refinement sphere was replaced by a refinement cylinder, with a diameter equal to the guide tube external diameter and a 14 mm height.

This last refinement was performed in order to have a higher grid resolution in the PIV measurements zone. Approximately 400'000 cells feature the resulting mesh, allowing a detailed description of the flow evolution since the entering section of the guide tube; a sectional detailed view of this mesh is shown in Figure 4.13b.

For what concerns the fan rotation simulation, it was carried out by means of the *Moving Reference Frame* (MRF) approach, a CFD modeling technique to simulate rotating machinery. In MRF model an unsteady problem (with respect to the absolute reference frame) becomes steady with respect to a moving reference frame. In other words the complete rotor domain is assumed to be rotating at the same angular velocity of the rotor (relative motion between cell regions). Inside this domain the momentum equation is modified to incorporate the additional Coriolis acceleration term (which occurs due to the transformation from the stationary to the moving reference frame). By solving this equation with a steady-state approach, the flow around the moving parts can be modeled. Consequently, thanks to MRF technique, the fan rotation simulation was obtained without a mesh motion. An example of the resulting flow field is shown in Figure 4.14.

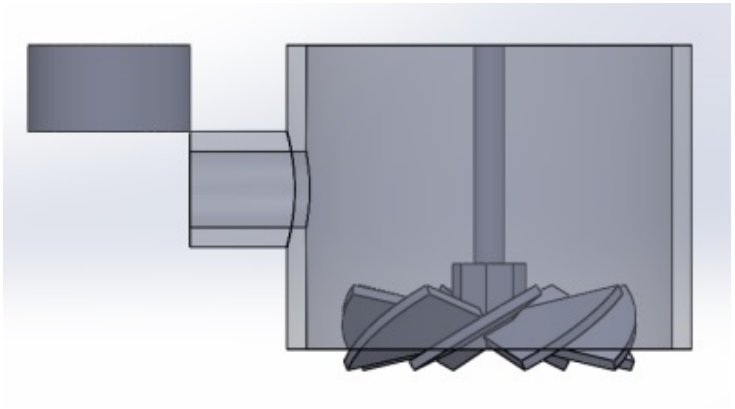

(a)

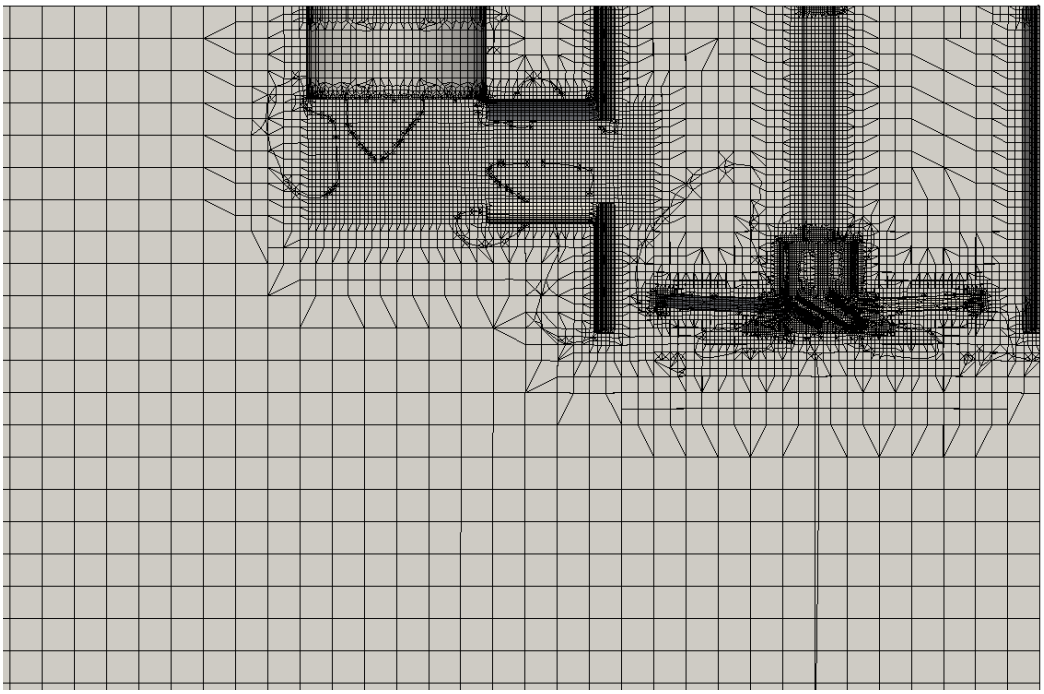

(b)

Figure 4.13: *PIV measurements analysis: the spark-plug adapter (top left) replaces the spark-plug geometry (a); sectional detailed view of the adopted mesh nearby the internal geometrical details (b).*

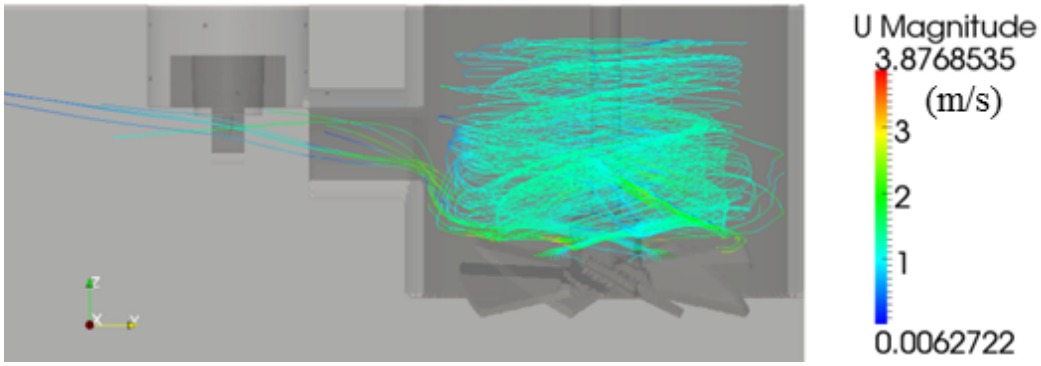

Figure 4.14: *Some flow field streamlines generated by a 3000 rpm rotation of fan-shaft coupling using the MRF approach.*

Table 4.2: *PIV test conditions investigated by numerical simulations.*

Propane with 20 % *EGR*					
Test $[n.]$	Φ	Pressure $[bar]$	Temperature $[K]$	Density $[kg/m^3]$	Fan speed $[rpm]$
1	0.9	4	453	3.16	3000
2	0.9	8	453	6.33	6000

4.2.2 Non-Reacting Flow Analysis

The correct initialization of reacting simulations is very important to obtain reasonable results in terms of flame propagation, because the flame interacts with the flow field and the turbulence in which it propagates. Therefore, a non-reacting flow analysis was carried out not only on the reacting test conditions chosen for the validation, but also on some flow field configurations used for PIV tests, in order to better understand the behaviour of the adopted numerical set-up (e.g. the turbulence model). Among the available PIV measurements (see Section 4.1.1), the conditions reported in Table 4.2 were investigated. Hence, a comparison of the numerical flow velocity magnitude and the PIV measured velocity was performed to understand the effect produced by a fan speed variation on the velocity distribution at the ignition zone. Trends were computed and measured along the linear path positioned at the spark-gap centreline and represented by the white line of Figure 4.15.

In Figure 4.16 the flow velocity distributions obtained experimentally, with the relative error bars, and numerically, by a time-averaged procedure, for the two cases of Table 4.2 were compared. Both trends were evaluated along the spark-gap centreline, starting from the bottom point until the flat surface of the spark-plug adapter. Despite

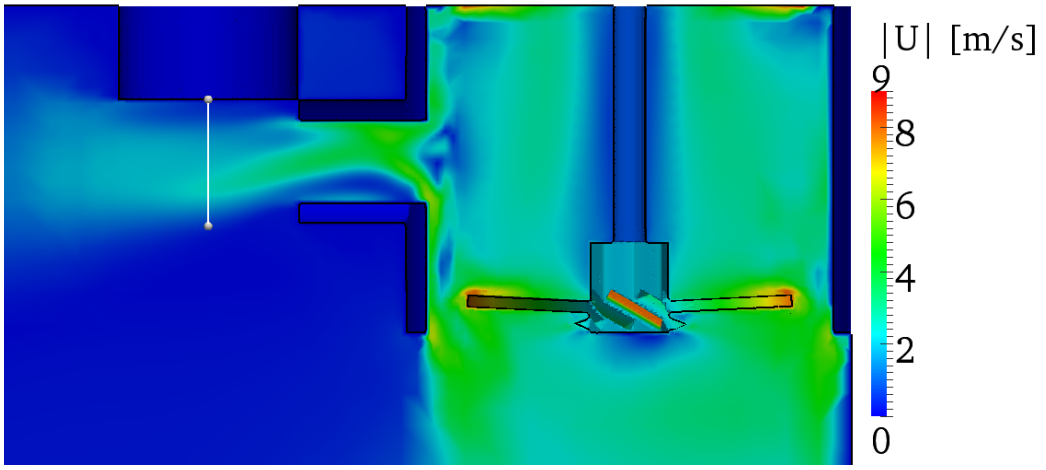

Figure 4.15: *Instantaneous flow velocity field inside the vessel, with* Test 2 *PIV condition (Table 4.2). The experimental and numerical investigated path is represented by the white line, which is positioned at the spark-gap centreline.*

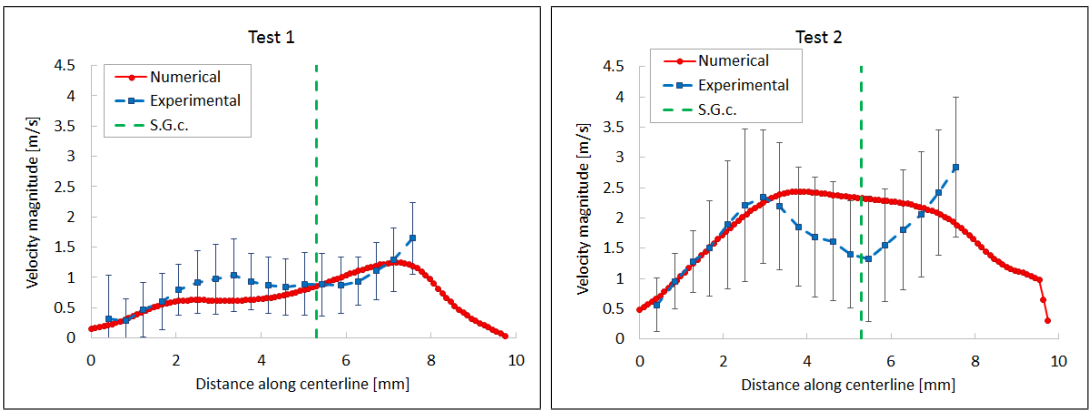

(a) **(b)**

Figure 4.16: *Experimental and numerical flow velocity magnitude along the spark-gap centreline shown in Figure 4.15:* Test 1 *(a) and* Test 2 *(b) of Table 4.2. The green vertical dashed line represents the spark-gap centre point (S.G.c.). The experimental data are represented with the relative error bars, while the numerical results are time-averaged values.*

Table 4.3: *Investigated reacting test conditions, chosen from Table 4.1.*

Propane with 20 % *EGR*					
Test $[n.]$	Φ	Pressure $[bar]$	Temperature $[K]$	Density $[kg/m^3]$	Fan speed $[rpm]$
2	0.7	8	453	6.21	3000
3	0.7	8	453	6.21	6000
6	0.7	16	453	12.42	3000
9	0.9	8	453	6.33	6000

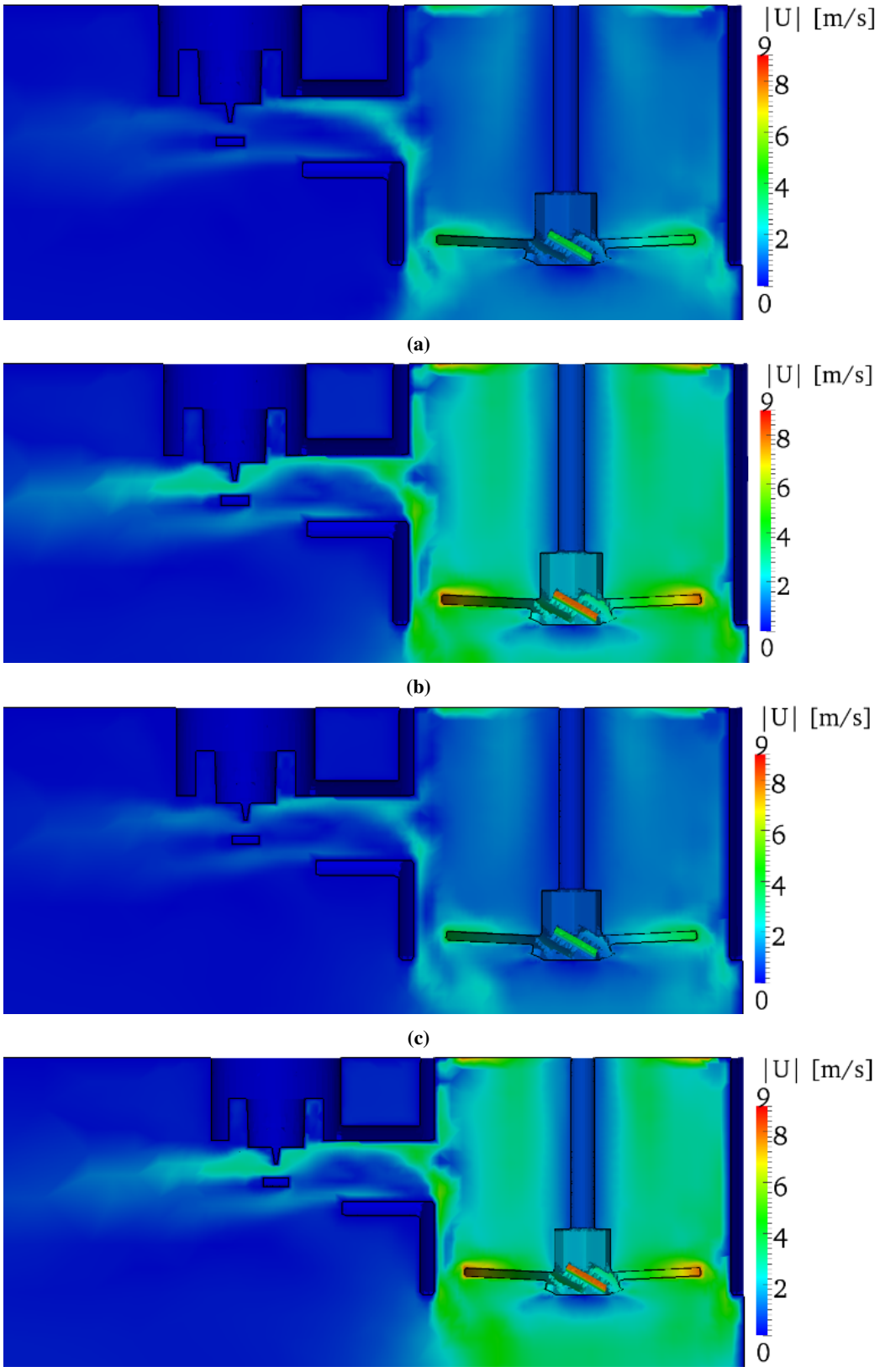

Figure 4.17: *Instantaneous flow velocity field inside the vessel before ignition (non-reacting conditions of Table 4.3):* Test 2 *(a);* Test 3 *(b);* Test 6 *(c);* Test 9 *(d).*

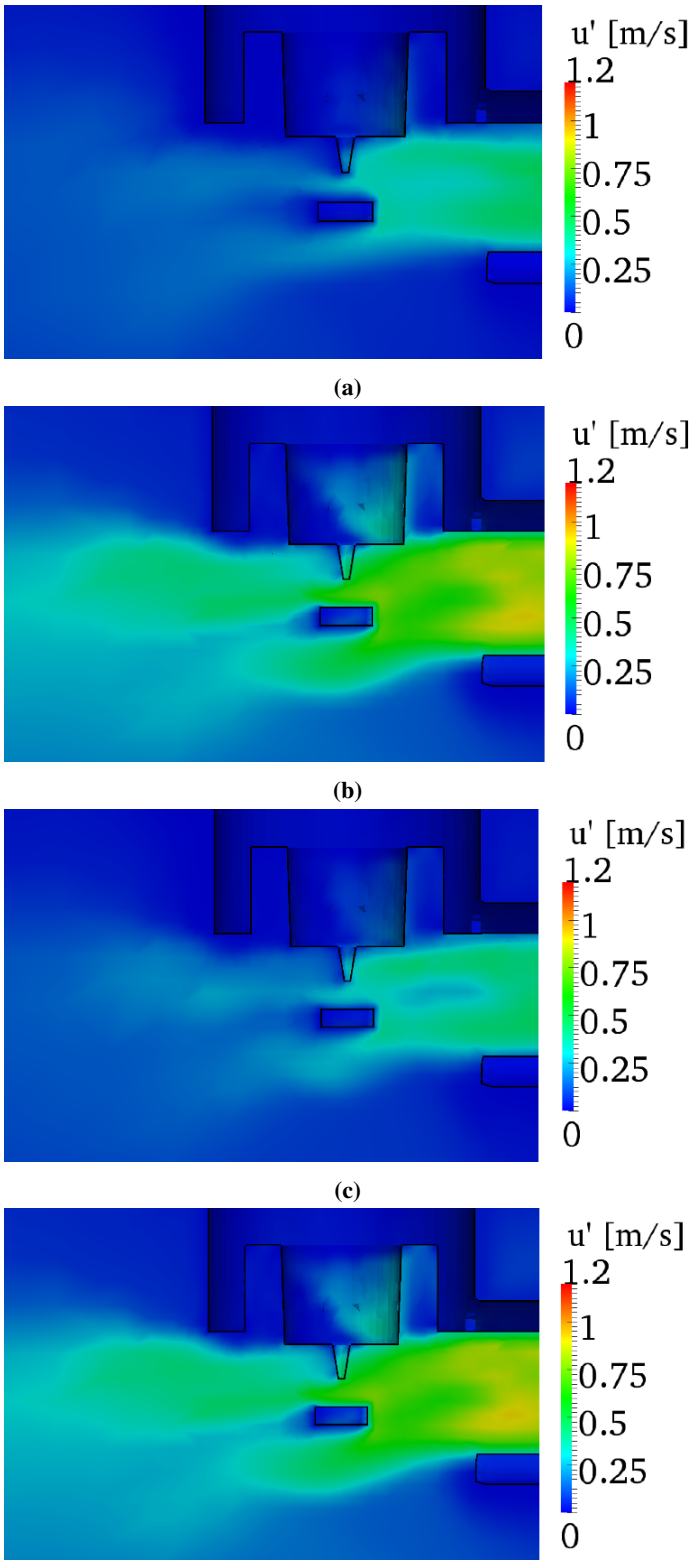

Figure 4.18: *Instantaneous turbulence intensity field inside the vessel before ignition (non-reacting conditions of Table 4.3):* Test 2 *(a);* Test 3 *(b);* Test 6 *(c);* Test 9 *(d).*

a not perfect agreement of the numerical velocity distribution with the experimental average trend in case of a high fan speed velocity (Figure 4.16b), the results can be considered rather satisfactory at all tested conditions. In fact:

1. for all the investigated tests, the average trend is quite well estimated on the region below the ignition zone;

2. for *Test 2* (high fan speed) the value of the estimated flux from the spark-gap until the flat adapter falls within the confidence interval of the experimental findings (Figure 4.16b);

3. for *Test 1* (low fan speed) the agreement between numerical and experimental values seems rather good also in terms of average trend (Figure 4.16a).

Concerning the initialization of combustion tests, in Table 4.3 the reacting conditions selected from available experimental data (see Table 4.1) are listed and chosen for the model validation. Non-reacting simulations were carried out for each test case, in order to obtain a nearly steady-state distribution for all the involved fields and fulfill a correct initialization of the further combustion event.

Figures 4.17 and 4.18 show, for each tested condition, the distribution of the velocity and turbulence intensity fields nearby the geometrical details inside the cubic vessel, respectively. As it is possible to notice in Figure 4.17, the use of the $k - \omega$ SST turbulence model, combined with a rather refined mesh, allowed to predict two "fluid jets" directed towards the ignition zone: the first one hits the upper electrode and is convected at the spark-gap; the second one, of lower intensity, is directed under the bottom electrode. On the other hand, the turbulence intensity level at the ignition zone seems to be rather related to the flow velocity, and consequently to the fan speed (Figures 4.18a and 4.18b): the higher the fan rotation velocity, the higher the turbulence intensity at the spark-gap. However, if the fan speed is kept constant in presence of a pressure increase, both velocity and turbulence fields seem to be a little more intensive, as it can be noticed by comparing Figures 4.17a – 4.17c and Figures 4.18a – 4.18c, respectively.

Table 4.4: *Measured values of breakdown energy E_{bd} and total released energy E_{tot} by the electrical circuit for the ignition of Table 4.3 test conditions.*

Test $[n.]$	E_{bd} $[mJ]$	E_{tot} $[mJ]$
2	5.19	31.20
3	5.70	37.48
6	19.00	46.00
9	7.31	35.18

4.2.3 Combustion results

The model validation was carried out by testing its behaviour under the reacting conditions of Table 4.3. This choice was justified by three main reasons:

1. The Michigan Tech pressurized vessel configuration allows to study the early flame propagation under conditions of highly inhomogeneous flow field distribution nearby the ignition zone, as shown by Figures 4.16 and 4.17.

2. The four test conditions of Table 4.3 enable to assess the model behaviour under variations of turbulence intensity (*Test 2* vs. *Test 3*), air/fuel ratio (*Test 3* vs. *Test 9*) and pressure (*Test 2* vs. *Test 6*).

3. A preliminary analysis of the combustion regimes (Figure 4.19) confirmed that all Table 4.3 conditions provide *wrinkled flamelets*; hence, the correct application of the selected turbulent combustion model is guaranteed.

Therefore, once provided the near steady-state non-reacting initialization of all mixture fields (like pressure, turbulence intensity and flow velocity) for *Tests 2*, *3*, *6* and *9*, the simple ignition of each analysed condition allowed to study the combustion phenomenon.

The electrical circuit set-up was performed according to ignition system features evaluated by experiments and specified in Table 4.4, where the total released energy E_{tot} represents the global amount of energy transferred from the electrical circuit to the gas phase.

The parameters $\alpha_{FSD} = 30$ and $\beta_{FSD} = 0.1$ were adopted in (1.19) and (1.20) for the Σ equation resolution, after a suitable calibration was carried out.

Simulations were performed in parallel over 3 processors with a suitable splitting of the mesh regions. In particular, the cell-set used for the MRF treatment and the

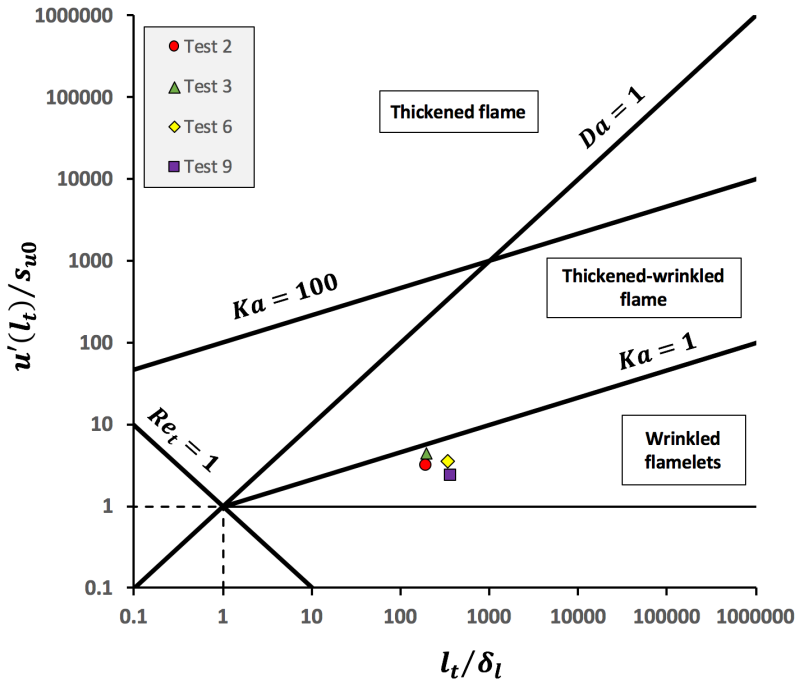

Figure 4.19: *The test conditions of Table 4.3 in the modified turbulent combustion diagram proposed by Peters, [91]. The combustion regimes are identified in terms of length* (l_t/δ_l) *and velocity* ($u'(l_t)/s_{u0}$) *ratios on a* log-log *scale.*

small region around the spark-gap (where the Lagrangian-Eulerian coupling was active) were assigned each one to single cores, in order to avoid problems derived by processor boundaries. The time spent for each computation was approximately 2 days. In order to compare consistently the obtained numerical results with the experimental evolution of the flame front position, the on-grid approach described by Figure 4.20 was employed. This allowed to compute the distance between the flame front and the spark-gap centre point similarly to the post-processing procedure adopted on Schlieren images (Figure 4.7).

Figure 4.21 shows comparisons between experimental and numerical flame front positions of Table 4.3 setup from the spark-time until the development of a fully turbulent flame front. Hence, for each shown comparison, the discharge event was completed before the final reported time. Rather satisfactory results were achieved at all tested conditions, especially for *Tests 2*, *6* and *9* (Figures 4.21a, 4.21c and 4.21d, respectively). Concerning *Test 3*, also if its global propagation trend was captured, a not perfect alignment with numerical findings was observed. However, as found with the

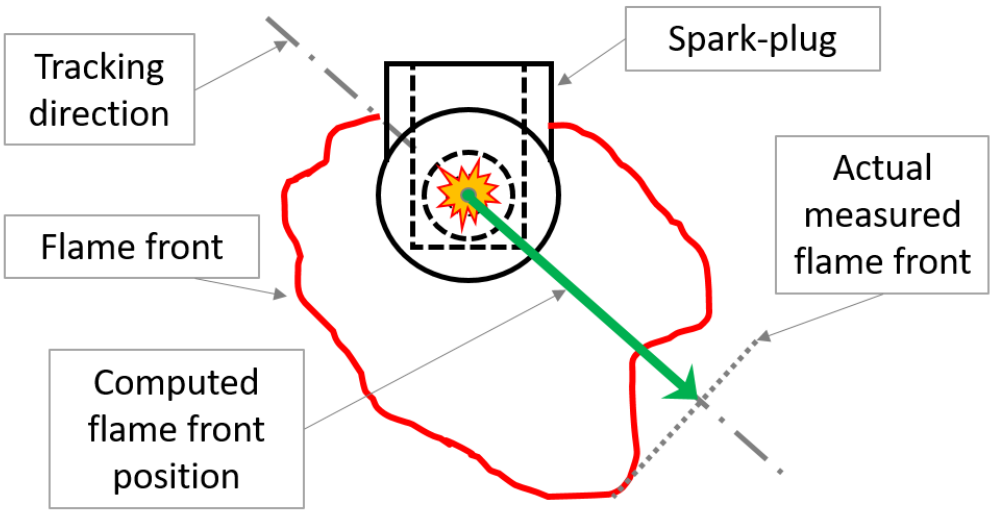

Figure 4.20: *Simplified description of the on-grid tracking algorithm adopted for the numerical computation of the flame front position.*

PIV analysis of Figure 4.16b, in presence of a 6000 rpm fan speed the predicted mean velocity profile was not perfectly achieved. Therefore, this could have a major impact on a flame propagating under lean conditions, with the consequent not perfect prediction of its evolution under such inhomogeneous flow velocity distribution. For the sake of clarity, because of:

1. numerical issues of the on-grid tracking algorithm,
2. the coarse mesh gathered by the flame outside the ignition zone,

the numerical trends of Figure 4.21 can sometimes show sudden but limited change of flame propagation speed.

The end time of the first discharge event (not of the total electrical discharge process) was reported in Figure 4.21 in order to show how much the first spark channel sustained the flame. This allowed the generation of a fully propagating turbulent flame also under such flow velocity conditions. As example, the complete ignition process and the further development of a self-sustained flame is shown in Figure 4.22, where *Test 9* of Table 4.3 was chosen. As soon as the first spark channel ended (before $t = 0.35\ ms$), a self-sustained flame was generated also under such inhomogeneous flow conditions. Before the end of discharge process, few restrike events happened with a relatively short duration. However, they did not have any effect on the generated flame.

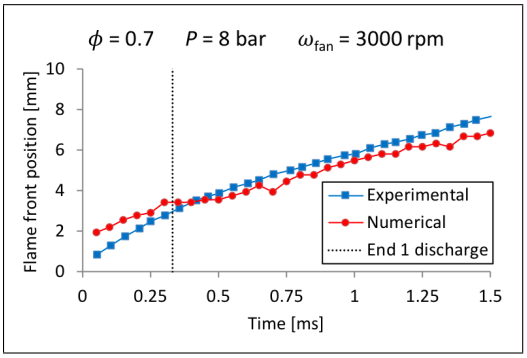

(a)

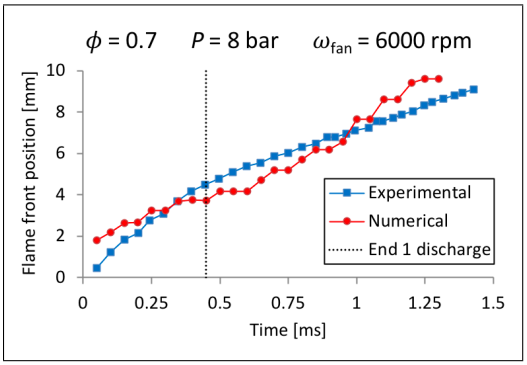

(b)

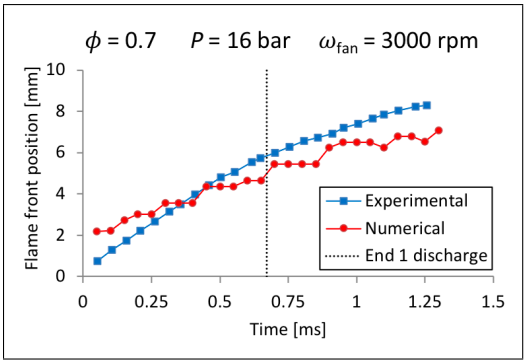

(c)

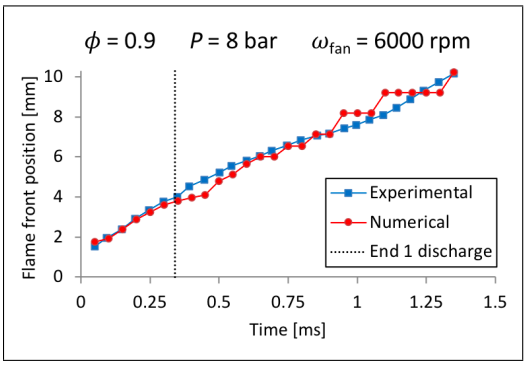

(d)

Figure 4.21: *Comparison between experimental and numerical flame front position for reacting conditions of Table 4.3:* Test 2 *(a);* Test 3 *(b);* Test 6 *(c);* Test 9 *(d). The black vertical dashed line represents the end of the* 1^{st} *discharge.*

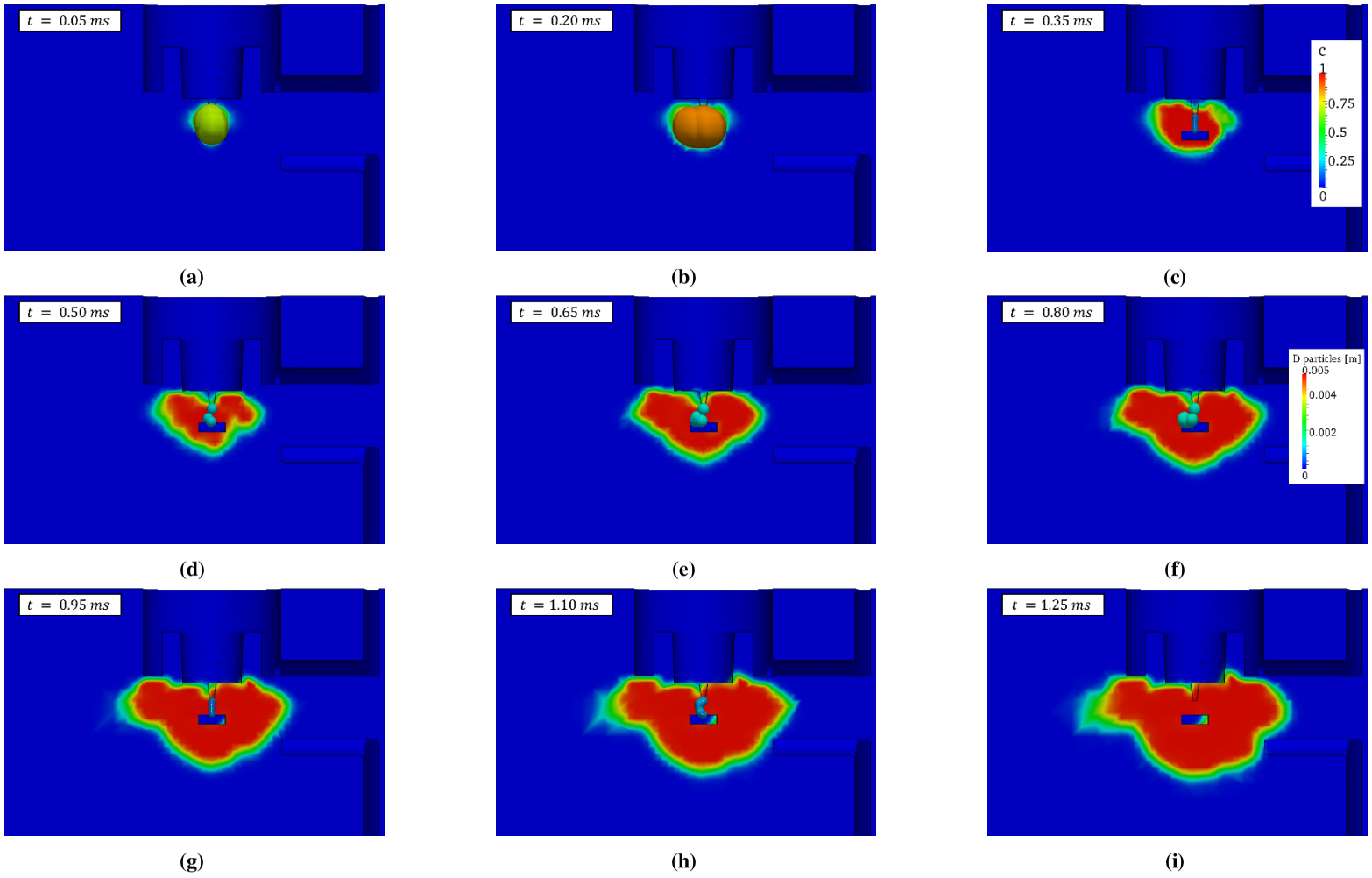

Figure 4.22: *The* Lagrangian-Eulerian *coupling from ignition until self-sustained flame,* Test 9 *of Table 4.3. At these conditions, the restrike events experienced after the completion of the first discharge do not influence the formation of a self-sustained propagating flame.*

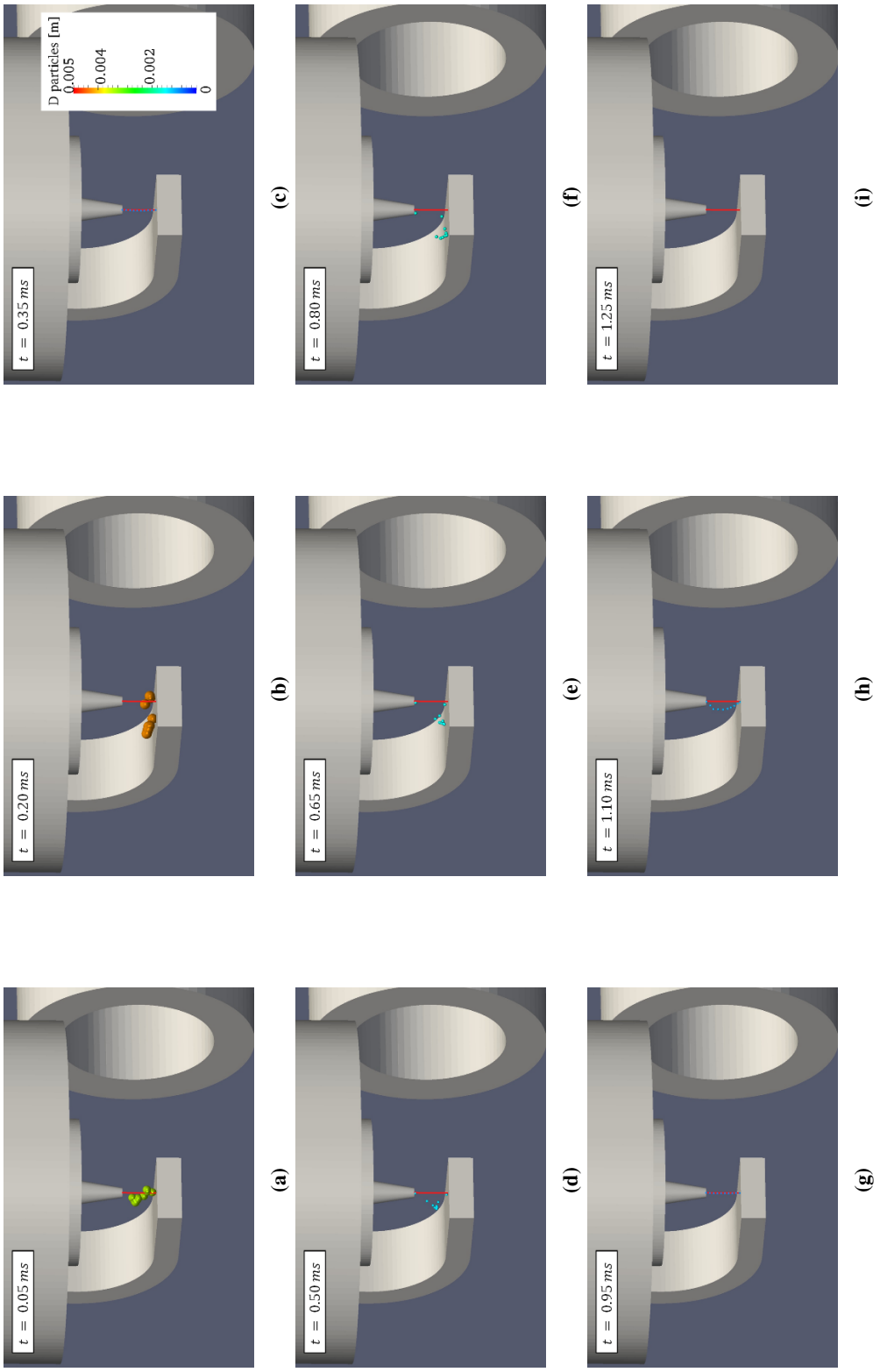

Figure 4.23: *The distribution of the Lagrangian particles at the same time-steps of Figure 4.22. Here, the actual dimension of each particle was reduced of a factor of* 10 *in order to appreciate their actual position. The bold red line represents the spark-gap centreline.*

In Figure 4.22, the spatial evolution of the first spark channel cannot be well identified. This is due to the relatively high energy deposited during the breakdown stage of *Test 9* first discharge (Table 4.4), which generated a mean Lagrangian particles radius of about 1 mm at the beginning of the arc stage, according to (1.2). Being this value comparable to the spark-gap distance (1.4 mm), it is very difficult to understand the effects of the local flow field on the channel geometry if the actual particles radius is represented into the computational domain. Hence, as shown in Figure 4.23, a factor of 10 was used to artificially decrease the Lagrangian particles dimension in order to better analyze all spark-channels behavior. As can be noticed from Figure 4.23, all spark-channel paths were strongly influenced by the local flow field distribution, also if during the first discharge the actual particles dimensions (Figure 4.22) seem to create a near-spherical flame shape.

Concerning the flame stretch, Figure 4.24 shows its distribution (where it is defined as $I_0 = s_u/s_{u0}$) over the computational domain for *Test 9* at three different times of the combustion process: 0.05, 0.50 and 0.95 ms. It is possible to notice that its contribution is important during the initial stage of the kernel growth. Here, with maximum values of about 0.6, affects significantly the flame front development, reducing its propagation rate. Instead, when a self-sustained flame is developed, the flame stretch tends to asymptotically vanish, assuming values close to 1. This is mainly due to the reduction of the local flame curvature when it departs from the ignition zone.

An important parameter that affects the flame stretch prediction is the Lewis number, whose distribution at three different times of the combustion process regarding *Test 9* is shown by Figure 4.25. As it can be observed, the Lewis number of a mixture of $\phi = 0.9$ assumes intermediate values between the typical Lewis numbers of propane (≈ 1.8) and air (≈ 1). Moreover, its value slightly changes according to local temperature (Figure 4.25, nearby the spark-gap) and pressure conditions (Figure 4.25a, with pressure waves generated by the spark-event), because the diffusivities of heat, deficient reactant and abundant reactant are function of these two parameters.

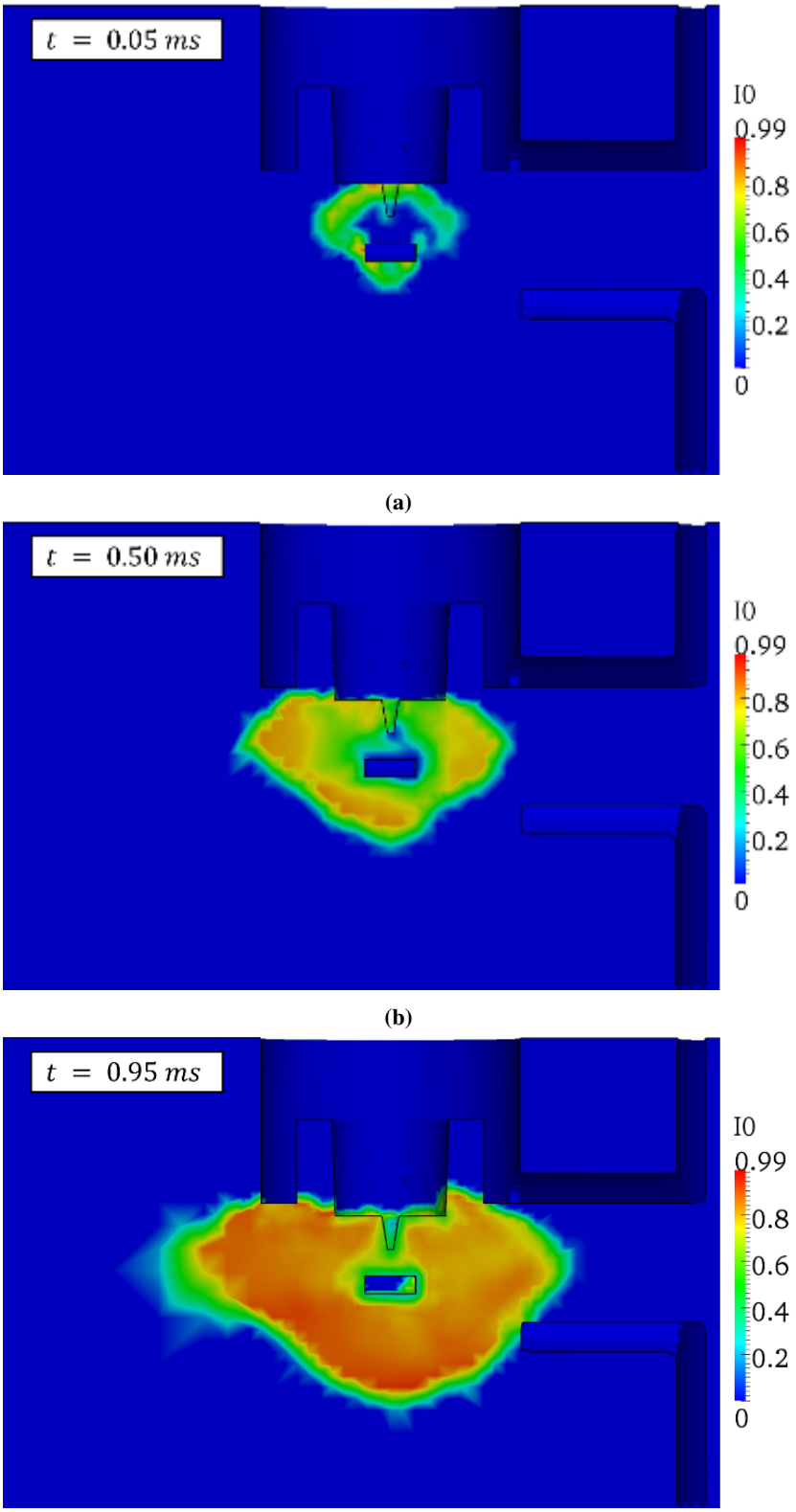

Figure 4.24: *The flame stretch distribution of* Test 9 *(Table 4.3). Fields values evaluated at different times from spark-onset ($t = 0.05\ ms$ (a), $t = 0.50\ ms$ (b), $t = 0.95\ ms$ (c)) in order to show how the flame stretch evolves during the combustion process. In legend, $I_0 = s_u/s_{u0}$.*

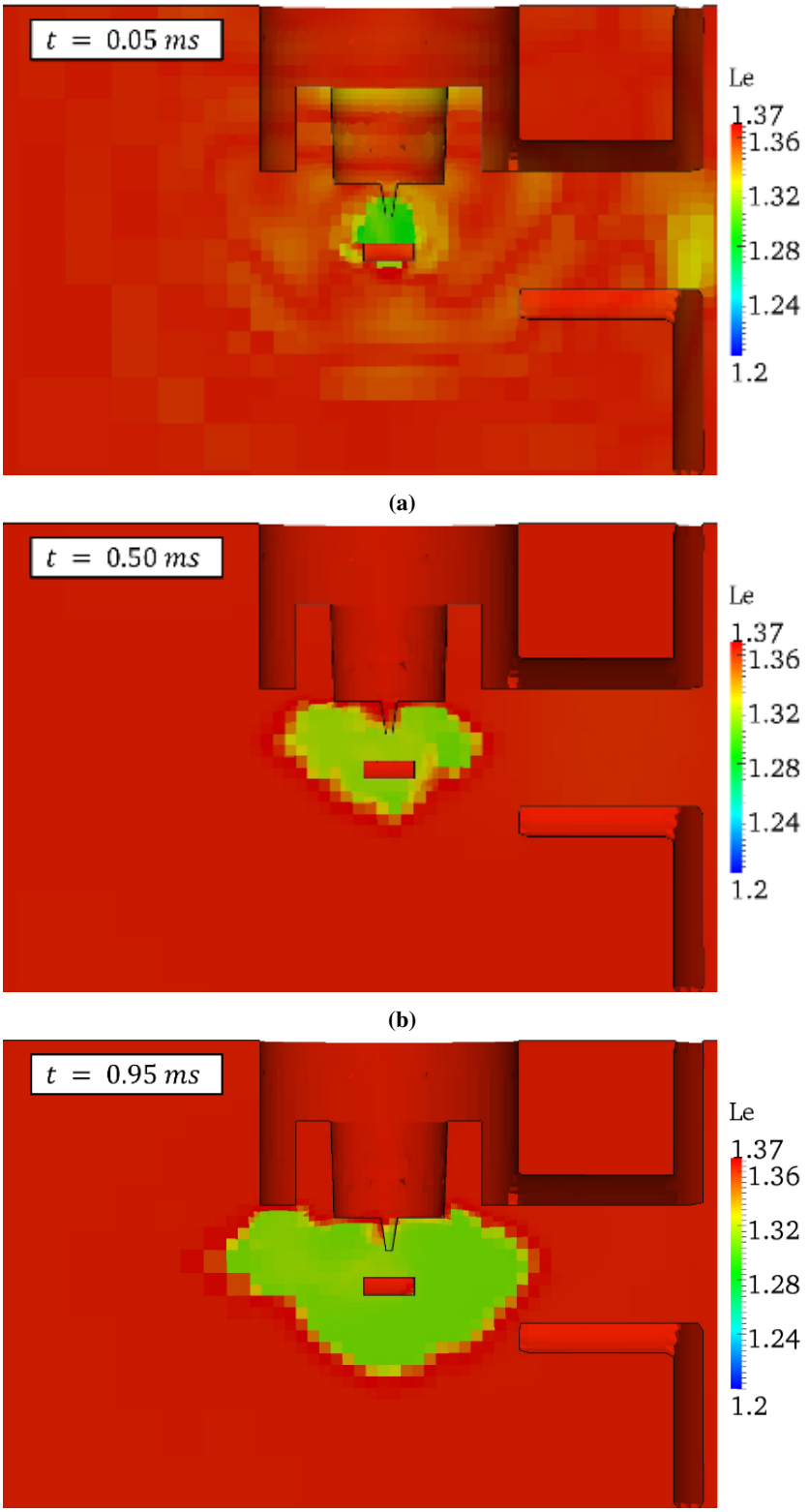

Figure 4.25: *The Lewis number distribution of* Test 9 *(Table 4.3). Fields values evaluated at different times from spark-onset ($t = 0.05\ ms$ (a), $t = 0.50\ ms$ (b), $t = 0.95\ ms$ (c)) in order to show the Lewis number evolution during the combustion process.*

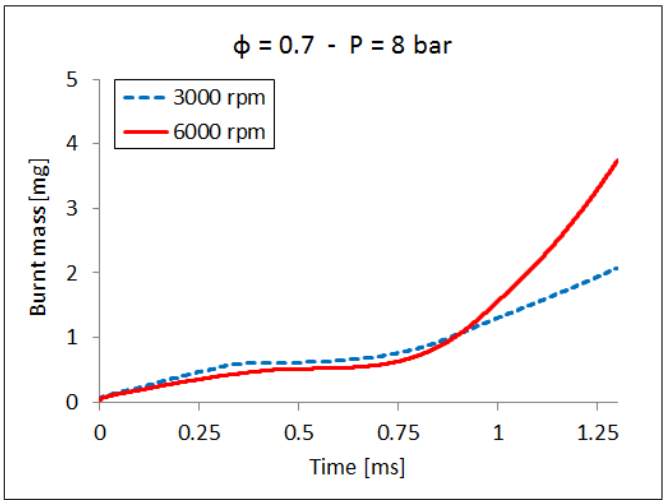

(a)

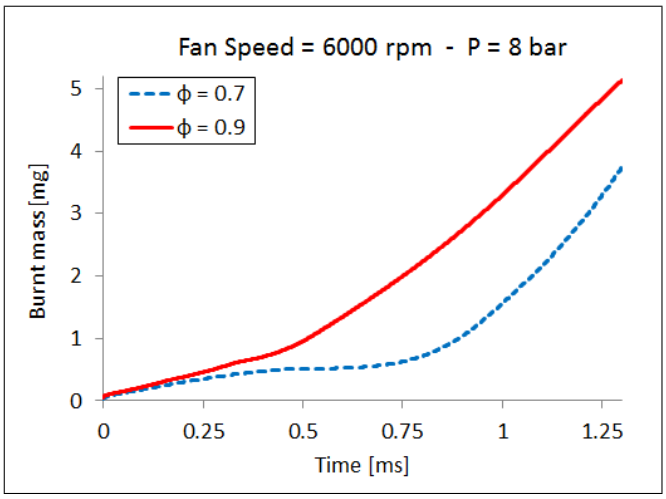

(b)

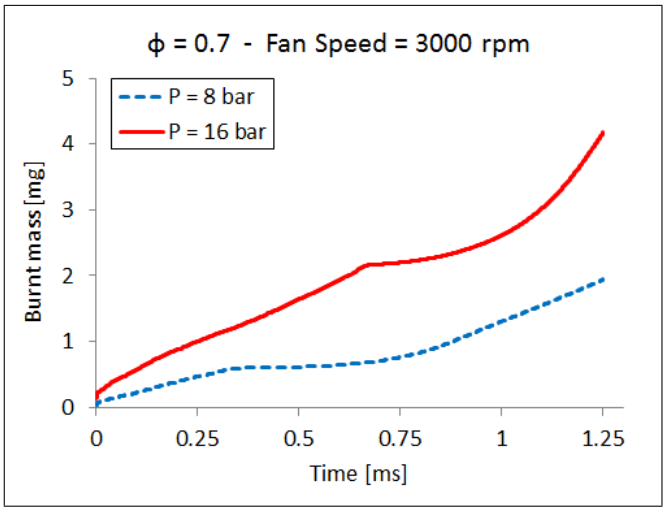

(c)

Figure 4.26: *Comparison between numerical burnt mass for reacting conditions of Table 4.3: turbulence intensity variation (*Test 2 *vs.* Test 3*) (a); equivalence ratio variation (*Test 3 *vs.* Test 9*) (b); pressure variation (*Test 2 *vs.* Test 6*) (c).*

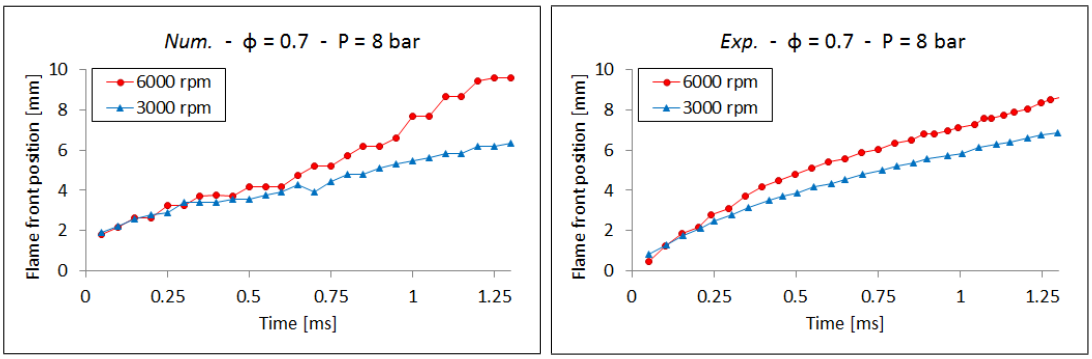

(a) **(b)**

Figure 4.27: *Comparison between* numerical *(left) and* experimental *(right) trends of flame front position under a* turbulence variation. *For each chart,* Test 2 *vs.* Test 3 *of Table 4.3 were used.*

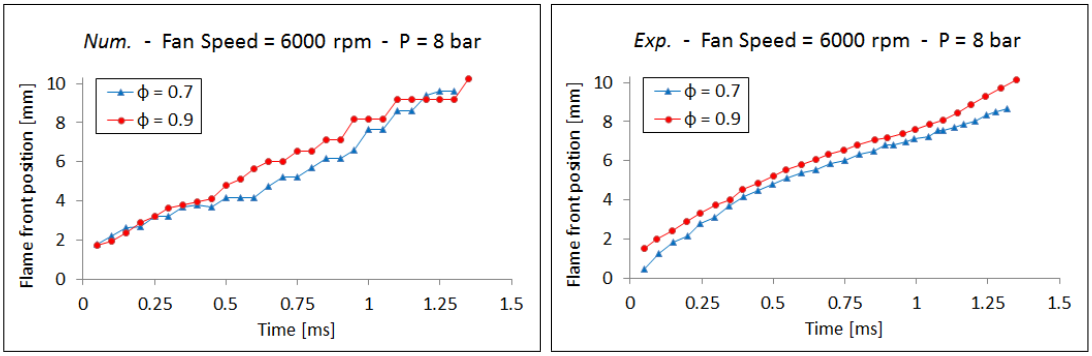

(a) **(b)**

Figure 4.28: *Comparison between* numerical *(left) and* experimental *(right) trends of flame front position under an* equivalence ratio variation. *For each chart,* Test 3 *vs.* Test 9 *of Table 4.3 were used.*

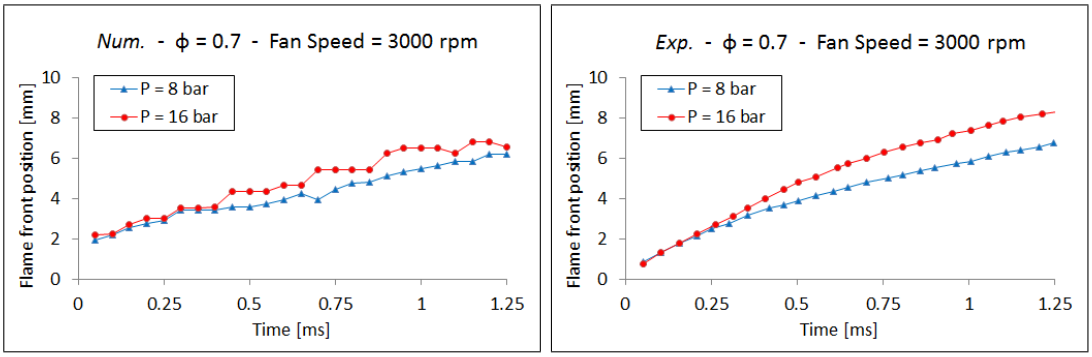

(a) **(b)**

Figure 4.29: *Comparison between* numerical *(left) and* experimental *(right) trends of flame front position under a* pressure variation. *For each chart,* Test 2 *vs.* Test 6 *of Table 4.3 were used.*

Finally, to support the consistency of computed results, a comparison between the mixture burnt masses was carried out. As Figure 4.26 shows, when a self-sustained flame is developed, an increase of turbulence intensity corresponds to a faster flame

front propagation (Figure 4.26a). On the other hand, as expected, a reduction of the mixture air/fuel ratio, namely of the equivalence ratio ϕ, generates a slower flame speed (Figure 4.26b). In presence of a pressure increase, Figure 4.26c shows that, as soon as a fully turbulent flame is formed, under conditions of $\phi = 0.7$ and fan speed 3000 rpm an higher pressure experiences a faster flame front propagation. The much higher kernel dimension formed in *Test 6* during the first breakdown event (see (1.2) considering that $E_{bd,Test\ 6} = 19mJ > 5.19mJ = E_{bd,Test\ 2}$, see Table 4.4) could explain this effect. In fact, when the dimension of the kernel structure is larger than a threshold value a higher pressure will enhance the propagation rate, as highlighted in Section 4.1.2.

Another comparison between the numerical and the experimental trends of the flame front position was performed under variations of:

1. Turbulence intensity (Figure 4.27).
2. Air/fuel ratio, or equivalence ratio (Figure 4.28).
3. Pressure (Figure 4.29).

As it is possible to notice, the results are quite satisfactory at all investigated variations, supporting again the validity of the implemented combustion model.

4.3 Summary

The Michigan Tech experimental rig, characterized by a pressurized, constant-volume combustion vessel, was chosen to validate the Comprehensive CFD model proposed in Chapter 1 under different conditions of turbulence, air/fuel ratio and pressure. In this configuration, a shrouded rotating fan coupled with a guide tube generates directly to the ignition zone a jet of fresh mixture with highly inhomogeneous flow and turbulence conditions.

First, an experimental campaign on the combustion process of lean and diluted *Propane-Air* mixtures was carried out under high temperature and pressure conditions at different turbulence levels. The flame kernel propagation rate was analyzed in terms of turbulence effect, pressure influence and flame structure. From achieved experimental findings, it can be concluded what follows:

- Turbulence increases the flame kernel propagation rate.

- The early flame kernel tends to have small complex structures under high pressures and turbulence velocities. An explanation of this phenomenon could be related to the higher energy amount introduced into the eddies spectrum, with a consequent extension of the Kolmogorov cascade towards small-scale eddies.
- When the initial dimension of the flame surface structures are *larger* than a threshold value, a pressure increase enhances the propagation rate. On the other hand, when the initial dimension of the flame surface structures are *lower* than a threshold value, a pressure increase suppresses the propagation rate.

Then, a non-reacting flow analysis was performed:

1. to initialize the flow field for combustion calculations,
2. to verify the proposed CFD setup in terms of turbulence model.

Regarding this last aspect, despite a not perfect agreement between PIV numerical and experimental trends under high fan speed velocities, the results could be considered rather satisfactory at all tested conditions.

Afterwards, combustion simulations were carried out. Computed results were compared consistently with the experimental data and rather satisfactory results were achieved for all tested conditions. In agreement with previous works on such topic, it was found that flame stretch mainly influences combustion development during its early propagation stage, while its effects vanish afterwards.

Finally, a comparison between numerical-only mixture burnt masses was carried out. As expected, when a self-sustained flame was developed, an increase of turbulence intensity corresponded to a faster flame front propagation, while a reduction of equivalence ratio produced a slower flame speed. This demonstrated the model capability to predict consistently the effects of fundamental parameters on the combustion development.

CHAPTER 5

The Darmstadt Turbulent Stratified Flame burner

The strategy to create a spatially non-uniform mixture distribution, also known as *charge stratification*, is practically used in IC engines to reduce fuel consumption, [106]. As a consequence, the regime of turbulent stratified combustion is usually exploited in practical applications, although some fundamental issues are still not fully understood. For example, when a stratified flame burns from locally stoichiometric to lean conditions, the resulting propagation speed is faster compared to the equivalent homogeneous setup. This can be justified by higher gas temperatures behind the flame front, which affect chemical kinetics together with heat and mass transport. However, the implication of this "history effect" on the turbulent stratified flame modelling is still an opened question, [99].

Therefore, to provide an experimental support to numerical models improvement and validation, a Turbulent Stratified Flame (TSF) series was investigated with the following design criteria:

- unlimited optical access by an opened flame;
- high Reynolds numbers;
- central pilot for flame stabilization;
- simple inflow conditions by fully developed pipe turbulence;
- independent control of shear and stratification in the turbulent mixing layer by two concentric feed lines.

Stationary conditions of *lean-lean* charge stratification were analyzed and measurements were carried out by using:

- Laser Doppler Velocimetry (LDV) for flow velocity components,
- 1D Raman/Rayleigh scattering for species mass fractions and temperature.

In this Chapter, a description of the TSF burner configuration and of the relative experimental investigation campaign performed by TU Darmstadt is reported. Then, a first numerical assessment of the ATF model proposed in Chapter 2 is carried out on the stationary TSF burner flame under a *lean-lean* charge stratification and assuming adiabatic conditions.

5.1 Burner set-up and experimental investigation

The experimental rig of the TSF burner is characterized by three concentric pipes, as shown by Figure 5.1.

The central one is the *Pilot*, whose aim is to release a flow of burnt products. This high temperature flow provides the heat necessary to ignite the surrounding fresh mixture, hence the combustion process can start just after its exit section.

The other two concentric tubes are called *Slot 1* and *Slot 2* (see also Figure 5.2). These annular slots are characterized by similar hydraulic diameters and can be operated, in terms of flow rates and equivalence ratios, independently from the Pilot and from each other. This allows a very flexible generation of *shear* and *global stratification* along the radial direction, enabling to investigate several configurations.

Pilot tube walls are made of ceramic, in order to limit as much as possible the thermal heat transfer from the hot burnt gases towards the radial direction (for more details,

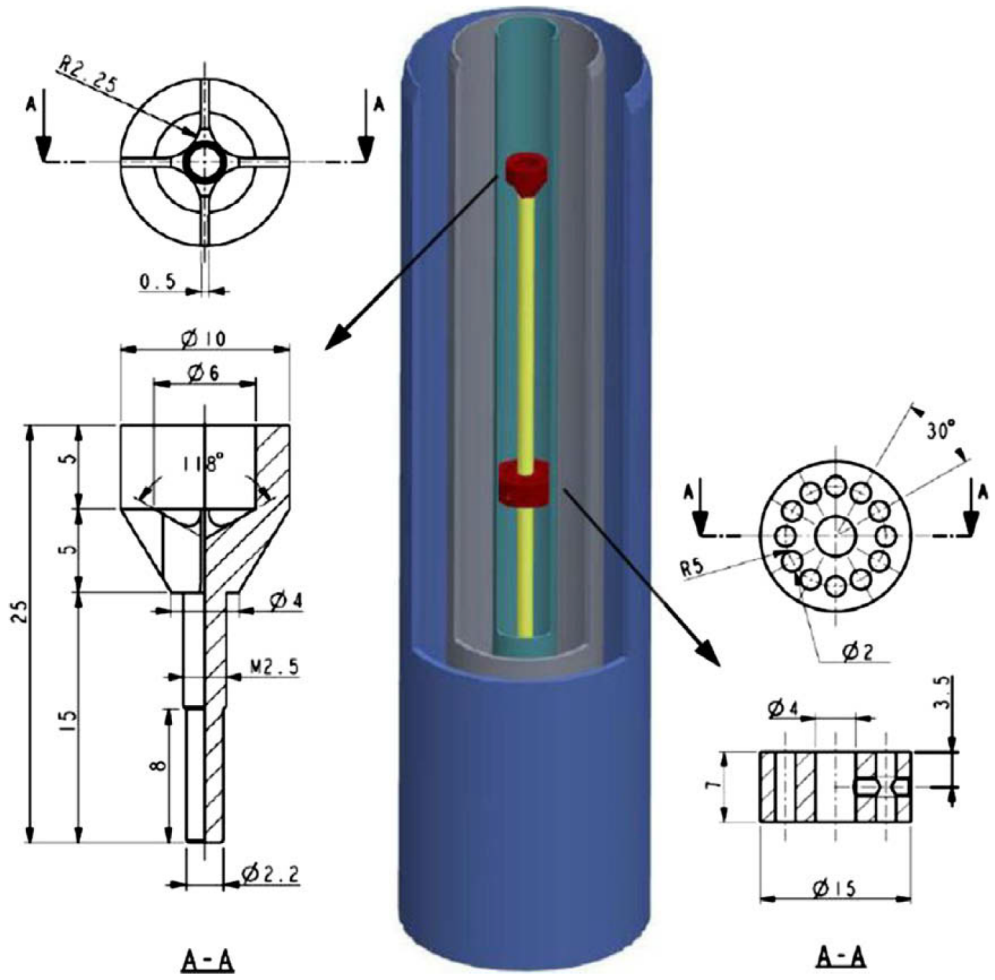

Figure 5.1: *The TSF burner: 3D rendering of the experimental rig, characterized by a central ceramic tube (*Pilot*) and two co-axial steel pipes with increasing radius (*Slot 1 *and* 2*, respectively), [99]. The* flame holder *and the* turbulence enhancing perforated plate *are highlighted inside the* Pilot*. Technical drawings of: the flame holder (left) and the turbulence enhancing perforated plate (right).*

see Chapter 6). On the other hand, Slot 1 and 2 pipes are made of stainless steel because they only handle fresh gases at ambient temperature ($T = 298\ K$).

The generation of hot burnt products inside the Pilot is carried out by igniting the mixture nearby the *flame holder*, which is a cylindrical ring located at 40 mm upstream the Pilot exit section and fixed at a central insert (see Figure 5.1). Its position was chosen as a trade-off between:

1. ensuring a fully burned flow at the Pilot exit,
2. minimizing the radial heat losses to the ceramic wall, namely the preheating of fresh gases ejected by Slot 1 (Chapter 6).

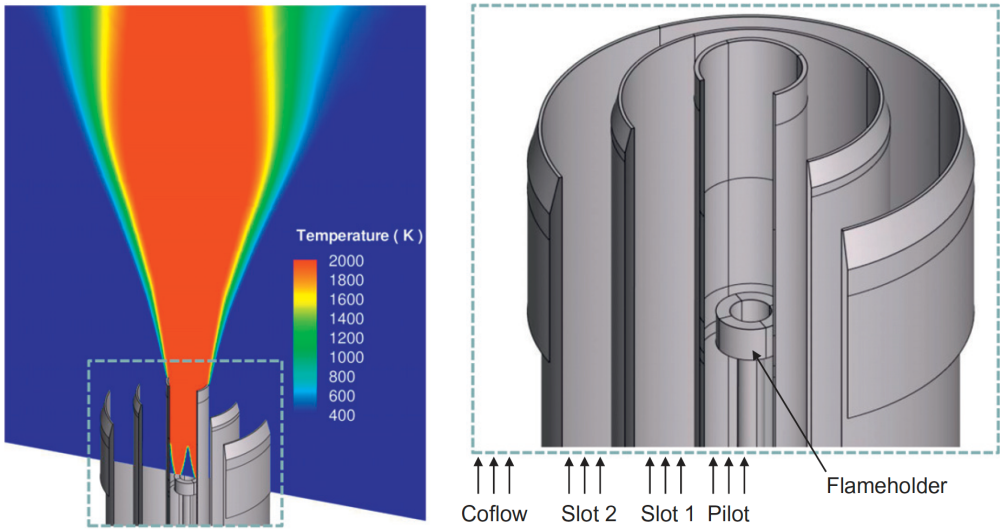

Figure 5.2: *The TSF burner geometry and flame stabilization: time-averaged temperature field taken from Kuenne's simulation (left); geometrical section of the burner exit region (right), [67].*

The wake region created by the flame holder presence allows to stabilize the flame, as shown by Kuenne's simulation results of Figure 5.2, and to achieve steady-state conditions.

The flame holder is not in contact with the Pilot wall, therefore its centering is guaranteed by a perforated plate, whose additional purpose is also to enhance the turbulence intensity upstream the flame holder position (Figure 5.1). Concerning the flow turbulence conditions of the two outer slots, their minimum length of about 500 mm (approximately 25 hydraulic diameters) together with 16 and 24 radial drill holes of 5 mm diameter positioned at Slot 1 and 2 inlets, respectively, ensure a fully developed turbulent flow at both pipe exits.

Finally, the burner is placed inside a 600 mm-wide air co-flow, characterized by a $U_y = 0.1\ m/s$ axial bulk velocity. Its function is to shield the flame front from the external environment and prevent the penetration of dust particles. This latter feature is crucial in the context of 1D Raman/Rayleigh scattering measurements, because it prevents dust-induced optical breakdown and reduces background illumination from Mie scattering.

For additional geometrical details about the TSF burner pipes, see Figure 5.3; for any further information, please refer to Seffrin [99].

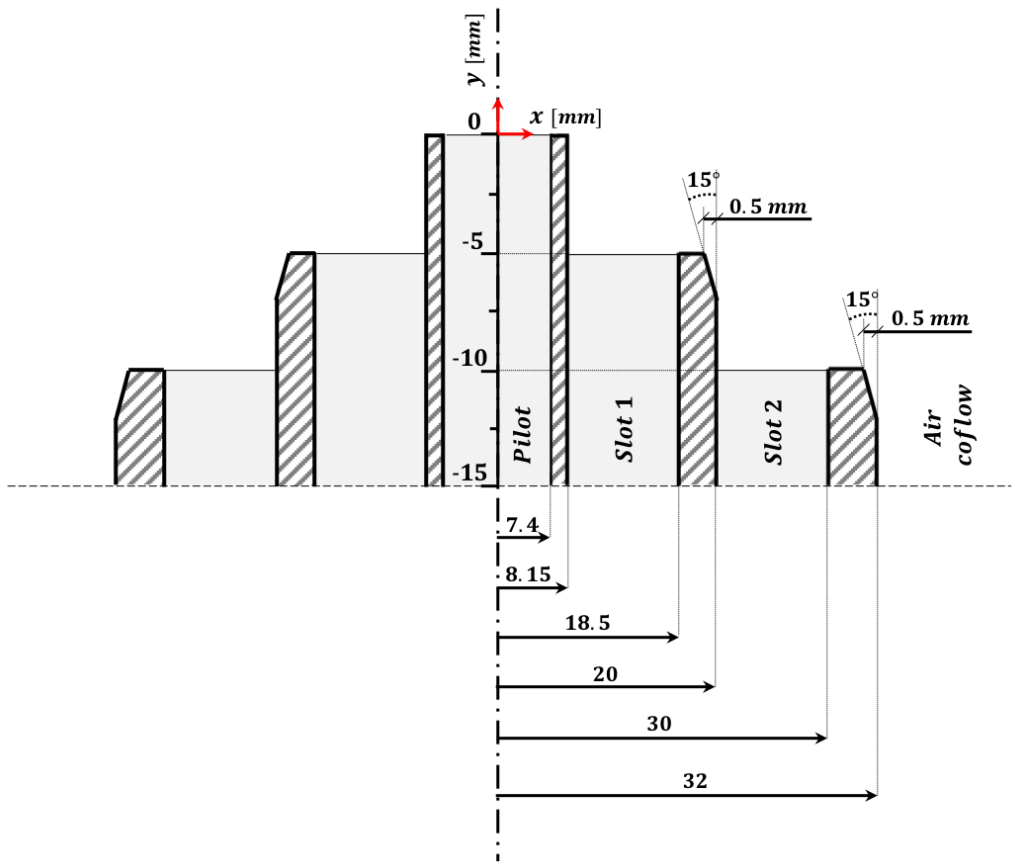

Figure 5.3: *Geometrical details of the TSF burner pipes: diameters, axial extensions of their final part, wall thicknesses and exit rims.*

Considering the burner flexibility to separately control each pipe feeding, a common feature adopted for all investigated set-up was to control along the radial direction shear (U_y) and global stratification (ϕ) in order:

- to minimize them between Pilot and Slot 1,
- to carry out their parametric variation between Slot 1 and 2.

Table 5.1 provides an overview of all investigated experimental conditions. Reported U_y values represent the actual unburned flow velocity for Slot 1 and 2 (since ignition takes place further downstream their exit sections) and the bulk velocity of the unburned flow upstream to the flame holder for Pilot. In fact, for reacting cases (the ones indicated with the *r* suffix), the inlet velocity of Pilot fresh mixture is calibrated in order to achieve a burnt gases velocity which approximately matches the U_y value

Table 5.1: *Investigated conditions on the TSF burner performed by TU Darmstadt, [99]. The extension* A ... K *indicates different flow conditions,* r *identifies the fully reacting cases,* i1 *denotes tests where only the mixture inside the Pilot is burning, while* i2 *refers to fully isothermal configurations. In the table:* ϕ *indicates the global equivalence ratio,* Re *the exit Reynolds number and* U_y *the axial unburned bulk velocity (according to the coordinate system of Figure 5.3). The fuel adopted for all tests and pipes is* Methane (CH_4)*, except* ϕ *values indicated with [*], which are referred to Ethylene* (C_2H_4).

Test	Pilot		Slot 1			Slot 2		
	ϕ_{Pilot} $[-]$	$U_{y,Pilot}$ $[m/s]$	ϕ_{Slot1} $[-]$	$U_{y,Slot1}$ $[m/s]$	Re_{Slot1} $[-]$	ϕ_{Slot2} $[-]$	$U_{y,Slot2}$ $[m/s]$	Re_{Slot2} $[-]$
A-r	0.9	1	0.9	10		0.6	10	
A-i1	0.9	1	0	10	13'800	0	10	13'300
A-i2	0	10	0	10		0	10	
B-r	0.9	1.5	0.9	15		0.6	15	
B-i1	0.9	1.5	0	15	20'700	0	15	20'000
B-i2	0	15	0	15		0	15	
C-r	0.9	1	0.9	10	13'800	0.6	5	6'700
C-i1	0.9	1	0	10		0	5	
D-r	0.9	1	0.9	10	13'800	0.6	20	26'600
D-i1	0.9	1	0	10		0	20	
E-r	0.9	1	0.9	10	13'800	0.9	5	6'700
F-r	0.9	1	0.9	10	13'800	0.75	10	13'300
G-r	0.9	1	0.9	10	13'800	0.9	10	13'300
H-r	0.9	0.6	0.6*	10	14'000	0.9*	5	6'800
I-r	0.9	0.6	0.6*	10	14'000	0.6*	10	13'500
J-r	0.9	0.6	0.6	10		0.9	5	
J-i1	0.9	0.6	0	10	13'700	0	5	6'600
J-i2	0	6	0	10		0	5	
K-r	0.9	0.6	0.6	10	13'700	0.6	10	13'300

of surrounding fresh mixture. This is performed with the final purpose to minimize the shear between Pilot and Slot 1. However, this approach was not adopted for cases *H*, *I*, *J* and *K* because the first two tests were operated with Ethylene (C_2H_4), instead with Methane (CH_4) as all other cases, and for stability reasons the Pilot axial velocity needed to be reduced from 1 m/s to 0.6 m/s. Last two tests adopted the same exception because thought as corresponding Methane configurations with respect to *H* and *I* cases.

By analyzing more in detail Table 5.1, some additional considerations can be performed. In particular, if between Slot 1 and 2 is present an equivalence ratio variation, the flame can be defined as *with stratification*, while in presence of a bulk exit velocity U_y change, the flame is considered as *with shear*. Therefore, the investigated tests can be classified as follows:

Test	**With stratification**	**With shear**	Methane	Ethylene
A	•		•	
B	•		•	
F	•		•	
E		•	•	
C	•	•	•	
D	•	•	•	
H	•	•		•
J	•	•	•	
G			•	
I				•
K			•	

As already mentioned, it can be noticed that all configurations are operated with Methane (CH_4), except *H* and *I* which are operated with Ethylene (C_2H_4). This choice was performed because Ethylene laminar burning velocity at $\phi = 1$ is approximately twice the Methane one, while the enthalpy of combustion is increased of about 1.6 times [99]. The Pilot is always operated at $\phi = 0.9$, except for *i2* fully isothermal configurations, (Table 5.1).

Figure 5.4 shows the flame classification into the regime diagram for turbulent premixed combustion [9, 67, 86, 87]. Although this is only a qualitative estimation based on order of magnitudes, it provides a general idea of the present *flame-turbulence* interaction. The classification is based on the turbulent kinetic energy and the integral length scale resulting from PIV measurements performed by Seffrin [98]. These magnitudes were evaluated along the mean flame position (see left image of Figure 5.4), leading to the regime of a *thickened-wrinkled* flame with relatively low Karlovitz numbers ($1 \leq Ka \leq 2.1$). Since the velocity fluctuation and the length scale increase with the distance from burner exit, further downstream an upper right shift in the regime diagram is expected, as indicated by the ellipse [67].

The flame photographs of all tested conditions reported in Table 5.1 are presented in Figure 5.5. Because their appearance significantly differs from typical round jet flames and the region of interest is close to the burner exit ($y < 300\ mm$, if the coordinates

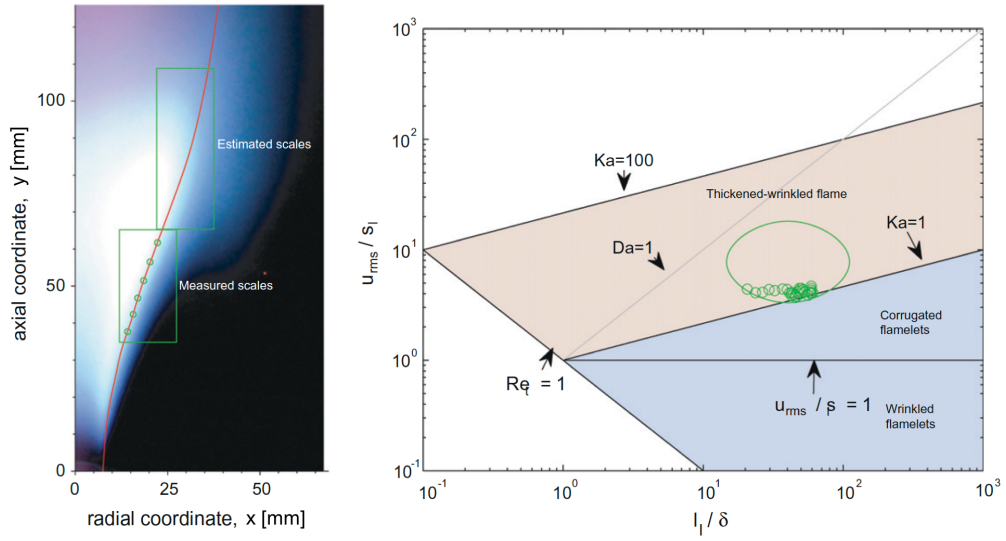

Figure 5.4: *Regime diagram classification of the* A-r *case: flame photograph with the mean flame position, which is highlighted in red (left); regime diagram with the classification based on measurements (circles) and estimated scales further downstream (ellipse), [67].*

system of Figure 5.3 is used), where the flow is not fully developed, the comparison between experimental findings and numerical results will be presented in physical, non normalized, space.

Finally, Figure 5.6 shows the adopted planes position for all performed measurements. In particular, the white dots indicate the positions where measurements of the flow field, in terms of bulk velocity and turbulence intensity, were carried out. On the other hand, black dots identify planes at which species mass fractions and temperature (mean and variance) were detected.

As previously mentioned, two different techniques were used for experimental measurements:

- the Laser Doppler Velocimetry (LDV) was adopted for turbulence and flow velocity components detection;
- 1D Raman/Rayleigh scattering was used for species mass fractions and temperature.

LDV is a technique which exploits the *Doppler shift* inside a laser beam to measure the velocity of transparent or semi-transparent fluid flows. In order to apply this concept, the investigated flow has to be filled with particles seeds; hence the Pilot, the

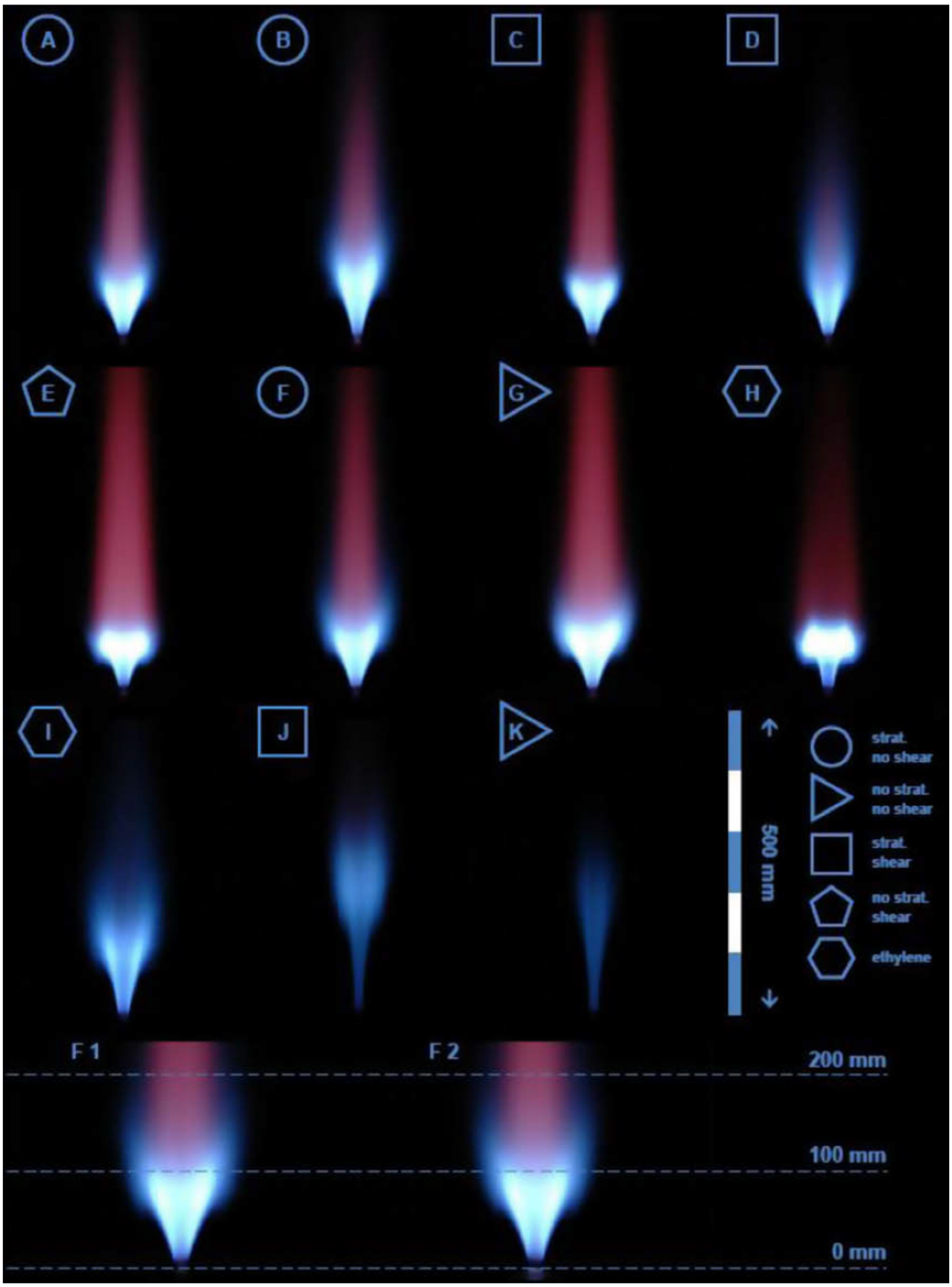

Figure 5.5: *Photographs of each reacting condition tested on the TSF burner and described in Table 5.1, [99]. Last row shows a comparison between* F *case for the original burner (*F1*) and a duplicate (*F2*), demonstrating the good reproducibility of the technical construction.*

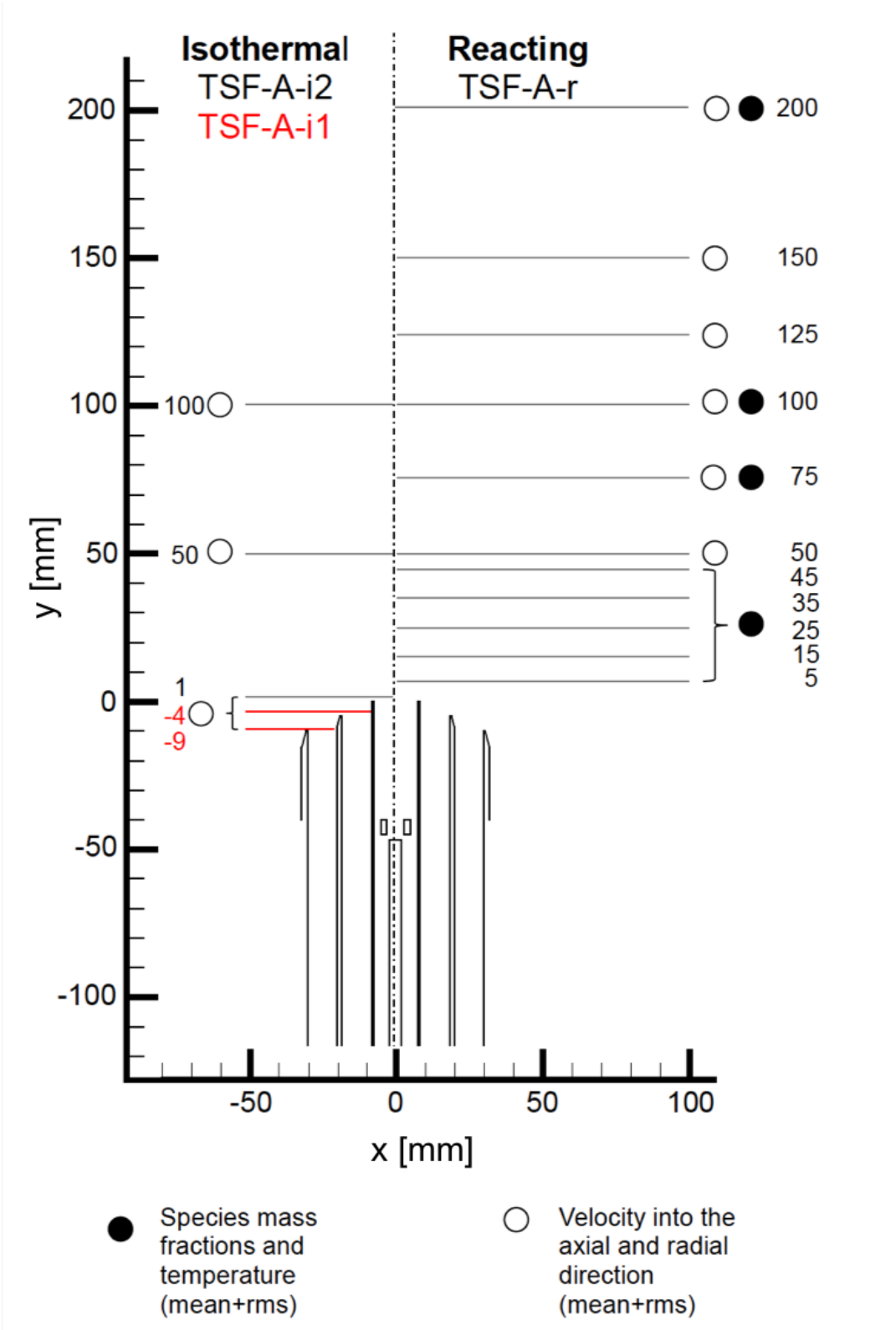

Figure 5.6: *Measurement planes position for the reacting case* A-r *and the corresponding isothermal case* A-i2*. The measurement planes for* A-i1 *case (in which only* Pilot *is burning) are highlighted in red.*

two annular slots and the air co-flow were equipped with individual seeding generators designed for the corresponding mass flow rates. As seeding material, dried and sieved magnesium oxide (MgO) was used. For a detailed description of the LDV experimental equipment and measurements, please refer to Seffrin [99].

On the other hand, 1D Raman/Rayleigh scattering technique exploits the interaction between photons of a laser beam and atoms or molecules of the investigated fluid itself. In fact, when photons collide with a molecule they can be scattered in two different ways:

1. elastically, if the scattered photons maintain the same energy of the incident ones (Rayleigh scattering), or

2. inelastically, if the scattered photons have a different energy with respect to the incident ones (Raman scattering), due to *photon-molecule* energy transfer.

Therefore, because the Raman/Rayleigh scattering ratio depends on the type and state of molecules making the fluid, the presence of different specie mass fractions and their temperature can be detected.

For TSF burner measurements, a system consisting of four frequency-doubled *Nd:YAG* lasers was used. The acquired data were evaluated by using the hybrid method [43–45] based on theoretically simulated Raman spectra and for Methane an empirical polynomial response was used [67]. At each location 500 single-shot measurements were recorded and then averaged with a post-processing procedure. The background channel was individually matched and subtracted for each axial position to account for the varying flame luminosity (see left image of Figure 5.4). For more details about the 1D Raman/Rayleigh measurements of species mass fractions and temperature, please refer to Kuenne [67].

Some experimental findings achieved on the TSF burner will be reported in next Section 5.2, in the context of the ATFM first numerical assessment. For all other measured data, please refer to [67, 99].

5.2 The *Artificially Thickened Flame Model*: first numerical assessment

The validation procedure of the Artificially Thickened Flame Model (ATFM), proposed in Chapter 2, was characterized by the following first step: an initial numerical assessment on the Test *A-r* condition of Darmstadt TSF burner (Table 5.1), with the assumption of adiabatic conditions (no heat transfer through pipe walls).

The governing equations were solved with the LES approach and the sub-grid fluxes of momentum were accounted for by the eddy viscosity approach proposed by Smagorinsky [104], where the model coefficient was obtained by the dynamic procedure of Germano [49] with Lilly's modification [71]. An exception concerned the 3D simulations with no flame thickening carried out to initialize the flame position: they adopted a RANS approach with a turbulence described by the $k - \omega$ SST model.

Three different computational domains, concerning the TSF burner exit and shown in Figure 5.7, were used for the described numerical assessment:

1. *M0*,
2. *M1*,
3. *M2*,

all characterized by structured meshes but each one thought for a specific target.

The *M0* mesh (Figure 5.7a), characterized by nearly $1.8\ mil$ cells, is the smallest domain and it was used to carry out an initial qualitative analysis of the ATFM correct behaviour with low computational efforts. In this context, the flame response to the thickening procedure was investigated in the region nearby the Pilot exit section; therefore:

- Nearly cubic refined cells, with an average side dimension of 0.3 mm, were created just above the Pilot tube wall, as shown by Figure 5.8a. This solution allowed to ensure an high quality mesh in the region where the steady-state cylindrical flame is closer to the pipe walls (Figure 5.4), hence where it is first encountered by the Slot 1 fresh mixture.
- An high level of refinement was performed on the radial direction at both sides of the Pilot wall, to avoid possible difficulties due to the application of high thick-

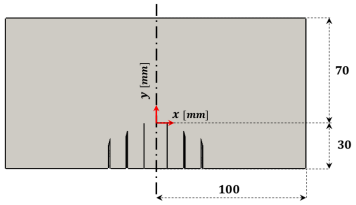

(a)

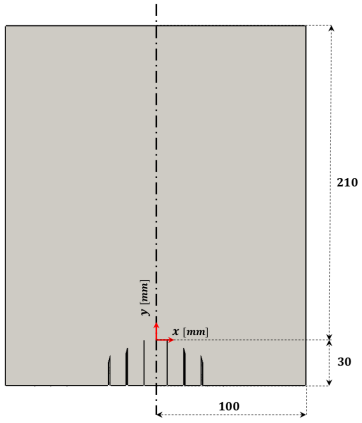

(b)

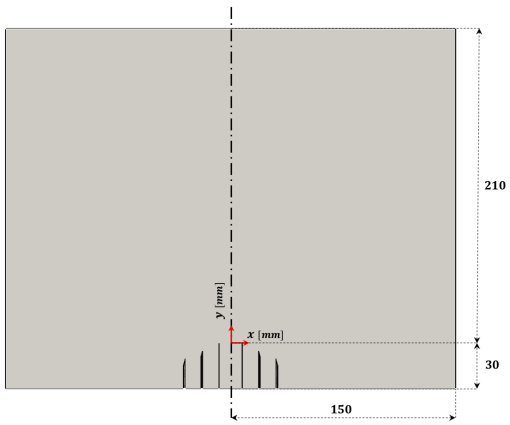

(c)

Figure 5.7: *Geometrical extension of adopted computational meshes concerning the TSF burner exit region:* M0 *mesh (a),* M1 *mesh (b) and* M2 *mesh (c).*

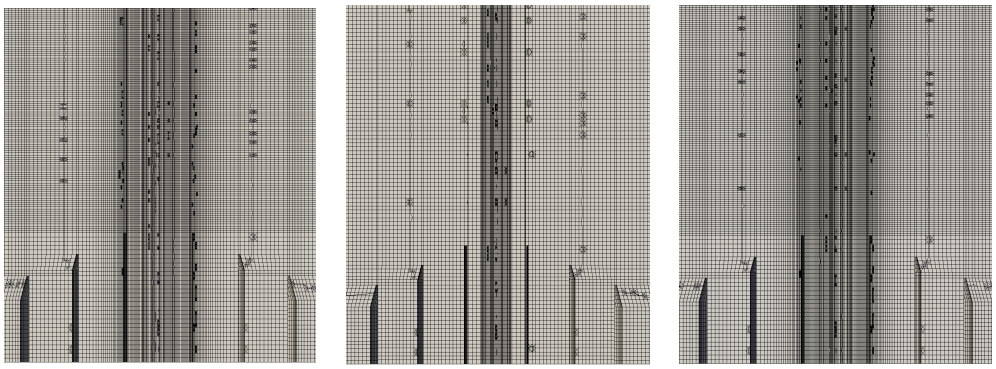

(a) (b) (c)

Figure 5.8: *Axial sections of Figure 5.7 meshes at the region close to the TSF burner exit:* M0 *mesh (a),* M1 *mesh (b) and* M2 *mesh (c). The drawn triangles are not part of the real mesh but are simply generated by the graphics display system.*

ening factors F. In fact, nearby the Pilot exit section the flame experiences its minimum inner diameter (Figure 5.4), hence an F value increase could create a too wide cylindrical reaction layer with possible contacts at its axis of symmetry. In particular, as shown by Figures 5.8a, 5.9a and 5.10a, two different refinement strategies were used:

1. at the pipe inner side (Pilot), the *o-grid* technique together with a nearly constant mesh dimension were adopted;
2. at pipe outer side (Slot 1) the *cell grading* approach was applied in order to avoid an unnecessary radial refinement far from the cylindrical flame axis of symmetry.

- A constant radial refinement of Slot 2 internal region, with a mesh spacing equal to Slot 1 wall inner part, was assumed (Figures 5.8a, 5.9a and 5.10a). This choice was performed in order to guarantee a nearly constant and rather refined cell size in the region of *flame-mixture stratification* overlapping, which is of major interest and positioned above Slot 1 wall, without an unnecessary high level of refinement. In fact, because at this region the cylindrical steady-state flame experiences a greater radius than immediately after the Pilot exit section (compare Figures 5.3 and 5.4), a lower radial refinement can be adopted with respect to Pilot wall sides.
- A radial cell coarsening was carried out over the co-flow region to minimize the total number of mesh cells in regions not crossed by the flame front (Figure 5.10a).

- An axial mesh refinement was imposed after Pilot exit section ($Y > 0\ mm$, see Figures 5.8a and 5.3) with the purpose to achieve a higher mesh refinement where the flame is positioned.

The second mesh, *M1* (Figure 5.7b), with about $3.1\ mil$ cells, is the intermediate numerical grid and it was thought to optimize the RANS unthickened simulations carried out for the flame position initialization. In fact *M1*, thanks to its higher extension along the axial direction but a constant radial dimension if compared with *M0*, allows to achieve unthickened flame results for each investigated position (see Figure 5.6, where $Y_{max} = 200\ mm$) without a useless increase of the computational time. As it can be evinced from Figures 5.8, 5.9 and 5.10, with respect to *M0* mesh:

- The radial mesh refinement inside Pilot and Slot 1 regions is considerably lower.
- A constant mesh spacing instead of the cell-grading technique is adopted inside Slot 1 pipe and at the co-flow region.
- The axial grid refinement after the Pilot exit section is lower, in particular it corresponds to the inner pipes one.

On the other hand, the *M2* mesh (Figure 5.7c), consisting of approximately $5.7\ mil$ cells, is the largest adopted domain and it was specifically selected to perform the final comparison between numerical results and experimental measurements. Compared to *M1* mesh, *M2* is characterized by the same axial extension but its radial dimension is increased of the 50%. This choice was justified by the need of minimizing the influence on numerical results of the external boundary of the cylindrical mesh (especially at axial positions far from the Pilot exit section) with the smallest increase of computational efforts. As Figures 5.8, 5.9 and 5.10 show, its refinement features are equal to those adopted for *M0* mesh.

In next sub-sections, the initialization of ATFM LES analysis through RANS simulations is first described. Then the flame sensor choice, followed by initial qualitative tests of the implemented ATF model are reported. Finally, the first ATFM numerical assessment is carried out on Test *A-r* condition of Darmstadt TSF burner (Table 5.1) under the assumption of adiabatic conditions.

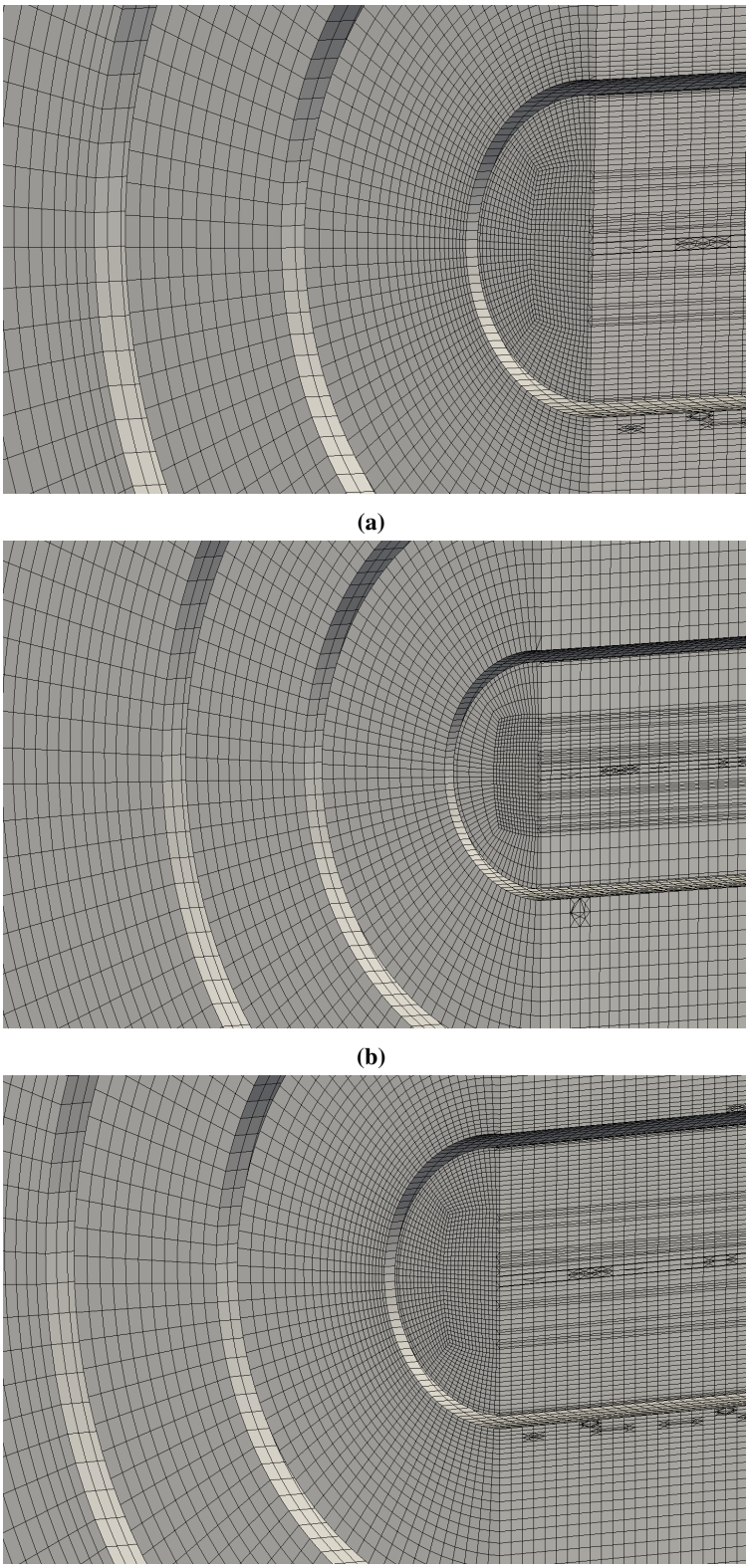

(a)

(b)

(c)

Figure 5.9: *Angular views of Figure 5.8 meshes in order to appreciate the mesh spacing inside the three annular concentric pipes:* M0 *mesh (a),* M1 *mesh (b) and* M2 *mesh (c). The drawn triangles are not part of the real mesh but are simply generated by the graphics display system.*

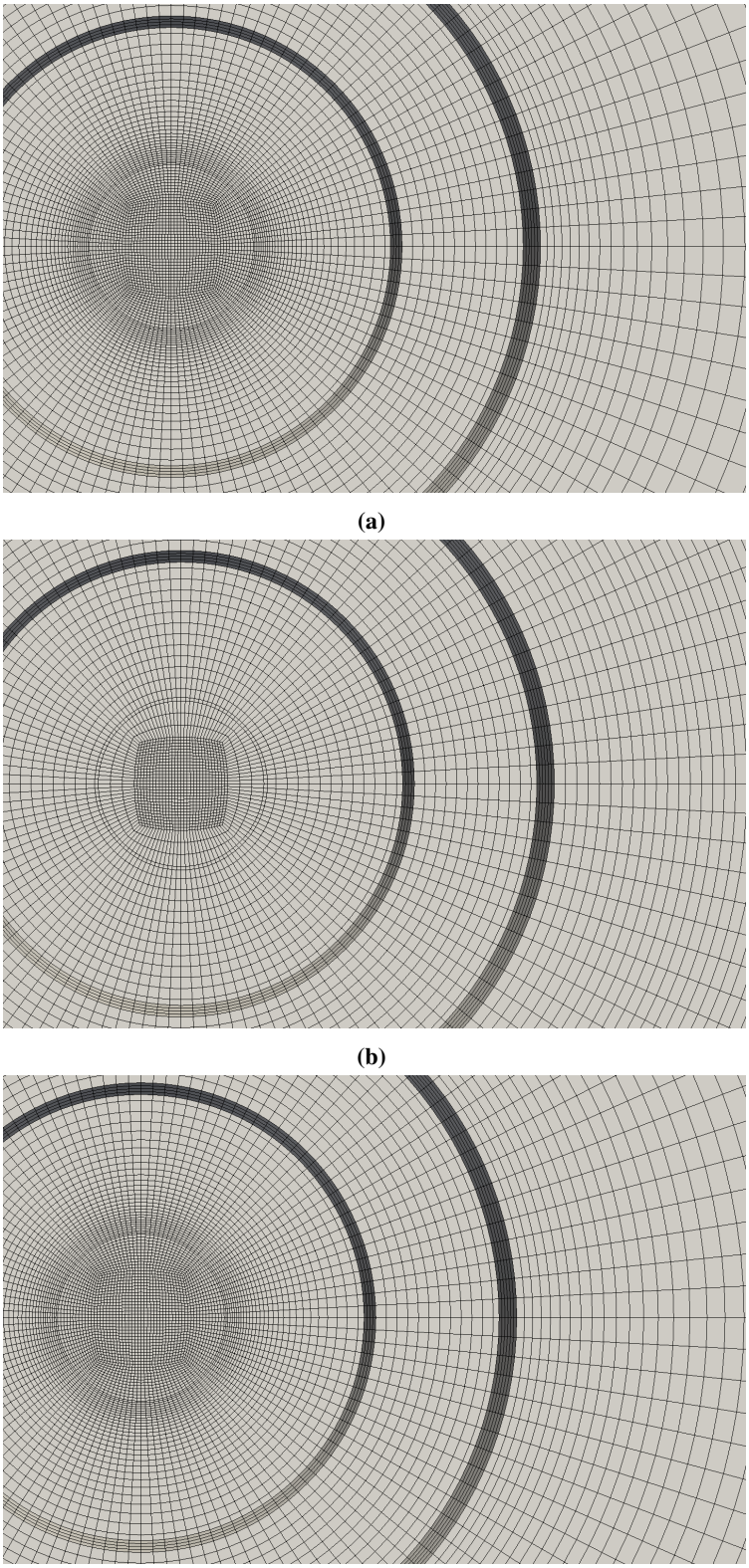

(a)

(b)

(c)

Figure 5.10: *Radial views of Figure 5.7 meshes at* $Y = -30\ mm$ *nearby the three annular concentric pipes:* M0 *mesh (a),* M1 *mesh (b) and* M2 *mesh (c).*

5.2.1 Initialization of LES analysis: 3D simulations with RANS approach and no thickening of the flame

The Artificially Thickened Flame Model was developed and implemented to work into a framework where the turbulence is described through a LES strategy. However suitable initial conditions for LES simulations, in particular for the flame front position, should be provided if the ATFM has to be tested on an steady-state case (if averaged in time) as the TSF burner one. A possible approach to fulfill this requirement is providing initial conditions as close as possible to the final time-averaged numerical solution not only for the flame position but also for other fields. This would help LES simulations to minimize the initial transition from provided conditions to final transient results, because the time-averaged initial distributions are close to final ones. As a consequence, computational time can be saved. Therefore, the use of 3D RANS simulations with no thickening of the flame, namely with the ATFM disabled ($F = E = 1$), allows to reach the previous target: time-averaged fields distribution (relatively close to the final time-averaged solution) to be used as initial conditions for the further LES analysis.

The procedure to achieve 3D RANS reacting results, as previously described, is the following:

1. First of all, a *cold flow* simulation should be initialized and then carried out.
2. Afterwards, cold flow results can be used to initialize the following *reacting* simulation.
3. Finally, at the end of this last simulation, the achieved results are available for the LES analysis initialization.

The major efforts related to above first step concerned the initialization of:

- the flow velocity and turbulence fields of the three annular pipes and of the co-flow;
- the mixture fraction Z distribution.

About velocity and turbulence initialization, *cyclic-flow* simulations were performed on three annular meshes representing the internal domain of Slot 1 and 2 pipes and of the

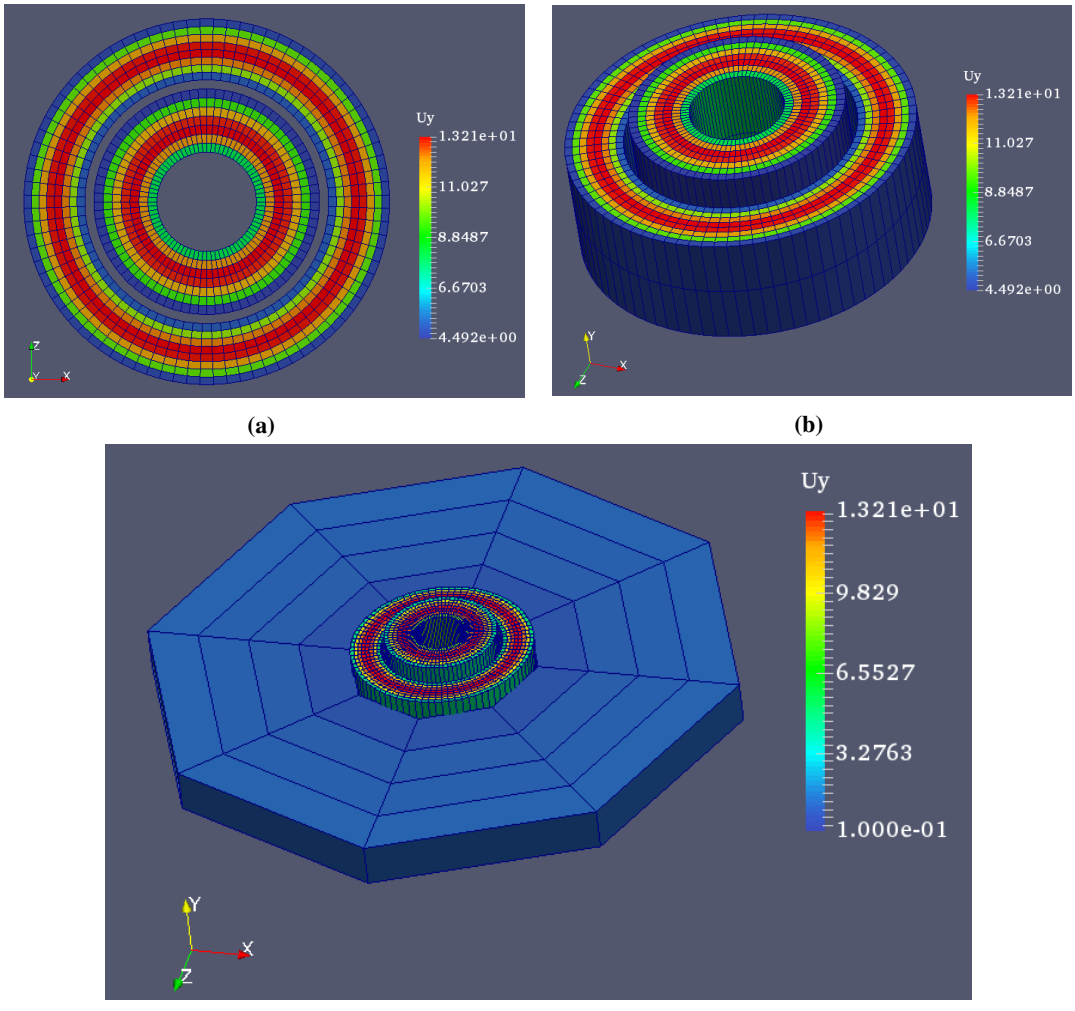

Figure 5.11: *Axial velocity distributions of cyclic-flow simulations performed on three concentric annular meshes. The inner two ones represent* Slot 1 *and* Slot 2 *internal volumes (top view (a) and angular view (b)), while the outer third one characterizes the* Co-flow *around* Slot 2 *wall (c).*

air co-flow region under Slot 2 wall outer rim. Figure 5.11 shows the achieved axial velocity distributions, starting from Test *A-r* available data (Table 5.1). The annular domains represented in Figure 5.11 are closely related to the complete geometry used for next RANS analysis, namely *M1* (Figure 5.7b), except for the cell refinements. In fact, along the axial direction only one cell is used for all three annulus, because cyclic-flow simulations basically provide 2D results on a pipe section. On the other hand, the radial cell refinement was independently chosen to guarantee a $y^+ \approx 30$ along each tube, allowing the application of *wall functions* for turbulence fields and a consequent reduction of computational costs. This strategy allowed to achieve flow velocity distributions and turbulence features typical of fully developed turbulent fields for Slots 1 and 2 (as specified in Table 5.1 ofr Test *A-r*), while for the air co-flow it helped to provide a better flow velocity initial condition.

To assess the quality of previous cyclic-flow simulations, Figure 5.12 shows a comparison between numerical axial flow velocity detected $15\ mm$ upstream the *Pilot* exit section with available experimental findings at: $Y = -4\ mm$ (Figure 5.12a) and $Y = -9\ mm$ (Figure 5.12b). Although these comparisons are not fully consistent because not performed at the same axial position, they provide an idea about the accuracy of numerical velocity profiles achieved for *Slot 1* and *2* with cyclic-flow simulations. The *numerical-experimental* match is not perfectly achieved, but the results can be considered globally satisfactory.

Once completed the cyclic-flow simulations, the computed distributions of flow velocity and turbulence fields were mapped on *M1* mesh, as shown in Figures 5.13a and 5.13b. To complete the RANS cold-flow initialization:

- Inside Pilot pipe, the flow velocity was imposed as specified in Table 5.1 (Test *A-r*, see also Figures 5.13a and 5.13b), namely with an axial bulk velocity of $U_y = 1\ m/s$ characterized by a uniform distribution; the turbulence field was imposed uniform too, with a reasonable low value. This strategy was adopted according to the laminar features of the Pilot fresh mixture for Test *A-r* and considering that during next combustion simulations a fully burnt mixture will be initialized inside Pilot *M0* mesh.

- The mixture fraction field was roughly initialized as shown by Figure 5.13c, im-

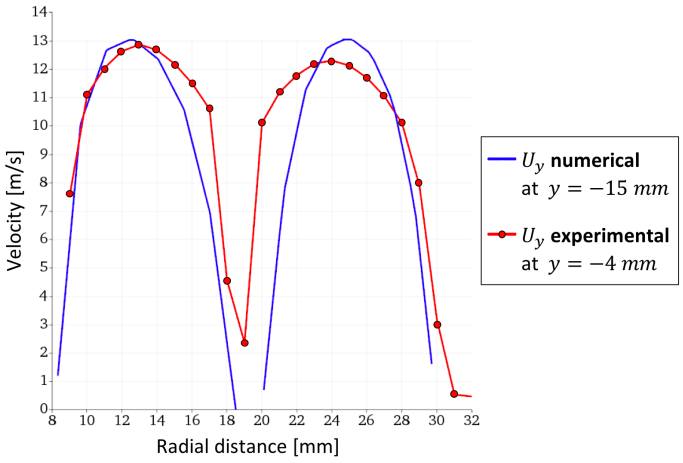

(a)

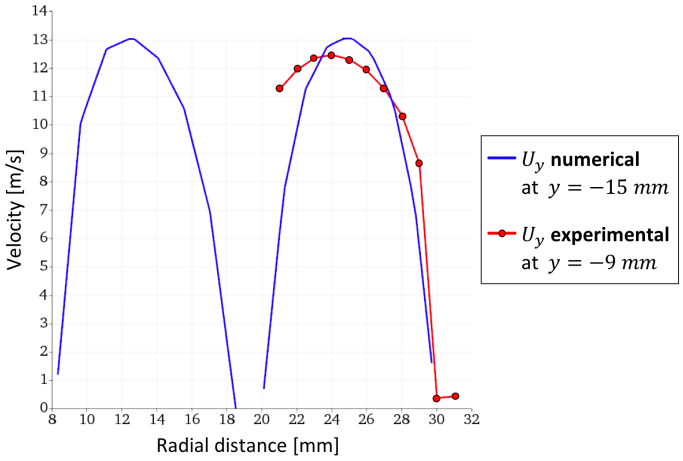

(b)

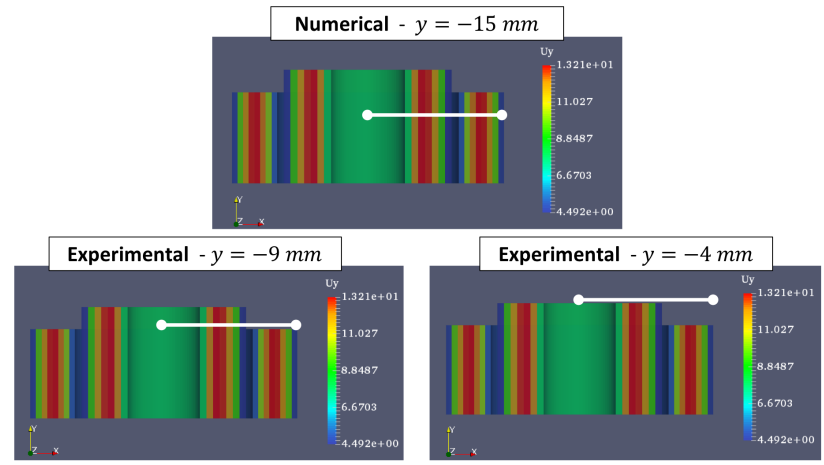

(c)

Figure 5.12: *Numerical axial flow velocity detected* $15\ mm$ *upstream the* Pilot *exit section and compared with available experimental findings at:* $Y = -4\ mm$ *(a) and* $Y = -9\ mm$ *(b) (see Figure 5.6). Although these comparisons are not fully consistent, they provide an idea about the accuracy of numerical velocity profiles achieved for* Slot 1 *and* 2 *with cyclic-flow simulations. Locations of investigated paths are shown in (c).*

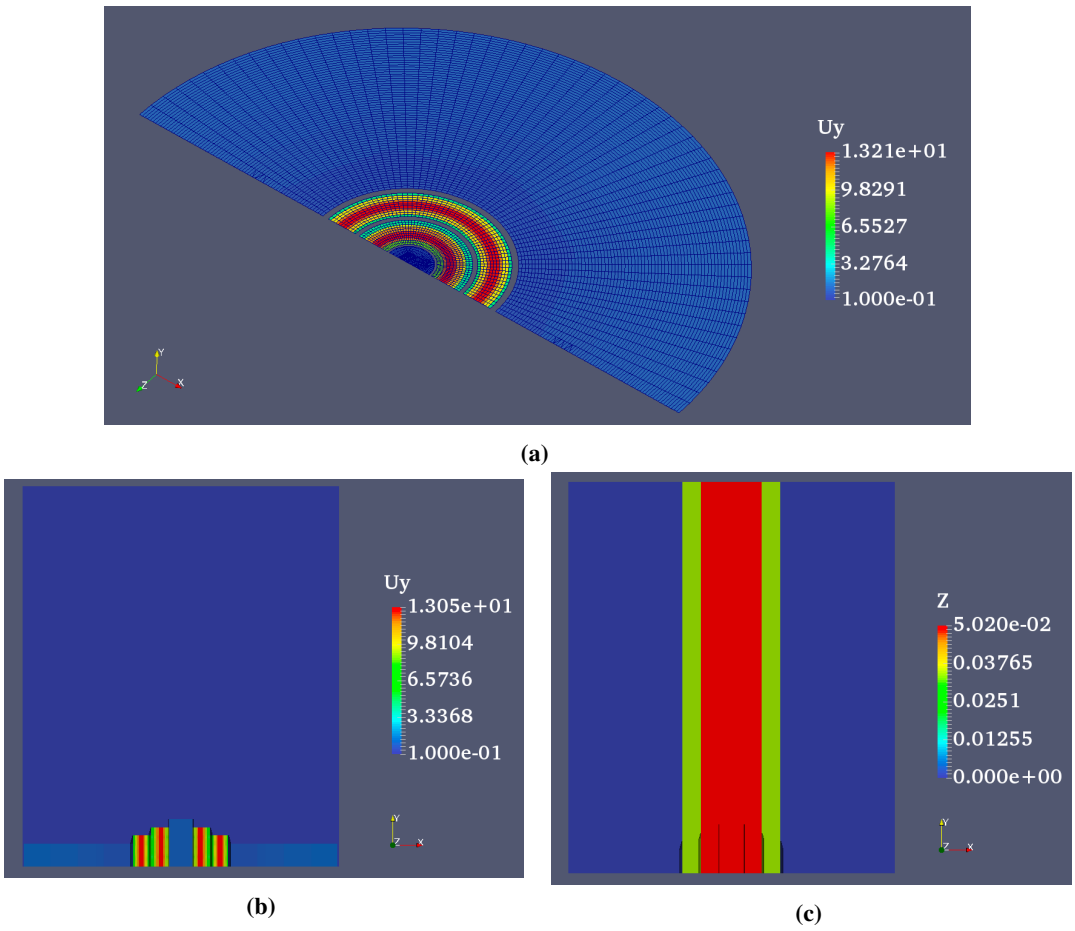

Figure 5.13: *Fields initialization of cold-flow 3D RANS simulations: axial velocity inlet patch (a) and sectional views of axial flow (b) and mixture fraction (c) fields distribution. The velocity field is initialized by mapping the cyclic-flow simulation results of Figure 5.11 on the adopted 3D mesh, namely* M1 *(Figure 5.7b).*

Table 5.2: *Boundary conditions for RANS simulations.* $\vec{U}$ *and* k *values at* Slot 1, 2 *and* Co-flow *inlet patches are mapped from cyclic-flow simulation results of Figure 5.11. On the other hand, at* Pilot *inlet patch* $\vec{U}$ *and* k *values are initialized to achieve a* $U_y = 10\ m/s$*, uniform and laminar flow of 100 % of burnt products. All other magnitudes (included Temperature) are achieved from the adopted tabulation strategy (Section 2.4), hence are imposed* zeroGradient *everywhere.*

Boundary	$\vec{U}$	k	Y_c (or PV)	P	Z
Inlet *Pilot*	fixedValue	zeroGradient	fixedValue	zeroGradient	fixedValue
Inlet *Slot 1*	fixedValue (*mapped*)	fixedValue (*mapped*)	fixedValue	zeroGradient	fixedValue
Inlet *Slot 2*	fixedValue (*mapped*)	fixedValue (*mapped*)	fixedValue	zeroGradient	fixedValue
Inlet *Co-flow*	fixedValue (*mapped*)	fixedValue (*mapped*)	fixedValue	zeroGradient	fixedValue
Outlet	inletOutlet	zeroGradient	zeroGradient	fixedValue	zeroGradient
Walls	fixedValue	wallFunction	zeroGradient	zeroGradient	zeroGradient
Co-flow	slip	zeroGradient	zeroGradient	zeroGradient	zeroGradient

posing a Z value at Pilot, Slots 1 and 2 inlet patches, according to Table 5.1 (Test *A-r*).

Finally, the RANS cold-flow simulation was carried out by adopting the boundary conditions specified in Table 5.2. Results are shown in Figure 5.14, where few modifications were introduced for the next RANS reacting simulation with no thickening of the flame. In particular, a rough flame front was initialized inside the Pilot pipe by imposing a linear axial variation of the non normalized progress variable PV (Figure 5.14b). Accordingly, a fully burnt mixture at laminar conditions and with an axial bulk flow velocity similar to the one inside Slot 1 ($U_y \approx 10\ m/s$) was imposed behind the reaction layer, as described by Seffrin [99] (see Figures 5.14a, 5.14b and 5.14c).

Some final results of a 3D RANS reacting simulation, with no thickening of the flame, are reported in Figure 5.15. As it can be noticed, the temperature profile distribution (Figure 5.15a) representing its time-averaged result has a similar shape with respect to Kuenne's one of Figure 5.2. Moreover, also the non-normalized progress variable shape of Figure 5.15c shows a tendency of the simulated flame front to assume the experimental shape reported in Figure 5.5. Therefore, the achieved results are in agreement to the initial target of this RANS analysis and can be used as initial conditions for next LES analysis.

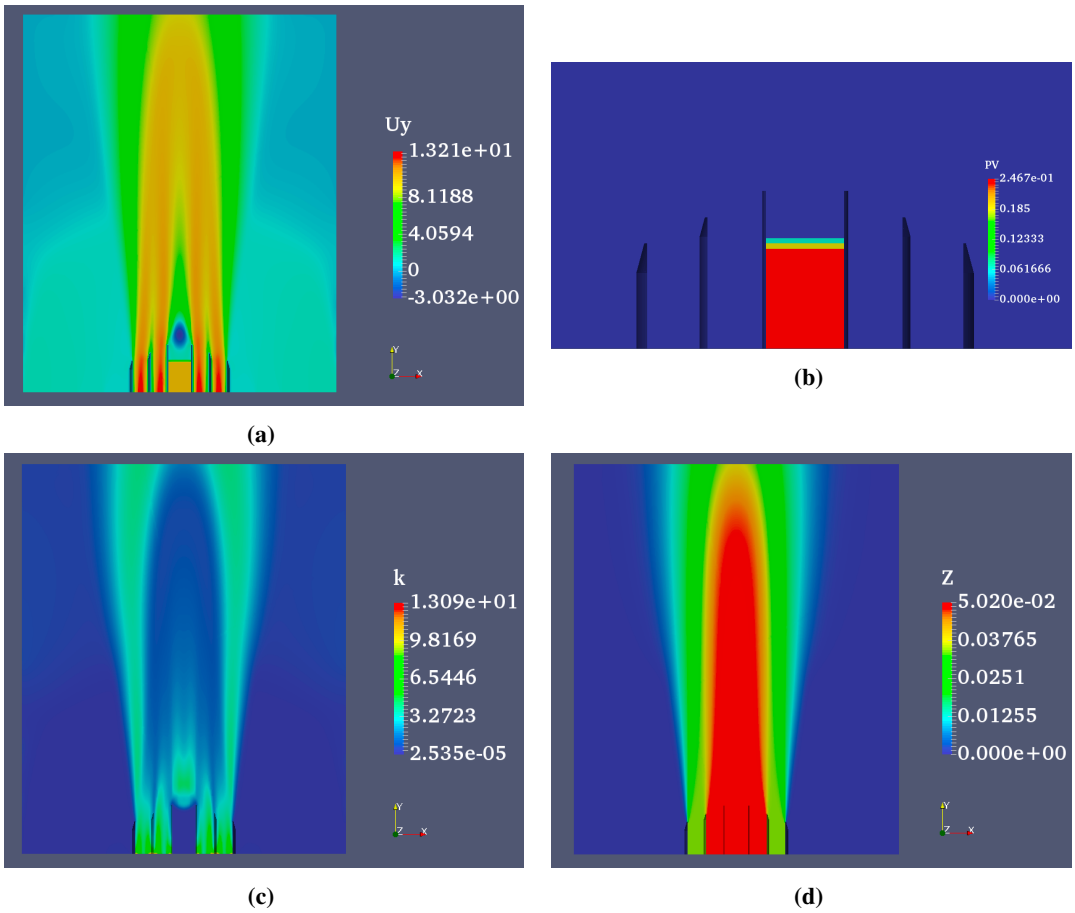

Figure 5.14: *Fields initialization of reacting 3D RANS simulations with no flame thickening, shown on sectional views of the 3D mesh domain. Axial velocity field (a), detail of the non normalized progress variable distribution inside the* Pilot *tube (b), turbulent kinetic energy (c) and mixture fraction (d) fields values.*

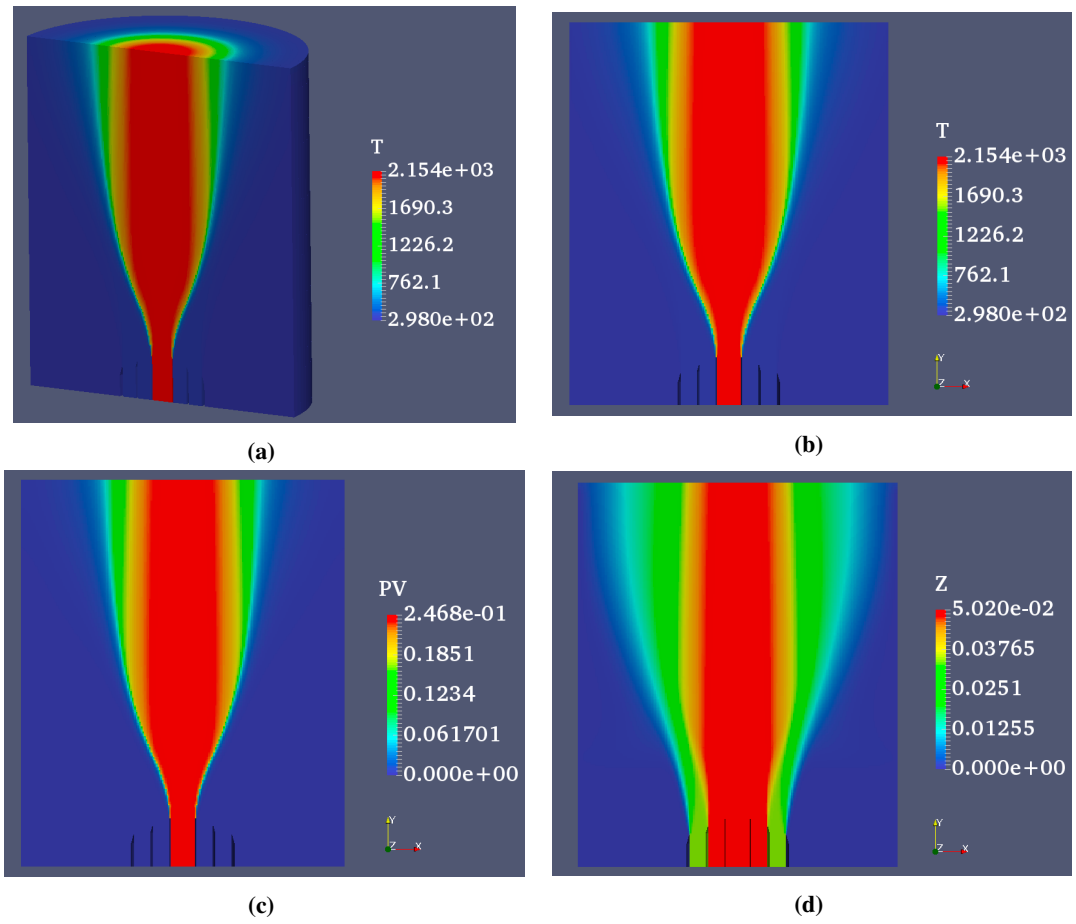

Figure 5.15: *Resulting field of reacting 3D RANS simulations with no flame thickening, shown on sectional views of the 3D mesh domain. Temperature distribution from angular (a) and side (b) views, non normalized progress variable (c) and mixture fraction (d) fields values.*

Table 5.3: *Boundary conditions for LES simulations. Differences from RANS boundary conditions (Table 5.2) are highlighted with bold text. At* Slot 1 *and* 2 *inlet patches, the $\vec{U}$ values are run-time mapped from a LES cyclic-flow simulation; this ensures to include LES computed velocity fluctuations of the turbulent flow inside the two pipes, with low computational and time efforts. All other magnitudes (included Temperature) are achieved from the adopted tabulation strategy (Section 2.4), hence are imposed* zeroGradient *everywhere.*

Boundary	$\vec{U}$	k	Y_c (or PV)	P	Z
Inlet *Pilot*	fixedValue	zeroGradient	fixedValue	zeroGradient	fixedValue
Inlet *Slot 1*	***mapped* (*run-time*)**	**zeroGradient**	fixedValue	zeroGradient	fixedValue
Inlet *Slot 2*	***mapped* (*run-time*)**	**zeroGradient**	fixedValue	zeroGradient	fixedValue
Inlet *Co-flow*	fixedValue	**zeroGradient**	fixedValue	zeroGradient	fixedValue
Outlet	**pressureInlet-OutletVelocity**	zeroGradient	zeroGradient	**totalPressure**	zeroGradient
Walls	fixedValue	**zeroGradient**	zeroGradient	zeroGradient	zeroGradient
Co-flow	slip	zeroGradient	zeroGradient	zeroGradient	zeroGradient

5.2.2 Flame Sensor choice

The last investigation, necessary for a full application of the ATFM, concerned the flame sensor choice. As described in Section 2.4.1, different flame sensor types are available:

- the *Box sensor* (2.37),
- the *Gaussian sensor* (2.38),
- the *Progress Variable Gradient Based sensor* (2.39),
- the *Flame sensor based on Progress Variable Gradient and Source Term* (2.40).

However, as it will be demonstrated hereafter, the application of last described sensor (2.40) for the flame detection represents the best solution between the aforementioned possibilities.

3D reacting simulation with LES approach and no thickening of the flame The realization of a 3D reacting simulation with no flame thickening but with a LES approach for turbulence description is a sort of bridge between the RANS investigation performed in Section 5.2.1 and the achievement of useful initial conditions for both the flame sensor choice and next ATFM assessment.

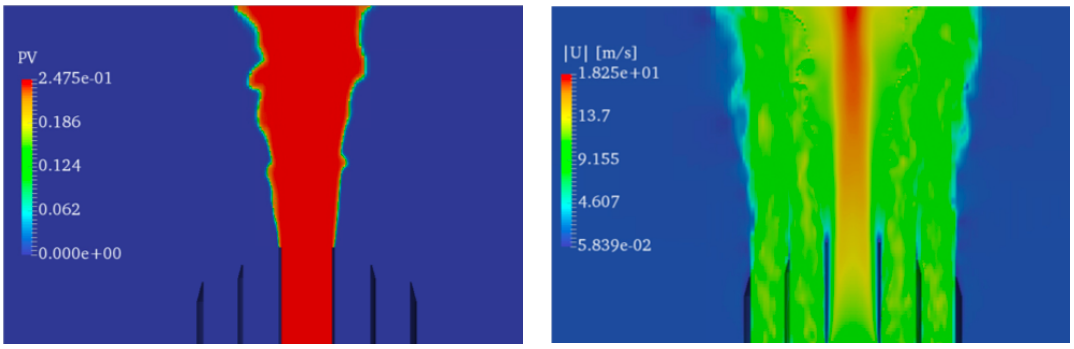

(a) **(b)**

Figure 5.16: *Instantaneous resulting field of reacting 3D LES simulations with no flame thickening, shown on sectional views of the* M0 *mesh (Figure 5.7a). Non normalized progress variable (a) and velocity magnitude (b) fields distributions.*

Therefore, RANS reacting results shown in Figure 5.15 were mapped on meshes *M0* and *M2* (Figure 5.7) and used as initial conditions for volume fields distributions. Indeed, LES simulations with no thickening of the flame were performed on both meshes that will be used during the flame sensor investigation and the ATFM assessment.

For what concerns boundaries, Table 5.3 specifies the adopted conditions, where differences from RANS ones are highlighted with bold text (compare with Table 5.2). It is worth to notice that at Slot 1 and 2 inlet patches, the $\vec{U}$ values are run-time mapped from a LES cyclic-flow simulation; this ensures to include LES computed velocity fluctuations of the turbulent flow inside the two pipes, with low computational and time efforts. All other magnitudes (included Temperature T) that are not specified in Table 5.3 were computed from the adopted tabulation strategy (Section 2.4), hence imposed *zeroGradient* at each boundary.

Figure 5.16 shows non normalized progress variable and velocity magnitude fields distributions on *M0* mesh, at a time instant, computed from a 3D reacting LES simulation with no thickening of the flame. As it can be observed, the interaction between largest turbulent structures and the flame front is computed and seems fully developed. This will be helpful to start next thickened flame simulations with a reduced transient time elapsing between initial time-averaged fields (as RANS ones) and typical unsteady LES ones, in which part of the *flame-turbulence* interactions are explicitly computed.

3D comparison between *Box* and *Gaussian* sensors: the "cascade" thickening effect The first step of the flame sensor choice investigation was focused to understand the differences between two sensor formulations, characterized by different concepts:

1. The *Box sensor*, which limits the ATF concept at the reaction zone without any flame structure deformation. In fact, the flame sensor value Ω is equal to 1 inside the flame and 0 outside (see (2.37)).

2. The *Gaussian sensor*, instead, computes the Ω value with a Gaussian shape determined as function of the normalized progress variable c distribution (see (2.38)). For this reason, the flame structure will be slightly deformed.

Therefore, 3D LES numerical simulations where performed on the *M0* mesh by applying the ATFM with two aforementioned flame sensors. As initial conditions, the results of 3D reacting LES simulation with no thickening of the flame (Figure 5.16) were imposed, and the boundary conditions specified in Table 5.3 were used.

A comparison between Box and Gaussian sensors applied with a flame thickened over only 1 cell (1CT) is shown in Figure 5.17. The most impressive result concerns the flame front over-thickening experienced when the Box sensor is used (Figures 5.17a and 5.17c), while if Gaussian sensor is applied the flame seems thickened as expected.

The phenomenon observed in Figures 5.17a and 5.17c can be defined as *"cascade" thickening effect* and it can be explained as follows. When the LES simulation including the flame thickening starts, an initial transition from un-thickened to thickened flame conditions is encountered. At the beginning, F value is applied with no modifications only on cells where the un-thickened flame is present. However, as the flame starts to increase its layer, new cells are covered by the Box sensor; hence, new cells start to be affected by the imposed original F value, with a cascade-effect in the flame thickening procedure. The major consequence is an uncontrolled flame thickness increase.

On the other hand, by using a Gaussian sensor (Figures 5.17b and 5.17d) it seems that the uncontrolled flame thickening is numerically avoided thanks to Ω Gaussian shape of (2.38). Indeed, by comparing Figures 5.18a and 5.18b, where a flame is thickened over 1 and 3 cells, respectively:

- the central region of the flame is extended over the desired cell number with an Ω

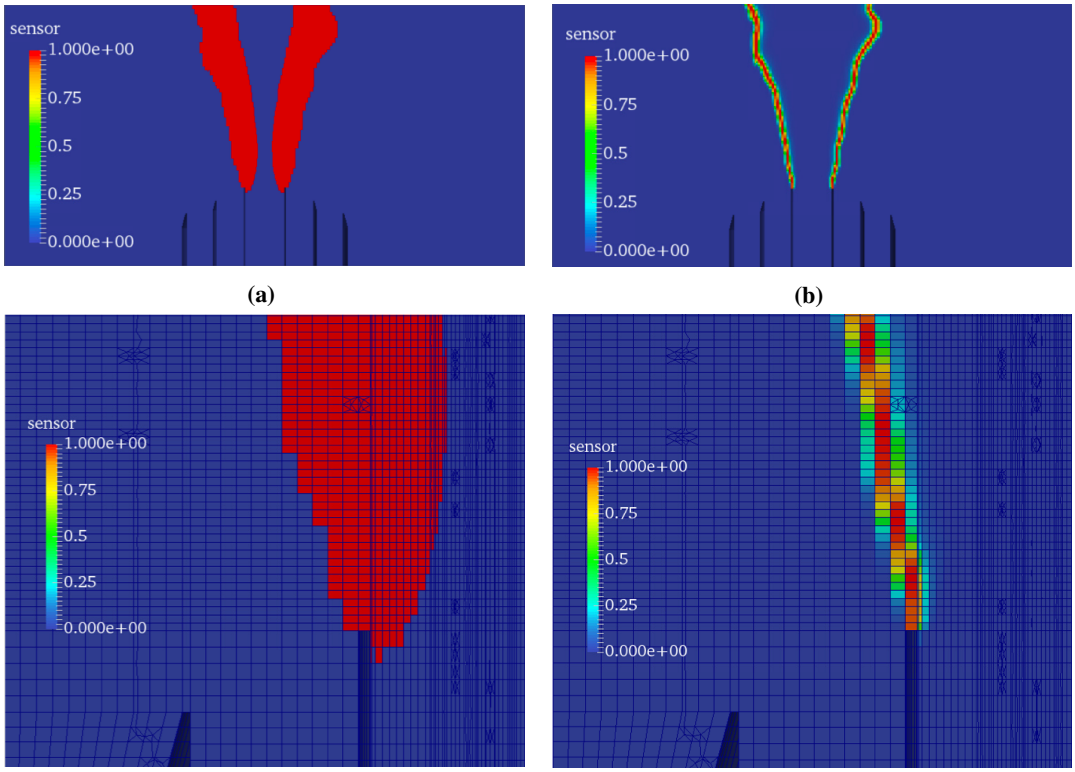

Figure 5.17: *Flame sensor value distributions of reacting 3D LES simulations with 1 cell (1CT) flame thickening, achieved by using: the* Box sensor *(a) and the* Gaussian sensor *(b) (zoomed images of these two sensors are shown, nearby the* Pilot *tube exit wall, in (c) and (d), respectively).*

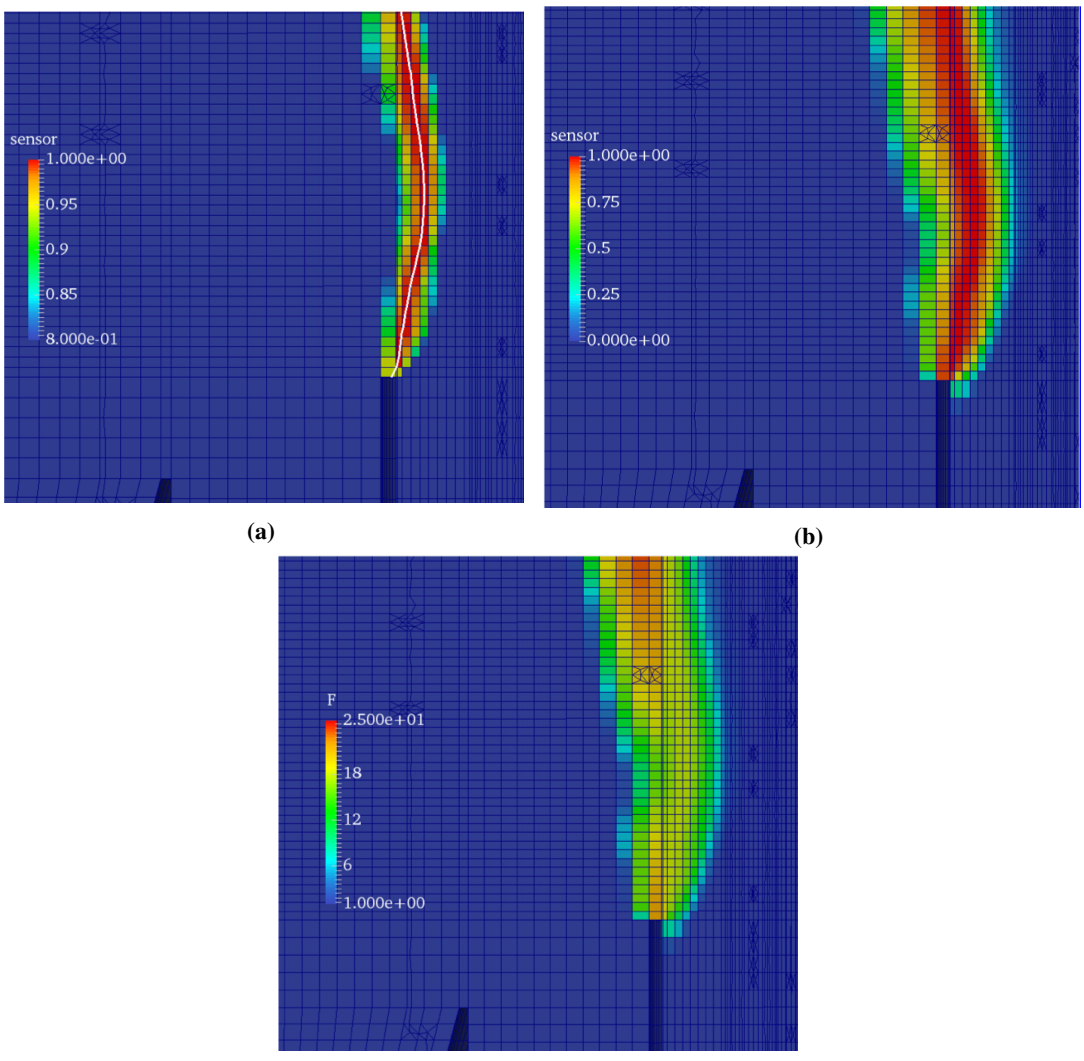

Figure 5.18: *Flame sensor value distributions, nearby the* Pilot *tube exit wall, of reacting 3D LES simulations achieved by using the* Gaussian sensor *with: 1 cell (1CT) (a) and 3 cells (3CT) (b) flame thickening. Image (c) shows the thickening factor F value smoothing in presence of a* Gaussian sensor *combined to a 3CT flame thickening. The white line of image (a) represents the normalized progress variable value of $c = 0.5$, namely the nearly central position of the flame front.*

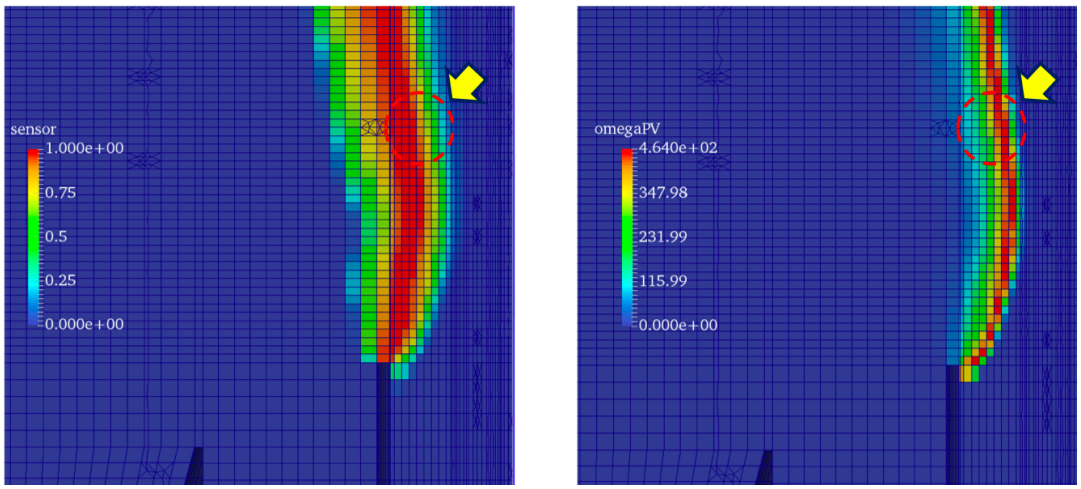

Figure 5.19: *Flame sensor (a) and progress variable reaction rate (b) fields distributions, nearby the* Pilot *tube exit wall, of reacting 3D LES simulations achieved by using the* Gaussian sensor *with 3 cells (3CT) flame thickening. Yellow arrows qualitatively highlight that, with the adopted setup, the peak of progress variable reaction rate corresponds to a non-unitary flame sensor value.*

value close to 1;

- the external boundaries of the reaction layer are deformed to numerically control the thickening procedure. In fact, F value is smoothed by the flame sensor according to (2.42), as shown by Figure 5.18c.

Consequently, it can be concluded that a flame sensor type which numerically avoids the cascade-thickening phenomenon (as the Gaussian one) allows to obtain the desired flame thickness increase, independently by the imposed F value.

However, some problems could be generated by using the Gaussian sensor type of (2.38), in particular for what concerns the correct prediction of the flame reaction rate. As shown in Figure 5.19 and highlighted by yellow arrows, in case of a flame thickened over 3 cells the peak of un-thickened progress variable reaction rate (extracted from the tabulation strategy) corresponds to a non-unitary flame sensor value. This means that the flame front deformation caused by the Gaussian sensor type could significantly affect an important flame thickness region, with a consequent error in the correct flame front speed prediction.

Therefore, an additional 1D analysis was carried out over the available flame sensor definitions to understand which is the best choice.

1D analysis for the Flame Sensor choice With the purpose to investigate the behavior of available flame sensors, a 1D analysis of a freely propagating flame with the ATF model was carried out by using Cantera, an open-source library of object-oriented software tools for problems involving chemical kinetics, thermodynamics, and transport processes.

The adopted setup can be summarized as follows:

- Methane(CH_4)/Air fresh mixture, characterized by an equivalence ratio of $\phi = 0.9$ and a unitary Lewis number.
- Two different definitions for the non normalized progress variable Y_c (or PV):
  1. $Y_c = CO_2$, which is the one commonly used for TSF burner analysis,
  2. $Y_c = CO + CO_2 + H_2 + H_2O$
- 1D domain length of $L = 100\ mm$
- A flame anchoring position of $x = 25\ mm$
- Uniform mesh grid with 501 cells.
- A reference solution for the unstretched laminar flame speed of $s_{u0} = 0.2729\, m/s$.

All 1D simulations with ATFM active were run over the $5 < F < 50$ range of values, starting from the s_{u0} reference solution. If for an F value results are missing, it means that solution did not converge.

Here are schematically reported the achieved results, with the actual thickening factor value computed according to (2.42) and investigating only flame sensor types which numerically avoid the cascade-thickening phenomenon:

1. The *Gaussian sensor* of (2.38). The resulting laminar burning velocity values, together with the relative deviations from the reference solution are, for the two Y_c definitions:

F	$Y_c = CO_2$		$Y_c = CO + CO_2 + H_2 + H_2O$	
	s_{u0} $[m/s]$	error $[\%]$	s_{u0} $[m/s]$	error $[\%]$
5	0.2736	0.25	0.2921	7.03
10	0.2728	0.04	0.2905	6.46
15	0.2731	0.06	-	-
20	0.2730	0.02	-	-
30	0.2727	0.09	-	-
50	-	-	-	-

As it can be evinced, the laminar burning velocity is preserved when $Y_c = CO_2$, also if a non-constant thickening is used through the flame front. However, if the alternative Y_c definition is applied, the agreement between s_{u0} reference solution and predicted one cannot be considered satisfactory.

Additional results are shown by Figures 5.20 and 5.21, where Y_c, F and Ω trends are reported for $Y_c = CO_2$ and $Y_c = CO + CO_2 + H_2 + H_2O$, respectively. It is worth to notice that the peak value of ω_{Y_c} (the progress variable source term) is always located into a deformed flame portion, as the flame sensor evolution demonstrates, supporting what highlighted by Figure 5.19. However, the flame front deformation caused by the Gaussian sensor provides twofold result types: a preservation of the laminar burning velocity when the non normalized progress variable is defined as $Y_c = CO_2$ and significant errors in s_{u0} prediction when $Y_c = CO + CO_2 + H_2 + H_2O$ is used. Therefore, it can be concluded that the laminar flame speed prediction provided by the Gaussian sensor is strongly dependent on Y_c definition.

2. Then the *Progress Variable Gradient Based sensor* of (2.39) was analyzed. The computed laminar burning velocity values, together with the relative deviations from the reference solution are, for the two Y_c definitions:

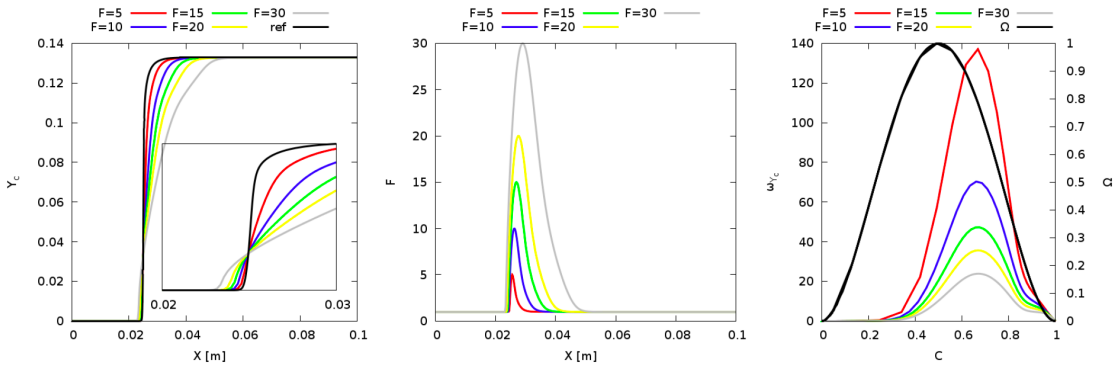

Figure 5.20: *Non normalized progress variable Y_c, thickening factor F, flame sensor Ω and source term of the progress variable ω_{Y_c} using the* Gaussian sensor *of* (2.38) *and* $Y_c = CO_2$

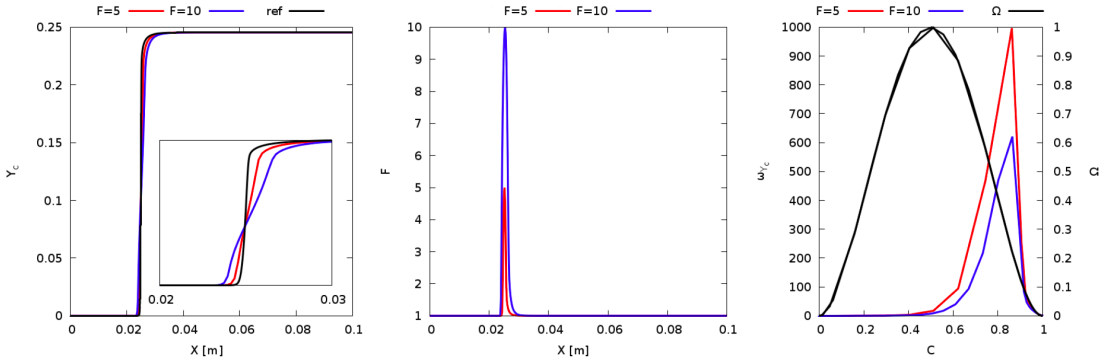

Figure 5.21: *Non normalized progress variable Y_c, thickening factor F, flame sensor Ω and source term of the progress variable ω_{Y_c} using the* Gaussian sensor *of* (2.38) *and* $Y_c = CO + CO_2 + H_2 + H_2O$

F	$Y_c = CO_2$		$Y_c = CO + CO_2 + H_2 + H_2O$	
	$s_{u0}\ [m/s]$	error $[\%]$	$s_{u0}\ [m/s]$	error $[\%]$
5	0.2871	5.21	0.2916	6.84
10	0.2805	2.78	0.2853	4.54
15	0.2779	1.83	0.2819	3.29
20	0.2764	1.30	0.2798	2.52
30	0.2749	0.73	-	-
50	0.2735	0.23	-	-

It can be observed that achieved results are less satisfactory than ones obtained with the Gaussian sensor with both progress variable definitions. On the other hand, the computed laminar flame speed values seem less dependent on Y_c choice. Further results concerning the Y_c, F and Ω trends and confirming previous obser-

vations are reported for $Y_c = CO_2$ and $Y_c = CO + CO_2 + H_2 + H_2O$ in Figures 5.22 and 5.23, respectively.

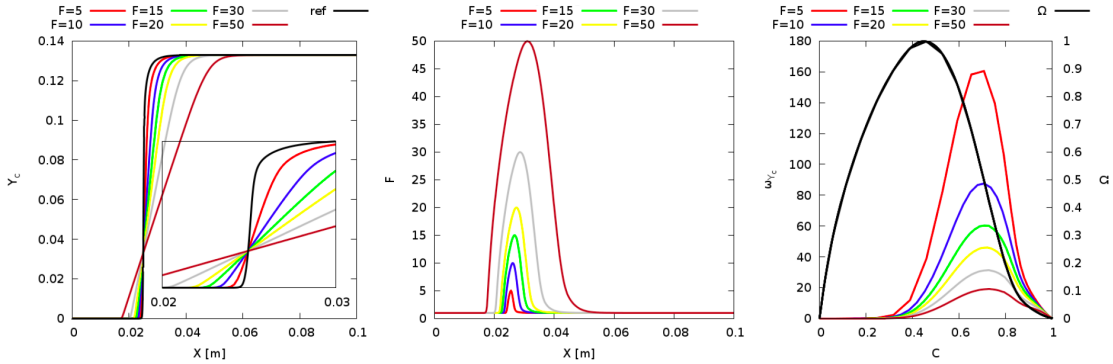

Figure 5.22: *Non normalized progress variable Y_c, thickening factor F, flame sensor Ω and source term of the progress variable ω_{Y_c} using the* Progress Variable Gradient Based sensor *of* (2.39) *and* $Y_c = CO_2$

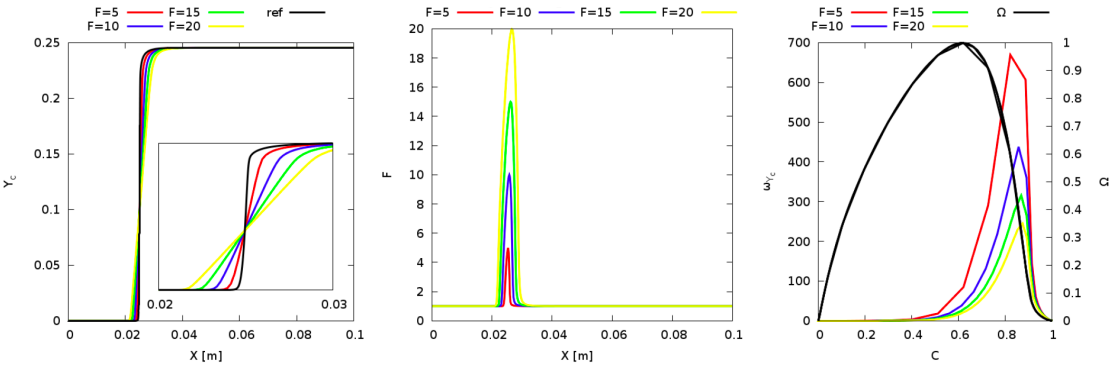

Figure 5.23: *Non normalized progress variable Y_c, thickening factor F, flame sensor Ω and source term of the progress variable ω_{Y_c} using the* Progress Variable Gradient Based sensor *of* (2.39) *and* $Y_c = CO + CO_2 + H_2 + H_2O$

3. Last investigation concerned the *Flame sensor based on Progress Variable Gradient and Source Term* of (2.40), proposed in this thesis work. For the two Y_c definitions, computed laminar burning velocity values, together with the relative deviations from the reference solution, are:

F	$Y_c = CO_2$		$Y_c = CO + CO_2 + H_2 + H_2O$	
	s_{u0} $[m/s]$	error $[\%]$	s_{u0} $[m/s]$	error $[\%]$
5	0.2791	2.29	0.2760	1.13
10	0.2751	0.81	0.2737	0.29
15	0.2739	0.36	0.2728	0.03
20	0.2733	0.13	0.2724	0.19
30	0.2726	0.10	-	-
50	0.2721	0.29	-	-

Results are rather satisfactory, with an unstretched laminar flame speed almost preserved for all tested thickening factor values and independently on the chosen progress variable definition. Figures 5.24 and 5.25 show additional results concerning the Y_c, F and Ω trends for $Y_c = CO_2$ and $Y_c = CO + CO_2 + H_2 + H_2O$ definitions, respectively. Looking at the flame sensor evolution, it is characterized by two peaks based on the maximum values of the the source term ω_{Y_c} and the gradient of the progress variable ∇Y_c. This allows a satisfactory resolution of the most important parts of the flame front (e.g.: the reaction rate peak position) by ensuring a nearly unitary flame sensor value in these regions. Instead, the flame front deformation seems to be limited on nearly negligible flame parts, in order to avoid the cascade-thickening effect. Between the two sensor peaks a local minimum is detected: however, its presence has minor impacts on the flame deformation phenomenon.

As previously mentioned in Section 2.4.1 and according to available results, the *Flame sensor based on Progress Variable Gradient and Source Term* of (2.40) was chosen as tabulated flame sensor type for the ATF model presented in this thesis work. In fact, it represents the best solution for the flame detection between the investigated possibilities because:

- Although Ω value changes rather slowly from 0 to 1 within the flame producing a slight flame front deformation, it allows to avoid the cascade-thickening effect.
- The slight flame deformation performed by (2.40) does not affect the capability to correctly predict the laminar flame velocity, also with different progress variable

definitions.

- Expression (2.40) is easy to tabulate and considers all relevant characteristics of a premixed flame, independently from the composition and progress variable definition.

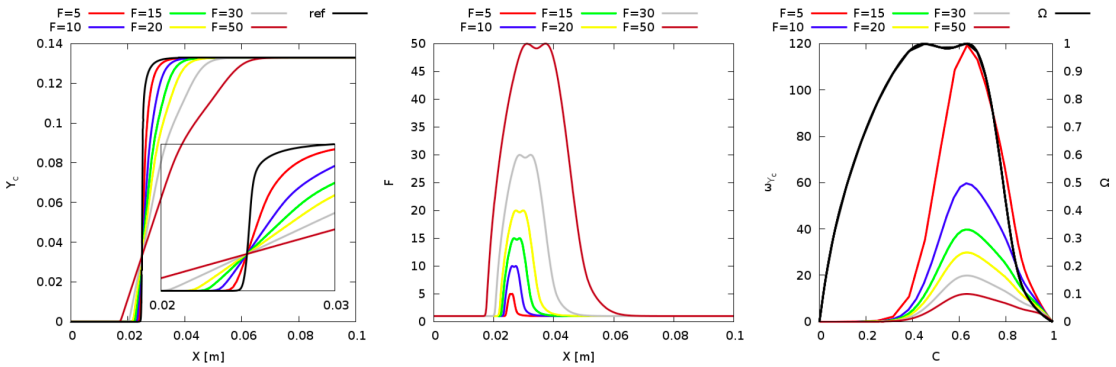

Figure 5.24: *Non normalized progress variable Y_c, thickening factor F, flame sensor Ω and source term of the progress variable ω_{Y_c} using the* Flame sensor based on Progress Variable Gradient and Source Term *of* (2.40) *and* $Y_c = CO_2$

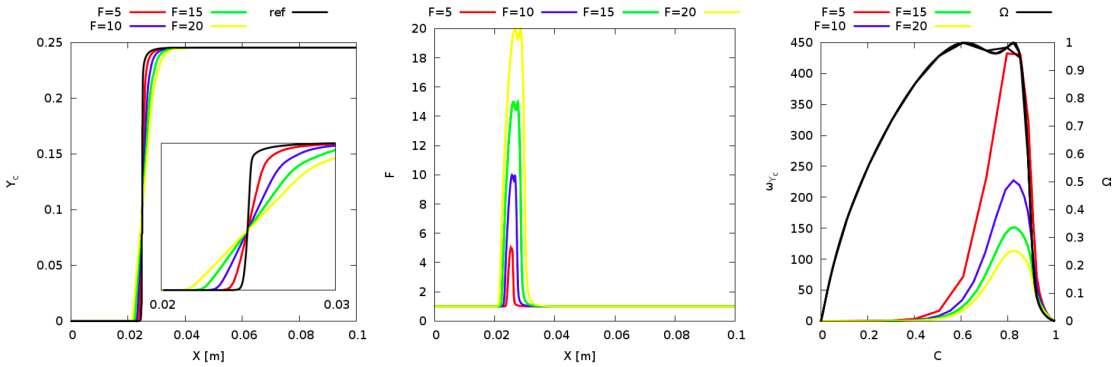

Figure 5.25: *Non normalized progress variable Y_c, thickening factor F, flame sensor Ω and source term of the progress variable ω_{Y_c} using the* Flame sensor based on Progress Variable Gradient and Source Term *of* (2.40) *and* $Y_c = CO + CO_2 + H_2 + H_2O$

5.2.3 ATFM initial assessment

Once initialized the LES 3D reacting fields with no thickening of the flame and selected the flame sensor formulation, the ATFM was ready to be fully tested on the Darmstadt TSF burner.

Before going directly to a quantitative *experimental-numerical* results comparison, the first chosen step was to assess the qualitative model behaviour in terms of:

- characteristic ATFM fields distributions (F, E and Ω) and
- evaluation of the $\vec{\nabla}\widetilde{Z}$ directional thickening.

With this purpose, a LES 3D reacting simulation, with the ATFM active, was carried out:

- on the *M0* mesh domain (Figure 5.7a);
- with a flame thickened over 10 cells (10CT);
- by defining the (tabulated) laminar flame thickness on the temperature gradient as

$$\delta_l = \frac{T_{max} - T_{min}}{(\Delta T)_{max}} \tag{5.1}$$

- starting from LES 3D reacting fields with no thickening of the flame as initial conditions (see Sections 5.2.1 and 5.2.2);
- by adopting the boundary conditions of Table 5.3.

As it can be observed by comparing Figures 5.26 and 5.5, all characteristic ATFM fields distributions follow with a reasonable accuracy the experimental flame shape detected by photographs of *A-r* condition (Table 5.1).

In particular, the grid adaptive thickening technique (Section 2.2.2) can be appreciated in Figure 5.26b, where the F value increases according to the mesh grid coarsening (compare with Figure 5.8a).

Also the efficiency function E presents a reasonable values distribution. In fact, because E changes in relation to the sub-grid scale turbulence intensity u'_Δ, hence to thickened flame thickness $\Delta = \delta_l^1$ value (see (2.60)), the efficiency function increases according to F distribution (remembering that $\Delta = F\delta_l^0 = \delta_l^1$).

For what concerns the $\vec{\nabla}\widetilde{Z}$ directional thickening, namely the approach proposed in Section 2.5.2 where the mixture fraction gradient is thickened only along the flame normal direction, a comparison was carried out with Kuenne's strategy to simply thicken the $\vec{\nabla}\widetilde{Z}$ without considering the flame orientation [67]. Figure 5.27 shows a comparison

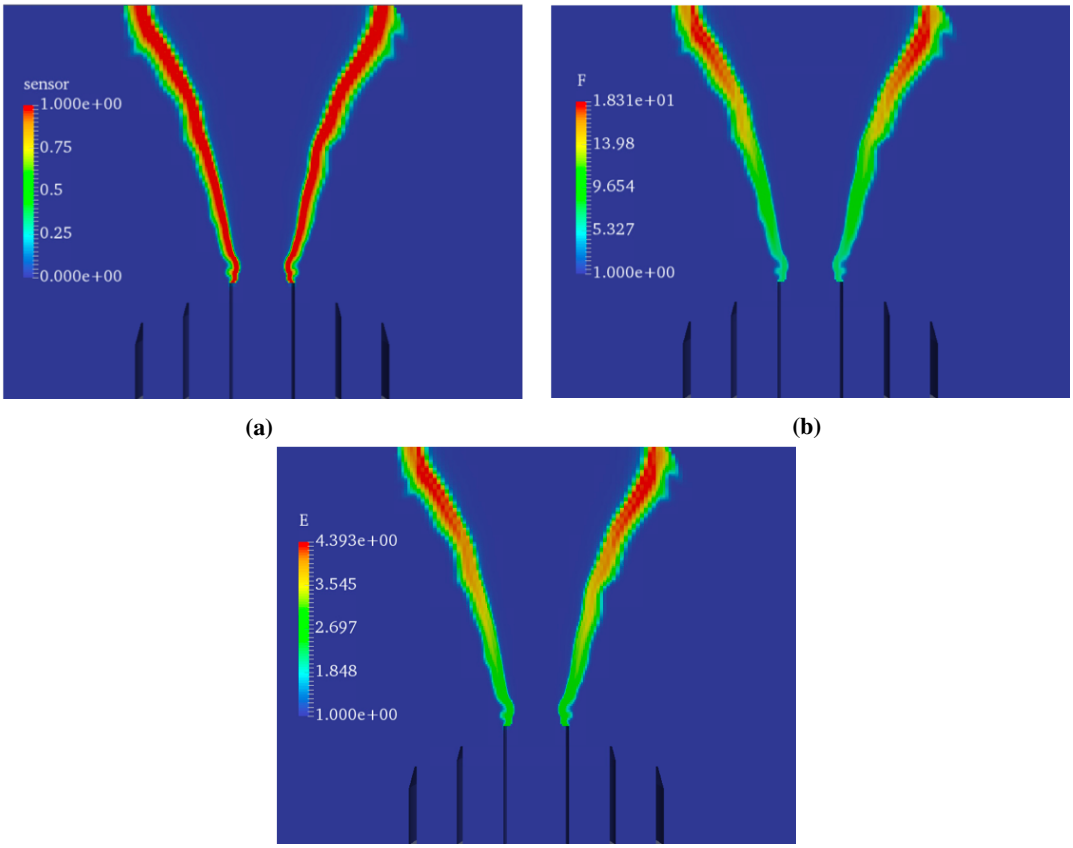

(a) **(b)**

(c)

Figure 5.26: *Characteristic ATFM fields resulting from a 3D reacting LES simulation with a flame thickened over 10 cells (10CT), shown on sectional views of* M0 *mesh (Figure 5.7a). Flame sensor based on Progress Variable Gradient and Source Term (a), thickening factor (b) and efficiency function (c) fields distributions.*

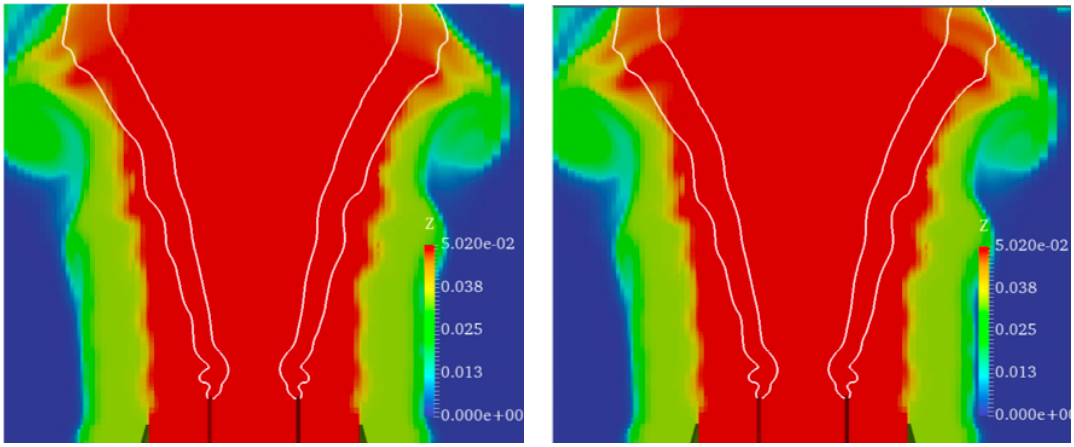

(a) **(b)**

Figure 5.27: *Mixture fraction Z fields resulting from ATFM 3D reacting LES simulations with a flame thickened over 10 cells (10CT), shown on sectional views of* M0 *mesh (Figure 5.7a). Mixture fraction gradient $\vec{\nabla}\widetilde{Z}$: thickened according to Kuenne [67] (a) and thickened only along flame normal direction, as proposed in Section 2.5.2 (b). The white lines represent the sensor threshold value of $\Omega = 0.3$, identifying the flame position.*

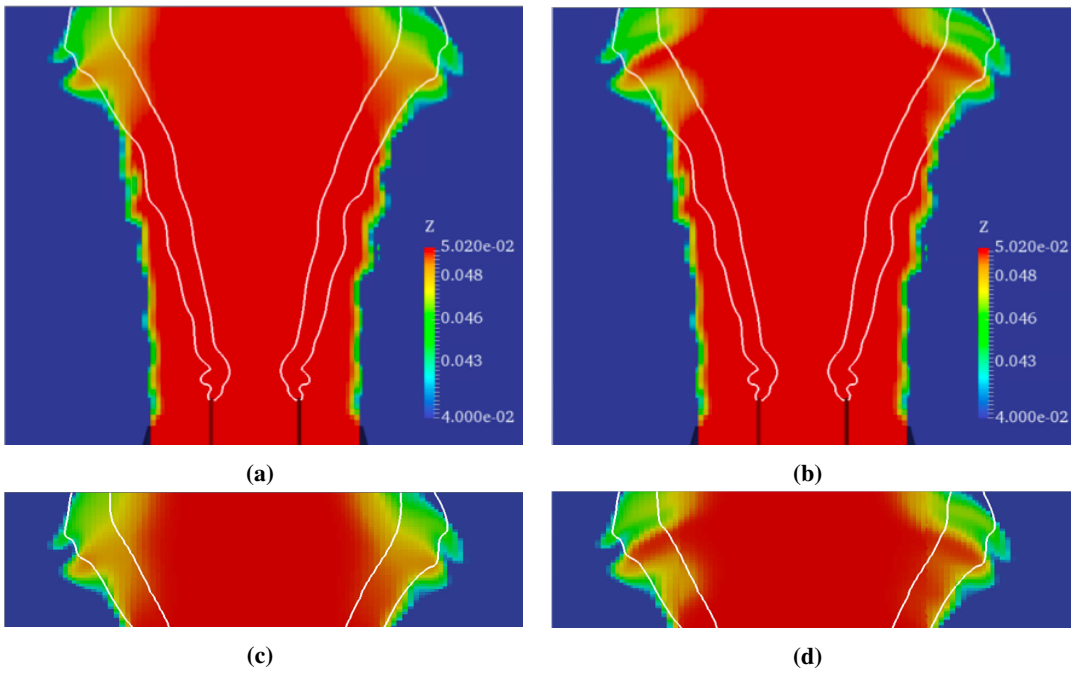

Figure 5.28: *Mixture fraction Z fields resulting from ATFM 3D reacting LES simulations with a flame thickened over 10 cells (10CT), shown on sectional views of* M0 *mesh (Figure 5.7a) and reported with a different values scale. Mixture fraction gradient $\vec{\nabla}\widetilde{Z}$: thickened according to Kuenne [67] (a) and thickened only along flame normal direction, as proposed in Section 2.5.2 (b). The white lines represent the sensor threshold value of $\Omega = 0.3$, identifying the flame position. Bottom images show in detail the mixture fraction gradient thickening performed where $\vec{\nabla}\widetilde{Z}$ overlaps the flame front: Kuenne's procedure (c) and new directional thickening along flame normal direction (b).*

between mixture fraction Z fields computed with these two $\vec{\nabla}\widetilde{Z}$ thickening strategies, while Figure 5.28 adopts a different values scale to observe in detail the mixture fraction gradient behaviour when it overlaps the flame front (here identified by white lines representing the sensor threshold value of $\Omega = 0.3$). As it can be evinced, in case of overlapping between $\vec{\nabla}\widetilde{Z}$ and $\vec{\nabla}\widetilde{Y}_c$ the directional thickening approach allows to consistently extend the ATF concept also to Z field, because along the flame tangential direction the mixture fraction field variation is not affected by the thickening procedure (Figures 5.28b and 5.28d). Conversely, if Kuenne's strategy is applied the $\vec{\nabla}\widetilde{Z}$ is thickened according to its own direction without considering the flame front orientation (Figures 5.28a and 5.28c).

5.2.4 ATFM assessment on TSF burner

The ATFM assessment was finally completed by a quantitative comparison between experimental findings collected on TSF burner and the computed numerical results.

In this context, LES 3D reacting simulations of Test *A-r* condition (Table 5.1), with the ATFM active, were carried out:

- on the *M2* mesh domain (Figure 5.7c);
- with two different thickening values, in particular:
  1. a flame thickened over 5 cells (*5CT*),
  2. a flame thickened over 10 cells (*10CT*);
- by defining the (tabulated) laminar flame thickness on the temperature gradient as (5.1);
- starting from LES 3D reacting fields with no thickening of the flame as initial conditions (see Sections 5.2.1 and 5.2.2);
- by adopting the boundary conditions of Table 5.3;
- with three different thickening solutions of the mixture fraction gradient $\vec{\nabla}\widetilde{Z}$:
  1. thickened according to its own direction, namely Kuenne's strategy [67] (*ZoldCorr*),
  2. thickened only along the flame normal direction (*Zcorr*, as proposed in Section 2.5.2),
  3. not thickened (*ZnoCorr*).

In next paragraph, first, the quantitative investigation concerned the radial distribution of the axial reacting velocity. Then, reacting scalars as temperature and mixture fraction were analyzed. Finally, some 3D results of the flame thickened over 10 cells are reported.

Reacting velocities In Figure 5.29 the experimental and numerical radial profiles of the mean axial velocity U_y are represented.

By comparing the numerical results obtained with the different thickening solutions of the mixture fraction gradient (*ZoldCorr*, *Zcorr* and *ZnoCorr*), no significant differences can be observed at all investigated conditions.

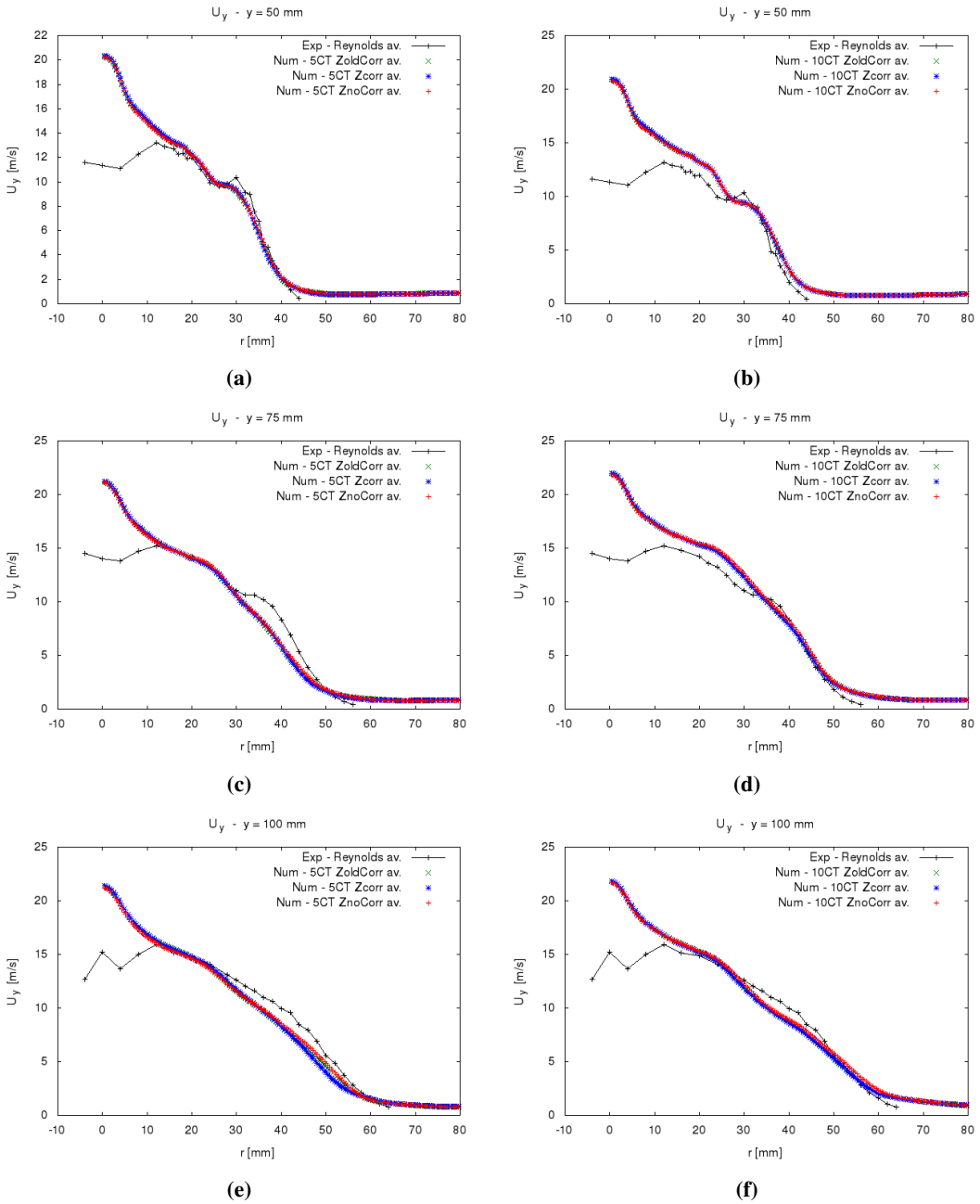

Figure 5.29: *Radial profiles of the mean axial velocity U_y. Comparison between experimental findings and numerical results at three different axial positions (see Figure 5.6): $Y = 50\ mm$ (a) and (b), $Y = 75\ mm$ (c) and (d), $Y = 100\ mm$ (e) and (f). Numerical results come from ATFM 3D reacting LES simulations with a flame thickened over 5 cells (*5CT*, left side images) and over 10 cells (*10CT*, right side images). In ATFM application, the mixture fraction gradient $\vec{\nabla}\widetilde{Z}$ is: thickened according to Kuenne [67] (*ZoldCorr*), thickened only along the flame normal direction (*Zcorr*, as proposed in Section 2.5.2) and not thickened (*ZnoCorr*).*

The lack of difference between *ZoldCorr* and *Zcorr* could be explained by a parallel alignment of scalar gradients defined by the intersection angle α of the mixing layer ($\vec{\nabla}\widetilde{Z}$) and the reaction layer ($\vec{\nabla}\widetilde{Y}_c$) (see Figure 2.6a). As observed by Kuenne [67], an increasingly parallel alignment is experienced with an axial position increase. A possible physical reason of this behaviour is related to the leaner flame observed at higher axial positions (Figure 5.5), which is characterized by a lower propagation speed; hence, the flame tends to a more parallel alignment to the convection direction, which in turn dominates the mixture fraction distribution.

On the other hand, the similarity between thickening (*ZoldCorr*, *Zcorr*) and not (*ZnoCorr*) the mixture fraction gradient, especially at high axial positions, could be explained by the Z diffusion effect. In fact, if close to the outer section of Slot 1 wall the $\vec{\nabla}\widetilde{Z}$ is significant (bottom part of Figure 5.27), at higher axial positions the Z diffusion increasingly smooth the field gradients, generating a smoother mixture fraction variation (top part of Figure 5.27). This effect will be observed also in next paragraph, where an *experimental-numerical* quantitative comparison will be performed on Z distribution. As a consequence, a lack of the mixing layer thickening could have a reduced and sometimes negligible impact on achieved results, because the overlapping between the mixing layer ($\vec{\nabla}\widetilde{Z}$) and the reaction layer ($\vec{\nabla}\widetilde{Y}_c$) can be observed only from axial positions of about $Y > 65\ mm$ (compare Figures 5.27 and 5.7a).

A comparison between experimental findings and numerical results of Figure 5.29 allows to state what follows:

- At all investigated numerical conditions, the mean axial velocity values above the Pilot region are significantly overestimated. The reason behind this result could be ascribed to computed Pilot mixture density, which is lower than experimental one due to the neglect of heat losses at Pilot walls. However, also a possible recalibration of the imposed U_y value for the Pilot burnt gases can be considered.

- An increase of the flame thickening (from left to right images of Figure 5.29) generates a flow field modification. In particular U_y values increase nearby the region where the flame is positioned.

- Close to burner exit section (Figures 5.29a and 5.29b) the experimental velocity

trend of both Slot 1 and 2 seems rather well captured. On the other hand, at higher axial positions (Figures 5.29c and 5.29d, 5.29e and 5.29f) Slot 2 velocity distribution is not perfectly matched, also if the transition from the bump structure of Figures 5.29a and 5.29b, due to the tripartite flow, to smoother conditions detected at $Y = 100\ mm$ seems predicted.

Reacting scalars Figures 5.30 and 5.31 compare the experimental and numerical radial profiles of the mean temperature and its standard deviation, respectively.

As reported by Kuenne [67], some discontinuities in the experimental measurements were unavoidable, mostly due to the fact that experimental data were stringed together from the different radial positions acquired. These lines were often not perfectly symmetric, especially in presence of high fluctuations. The discontinuities can be observed in all next Figures reported for the reacting scalar investigation. On the other hand, numerical results were, similarly, averaged not only in time but also along the circumferential direction, exploiting TSF burner symmetry.

By comparing numerical results on mean temperature (Figure 5.30) obtained with the different thickening solutions of the mixture fraction gradient (*ZoldCorr*, *Zcorr* and *ZnoCorr*), no significant differences can be observed at almost all investigated conditions. The physical explanation of this phenomenon is similar to what concluded in previous paragraph.

For what concerns the *experimental-numerical* comparison, Figure 5.30 allows to assert that:

- The experimental burnt mixture temperature close to the centerline is always lower than the computed one at the investigated axial positions. This numerical overestimation can be explained by the neglect of heat losses at Pilot walls, because adiabatic conditions were assumed during this first ATFM assessment.
- The agreement between numerical and experimental mean temperature profiles is rather satisfactory, especially with the 10 cells thickening (right images of Figure 5.30).
- At $r \approx 50\ mm$ of Figures 5.30k and 5.30l ($Y = 75\ mm$ axial plane) the experimental mean temperature profile shows a second peak that numerical simulations

are not able to detect (in this region the temperature is under predicted). This phenomenon is coupled with an increased standard deviation (see $r \approx 50\ mm$ in Figure 5.31f) and the same inability to numerically predict the experimental measurement. Kuenne [67] applied a single shot analysis of the probe volume covering this position, by using the measured data, to gain further insight into this phenomenon. The investigation revealed a non-negligible amount of events with a significant temperature increase towards higher radii and a contemporary detection of unburnt conditions closer to the centerline. Therefore, it was concluded that a large scale phenomenon is taking place, but the physical mechanism requires further experimental investigations. From the numerical point of view, the lean flammability limit choice concerning the tabulated chemistry can be a possible cause of this prediction inability, because the analyzed position is characterized by rather lean conditions (see $r \approx 50\ mm$ in Figure 5.32l). Nevertheless, further investigations are required.

The experimental temperature fluctuations, shown in Figure 5.31, are larger at higher axial positions according to the increase of the turbulent flame brush thickness (Figure 5.30), because the distribution of taken samples becomes increasingly bimodal [67]. Since the resolved fluctuations decrease with the following decreasing ratio:

$$\frac{Thickness\ of\ the\ turbulent\ flame\ brush}{Thickness\ of\ the\ flame} \tag{5.2}$$

the ATF concept generates a numerical underestimation of temperature fluctuating part. This explains the main difference between experimental findings and computed results reported in Figure 5.31. However, the experimental tendency of larger fluctuations at higher axial positions is numerically predicted.

Then, a quantity of major interest is investigated: the mean mixture fraction, which according to Barlow and Frank [6], is defined by the elemental mass fractions of carbon and hydrogen in relation to their values in pure fuel. Therefore, its maximum for this experimental configuration is $Z = 0.05$, which corresponds to $\phi = 0.9$ (the equivalence ration of Slot 1 fresh mixture for Test *A-r*, see Table 5.1). In Figure 5.32 the experimental and numerical mean Z trends are plotted.

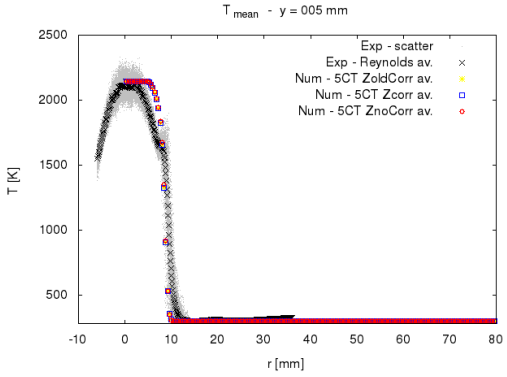
T mean - y = 005 mm
Exp - scatter
Exp - Reynolds av.
Num - 5CT ZoldCorr av.
Num - 5CT Zcorr av.
Num - 5CT ZnoCorr av.
T [K]
r [mm]

(a)

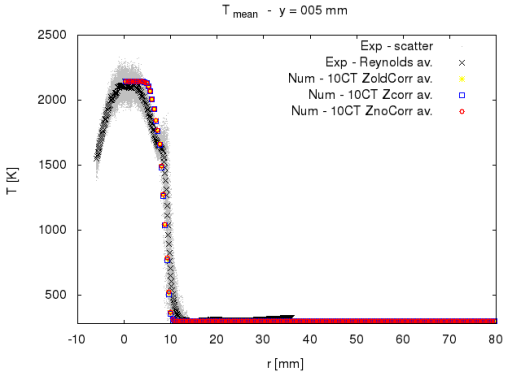
T mean - y = 005 mm
Exp - scatter
Exp - Reynolds av.
Num - 10CT ZoldCorr av.
Num - 10CT Zcorr av.
Num - 10CT ZnoCorr av.
T [K]
r [mm]

(b)

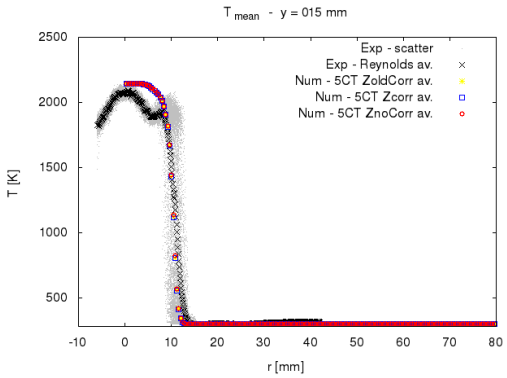
T mean - y = 015 mm
Exp - scatter
Exp - Reynolds av.
Num - 5CT ZoldCorr av.
Num - 5CT Zcorr av.
Num - 5CT ZnoCorr av.
T [K]
r [mm]

(c)

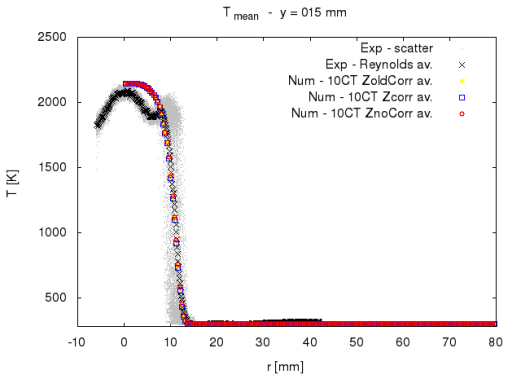
T mean - y = 015 mm
Exp - scatter
Exp - Reynolds av.
Num - 10CT ZoldCorr av.
Num - 10CT Zcorr av.
Num - 10CT ZnoCorr av.
T [K]
r [mm]

(d)

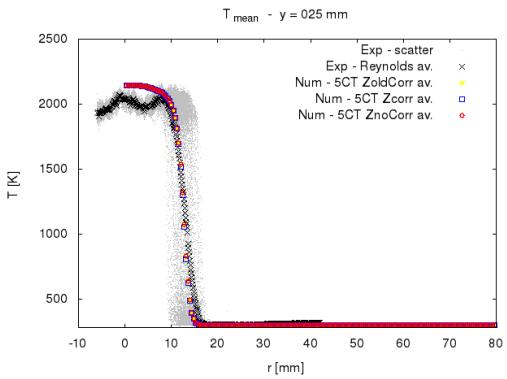
T mean - y = 025 mm
Exp - scatter
Exp - Reynolds av.
Num - 5CT ZoldCorr av.
Num - 5CT Zcorr av.
Num - 5CT ZnoCorr av.
T [K]
r [mm]

(e)

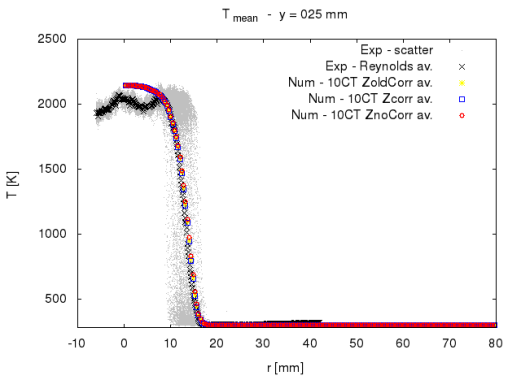
T mean - y = 025 mm
Exp - scatter
Exp - Reynolds av.
Num - 10CT ZoldCorr av.
Num - 10CT Zcorr av.
Num - 10CT ZnoCorr av.
T [K]
r [mm]

(f)

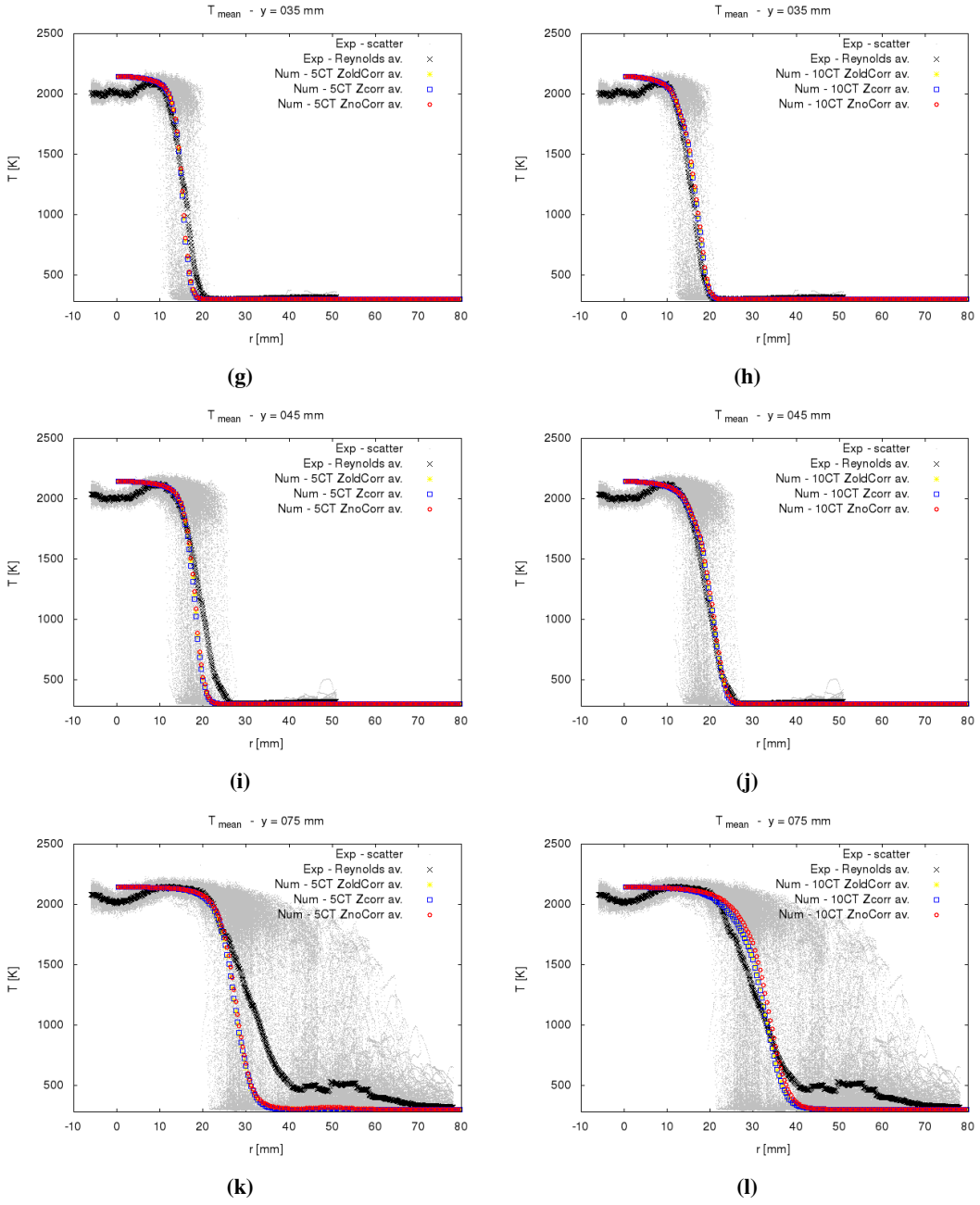

Figure 5.30: *Radial profiles of the mean temperature T_{mean}. Comparison between experimental findings and numerical results at six different axial positions (see Figure 5.6): $Y = 5$ mm (a) and (b), $Y = 15$ mm (c) and (d), $Y = 25$ mm (e) and (f), $Y = 35$ mm (g) and (h), $Y = 45$ mm (i) and (j), $Y = 75$ mm (k) and (l). Numerical results come from ATFM 3D reacting LES simulations with: a flame thickened over 5 cells (*5CT*, left side images) and over 10 cells (*10CT*, right side images). In ATFM application, the mixture fraction gradient $\vec{\nabla}\widetilde{Z}$ is: thickened according to Kuenne [67] (*ZoldCorr*), thickened only along the flame normal direction (*Zcorr*, as proposed in Section 2.5.2) and not thickened (*ZnoCorr*).*

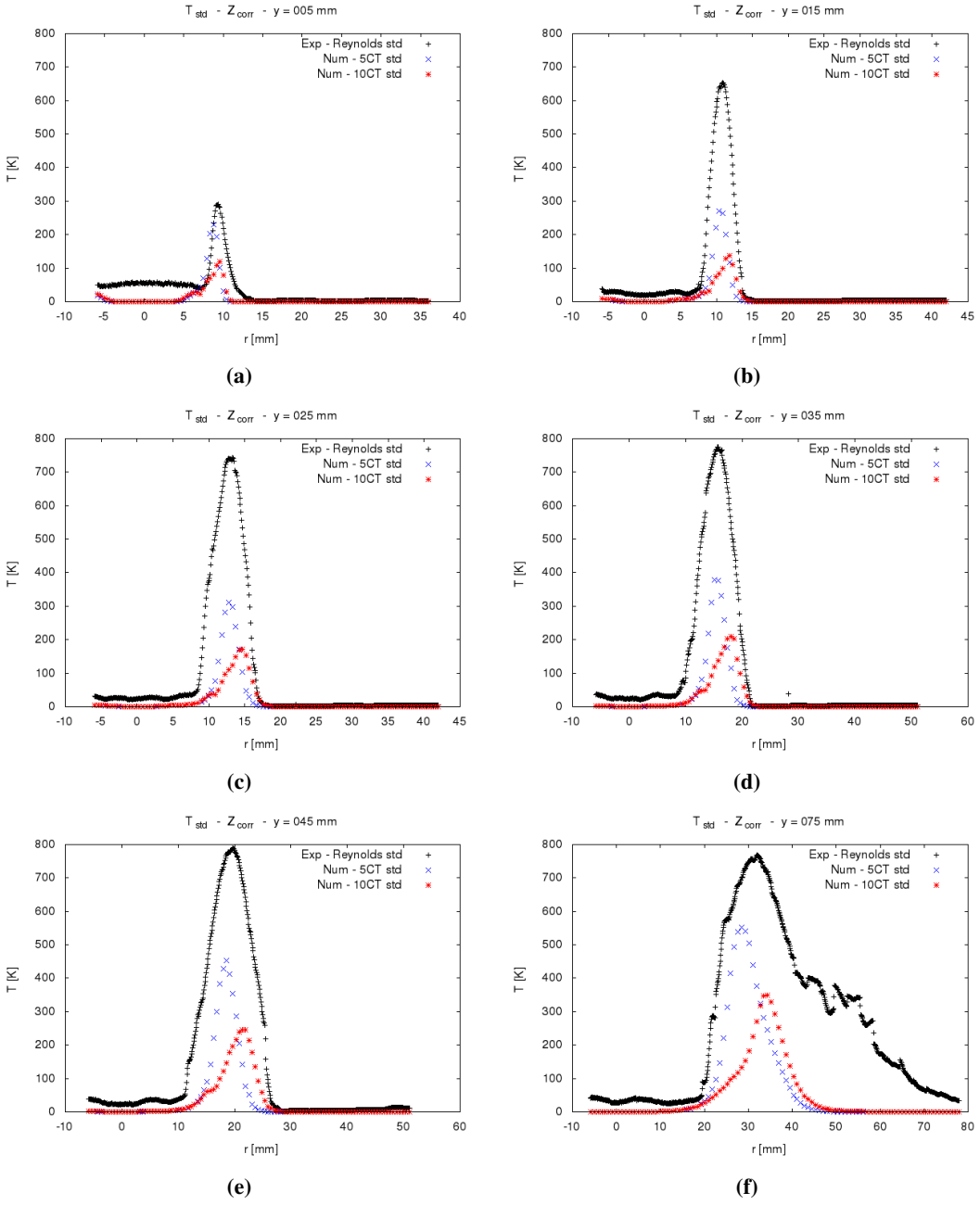

Figure 5.31: *Radial profiles of the temperature standard deviation T_{std}. Comparison between experimental findings and numerical results at six different axial positions (see Figure 5.6): $Y = 5\ mm$ (a), $Y = 15\ mm$ (b), $Y = 25\ mm$ (c), $Y = 35\ mm$ (d), $Y = 45\ mm$ (e), $Y = 75\ mm$ (f). Numerical results come from ATFM 3D reacting LES simulations with: a flame thickened over 5 cells (*5CT*) and over 10 cells (*10CT*); a mixture fraction gradient $\vec{\nabla}\widetilde{Z}$ thickened only along the flame normal direction (*Zcorr*), as proposed in Section 2.5.2.*

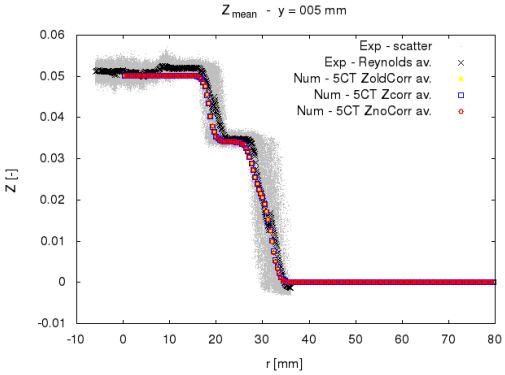
Z mean - y = 005 mm
Exp - scatter
Exp - Reynolds av.
Num - 5CT ZoldCorr av.
Num - 5CT Zcorr av.
Num - 5CT ZnoCorr av.
Z [-]
r [mm]

(a)

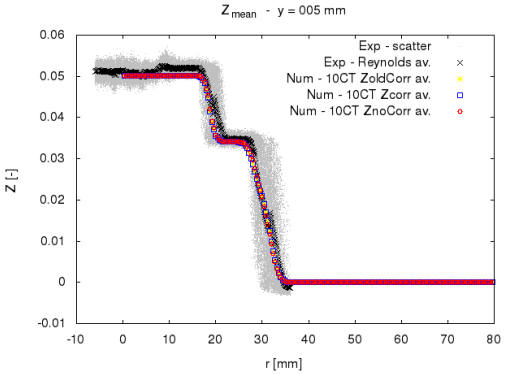
Z mean - y = 005 mm
Exp - scatter
Exp - Reynolds av.
Num - 10CT ZoldCorr av.
Num - 10CT Zcorr av.
Num - 10CT ZnoCorr av.
Z [-]
r [mm]

(b)

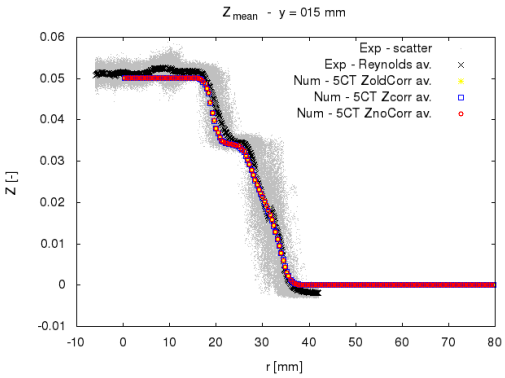
Z mean - y = 015 mm
Exp - scatter
Exp - Reynolds av.
Num - 5CT ZoldCorr av.
Num - 5CT Zcorr av.
Num - 5CT ZnoCorr av.
Z [-]
r [mm]

(c)

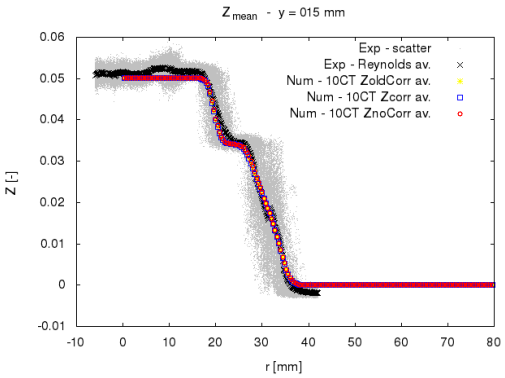
Z mean - y = 015 mm
Exp - scatter
Exp - Reynolds av.
Num - 10CT ZoldCorr av.
Num - 10CT Zcorr av.
Num - 10CT ZnoCorr av.
Z [-]
r [mm]

(d)

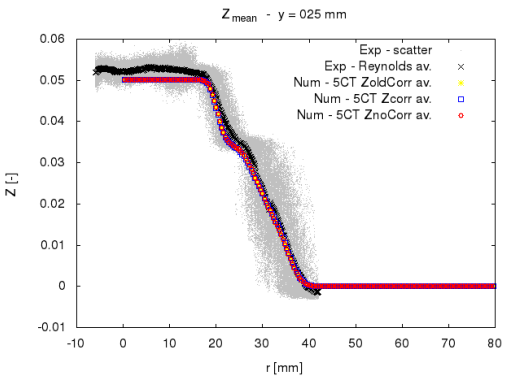
Z mean - y = 025 mm
Exp - scatter
Exp - Reynolds av.
Num - 5CT ZoldCorr av.
Num - 5CT Zcorr av.
Num - 5CT ZnoCorr av.
Z [-]
r [mm]

(e)

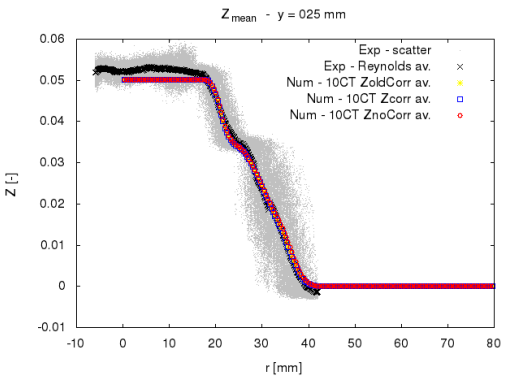
Z mean - y = 025 mm
Exp - scatter
Exp - Reynolds av.
Num - 10CT ZoldCorr av.
Num - 10CT Zcorr av.
Num - 10CT ZnoCorr av.
Z [-]
r [mm]

(f)

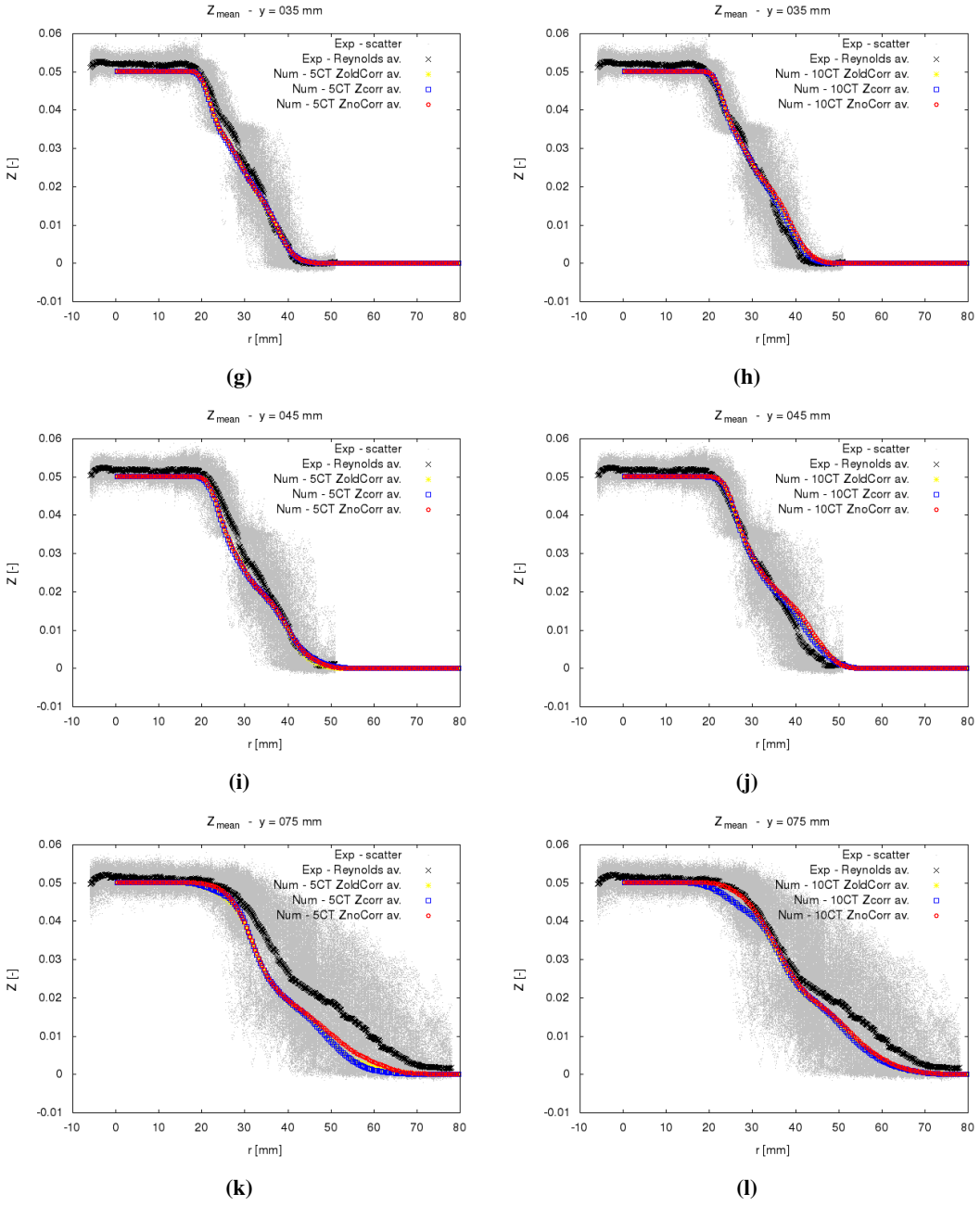

Figure 5.32: *Radial profiles of the mean mixture fraction Z_{mean}. Comparison between experimental findings and numerical results at six different axial positions (see Figure 5.6): $Y = 5\ mm$ (a) and (b), $Y = 15\ mm$ (c) and (d), $Y = 25\ mm$ (e) and (f), $Y = 35\ mm$ (g) and (h), $Y = 45\ mm$ (i) and (j), $Y = 75\ mm$ (k) and (l). Numerical results come from ATFM 3D reacting LES simulations with: a flame thickened over 5 cells (*5CT*, left side images) and over 10 cells (*10CT*, right side images). In ATFM application, the mixture fraction gradient $\vec{\nabla}\widetilde{Z}$ is: thickened according to Kuenne [67] (*ZoldCorr*), thickened only along the flame normal direction (*Zcorr*, as proposed in Section 2.5.2) and not thickened (*ZnoCorr*).*

The comparison between numerical results obtained with the different thickening solutions of the mixture fraction gradient (*ZoldCorr*, *Zcorr* and *ZnoCorr*) does not highlight significant differences at low axial positions, because the mixing layer ($\vec{\nabla}\widetilde{Z}$) and the reaction layer ($\vec{\nabla}\widetilde{Y}_c$) are not yet overlapped. Instead, when axial positions increases at $Y > 65\ mm$ values and the flame starts to experience the mixture stratification between Slot 1 and 2 (compare Figures 5.27 and 5.7a), a difference between thickening (*ZoldCorr*, *Zcorr*) and not (*ZnoCorr*) the mixture fraction gradient is appreciated. In particular, Figures 5.32k and 5.32l show how at $r \approx 25\ mm$, which corresponds approximately to the average flame centre position (see Figure 5.4), the Z gradient is smoothed only in the overlapping region. This demonstrates how the flame sensor application allow to limit the ATF concept only in the flame thickness region, without affecting pure mixing zones.

The lack of difference between *ZoldCorr* and *Zcorr* could be explained similarly to what concluded for mean axial velocity trends, namely by a parallel alignment of scalar gradients defined by the intersection angle α of the mixing layer ($\vec{\nabla}\widetilde{Z}$) and the reaction layer ($\vec{\nabla}\widetilde{Y}_c$) (see Figure 2.6a).

On the other hand, the general agreement between numerical computations and experimental measurements can be considered satisfactory. In fact, at low axial positions the sharp mixture stratifications between the two slots and from Slot 2 to the air co-flow are well detected, while the gradual smoothing of Z gradient in presence of increasing Y values is satisfactory captured.

To further support the ATFM assessment, in Appendix B also the experimental and numerical radial profiles of the mean CO_2 and CH_4 mass fractions are reported and commented.

Final results of a flame thickened over 10 cells To complete previous quantitative and detailed analysis, numerical results achieved with a 10 cells thickened flame and concerning the fields of major interest are shown on a sectional view of the adopted 3D mesh domain, namely *M2*.

In particular, the following instantaneous and time-averaged fields are reported:

- flow velocity $\vec{U}$ (Figure 5.33),

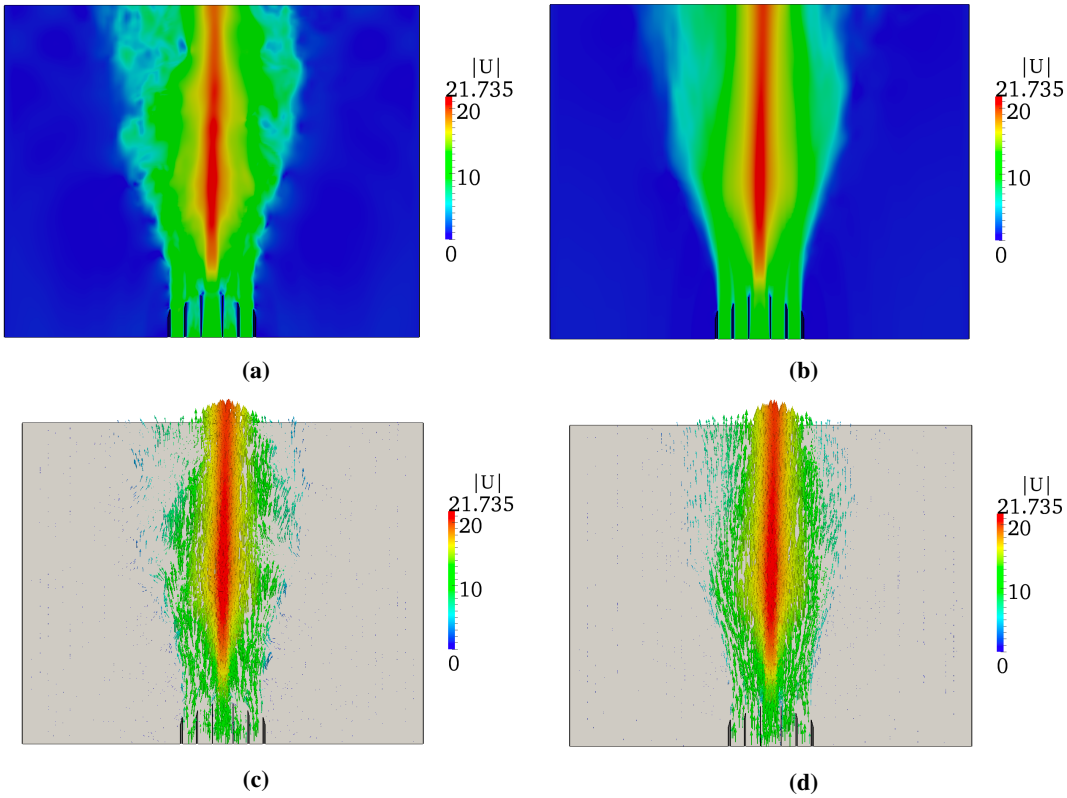

Figure 5.33: *Flow velocity field resulting from a reacting 3D LES simulation with a flame thickened over 10 cells, shown on a sectional view of the adopted 3D mesh domain, namely* M2 *(Figure 5.7c). On first row the velocity magnitude is reported at each cell position, while on the second row velocity directions are also represented. Left images (a) and (c) depict instantaneous conditions, while right ones (b) and (d) show averaged values in time.*

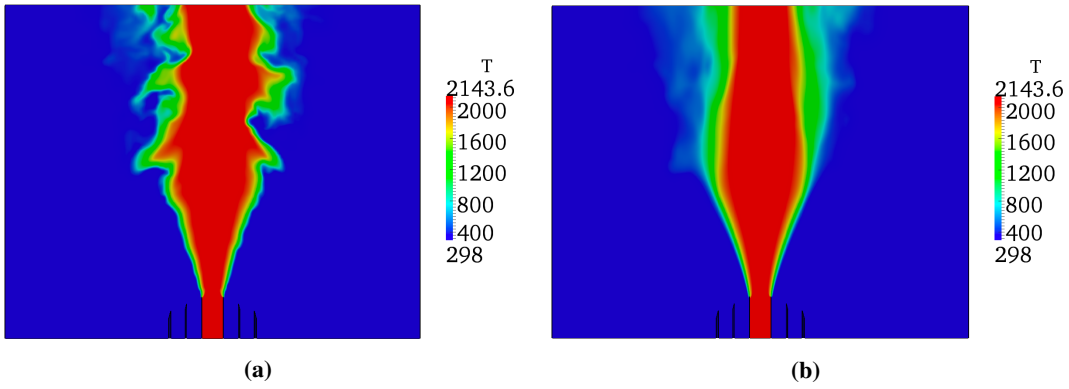

Figure 5.34: *Temperature T field resulting from a reacting 3D LES simulation with a flame thickened over 10 cells, shown on a sectional view of the adopted 3D mesh domain, namely* M2 *(Figure 5.7c): instantaneous conditions (a) and averaged values in time (b).*

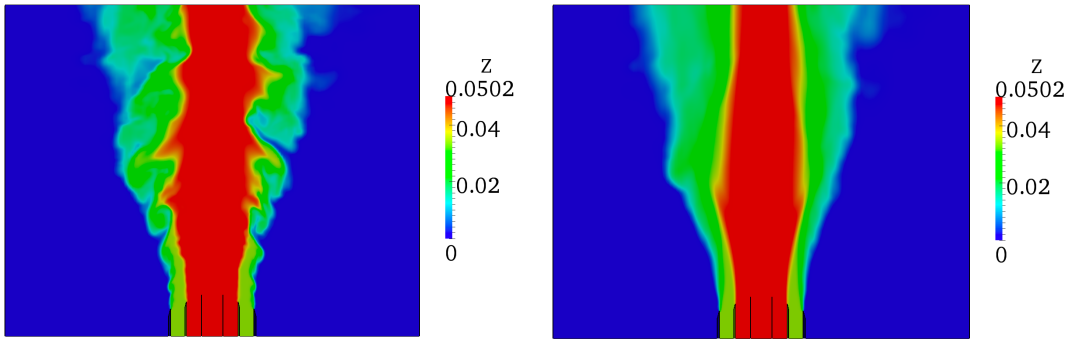

(a) **(b)**

Figure 5.35: *Mixture fraction Z field resulting from a reacting 3D LES simulation with a flame thickened over 10 cells, shown on a sectional view of the adopted 3D mesh domain, namely* M2 *(Figure 5.7c): instantaneous conditions (a) and averaged values in time (b).*

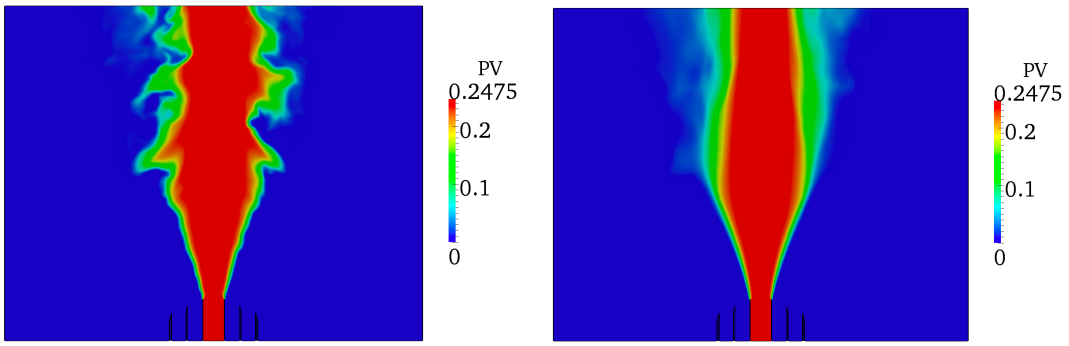

(a) **(b)**

Figure 5.36: *Non normalized progress variable Y_c (also called PV) field resulting from a reacting 3D LES simulation with a flame thickened over 10 cells, shown on a sectional view of the adopted 3D mesh domain, namely* M2 *(Figure 5.7c): instantaneous conditions (a) and averaged values in time (b).*

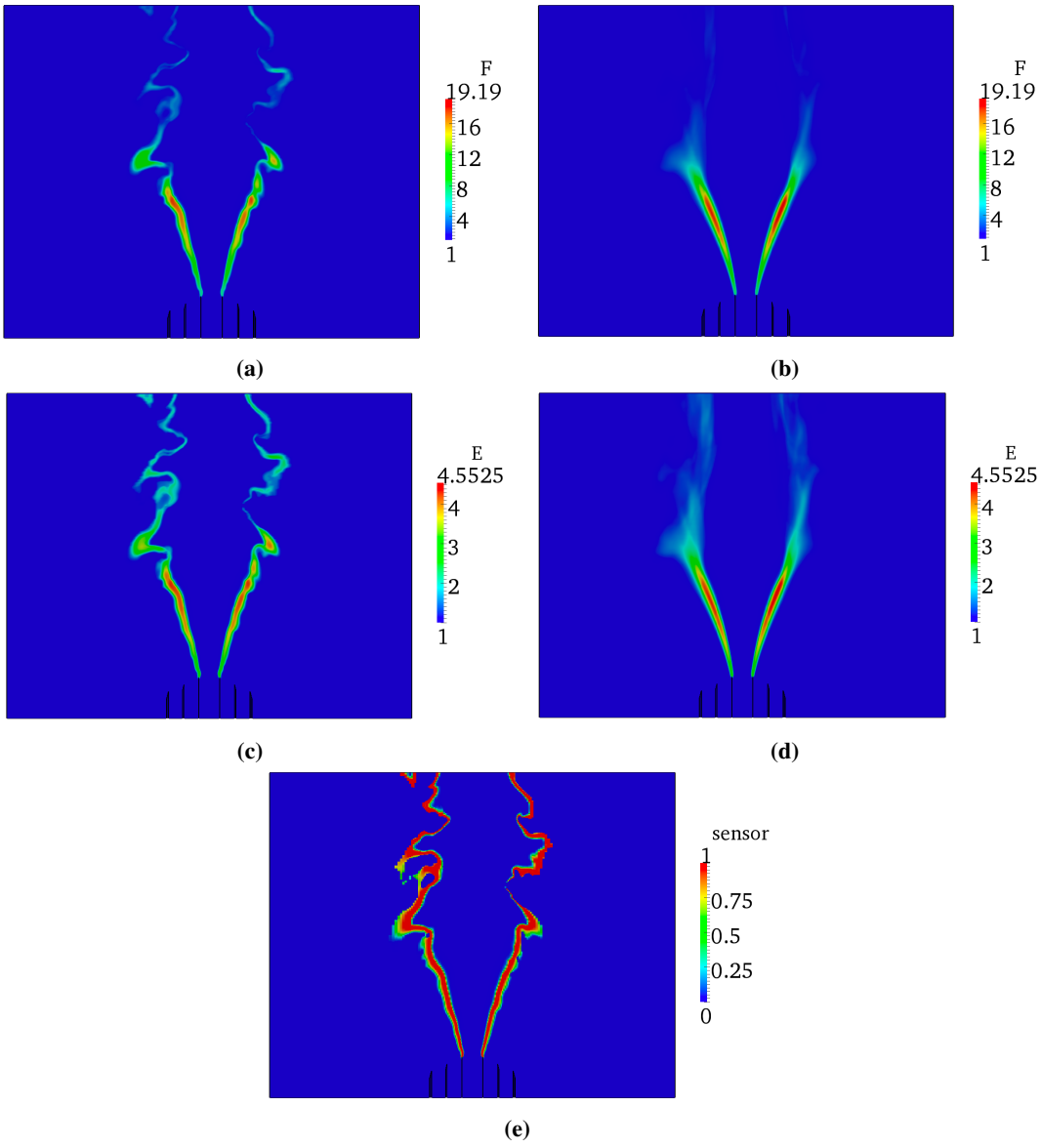

Figure 5.37: *Characteristic ATFM fields resulting from a reacting 3D LES simulation with a flame thickened over 10 cells, shown on sectional views of the adopted 3D mesh domain, namely* M2 *(Figure 5.7c): the thickening factor F (a) and (b), the efficiency function E (c) and (d), the* Flame sensor based on Progress Variable Gradient and Source Term *of* (2.40) *(e). Images (a), (c) and (e) depict instantaneous conditions, while (b) and (d) ones show averaged values in time.*

- temperature T (Figure 5.34),
- mixture fraction Z (Figure 5.35),
- non normalized progress variable Y_c (also called PV, Figure 5.36),
- thickening factor F (Figures 5.37a and 5.37b),
- efficiency function E (Figures 5.37c and 5.37d), and
- flame sensor Ω (instantaneous field only, Figure 5.37e).

It is worth to notice how the qualitative flame shape provided by the time-averaged progress variable distribution (Figure 5.36) is almost similar to photographs of the experimental Test *A-r* flame (Figure 5.5), although numerical simulation would have needed more time to fully achieve the averaged distribution at high axial values.

As already observed in Section 5.2.3, the grid adaptive thickening technique can be appreciated in Figures 5.37a and 5.37b, where the F value increases according to the mesh grid coarsening (compare with Figure 5.8c). As expected, the efficiency function E changes its value according to F distribution.

Finally, it can be noticed how in Figure 5.37e the *Flame sensor based on Progress Variable Gradient and Source Term* assumes values nearly unitary over a large portion of the flame thickness, especially in the region where reaction rate is high (flame burnt side). Then, it quickly goes to zero, minimizing the flame structure deformation.

5.3 Summary

The experimental configuration of the Darmstadt Turbulent Stratified Flame (TSF) burner was selected to assess the ATFM behaviour. The experimental rig is characterized by three concentric pipes: a central *Pilot*, whose aim is to release a flow of burnt products, and two outer concentric tubes ejecting fresh mixture, called *Slot 1* and *Slot 2*. These last two annular slots can be operated, in terms of flow rates and equivalence ratios, independently from the Pilot and from each other. Therefore, a very flexible generation of shear and global stratification is allowed along the radial direction, enabling to investigate several configurations. During this first investigation, a *lean-lean* charge stratification was analyzed and adiabatic conditions were assumed.

First, the *Flame sensor based on Progress Variable Gradient and Source Term*, proposed in Section 2.4.1, was successfully tested on a 1D flame configuration. Here are reported its observed features:

1. It allows to avoid the "cascade" thickening effect, namely an uncontrolled thickening of the flame.

2. Although it slightly deforms the flame front, the capability to predict correctly the laminar flame velocity is not affected.

3. It is easy to tabulate and considers all relevant characteristics of a premixed flame, independently from the composition and progress variable definition.

Then, a qualitative model behaviour was analyzed in terms of:

- characteristic ATFM fields distributions (F, E and Ω),

- evaluation of the $\vec{\nabla}\widetilde{Z}$ directional thickening.

As observed, all ATFM fields distributions follow with a reasonable accuracy the experimental flame shape detected by photographs of the investigated working condition. For what concerns the $\vec{\nabla}\widetilde{Z}$ directional thickening, a comparison was carried out with Kuenne's strategy to simply thicken the $\vec{\nabla}\widetilde{Z}$ without considering the flame orientation. As shown by numerical results, the directional thickening approach allows to consistently extend the ATF concept also to Z field, because along the flame tangential direction the $\vec{\nabla}\widetilde{Z}$ is not affected by the thickening procedure. Conversely, with Kuenne's strategy the mixing layer is thickened according to its own direction, as expected.

Afterwards, the ATFM assessment was finally completed by a quantitative comparison between experimental findings collected on TSF burner and the computed numerical results. Here below are listed the drawn conclusions for each investigated magnitude:

1. *Reacting axial velocity*

    - No significant differences were observed by comparing numerical results obtained with the different thickening solutions of the mixture fraction gradient,

in particular: $\vec{\nabla}\widetilde{Z}$ thickened according to its own direction (Kuenne's strategy, called *ZoldCorr*), thickened along the flame normal direction (*Zcorr*, also called directional thickening) and not thickened (*ZnoCorr*).

The lack of difference between *ZoldCorr* and *Zcorr* could be explained by a parallel alignment of scalar gradients defined by the intersection angle α of the mixing layer ($\vec{\nabla}\widetilde{Z}$) and the reaction layer ($\vec{\nabla}\widetilde{Y}_c$), as observed by Kuenne. On the other hand, the similarity between thickening (*ZoldCorr*, *Zcorr*) and not (*ZnoCorr*) the mixture fraction gradient, especially at high axial positions, could be explained by the Z diffusion effect.

- At all investigated numerical conditions, the mean axial velocity values above the Pilot region were significantly overestimated with respect to experimental findings. This could be a consequence of the adiabatic conditions adopted during this first ATFM assessment. However, also a possible recalibration of the imposed axial velocity value for the Pilot burnt gases can be considered.
- An increase of the flame thickening generates a flow field modification. In particular, the axial velocity values increase nearby the region where the flame is positioned.
- Close to burner exit section the experimental velocity trend seemed rather well captured. On the other hand, at higher axial positions the velocity distribution was not perfectly matched, also if the transition from the initial bump structure (due to the tripartite flow) to smoother conditions detected downstream seemed predicted.

2. *Reacting temperature*

- No significant differences were observed by comparing numerical results obtained with the different thickening solutions of the mixture fraction gradient (*ZoldCorr*, *Zcorr* and *ZnoCorr*). The physical explanation of this phenomenon is similar to what concluded for the reacting axial velocity.
- The experimental burnt mixture temperature close to the centerline is always lower than computed one at the investigated axial positions. This numerical

overestimation can be explained by the neglect of heat losses at Pilot walls, because adiabatic conditions were assumed.

- The agreement between numerical and experimental mean temperature profiles was rather satisfactory, especially with the 10 cells thickening.
- At high radial and axial positions, the experimental mean temperature profile shows a second peak that numerical simulations were not able to detect (in this region the temperature is under predicted). This phenomenon is coupled with an increased standard deviation and the same inability to numerically predict the experimental measurement. Form a previous work (Kuenne), it was concluded that a large scale phenomenon is taking place, but the physical mechanism requires further experimental investigations. From the numerical point of view, the lean flammability limit choice concerning the tabulated chemistry could be a possible cause of this prediction inability, because the analyzed position is characterized by rather lean conditions.
- Since the resolved fluctuations decrease with the decreasing ratio *turbulent flame brush thickness/flame thickness*, the ATF concept generates a numerical underestimation of temperature fluctuating part. This explains the main difference observed between experimental findings and computed results. However, the experimental tendency of larger fluctuations at higher axial positions was numerically predicted.

3. *Reacting mixture fraction*

- The comparison between numerical results obtained with the different thickening solutions of the mixture fraction gradient (*ZoldCorr*, *Zcorr* and *ZnoCorr*) did not highlighted significant differences at low axial positions, because in this region the mixing layer ($\vec{\nabla}\widetilde{Z}$) and the reaction layer ($\vec{\nabla}\widetilde{Y}_c$) are not yet overlapped.
- Instead, when at higher axial positions the flame starts to experience the mixture stratification, a difference between thickening (*ZoldCorr*, *Zcorr*) and not (*ZnoCorr*) the mixture fraction gradient is appreciated. In particular, the Z gradient is smoothed only in the overlapping region. This demonstrates how

the flame sensor application allow to limit the ATF concept only in the flame thickness region, without affecting pure mixing zones.

- The lack of difference between *ZoldCorr* and *Zcorr* could be explained similarly to what concluded for mean reacting axial velocity trends.
- Finally, the general agreement between numerical computations and experimental measurements could be considered satisfactory.

Part

First steps towards additional validations

CHAPTER 6

The Darmstadt Turbulent Stratified Flame burner: heat losses analysis

The importance of considering heat-losses at Pilot tube exit, where fully burnt products are in contact with the pipe, was assessed in [42] by comparing simulations with adiabatic and isothermal boundary conditions at the Pilot walls. In fact, under adiabatic assumptions a flame anchored to burner lip was predicted, while non-adiabatic simulations evidenced a flame lift-off of one-half Pilot diameter and a better agreement with experimental findings of temperature and species concentrations. This was confirmed also by Kuenne in [65].

Therefore, as a first step towards non-adiabatic investigations of the TSF burner with the ATFM of Chapter 2, *Conjugated Heat Transfer* (CHT) simulations were carried out in the aforementioned heat-losses region. Purpose of this analysis is to get more insight on the heat transfer phenomenon happening at Pilot walls and to estimate suitable boundary conditions for future non-adiabatic simulations.

6.1 Experimental measurements and numerical setup

The considered configuration for the heat transfer analysis is the *TSF-A-r* flame [99], for which detailed temperature measurements of the Pilot wall inner and outer surfaces are available, [65].

In particular, as described by Kuenne in [65], the *phosphor thermometry* technique was used to measure the surface temperature of both Pilot wall sides, according to the experimental setup shown in Figure 6.1a. Phosphor thermometry is an optical semi-invasive temperature measurement technique, which is robust against chemiluminescence and can be used for spatially resolved measurements, [21].

In this experimental campaign, a dispersion of $Mg_4GeO_6F : Mn$ and binder SP-115 was applied with an airbrush to the Pilot tube surface, which is made of ceramic. This coating was exited by a $10\ Hz$ pulsed *Nd:YAG* laser and the temperature dependent luminescence was recorder by an high speed CMOS camera, whose image size was 64×64 pixels. A number of 200 loops, with 200 images each one, was recorded with a repetition rate of 360 kHz. The evaluation of luminescence lifetime was carried out by using:

- an iterative fitting algorithm [20],
- a linear regression of the sum method [46]

after the non-linearity correction [112]. Finally, a calibration measurement allowed to convert the luminescence lifetime to a temperature, as described by Kissel [62].

The obtained temperature map shows a shot-to-shot standard deviation below $2\ K$ in most of the investigated area. A slight radial asymmetric distribution is also present because, during the measurements, a not perfect flame holder centering with respect to the ceramic Pilot tube was experienced. Hence, the mean temperature profiles along burner axial direction were computed taking into account the aforementioned asymmetry; the results for both inner (Pilot side) and outer (Slot 1 side) surfaces of Pilot wall are reported in Figure 6.1b. For further details, please refer to [65].

To get more insight on the heat transfer phenomenon identified at the Pilot tube exit, where fully burnt products completely fill the central pipe and are in contact with the surrounding ceramic wall, CHT numerical simulations were performed.

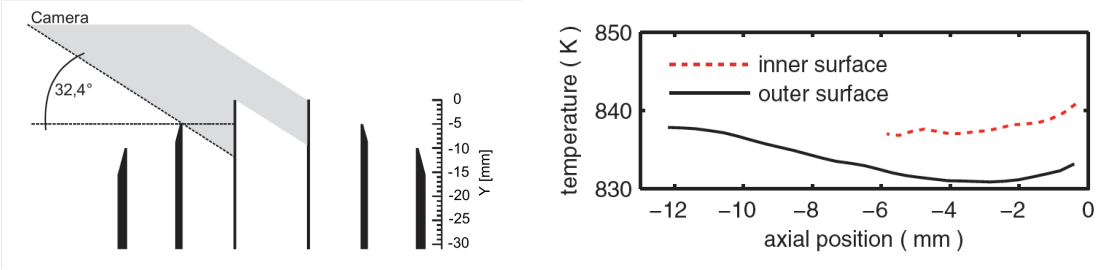

(a) **(b)**

Figure 6.1: *Exit of the Darmstadt TSF burner with the lines of sight of the temperature detection system (a). Axial temperature profiles of both inner and outer ceramic surface of the Pilot tube (b), where $Y = 0\ mm$ corresponds to the Pilot exit section, [65].*

The CHT approach was selected in order to simulate the *fluid-solid-fluid* heat exchange happening between *burnt products-ceramic wall-fresh mixture* in the final part of the burner geometry. This technique allows the prediction of heat transfer between solid and fluid domains by exchanging thermal energy at the interfaces between them. As a consequence, it requires a multi-region mesh to have a clear definition of the interfaces in the computational domain.

For the investigation of this axis-symmetrical heat transfer problem, a 2D RANS approach was used in order to achieve numerical results comparable to mean experimental findings reported in Figure 6.1b. Three separated meshes, each one characterized by homogeneous properties, were used for:

- Pilot burnt products,
- ceramic pipe wall,
- Slot 1 fresh mixture,

respectively. The interested region by CHT simulations is highlighted in Figure 6.2 and the consequent global computational domain (achieved by the summation of aforementioned separated meshes) is shown in Figure 6.3. In fact, after the mixture ignition nearby the flame holder, the flame front stabilizes its shape according to Figure 6.2. Hence, the region which is significantly affected by heat-losses starts from the flame attachment point to Pilot wall, where a suitable *flame brush* is generated [1], and finishes at the central pipe exit section.

[1] Because the wall adiabatic conditions are removed, when the Pilot pipe is approached by the flame front this starts to be affected by heat losses. As a direct consequence, a flame brush is generated at the flame attachment point because the adiabatic flame temperature value cannot be reached at the ceramic wall position.

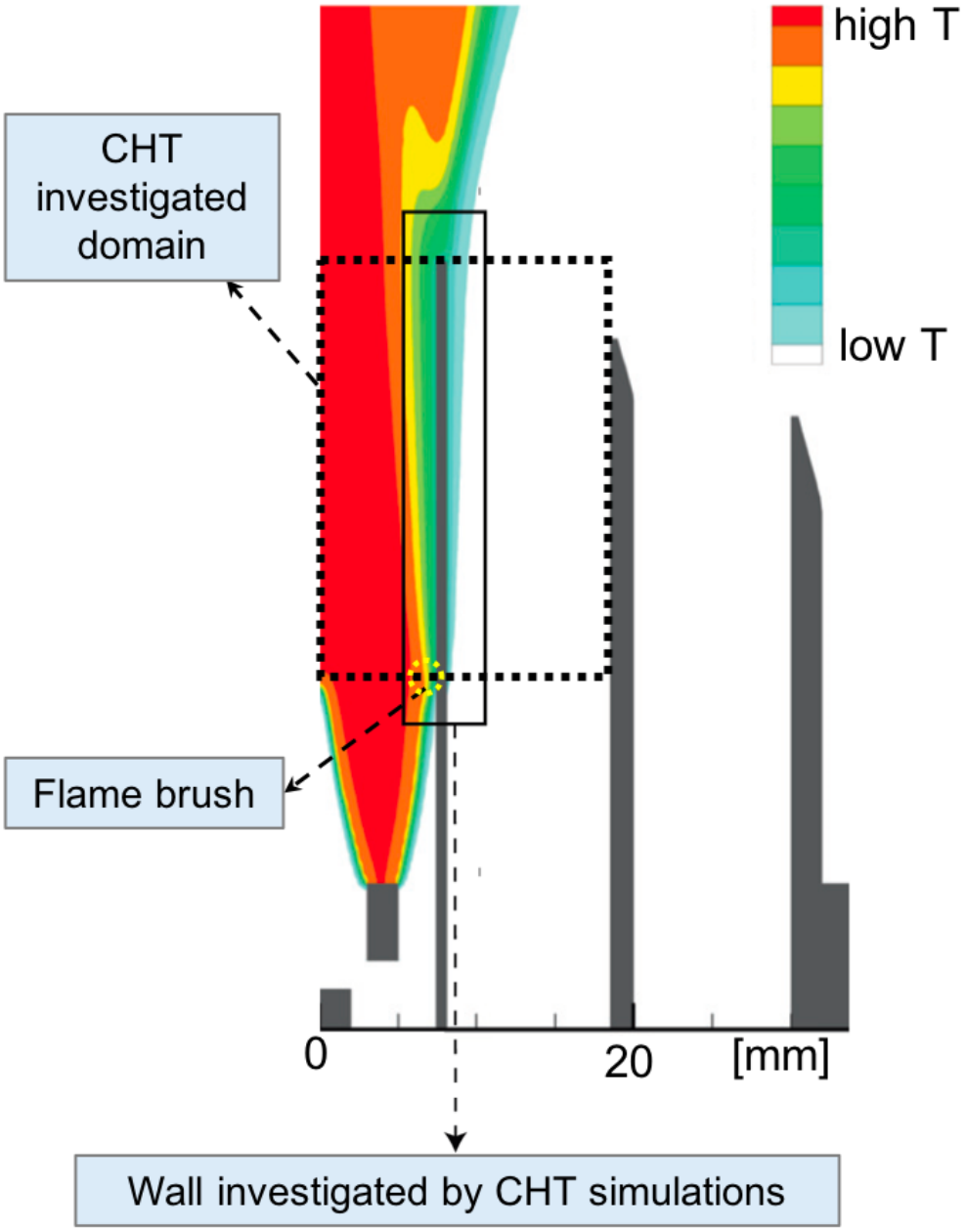

Figure 6.2: *Schematic of the investigated problem: the* flame-wall *interaction nearby the* Pilot *exit section generates some heat transfer from the hot burnt gases to* Slot 1 *fresh mixture. The adopted domain for CHT simulations involves* Pilot *and* Slot 1 *gases, as well as* Pilot *ceramic wall, starting from the flame attachment to the wall (flame brush) until the* Pilot *exit section. Here only a 2D wedge of the domain is depicted because the problem is axis-symmetric and qualitative numerical results of temperature, achieved by Kuenne in [65], are reported.*

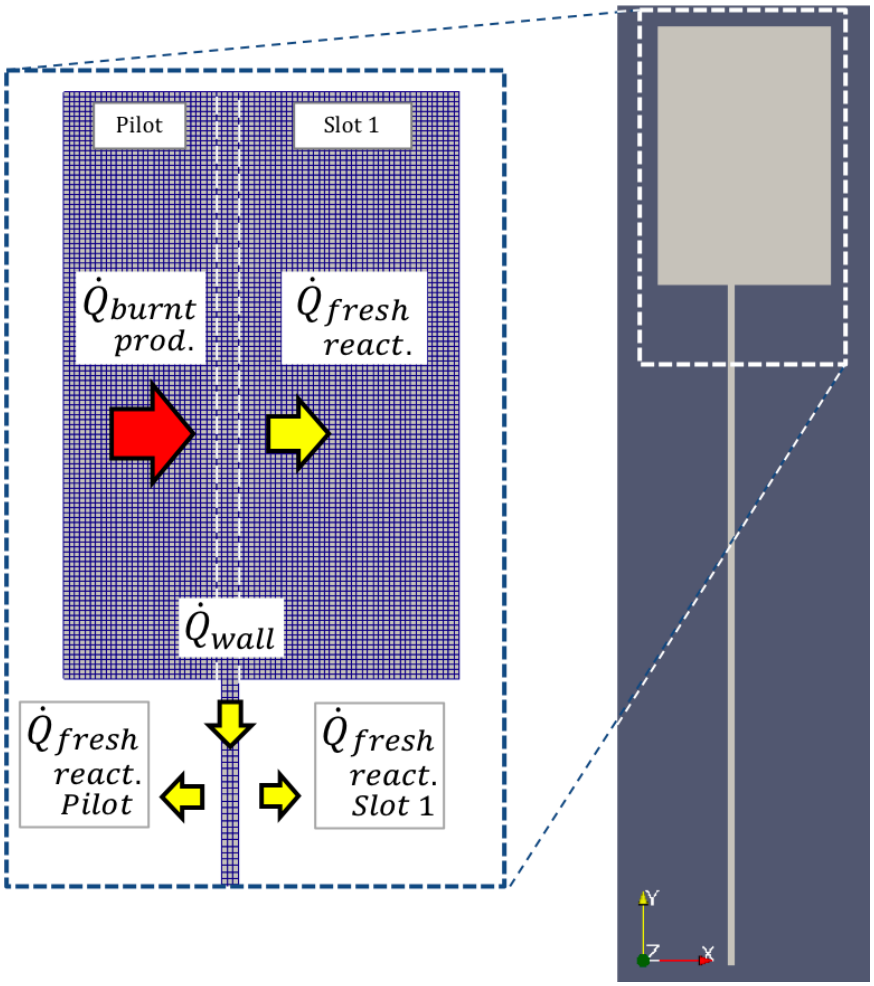

Figure 6.3: *Computational domain adopted for CHT simulations. According to Figure 6.2, a 2D wedge mesh of the* Pilot-Slot 1 *region in between the flame attachment position and the* Pilot *exit section (positioned at* $Y = 0\ mm$ *as in Figure 6.1) was used. The* X *axis corresponds to radial direction, starting from the burner axis of symmetry. In addition, the* Pilot *wall upstream to flame attachment was included to consider possible heat transfer along the wall itself.*

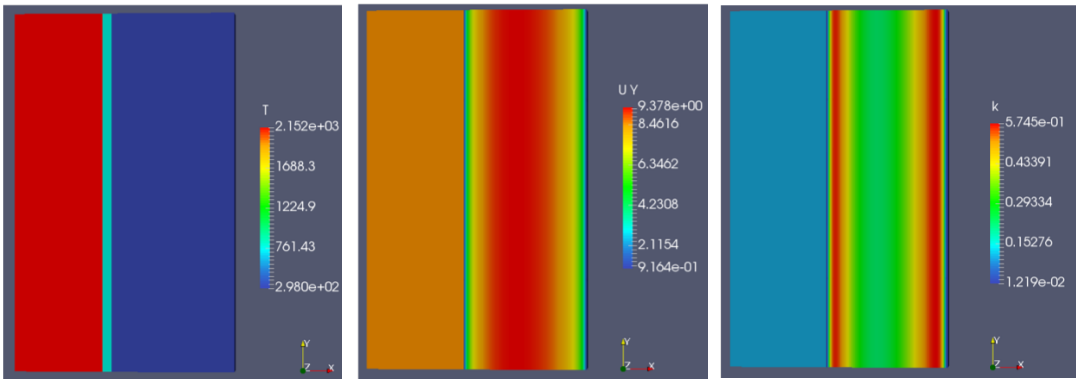

(a) **(b)** **(c)**

Figure 6.4: *Fields initial conditions before CHT simulations for: temperature* T *(a), axial velocity* U_y *(b) and turbulent kinetic energy* k *(c).* Pilot *fields are laminar, while* Slot 1 *fields are turbulent.*

However, as shown in Figure 6.3, the heat provided by burnt products to the Pilot wall does not flow totally to Slot 1 fresh mixture but can also be transferred along the wall itself. Therefore, the ceramic wall mesh was extended upstream to flame attachment position (assumed to be at $Y = -27.5\ mm$ according to Kuenne estimation [65]) in order to simulate a possible heat conduction towards colder regions. It is worth to notice that before the mixture ignition, the central pipe wall is surrounded by fresh gases on both sides. This condition, which could enhance the aforementioned heat transfer along the wall, was modelled along the extended solid region boundaries by simply considering that Pilot and Slot 1 fresh mixtures behave as heat-sinks unaffected by a transfer of heat (in this region the CHT can be reasonably neglected).

Regarding the computational domain details, each single region-mesh is a 2D wedge characterized by cubic cells of 0.23 mm axial and 0.05 mm radial sides. This choice was performed to use a globally uniform grid dimension and, at the same time, avoiding the use of wall functions on Slot 1 side. In fact, as shown in Table 5.1, *A-r* configuration is characterized by turbulent Slot 1 fresh reactants ($Re_{slot1} \approx 13'800$) at ambient temperature ($T_{slot1} = 298\ K$), therefore the use of wall functions has to be evaluated in the light of adopted boundary layer (namely, radial) resolution. Considering that this work was carried out by using the $k - \omega$ RANS turbulence model, along wall boundaries the y^+ value was maintained $y^+ < 1$ in the 1^{st} nearest cell and $y^+ < 5$ in the 2^{nd} one, thanks to the adopted radial mesh resolution. This allowed the use of fixed boundary conditions for turbulence magnitudes ($k = 10^{-5}$ and $\omega = 10^5$) because the resolution of boundary layers was ensured.

On the other hand, Pilot burnt products properties were computed by using the *equilibriumFlameT* OpenFOAM® utility, in which the equilibrium flame temperature T_{ad} is calculated from the provided fuel type, pressure, unburned gas temperature and equivalence ratio. Therefore, the $T_{ad,pilot} = 2151.73\ K$ value was predicted and the resulting Reynolds number $Re_{pilot} \approx 320$ was estimated, demonstrating how the hot burnt products flowing along central pipe can be considered in laminar conditions.

As shown in Figure 6.4, the temperature T, the axial velocity U_y and the turbulence kinetic energy k fields were initialized before CHT simulations according to previous considerations. In particular:

- Burnt products and fresh reactants temperatures were initialized as homogeneous (Figure 6.4a).

- Pilot wall temperature was initialized with an intermediate value to ease convergence (Figure 6.4a).

- Slot 1 U_y and k were initialized thanks to a *cyclic-flow* simulation, in order to provide a fully developed turbulent boundary layer (Figures 6.4b and 6.4c).

- The U_y field is also initialized in order to match *A-i1* configuration axial velocity, measured at $Y = 1\ mm$ (Figure 6.4b). Although a comparison between:

  1. numerical U_y distribution of *A-r* conditions at Pilot exit section $Y = 0\ mm$,
  2. experimental findings of U_y at *A-i1* conditions and $Y = 1\ mm$

  is not fully consistent, this is the best solution to reasonably calibrate Pilot and Slot 1 velocities in order to minimize the CHT results dependency on initial flow velocity conditions (see, as example, the calibration procedure shown in Figure 6.7).

For what concerns the temperature boundary conditions the following constraints were adopted:

- as previously mentioned, a heat flux condition was imposed at the extended solid region boundaries (bottom part of Figure 6.3) with a fixed convective heat transfer coefficient $h\ [W/(m^2\ K)]$ and temperature T, in order to consider the Pilot and Slot 1 fresh mixtures as heat-sinks unaffected by a transfer of heat.

- a zero-gradient condition was assumed at the exit section ($Y = 0\ mm$, Figures 6.1a and 6.3).

- constant and fixed values were imposed at the inlet sections ($Y = -27.5\ mm$, Figures 6.1a and 6.3), in particular $T = T_{ad,pilot} = 2151.73\ K$ and $T = T_{slot1} = 298\ K$ for the Pilot and Slot 1, respectively. An exception was represented by the flame brush (see Figure 6.2), along which the assumption of zero-gradient was used. This allowed to consider the heat-losses effects at flame attachment position.

- at Slot 1 outer wall (the one which separates Slot 1 and 2) a constant value of $T = 298\ K$ was imposed, because at that radial position the heat transfer process can be neglected.

However, because:

1. the flame brush extension cannot be predicted without the flame holder simulation,
2. the correct ceramic thermal conductivity value $k_{ceramic}$ depends on the used ceramic materials,

these two parameters needed to be calibrated in order to match experimental findings presented in Figure 6.1b. With this approach a complete understanding of the heat transfer phenomenon at Pilot exit can be achieved and suitable wall boundary conditions for future TSF burner non-adiabatic simulations can be provided.

6.2 Flame brush and ceramic properties calibration: first CHT results

The calibration procedure of:

1. the flame brush extension,
2. the ceramic thermal conductivity $k_{ceramic}$

was carried out by making an initial reasonable hypothesis on the $k_{ceramic}$ value and optimizing the radial length on which the burnt products temperature drops from $T_{ad,pilot} = 2151.73\ K$ to a $T_{wall} < T_{ad,pilot}$. This last value is *a priori* not known because dependent on the next CHT simulation.

Therefore, assuming $k_{ceramic} = 2.2\ W/(m\ K)$, three different flame brush values (see Figure 6.2) were tested:

Test	$k_{ceramic}\ [W/(m\ K)]$	Flame brush $[mm]$
1	2.2	**0.35**
2	2.2	**0.30**
3	2.2	**0.25**

Figure 6.5a shows a comparison between the temperature distribution along *Pilot* wall inner surface measured with phosphor thermometry technique (red dashed line of Figure 6.1b) and computed by CHT simulations of this initial calibration. From a first

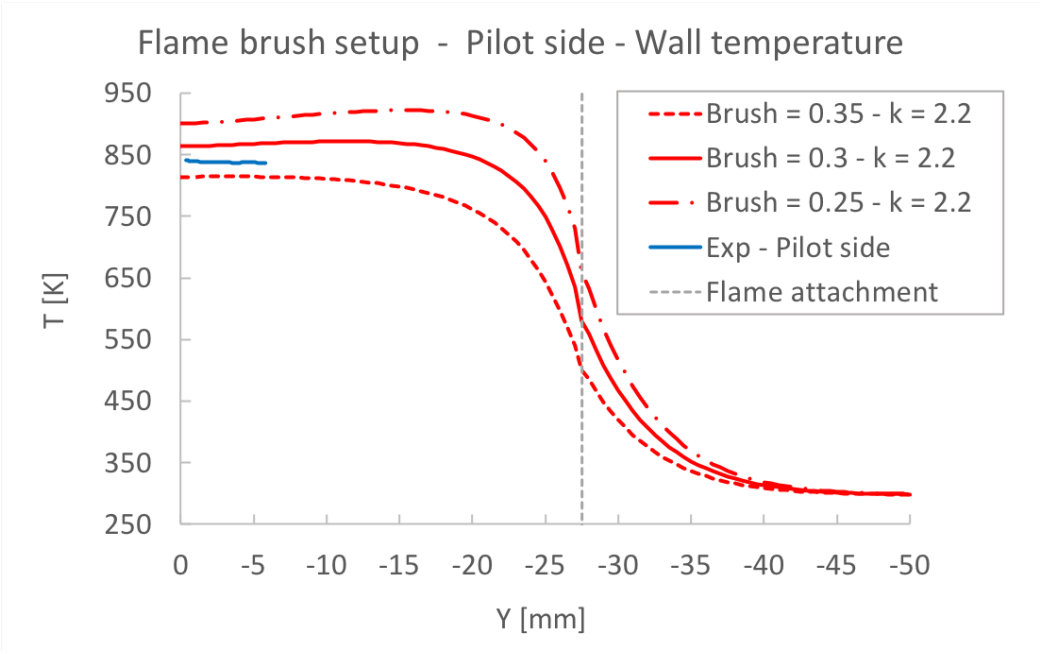

(a)

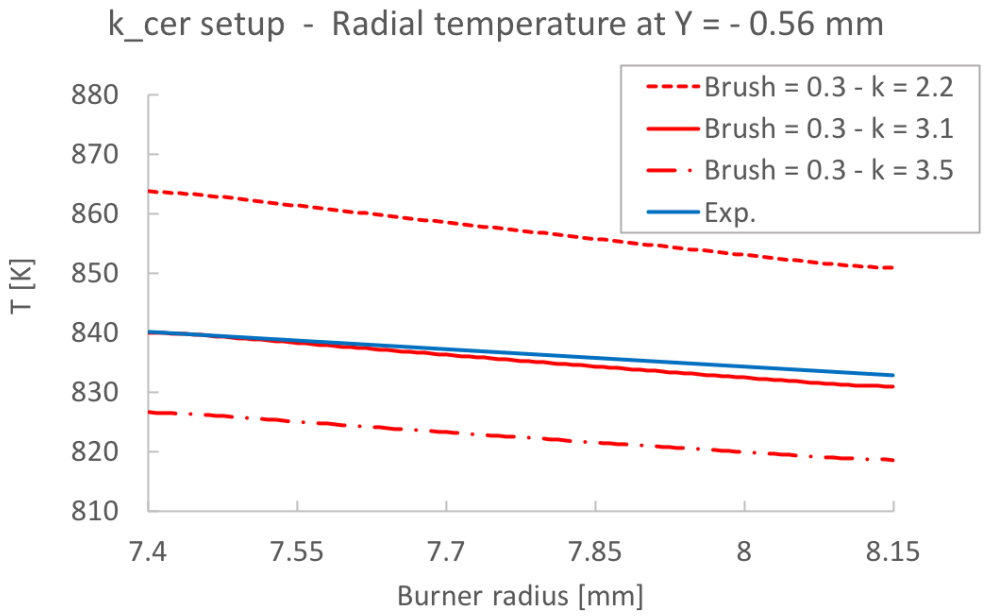

(b)

Figure 6.5: *Calibration of: the flame brush dimension at flame attachment position to* Pilot *wall (see Figure 6.2) by analyzing the temperature distribution along* Pilot *wall inner surface (a); the thermal conductivity coefficient* $k = k_{ceramic}$ $[W/(m\ K)]$ *characterizing the* Pilot *ceramic wall by investigating the temperature variation across the inner tube wall at* $Y = -0.56$ mm *(b). Taking as a reference Figure 6.3, the* Y *value becomes negative by traveling form* Pilot *exit section to the inner part of the pipe, while the burner radius corresponds to* X *axis.*

sight, it seems that both *Tests 1* and *2* could be equivalent satisfactory solutions. However, by comparing *Test 2* temperature variation across the inner tube wall at $Y = -0.56\ mm$ with the related experimental measurement (Figure 6.5b) it can be noticed that the temperature drop is overestimated of $\approx 78\%$ because $\Delta T_{Test1} = 12.87\ K > \Delta T_{Exp} = 7.22\ K$. Therefore, because the $k_{ceramic}$ should be increased to limit this overestimation and the inner surface temperature tendency is to decrease if a constant flame brush is adopted (see Figure 6.5b), the flame brush value of $0.3\ mm$ has to be selected.

The second part of the calibration process consisted in comparing three different $k_{ceramic}$ values, assuming a constant and equal to $0.3\ mm$ flame brush:

Test	$k_{ceramic}\ [W/(m\ K)]$	Flame brush $[mm]$
2	**2.2**	0.3
4	**3.1**	0.3
5	**3.5**	0.3

where *Test 2* simulation was already carried out. Figure 6.5b shows a comparison between experimental and numerical temperature variation across the inner tube wall at $Y = -0.56\ mm$ for rising $k_{ceramic}$ values. What can be concluded is that $k_{ceramic} = 3.1\ [W/(m\ K)]$ combined to a flame brush value of $0.3\ mm$ is the optimal setup because:

- it allows a very satisfactory prediction of the inner surface temperature of Pilot wall (numerical and experimental values are practically overlapped);
- it provides a significant reduction of the temperature drop overestimation, which now is $\approx 26\%$, being $\Delta T_{Test4} = 9.09\ K > \Delta T_{Exp} = 7.22\ K$.

In the light of these encouraging results, the final comparison between experimental and numerical temperature distributions along the inner and outer surfaces of Pilot wall was performed. Results are shown in Figure 6.6a. Despite a discrepancy in the temperature gradient at Pilot exit ($Y = 0\ mm$), which is due to the zero-gradient assumption used at the wall exit section [2], a satisfactory agreement on the whole outer wall surface

[2] This is the major limitation of the simplified investigation here presented. In fact, from experimental findings, it seems that the flame positioned over the wall exit section plays a role in increasing the Pilot pipe temperature nearby the $Y = 0\ mm$ position. However, this effect cannot be considered except by increasing the complexity of the CHT investigation and simulating also the flame front evolution.

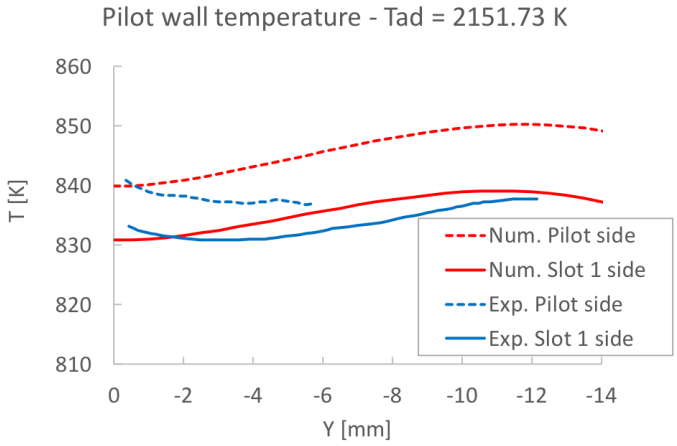

(a)

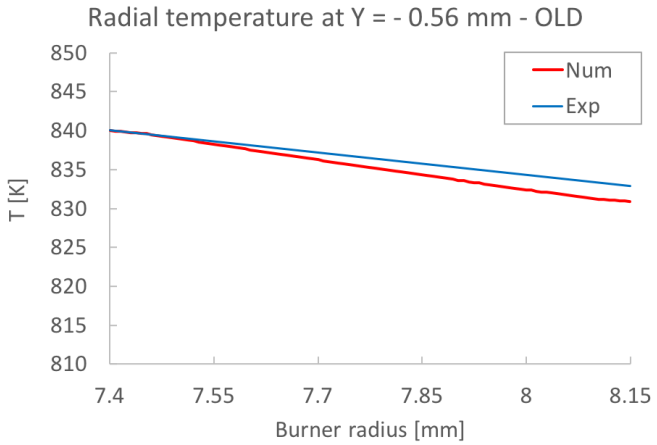

(b)

Figure 6.6: *Comparison between experimental findings of [65] and first CHT results after the flame brush and ceramic properties calibrations. Temperature distribution along* Pilot *wall inner (*Pilot *side) and outer (*Slot 1 *side) surfaces (a); temperature variation across the ceramic wall at* $Y = -0.56\ mm$ *(b). Taking as a reference Figure 6.3, the* Y *value becomes negative by traveling form* Pilot *exit section to the inner part of the pipe, while the burner radius corresponds to* X *axis.*

(Slot 1 side) is achieved. However, the numerical inner wall temperature (Pilot side) seems to be slightly overestimated with respect to the experimental one.

As a consequence, in next sub-section an improvement on burnt products properties computation will be performed in order to improve the $T_{ad,pilot}$ estimation and, consequently, the agreement between numerical and experimental inner wall surface temperature.

Figure 6.6b, already discussed, simply completes the *experimental-numerical* comparison.

6.3 Improved computation of burnt product properties: final CHT results

As a consequence of the numerical overestimation of Pilot inner wall temperature, shown in Figure 6.6a, an improvement in burnt product properties computation was performed. In particular, instead of using the *equilibriumFlameT* OpenFOAM® utility as in Section 6.1, a detailed chemistry 1D flame simulation was carried out with Cantera code by assuming:

- an equivalence ratio $\phi = 0.9$ for the fresh mixture to be ignited inside the Pilot pipe (according to *A-r* configuration, see Table 5.1),
- the achievement of almost equilibrium conditions.

Following this approach, the new estimation of burnt products temperature becomes lower than previous one, being $T_{ad,pilot,cantera} = 2124.42\ K < T_{ad,pilot} = 2151.73\ K$.

Hence, as first step, a re-calibration of the initial axial velocity U_y field in order to minimize the discrepancy between:

1. numerical U_y distribution of *A-r* conditions at Pilot exit section $Y = 0\ mm$,
2. experimental findings of U_y at *A-i1* conditions and $Y = 1\ mm$

was carried out similarly to what described in Section 6.1. The *experimental-numerical* agreement achieved after this re-calibration process is shown in Figure 6.7.

Then, by keeping constant both $k_{ceramic} = 3.1\ [W/(m\ K)]$ and the flame brush value of $0.3\ mm$ (see Section 6.2), CHT simulations results were compared with experimental phosphor thermometry measurements. The following trends were analyzed:

- The temperature distribution along inner (Pilot side) and outer (Slot 1 side) Pilot wall surfaces (Figure 6.8a).
- The temperature variation across the ceramic wall at $Y = -0.56\ mm$ (Figure 6.8b).

As it can be observed in Figure 6.8a, the inner wall temperature (Pilot side) now seems rather well predicted thanks to the improvement in estimating the adiabatic flame

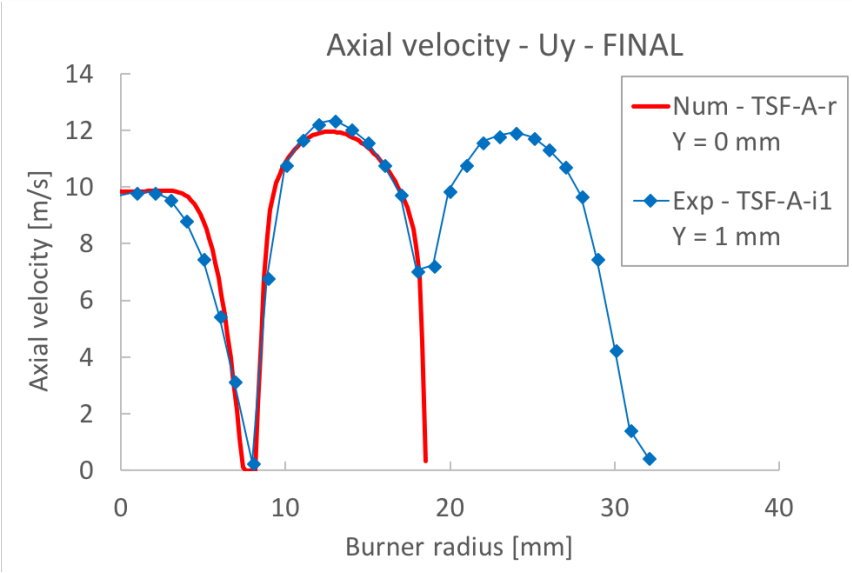

Figure 6.7: *Example of the calibration procedure performed on* Pilot *and* Slot 1 *inlet velocities: their value was chosen in order to achieve a satisfactory agreement between experimental* A-i1 *axial velocity U_y measured at $Y = 1\ mm$, [99], and CHT numerical results computed with* A-r *mixture properties at* Pilot *exit section ($Y = 0\ mm$).*

temperature of Pilot burnt products. On Slot 1 side (the outer wall surface) the computed temperature trend is slightly underestimated with respect to Figure 6.6a; however, the maximum *numerical-experimental* error is very low ($\approx 1\%$), hence the results can be considered satisfactory.

Concerning the temperature variation across the Pilot wall, Figure 6.8b shows how the numerical overestimation of experimental ΔT is still rather low (the $k_{ceramic}$ was kept constant). Now there is a general underestimation of the experimental temperature values on both wall sides with respect to Figure 6.6b results but, as previously mentioned, it is lower than 1%.

Finally, to complete the understanding of the heat transfer phenomenon, the CHT simulation results in terms of:

- numerical temperature trend from Pilot exit section ($Y = 0\ mm$) to $50\ mm$ inside the pipe on both inner and outer surfaces,
- numerical temperature T and axial velocity U_y fields

are shown in Figure 6.8c and 6.9, respectively. In the light of these results, the following conclusions can be drawn:

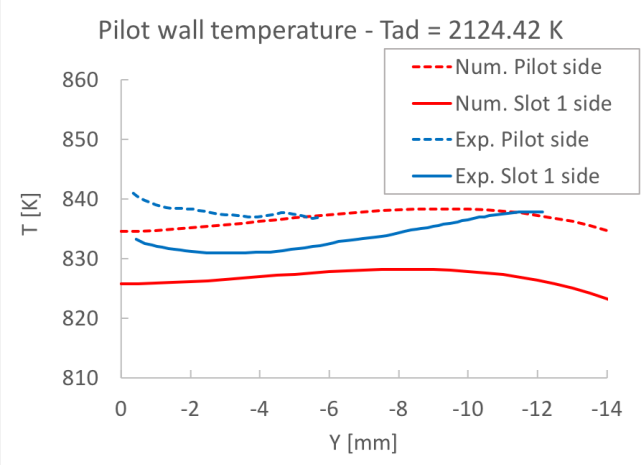

(a)

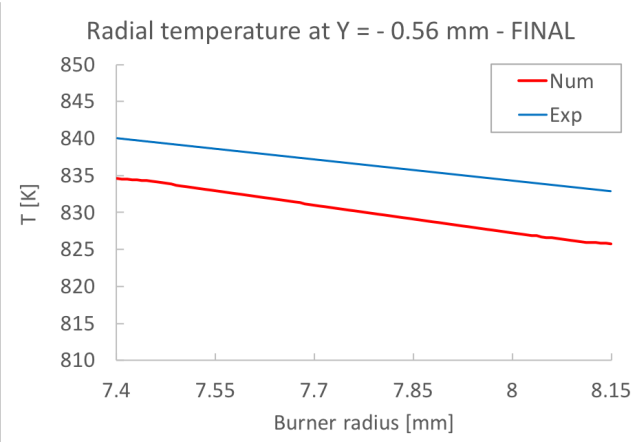

(b)

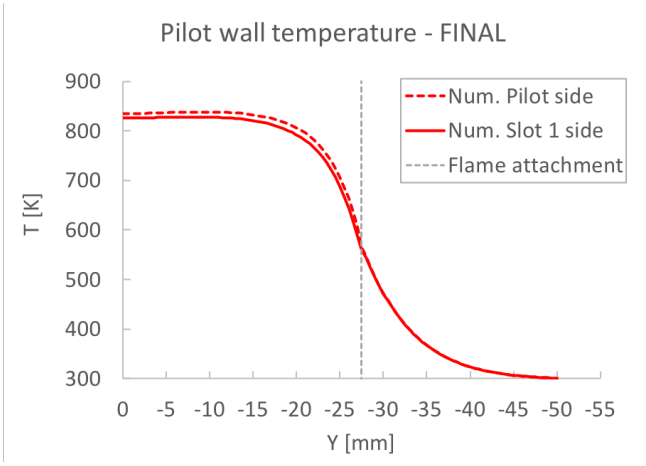

(c)

Figure 6.8: *Comparison between experimental findings of [65] and final CHT results after the improved computation of burnt products properties: temperature distribution along* Pilot *wall inner (*Pilot *side) and outer (*Slot 1 *side) surfaces (a); temperature variation across the ceramic wall at* $Y = -0.56\ mm$ *(b). The only numerical temperature trend from* Pilot *exit section (*$Y = 0\ mm$*) to* $50\ mm$ *inside the pipe on both inner and outer surfaces (flame attachment at* $Y = -27.5\ mm$*, [65]) is shown in (c). Taking as a reference Figure 6.3, the* Y *value becomes negative by traveling form* Pilot *exit section to the inner part of the pipe, while the burner radius corresponds to* X *axis.*

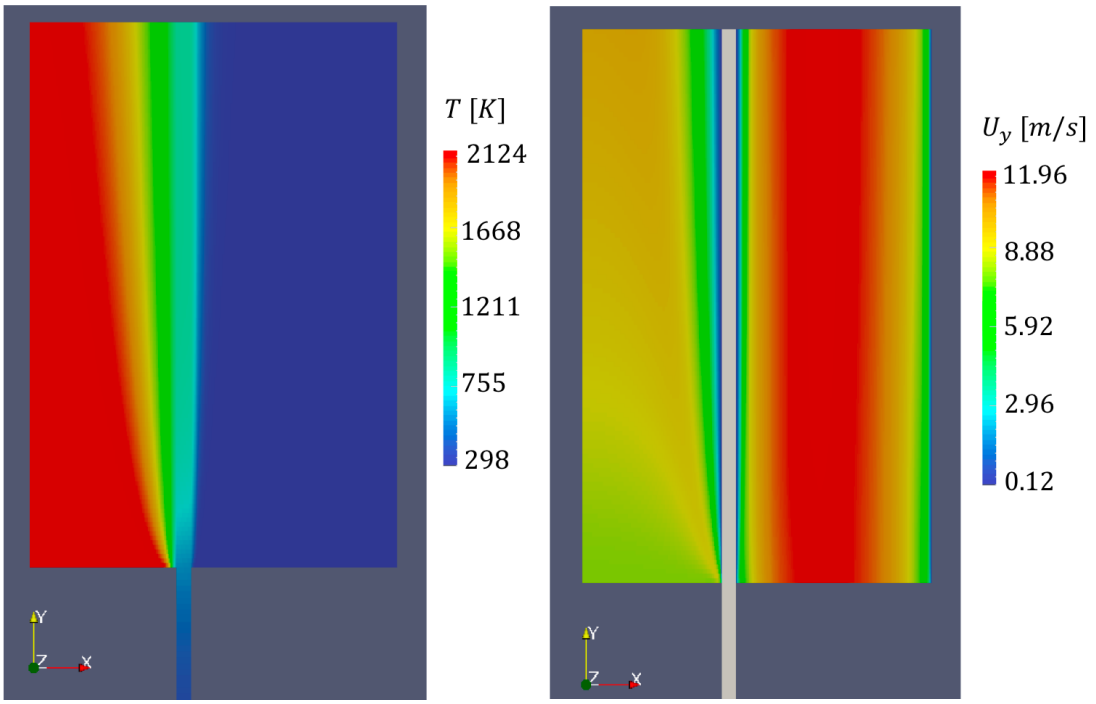

(a) (b)

Figure 6.9: *Numerical CHT results achieved after the improved computation of burnt products properties: temperature T (a) and axial velocity U_y (b) fields.*

1. The radial heat-losses experienced by the burnt products nearby the Pilot exit section are not negligible and should be considered in a future detailed TSF burner investigation.

2. The heat conduction phenomenon along ceramic wall towards colder mixture regions (located upstream the flame attachment position) is not negligible and reduces the "nearly constant" temperature region.

3. In case simplified boundary conditions would be used for Pilot wall surfaces, constant values of temperature can be imposed, in particular $T_{pilot\ side} \approx 837\ K$ and $T_{slot1\ side} \approx 827\ K$. This can be performed according to the "nearly constant" value assumed by the temperature along both wall sides from the burner exit section until $\approx 15\ mm$ inside the pipe.

4. If detailed temperature boundary conditions would be used for Pilot wall surfaces, the temperature distributions reported in Figure 6.8c have to be imposed.

6.4 Summary

The importance of considering heat-losses at TSF burner Pilot tube exit, where fully burnt products are in contact with the pipe, was already assessed by previous works (Fiorina and Kuenne). In fact, under adiabatic assumptions a flame anchored to the burner lip was predicted, while non-adiabatic simulations evidenced a flame lift-off and a better agreement with experimental findings of temperature and species concentrations.

Therefore, as a first step towards non-adiabatic investigations of the TSF burner with the ATFM of Chapter 2, *Conjugated Heat Transfer* (CHT) simulations were carried out in the aforementioned heat-losses region.

First, a calibration procedure of:

1. the flame brush extension, positioned where the flame front approaches the inner Pilot wall,

2. the ceramic thermal conductivity $k_{ceramic}$ of Pilot pipe wall

was carried out. From a comparison between available experimental findings and numerical results, it was concluded that $k_{ceramic} = 3.1\ [W/(m\ K)]$ combined to a flame brush value of $0.3\ mm$ represent the optimal setup.

Then, CHT simulations were carried out with different strategies to compute the properties of Pilot burnt products. In the light of achieved results, the following conclusions can be drawn:

1. The radial heat-losses experienced by the burnt products nearby the Pilot exit section are not negligible and should be considered in a future detailed TSF burner investigation.

2. The heat conduction phenomenon along ceramic wall towards colder mixture regions (located upstream the flame attachment position) is not negligible and reduces the "nearly constant" temperature region.

3. In case simplified boundary conditions would be used for Pilot wall surfaces, constant values of temperature can be imposed, in particular $T_{pilot\ side} \approx 837\ K$ and

$T_{slot1\ side} \approx 827\ K$. This can be performed according to the "nearly constant" value assumed by the temperature along both wall sides from the burner exit section until $\approx 15\ mm$ inside the pipe.

4. If detailed temperature boundary conditions would be used for Pilot wall surfaces, the temperature distributions computed by CHT simulations have to be imposed.

CHAPTER 7

The Orleans vessel

The premixed flames in SI engines are characterized by complex phenomena, as:

- the flame-turbulence interaction,
- curvature effects,
- thermo-diffusive instabilities.

The understanding of their influence on the initial kernel growth stage is a crucial issue. First, to figure out the behaviour of a given fuel under particular conditions of air/fuel ratio and turbulence intensity. Then, to assess the capability of available numerical models to predict the experimental observations, with the final purpose of improving the combustion process.

In this context, the Orleans vessel was chosen to carry out this investigation because of its very simple configuration. It is characterized not only by comfortable optical accesses but also by a simple layout: a spherical constant volume with a central igni-

tion and the capability to generate and control a nearly isotropic turbulence intensity at the ignition zone (thanks to rotating fans). Hence, this simplified rig allows to isolate and study the aforementioned phenomena by minimizing the uncertainties and the complexities introduced by classical configurations, as optical engines.

In this chapter, the complete experimental characterization of the Orleans vessel is carried out. First of all, its geometrical features are presented in detail. Then, its cold-flow characterization is performed thanks to a brief description of the experimental results obtained by Galmiche [48]. Finally, the premixed combustion study is addressed. Different air/fuel ratio, turbulence, pressure and fuel type conditions were tested to analyse all the phenomena involved in the early flame kernel development. It is worth to mention that the activities described in this chapter concern only the first part of the planned working schedule, which consists also in a second step: a complete vessel numerical investigation. This will allow a further validation of the Comprehensive CFD model for premixed SI combustion proposed in Chapter 1 and the evaluation of its possible improvements.

7.1 Vessel set-up

7.1.1 Chamber geometry and features

The Orleans vessel geometry, shown in Figure 7.1a, is a spherical closed volume in which high-pressure and high-temperature mixtures can be employed for both laminar and turbulent premixed flame investigations.

The spherical chamber has stainless steel walls with an inner diameter of 200 mm, while on the outer surface a heater wire resistance performs the initial gaseous mixture heating. At this stage, the maximum achievable temperature is 473 K, with an estimated fluctuation of less than 2 K around the target desired temperature value. The initial pressure inside the vessel can be controlled by using different flow-meters (as it will be explained in Section 7.1.2), and its maximum value is limited to 10 bar. The highest deviation between the effective and the set-point (namely the desired) mixture initial pressure is estimated in about 3 $\%$.

For turbulence initialization, the vessel is equipped with six identical four-blades

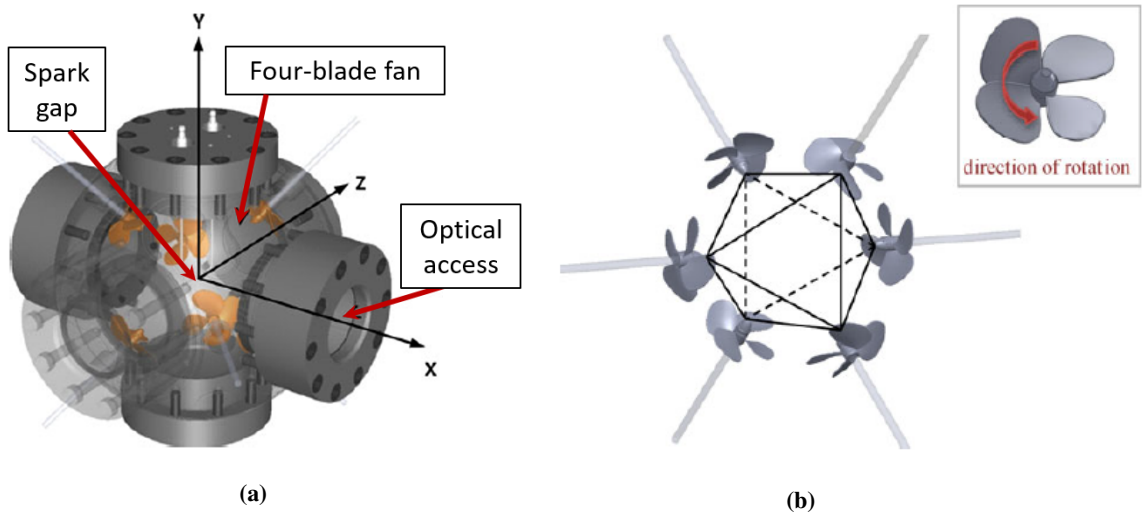

Figure 7.1: *The Orleans spherical vessel (a) and the detail of fans configuration and rotation (b), [48].*

fans of 40 mm diameter, located close to the chamber walls and positioned in a regular octahedral configuration (see Figure 7.1b). In this study, the fan rotation is chosen in order to direct the flow towards the centre of the vessel. Each fan is directly coupled to an electric motor, in order to control its speed between 1000 and 17000 rpm with an accuracy of about 0.1 $\%$, and runs continuously also during the flame propagation process.

Four optical quartz windows, located perpendicularly to X and Z axis (Figure 7.1a), provide optical access to the vessel. Finally, the mixture is ignited at the centre of the spherical volume by a spark produced between two tungsten wire electrodes of 0.5 mm diameter, fixed at the top vessel flange (Figure 7.1a).

Any further detail can be found in [17, 18, 47, 48].

7.1.2 Mixture preparation

The scheme of the mixture admission system to the vessel is represented in Figure 7.2. Here below, its particular features are briefly summarized.

First of all, a seeding line (highlighted in red in Figure 7.2) is connected in parallel to the air admission line in order to introduce a tracer into the mixture, if needed. Hence, also measurement techniques demanding a particles dispersion inside the vessel mixture can be used, as the:

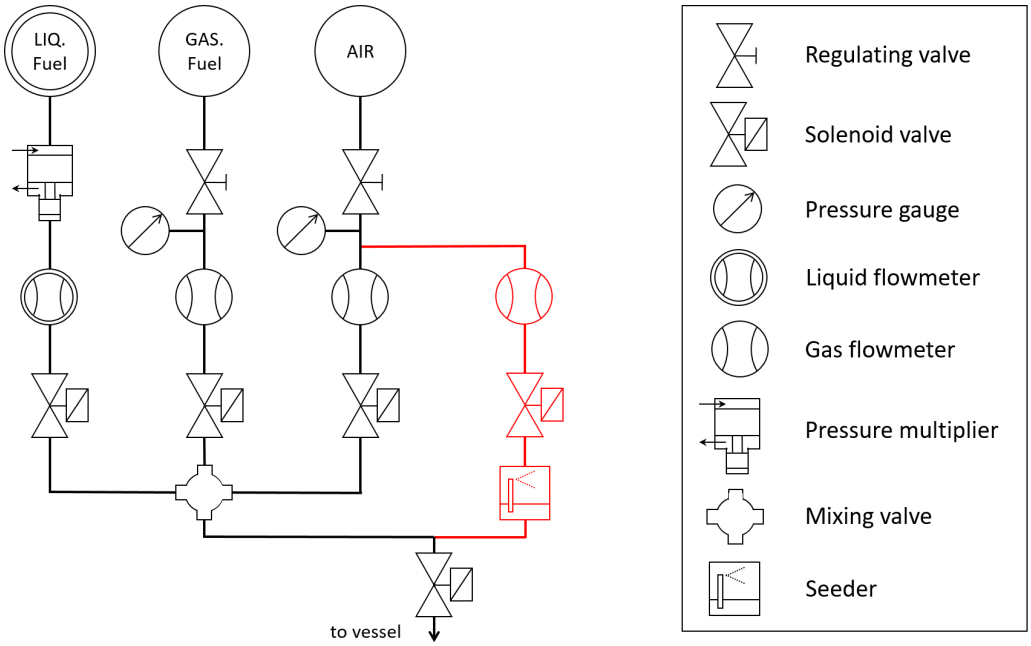

Figure 7.2: *Experimental layout of the mixture preparation for the Orleans vessel. The seeding line is highlighted in red.*

- Particle Image Velocimetry (PIV),
- Laser Doppler Velocimetry (LDV),
- laser tomography based on Mie scattering.

Secondly, dedicated admission lines for both liquid and gaseous fuels afford to test almost all types of premixed air/fuel mixture, including commonly used gasoline.

Finally, suitable couplings of solenoid valves/flow-meter governed by a user-defined software allows an accurate control on mixture composition and vessel pressure.

7.2 Experimental investigation

Since a solid knowledge of the aerodynamic features of the vessel provides a safe starting point for the more complex combustion investigation, as a first step an accurate characterization of the turbulent non-reacting flow was experimentally performed by Galmiche [47, 48].

Afterwards, an experimental investigation campaign was carried out on reacting conditions in order to understand the influence of an:

1. equivalence ratio,
2. turbulence intensity,
3. pressure,
4. Lewis number

variation on the flame propagation. In particular, an *Isooctane-Air* premixed mixture was adopted for the first three analysis, while for the last one a comparison between two different lean fuel mixtures (*Isooctane-Air* vs. *Hydrogen-Air*) featured by the same unstretched laminar flame speed s_{u0} was performed.

In next sections only the most interesting cold-flow experimental findings will be mentioned, while a detailed explanation of the combustion analysis in terms of measurement set-up, images post-processing and achieved results will be depicted.

7.2.1 Cold-flow characterization

In the study performed by Galmiche [47, 48] the flow turbulence and velocity were accurately investigated by using complementary experimental techniques:

- the Laser Doppler Velocimetry (LDV),
- the standard Particle Image Velocimetry with Low temporal and spatial Resolution (LR-PIV),
- the time-resolved Particle Image Velocimetry with High temporal and spatial Resolution (HR-PIV).

This work mainly established that in this vessel configuration the fans are able to generate a nearly homogeneous and isotropic turbulence field within the central region, namely where the mixture is going to be ignited. Here, the turbulence intensity was found nearly proportional to the fan speed with a negligible mean flow velocity. Finally, an analysis on the turbulent length scales highlighted how a pressure variation does not influence the integral length scale l_t, while it reduces the Taylor λ and Kolmogorov l_k length scales.

Measurements set-up The non-reacting characterization of the vessel was carried out by testing different fans speeds (from 1000 to 15000 rpm) under pressure and temperature conditions ranging between 1÷10 bar and 300÷423 K, respectively. At all tested conditions, the vessel was filled with suitable pressurized pure Air mixed with a silicone oil tracer, in order to perform LDV and PIV measurements. The preparation of the mixture was performed according to the system described in Section 7.1.2.

However, only the most important findings of Galmiche analysis will be reported afterwards, in order to provide a good basis for the next discussion about combustion results. For any further detail about the used optical diagnostic techniques, in particular regarding the experimental equipment (cameras, lasers and lenses), and the complete set of achieved results, please refer to [47, 48].

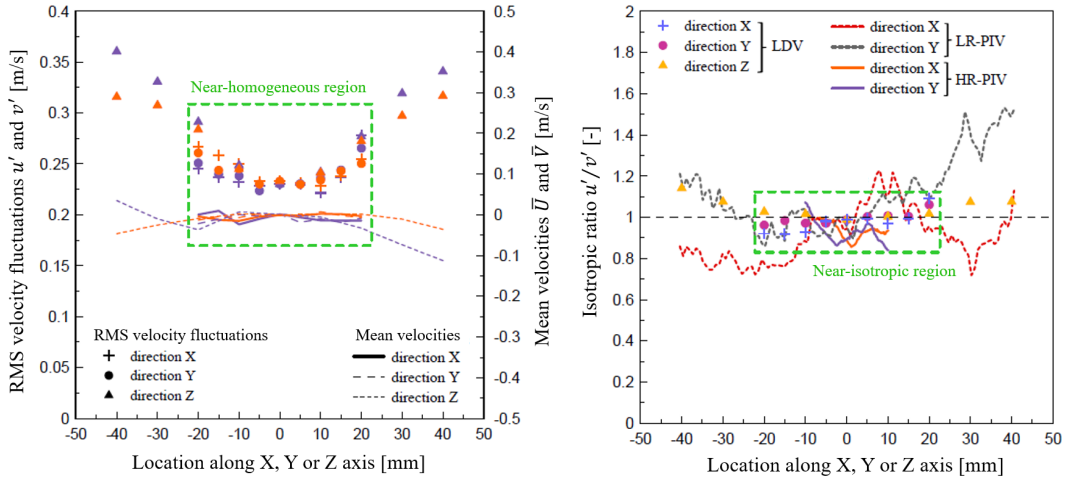

Figure 7.3: *Spatial evolution of the mean velocities and the rms velocity fluctuations (LDV measurements) (a) and the isotropic ratio along the three directions (LDV, LR-PIV and HR-PIV measurements) (b) at the fan speed $\omega = 2000$ rpm, [48]. In Figure (a) the U component is shown in purple and the V one in orange.*

Results and discussion The main results of the experimental activity were achieved at the following conditions:

- atmospheric pressure ($P = 1$ bar),
- ambient temperature ($T = 300$ K),
- fan speed $\omega = 2000$ rpm,

inside a region of 20 mm radius centred with respect to the spherical vessel, as shown by Figure 7.3. In particular, inside this region an almost negligible mean flow velocity and a nearly constant and isotropic turbulence intensity were observed (Figure 7.3a). This last statement was supported by the spatial behaviour of the isotropic ratio u'/v', which assumes a nearly unitary and constant value in the previously mentioned central region (Figure 7.3b).

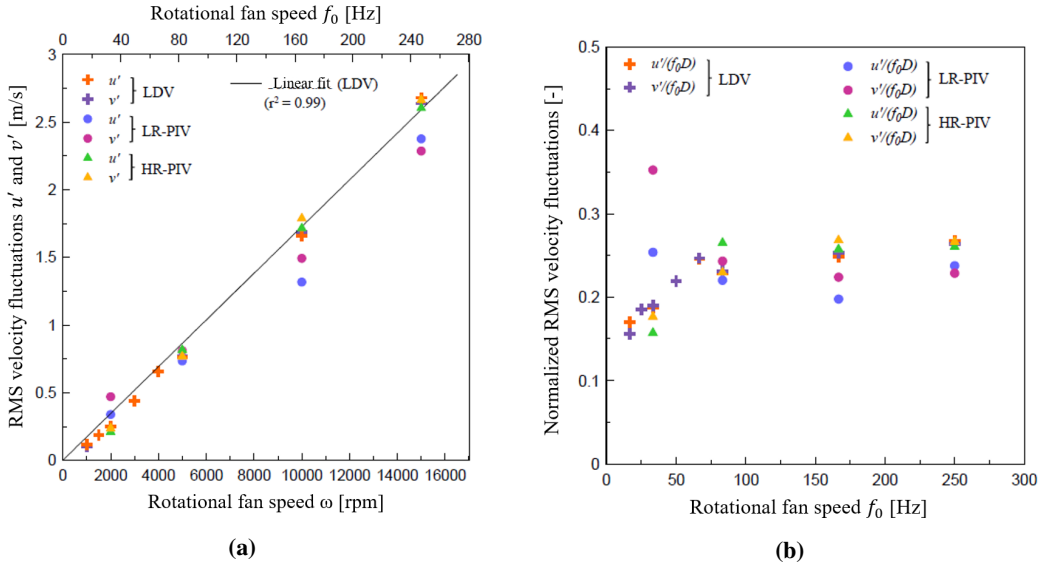

Figure 7.4: *Dependency of the rms velocity fluctuations u' and v' (a) and their normalization $u'/(f_0D)$ and $v'/(f_0D)$ (b) on the fan rotational speed (LDV and PIV measurements), [48].*

Concerning the fan rotational speed effect on the rms velocity fluctuations u' and v', both LDV and PIV measurements were employed to understand this topic. As reported in Figure 7.4, where u' and v' are plotted as function of the fan rotational speed ω and its associated frequency f_0 (where $f_0 = \omega/60$), a linear relationship between the velocity fluctuations and the fan speed is evinced. In fact, applying a linear fit on the LDV measurements by using the least-square technique yields (Figure 7.4a):

$$u' \approx v' = Af_0 \tag{7.1}$$

where $A = 0.0104\ m$ is a constant value. The validity of (7.1) relation was confirmed by the dimensionless velocity fluctuations $u'/(f_0D)$ and $v'/(f_0D)$ behaviour, where D is the fan diameter. Indeed, these two ratios are almost constant beyond $f_0 = 83\ Hz$ ($\omega = 5000\ rpm$) as displayed by Figure 7.4b, which means that the turbulence intensity

experiences a linear increase with fan speeds greater than 5000 rpm.

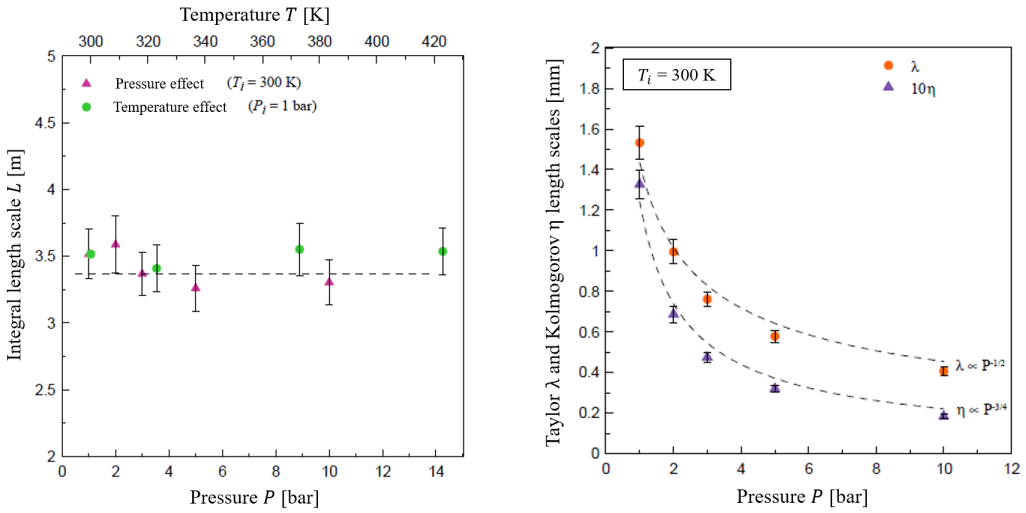

Figure 7.5: *Effect of the gas pressure and temperature on the integral length scale l_t (a) and the evolution of Taylor λ and Kolmogorov l_k length scales with pressure (b) at the fan speed $\omega = 2000\ rpm$, [48].*

Finally, the pressure effects on the characteristic turbulent length scales is described. As observed in Figure 7.5a, the integral length scale l_t is almost constant over the investigated pressure interval with a fluctuation of $\pm 6\%$ around the mean value determined by Galmiche [48] and displayed by a dashed line ($l_t = 3.4\ mm$). On the other hand, Figure 7.5b shows how Taylor λ and Kolmogorov l_k length scales become smaller with a pressure increase. This can be explained by the higher energy amount stored in high frequencies (namely, the small time-scale turbulent structures) when pressure grows up, implying increasingly smaller eddies [48].

7.2.2 Combustion analysis

The results achieved during the non-reacting vessel characterization (see Section 7.2.1) had a significant impact on the further combustion analysis, which will be discussed in this section. Indeed, the capability to generate homogeneous and isotropic turbulence conditions at the ignition zone, together with a negligible flow velocity, allows to study each reacting test with the easiest and most "comfortable" cold-flow features. Therefore, additional uncertainties introduced by more complex aerodynamic characteristics are avoided and a more confident analysis on the initial flame propagation behaviour

could be performed.

In this context, the main target of the fulfilled combustion investigation was to clarify the influence on flame propagation not only of the basic combustion parameters (equivalence ratio, turbulence intensity and pressure) but also of Lewis number, which takes into account the laminar premixed flames intrinsic instabilities called thermal-diffusional effects.

Table 7.1: *Investigated reacting conditions. In last column is reported the correction factor for Schlieren data.*

Test $[-]$	Fuel $[-]$	ϕ $[-]$	Fan speed $[rpm]$	u' $[m/s]$	P $[bar]$	T $[K]$	s_{u0} $[cm/s]$	u'/s_{u0} $[-]$	Correction factor $[-]$
1	Isooctane	1	6000	1	1	423.15	60.9	1.64	0.77
2	Isooctane	0.85	6000	1	1	423.15	47.95	2.09	0.75
3	Isooctane	1	9000	1.42	1	423.15	60.9	2.33	0.74
4	Isooctane	1	6000	1	5	423.15	43.97	2.27	0.74
5	Hydrogen	0.41	6000	1	1	423.15	60.2	1.66	0.77
6	Hydrogen	0.38	6000	1	1	423.15	45.35	2.21	0.74
7	Hydrogen	0.39	6000	1	1	423.15	50.49	1.98	0.75

For this reason, the experimental conditions of Table 7.1 were chosen, where all tests were performed at 423.15 K and the unstretched laminar flame speed s_{u0} was computed from CHEMKIN computations. In particular the kinetic schemes of Hasse [53] and O'Connaire [83] were used for *Isooctane-Air* and *Hydrogen-Air* mixtures, respectively.

Going into details of Table 7.1, an *Isooctane-Air* premixed mixture was used to assess:

1. an equivalence ratio ϕ reduction (*Test 1* vs. *Test 2*),

2. a turbulence intensity increase (*Test 1* vs. *Test 3*), and

3. a pressure enhancement (*Test 1* vs. *Test 4*).

On the other hand, a Lewis number reduction from $Le > 1$ to $Le < 1$ was achieved by passing from an *Isoocatane*-lean mixture to an *Hydrogen*-lean one [88]. This variation was evaluated in presence of two different (and fixed) s_{u0} values:

1. $s_{u0} \simeq 60\ cm/s$ (*Test 1* vs. *Test 5*), and

2. $s_{u0} \simeq 48\ cm/s$ (*Test 2* vs. *Test 6*/*Test 7*).

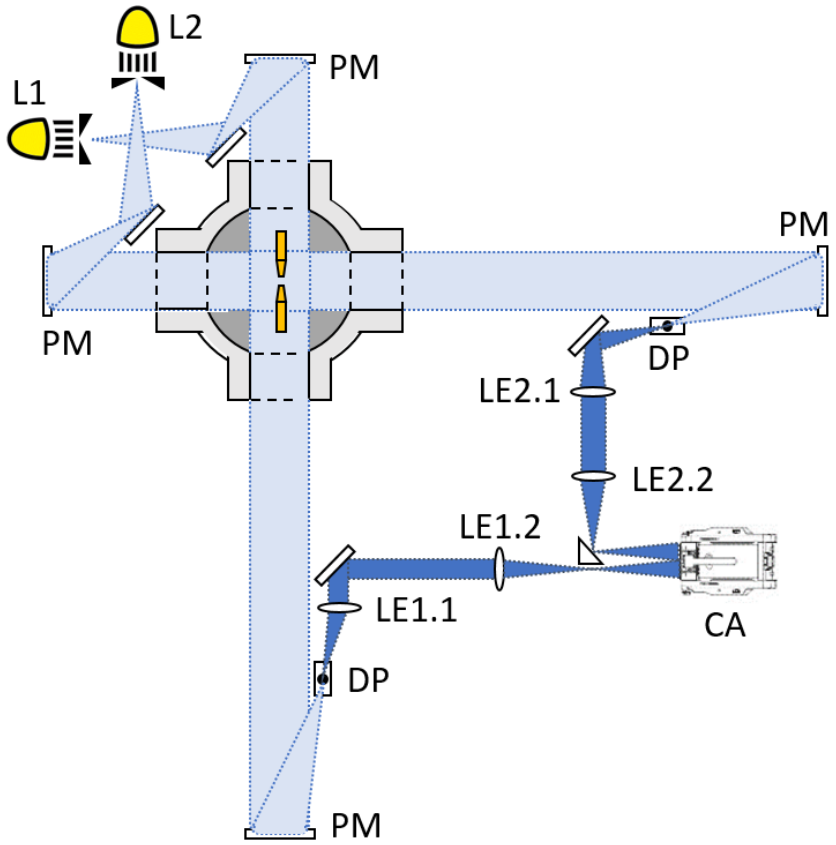

Figure 7.6: *Schematic of the 2-Views Schlieren acquisition rig.* L1 *and* L2 *are the LEDs,* PM *is a parabolic mirror,* CA *the camera,* DP *a dot point and* LE *the lenses.*

This last comparison was carried out between three test conditions because, fixed an s_{u0} variation, an Hydrogen-Air lean mixture experiences a much lower ϕ reduction with respect to the corresponding Isooctane-Air lean mixtures. Hence, the flow-meters (see Section 7.1.2) were not able to guarantee the same level of accuracy for both mixtures, therefore for Hydrogen were chosen the two closest conditions to Test 2 in terms of s_{u0} value (namely Tests 6 and 7). The aforementioned explanation can be clarified by observing from Table 7.1 what follows:

Test	Fuel	ϕ	$\boldsymbol{\phi}$ **variation [%]**	$s_{u0}[cm/s]$	$\boldsymbol{s_{u0}}$ **variation [%]**
1	Isooctane	1	**15**	60.9	$\sim$ **23**
2		0.85		47.95	
5	Hydrogen	0.41	**7**	60.2	$\sim$ **23**
6		0.38		45.35	

Measurements set-up and post-processing The measurements campaign was carried out by using the high speed imaging system of Figure 7.6, which consists in a 2-Views Schlieren acquisition rig similar to the one used by Brequigny [18]. In this configuration two LEDs (CBT120) coupled with:

- a 1 mm pin-hole to achieve a point source, and
- two parabolic mirrors of 864 mm focal length

generate two perpendicular light paths intersecting at the ignition zone. For both of them, a dot point of 0.5 mm diameter is positioned at the focal point of the second mirror and two lenses (200 mm and 160 mm of focal length, respectively) allow to focus each image directly on the CMOS chip. With this configuration, two perpendicular views of the ignition zone are simultaneously available and recorded by the same high speed camera (Phantom v1610) at full resolution (1280x800 px^2), frame rate of 12000 Hz and magnification ratio of 0.11 mm/px.

The images post-processing was carried out as follows:

1. A manual selection of the camera original images was performed in order to keep only frames including the flame front (Figure 7.7a).
2. The camera original images were split from full resolution (1280x800 px^2) into two frames of partial resolution (640x800 px^2), called raw images, for a separate filtering of the available Schlieren views (Figures 7.7b and 7.7c).
3. A background image with no combustion was subtracted to each raw image with the purpose to remove the environmental noise generated by LEDs reflections on the electrodes, internal walls, fans and optical quartz windows; hence, corrected images were obtained.

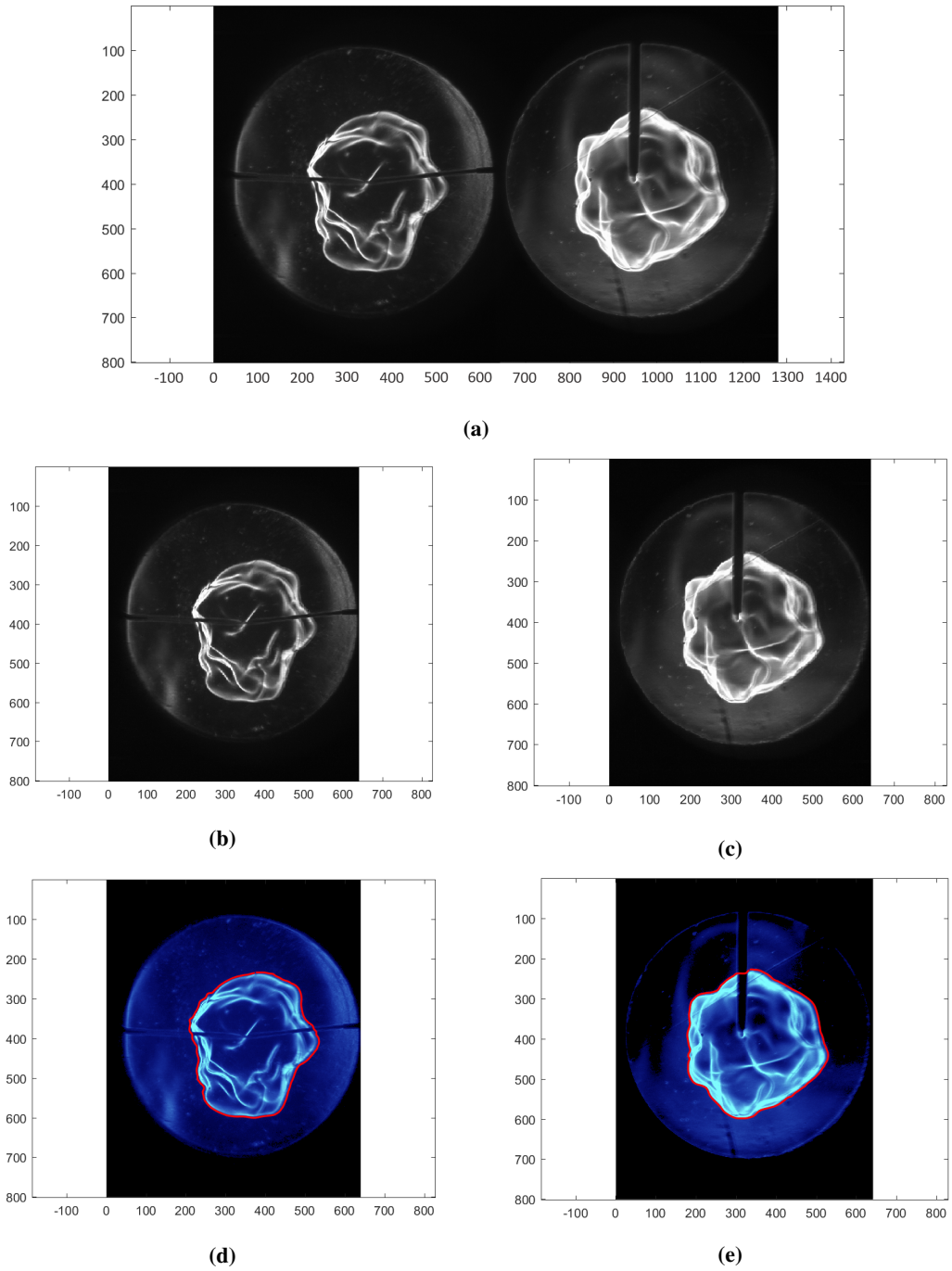

Figure 7.7: *Main steps of Schlieren images post-processing: original camera image (1280x800 px^2) (a), splitting of the two perpendicular views (640x800 px^2) (b and c), and flame contour detection (d and e). Both axis of all figures are in pixels.*

4. The threshold value choice for the flame front detection was performed manually by analysing the grey levels difference between shady and bright areas (the fresh mixture and burnt gases, respectively) of each corrected image. From this

procedure, binary images were obtained.

5. The flame front contour detection was performed on each binary image. The electrodes shady areas influence was avoided by applying a suitable mask at their position and by approximating with a linear segment the flame front behind them. The final result is shown by Figures 7.7d and 7.7e.

6. As described in [12, 18], the flame radius R_f (namely the spherical flame front position) was computed from the circular area equivalent to the flame area measured inside the detected contour (A_f):

$$R_f = \sqrt{\frac{A_f}{\pi}} \tag{7.2}$$

This choice was justified by the cold-flow features of the Orleans vessel (see Section 7.2.1), which allow the generation of a nearly spherical flame shape.

7. In addition to (7.2), another approach was used for the flame radius R_f computation. As proposed by Brequigny [18], the nearly spherical flame volume V_f could be reconstructed from the two perpendicular Schlieren views by using elliptical surfaces, and then its equivalent spherical volume exploited to compute R_f as:

$$R_f = \sqrt[3]{\frac{3V_f}{4\pi}} \tag{7.3}$$

In fact, as shown by Figure 7.8, an elliptical surface could be defined by fitting the four points belonging to both detected contours of the flame front at a fixed Z value. Then, by integrating along the Z direction all elliptical surfaces defined as before, the flame volume V_f can be determined.

8. Finally, the flame total stretch, defined as [13]:

$$\kappa_f = \frac{1}{A_f}\frac{dA_f}{dt} \tag{7.4}$$

and including both the flame curvature and the flow/turbulence velocities effects, was computed by using (7.4) with the flame area A_f measured from each Schlieren image.

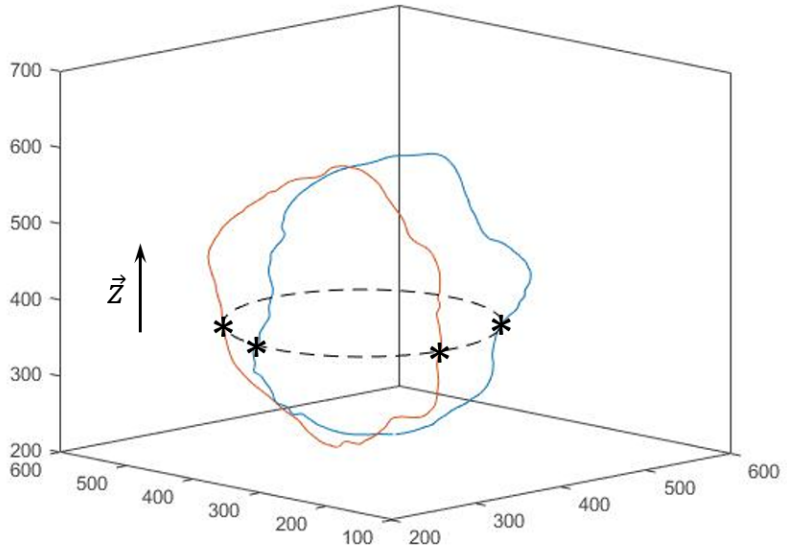

Figure 7.8: *Example of flame volume reconstruction form the 2-Views Schlieren acquisition system. The two perpendicular detected contours of Figures 7.7d and 7.7e are reported with a blue and a red line, respectively. Here only one elliptical surface (black dashed line), used for the flame volume reconstruction, is shown.*

Results and discussion The previous images post-processing was completed with a suitable analysis of the achieved results (flame radius R_f and flame total stretch κ_f), in order to fulfil the set goals.

First, at fixed conditions (e.g. *Test 1* of Table 7.1), all values of R_f and κ_f belonging to the same time instant were collected.

The sample mean

$$\bar{x} = \frac{1}{N}\sum_{i=1}^{N} x_i \tag{7.5}$$

and the corrected sample standard deviation

$$\sigma = \sqrt{\frac{\sum_{i=1}^{N}(x_i - \bar{x})^2}{N-1}} \tag{7.6}$$

were computed for both magnitudes, with N the number of measurements that characterize the sample and x_i the *i*-th measurement. Eq. (7.6), which represents the sample standard deviation with Bessel correction, was used because the sample mean computed

in (7.5) is only an estimation of the measurements population mean.

In particular, considering that each test of Table 7.1 was repeated about 6 times, each one generating 2 Schlieren images of the flame area:

- $\bar{x}$ and σ of the flame radius R_f were computed from both the post-processed equivalent flame area and the volume, in order to maximize N (total number of exploited measurements: about $N = 18$);

- $\bar{x}$ and σ of the flame total stretch κ_f were computed from the post-processed equivalent flame area only (with about $N = 12$).

Second, as suggested by Bradley [12], the R_f value computed from Schlieren images was corrected with a suitable factor C_{schl}. In fact, radii computed by using the Mie-Scattering tomography are smaller than those obtained from Schlieren images due to a basic difference between these two techniques: the first one is a 2D cut, while the second one is a 3D projection. Hence, being the tomography more accurate than Schlieren procedure, the correction factor C_{schl} can be calculated by averaging on the flame propagation duration the ratio between the flame speed measured with Mie-Scattering tomography and the flame speed achieved from Schlieren images. However, according to Brequigny investigation [18], C_{schl} was computed by applying the following empirical correlation

$$C_{schl} = a \, \frac{u'}{s_{u0}} + b \tag{7.7}$$

where $a = -4.383 \cdot 10^{-2}$ and $b = 0.84$. The correction factor C_{schl} values of each investigated condition are reported in Table 7.1.

Nevertheless, instead of correcting the R_f value before computing $\bar{x}$ and σ for κ_f and R_f itself, in this work the correction was performed directly on all $\bar{x}$ and σ computed with the Schlieren images flame radius. In fact, at fixed conditions, the corrected sample mean of the flame radius $\bar{R}_{f,corr}$ can be computed as follows

$$\bar{R}_{f,corr} = \frac{C_{schl} R_{f,1} + C_{schl} R_{f,2} + ... + C_{schl} R_{f,N}}{N} = C_{schl} \, \bar{R}_f \tag{7.8}$$

Similarly, the corrected sample standard deviation of the flame radius $\sigma_{R_{f,corr}}$ can be

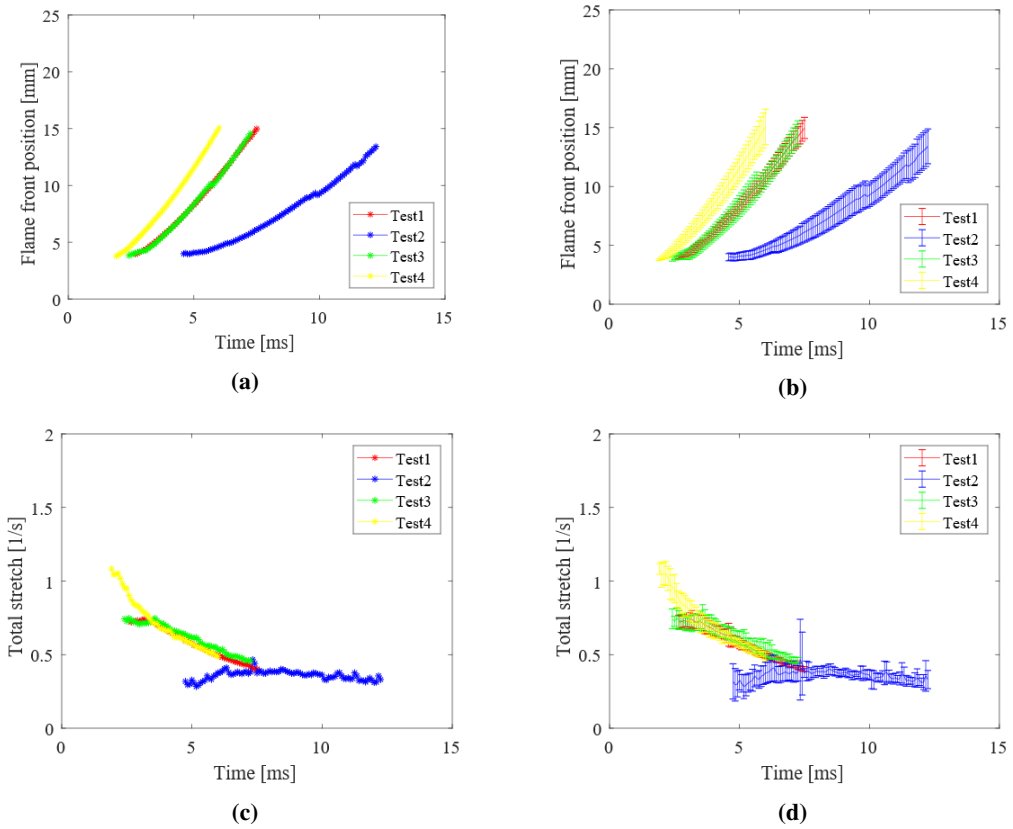

Figure 7.9: *Time evolution of the corrected mean flame front position (a) and mean total flame stretch (c) of the Isooctane-Air mixtures reported in Table 7.1. Figures (b) and (d) show same results of Figures (a) and (c), respectively, with in addition the related standard deviations (the error-bars).*

achieved as

$$\sigma_{R_{f,corr}} = \sqrt{\frac{C_{schl}^2}{N-1}\sum_{i=1}^{N}(R_{f,i} - \bar{R}_f)^2} = C_{schl}\,\sigma_{R_f} \tag{7.9}$$

For what concerns, instead, the corrected flame total stretch $\kappa_{f,corr}$ computation, no C_{schl} is needed because

$$\begin{cases} A_{f,corr} = \pi\left(C_{schl}R_f\right)^2 = C_{schl}^2\pi R_f^2 = C_{schl}^2 A_f \\ \kappa_{f,corr} = \dfrac{C_{schl}^2}{A_f}\dfrac{d\left(\frac{A_f}{C_{schl}^2}\right)}{dt} = \dfrac{1}{A_f}\dfrac{C_{schl}^2}{C_{schl}^2}\dfrac{dA_f}{dt} = \kappa_f \end{cases} \tag{7.10}$$

where A_f is the flame area and $A_{f,corr}$ its corrected value.

Finally, the corrected values of mean flame radius $\bar{R}_{f,corr}$ and mean total stretch $\kappa_{f,corr}$ achieved for the tests of Table 7.1 were compared in order to understand the influence of an:

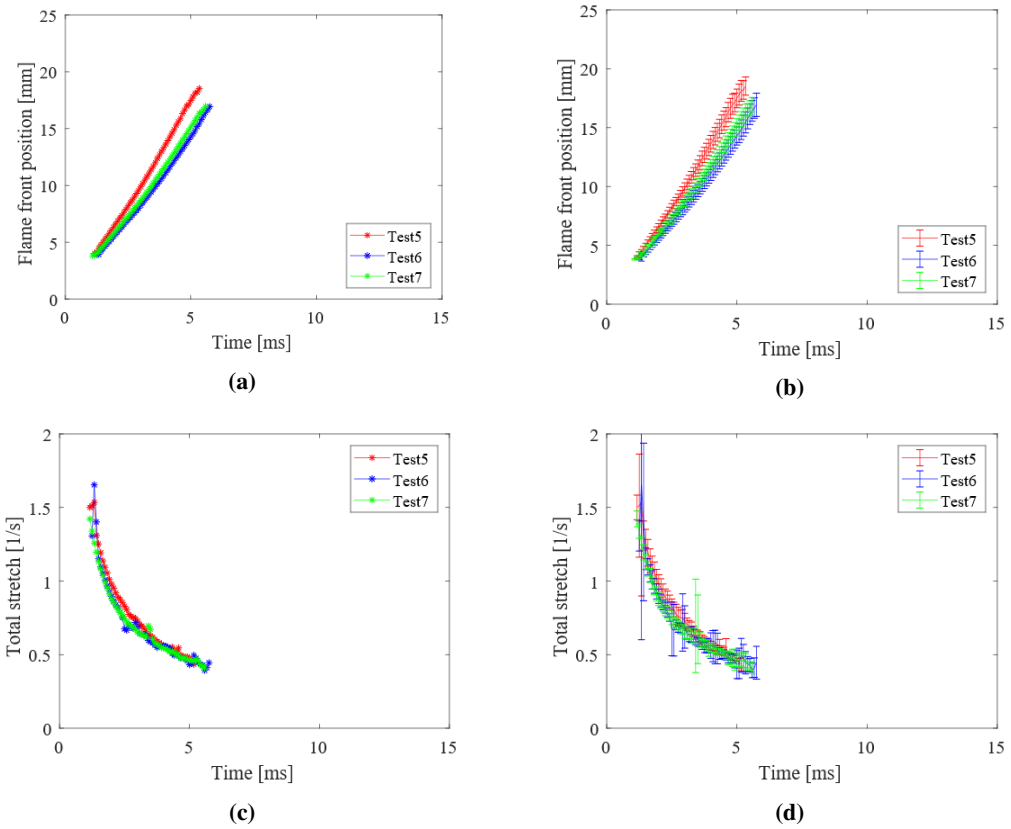

Figure 7.10: *Time evolution of the corrected mean flame front position (a) and mean total flame stretch (c) of the Hydrogen-Air mixtures reported in Table 7.1. Figures (b) and (d) show same results of Figures (a) and (c), respectively, with in addition the related standard deviations (the error-bars).*

1. equivalence ratio,
2. turbulence intensity,
3. pressure,
4. Lewis number

variation on the flame propagation. As previously mentioned, the first three analysis were mainly performed on an *Isooctane-Air* premixed mixture, while the last one was fulfilled through a comparison between two different lean fuel mixtures (*Isooctane-Air* vs. *Hydrogen-Air*) featured by the same unstretched laminar flame speed s_{u0}.

As Figure 7.9a shows, in case of an equivalence ratio reduction (from *Test 1* to *Test 2*) a leaner mixture is obtained and, as expected, a slower flame speed is experienced. An interesting aspect can be appreciated by comparing Figure 7.9a and Figure 7.9c at $\bar{R}_{f,corr} \approx 5mm$: the great stability of Test 1 stoichiometric mixture allows a faster

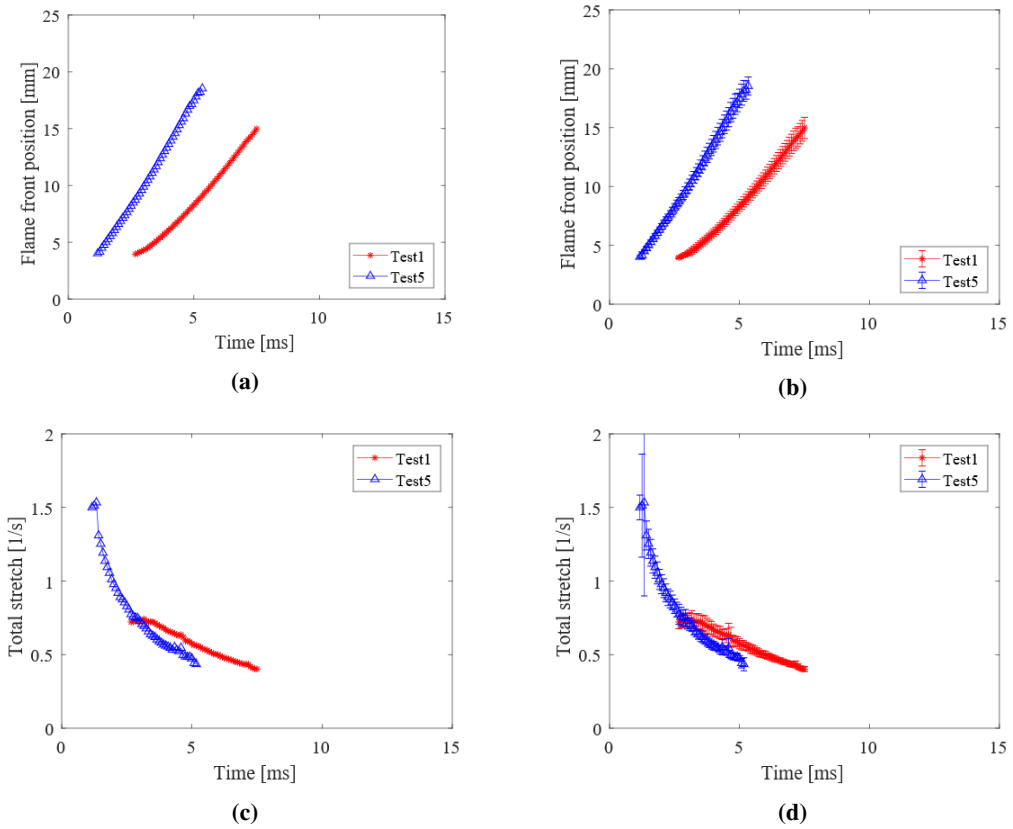

Figure 7.11: *Time evolution of the corrected mean flame front position (a) and mean total flame stretch (c) of the mixtures characterized by an unstretched laminar flame speed of $s_{u0} \simeq 60\ cm/s$ (see Table 7.1). Figures (b) and (d) show same results of Figures (a) and (c), respectively, with in addition the related standard deviations (the error-bars).*

flame propagation with respect to Test 2 flame also in presence of an higher total stretch value during the initial propagation stage. Similar conclusions can be drawn for an *Hydrogen-Air* premixed mixture (see Figure 7.10, *Test 5* vs. *Test 6*).

The flame speed behaviour under a variation of the turbulence intensity was assessed by comparing *Test 1* and *Test 3*. As observed in Figure 7.9a, the expected positive correlation between the flame speed value and the turbulence intensity level is achieved. However the flame speed increase seems not very sensitive to a turbulence intensity variation ($u'_{Test2} \approx 1.4u'_{Test1}$); this could be explained by the total stretch increase measured by moving to higher turbulence values (see Figure 7.9c) which tends to slow down the flame front.

Then, a comparison between *Test 1* and *Test 4* was performed to evaluate the influence of a pressure increase on the flame front propagation. As Figure 7.9a shows, a

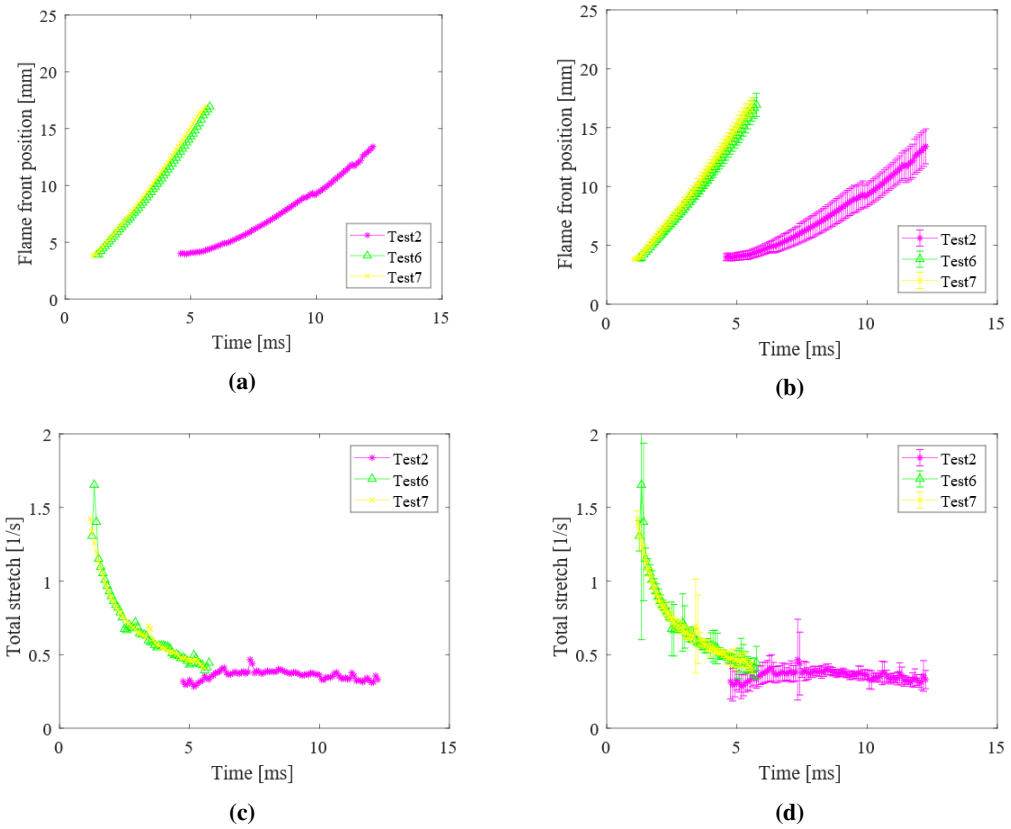

Figure 7.12: *Time evolution of the corrected mean flame front position (a) and mean total flame stretch (c) of the mixtures characterized by an unstretched laminar flame speed of $s_{u0} \simeq 48\ cm/s$ (see Table 7.1). Figures (b) and (d) show same results of Figures (a) and (c), respectively, with in addition the related standard deviations (the error-bars).*

faster flame front is achieved if the pressure is raised from 1 to 5 bar. This agrees to what observed during the cold-flow characterization of the vessel, described in Section 7.2.1. In fact, as observed in Figure 7.5, in case of a pressure increase the integral length scale l_t remains almost constant (Figure 7.5a), while the small time-scale turbulent structures (Taylor λ and Kolmogorov l_k length scales) become increasingly smaller (Figure 7.5b). This reflects on a more energetic turbulence spectrum (more energy is stored in small eddies), hence if the Kolomogorov l_k length scale remains greater than the flame thickness an increased surface enhancement results from the flame-turbulence interaction.

The final investigation concerning the influence of a Lewis number variation on the flame speed behaviour was carried out in presence of two different (and fixed) s_{u0} values:

1. $s_{u0} \simeq 60\ cm/s$ (*Test 1* vs. *Test 5*, Figure 7.11),

2. $s_{u0} \simeq 48\ cm/s$ (*Test 2* vs. *Test 6*/*Test 7*, Figure 7.12).

As Figures 7.11 and 7.12 show, when the Lewis number is reduced from $Le > 1$ to $Le < 1$ by moving from an *Isoocatane*-lean mixture to an *Hydrogen*-lean one the flame front propagation is significantly increased. Moreover, during the initial flame evolution the *Hydrogen*-lean mixtures experience a greater total stretch than the corresponding *Isoocatane*-lean ones (compare at $\bar{R}_{f,corr} \approx 5\ mm$ Figures 7.11a - 7.11c and Figures 7.12a - 7.12c). This is in full agreement with the available literature about the thermodiffusive instabilities of laminar flame speed. In fact, as mentioned in [88, 91], when the mixture Lewis number is

- $Le < 1$ the flame front is unstable and the flame wrinkling, as well as the flame surface, strongly increase with a consequent intensive flame speed enhancement.

- $Le > 1$ the flame front is in a stable condition and both increases of flame wrinkling and flame surface are limited; thus the flame front velocity increase is reduced.

7.3 Summary

In order to further assess the Comprehensive CFD model behavior, proposed in Chapter 1, and to consider possible improvements for its sub-models, additional simplified experimental configurations have to be analyzed.

In this context, the Orleans vessel represents the ideal experimental rig thanks to its very simple configuration. In fact, it is characterized by a spherical constant volume with a central ignition and the capability to generate and control a nearly isotropic turbulence intensity at the ignition zone. This allows to isolate and study several phenomena affecting premixed SI combustion by minimizing the uncertainties and the complexities introduced by classical configurations, as optical engines.

First, its cold-flow characterization was performed thanks to a brief description of the experimental results obtained by Galmiche. In particular, it was underlined that:

- Inside a region of 20 mm radius centred with respect to the spherical vessel, an almost negligible mean flow velocity and a nearly constant and isotropic turbulence

intensity are observed.

- A linear relationship between the velocity fluctuations (namely, the turbulence) and the fan speed is evinced.

- A pressure increase has no influence on the integral length scale of turbulence l_t, while Taylor λ and Kolmogorov l_k length scales becomes smaller. This can be explained by the higher energy amount stored in high frequencies (namely, the small time-scale turbulent structures) when pressure grows up, implying increasingly smaller eddies.

Then, an experimental combustion investigation was carried out to clarify the influence on flame propagation not only of the basic combustion parameters (equivalence ratio, turbulence intensity and pressure) but also of Lewis number, which takes into account the laminar premixed flames intrinsic instabilities (called thermal-diffusional effects). The analysis was performed on an *Isooctane-Air* premixed mixture, except the Lewis number investigation, which was fulfilled through a comparison between two different lean fuel mixtures (*Isooctane-Air* vs. *Hydrogen-Air*) featured by the same unstretched laminar flame speed. Here are summarized the achieved results:

- In presence of an equivalence ratio reduction a leaner mixture was obtained and, as expected, a slower flame speed was experienced.

- The expected positive correlation between flame speed and turbulence intensity was measured. However the flame speed increase seemed not very sensitive to a turbulence intensity variation. This could be explained by the total stretch increase measured by moving to higher turbulence values, which tends to slow down the flame front.

- A faster flame front was observed in presence of a pressure increase. This agrees to what observed during the cold-flow characterization of the vessel: when pressure increases a more energetic turbulence spectrum is achieved, hence if the Kolomogorov l_k length scale remains greater than the flame thickness the flame-turbulence interaction results in an increased surface enhancement.

- A Lewis number reduction from $Le > 1$ to $Le < 1$ significantly increased the flame front propagation. Moreover, during the initial flame evolution the *Hydrogen*-lean mixtures ($Le < 1$) experienced a greater total stretch than the corresponding *Isoocatane*-lean ones ($Le > 1$). This is in full agreement with the available literature about the thermodiffusive instabilities of laminar flame speed. In fact, when:

  1. $Le < 1$ the flame front is unstable and the flame wrinkling, as well as the flame surface, strongly increase with a consequent intensive flame speed enhancement.
  2. $Le > 1$ the flame front is in a stable condition and both increases of flame wrinkling and flame surface are limited; thus the flame front velocity increase is reduced.

Conclusions and future developments

The evolution of transportation system, which nowadays represents almost a quarter of Europe's greenhouse gas emissions and is the main cause of air pollution in cities, requires that high efficient and ultra clean IC engines using renewable low carbon fuels become a key element of an electrified/hybridised powertrain. In this context, the Spark-Ignition (SI) engine plays a key role because of its capability to exploit alternative fuels. Therefore, the correct prediction of in-cylinder phenomena, such as combustion and air/fuel mixture formation, becomes crucial in the development of future SI engines.

The main target of this thesis work is the development of a Comprehensive CFD Model for premixed combustion of SI engines. An improved version of the Artificially Thickened Flame Model (ATFM) is also developed, in order to get additional insight in available turbulent combustion models and to provide an alternative to the one used in this thesis work (i.e. the Coherent Flamelet Model - CFM).

The proposed Comprehensive Model was validated on a pressurized, constant-volume vessel (Michigan Tech experimental rig) under different conditions of turbulence, air/-fuel ratio and pressure. The improved ATFM version was assessed on the Darmstadt TSF burner, characterized by three concentric pipes, under a *lean-lean* charge stratification and assuming adiabatic conditions.

Finally, first steps towards additional validations of the aforementioned models were

also considered. The heat-losses at TSF burner exit were investigated through Conjugated Heat Transfer (CHT) simulations, as a first step towards ATFM non-adiabatic applications. Premixed combustion tests were carried out on the Orleans experimental rig, a spherical constant volume vessel characterized by a central ignition, with the purpose to further assess the proposed Comprehensive Model behavior and to consider possible improvements for its sub-models.

All numerical simulations were carried out on the open-source platform *OpenFOAM®*, which involves a 3-D finite volume discretization, and the additional use of suitable libraries (*Lib-ICE*) developed for combustion modeling.

The Comprehensive CFD Model

- The proposed CFD model, developed for premixed SI engines combustion, is characterized by a *comprehensive* structure with an *Eulerian-Lagrangian* run-time coupling. The Lagrangian framework allows to account for the electrical circuit effects with the minimum computational effort. The final objective was to simulate in detail the spark-discharge evolution and the further turbulent flame propagation.
- Specific sub-models are included to properly consider each phenomenon affecting the combustion process. This methodology has a twofold advantage: it allows to handle the interplay between different and complex phenomena with a clear and schematic work-flow, providing at the same time unlimited and smooth extendibility of current modelling capabilities.
- The developed approach accounts properly for the influence of:

  1. the electrical circuit features,
  2. possible laminar flame instabilities,
  3. *flame-turbulence* interaction

  on the ignition and the further combustion process. In particular:

  – Specific improvements concerned the first two aforementioned phenomena, such as the effective Lewis number prediction of a premixed mixture and different strategies to model the arc and glow phases of the spark-discharge.

  - On the other hand, the third phenomenon was improved thanks to a modified strategy to consider flame stretch effects into ignition and premixed combustion prediction. In particular, the thermal effects of the electrical circuit (modelled by a set of Lagrangian particles, introduced to mimic the plasma channel shape) were fully decoupled from the chemical contribution of the laminar/turbulent flame speed. This last aspect was completely carried out by the Eulerian CFD solver, where a flame stretch model, recently verified by DNS studies, was adopted.

Validation

- The aforementioned strategies to model flame stretch and electrical circuit effects were preliminary assessed over simplified configurations, in order to understand separately their predicting capabilities.

  Considering the flame stretch, numerical simulations were carried out using the proposed two different approaches:

  - the Herweg and Maly
  - the Bradley, Lau and Lawes

  stretch models. From achieved results, both of them can fairly predict the flame stretch phenomenon.

  Regarding the electrical circuit effects, two different systems were investigated:

  - the TCI, characterized by long discharge times (of the order of ms),
  - the CDI, characterized by short discharge durations (μs).

  The results, achieved under a variation of the spark-gap mean flow velocity, allowed to assert that numerical results were in accordance to available experimental findings on both ignition system types. This demonstrated the capability of the model to predict completely different spark events.

- The Michigan Tech experimental rig, characterized by a pressurized, constant-volume combustion vessel, was chosen to validate the proposed Comprehensive CFD model under different conditions of turbulence, air/fuel ratio and pressure.

In this configuration, a shrouded rotating fan coupled with a guide tube generates directly to the ignition zone a jet of fresh mixture with highly inhomogeneous flow and turbulence conditions.

First, an experimental campaign on the combustion process of lean and diluted *Propane-Air* mixtures was carried out under high temperature and pressure conditions at different turbulence levels. The flame kernel propagation rate was analyzed in terms of turbulence effect, pressure influence and flame structure.

Then, a non-reacting flow analysis was performed:

1. to initialize the flow field for combustion calculations,
2. to verify the proposed CFD setup in terms of turbulence model.

Regarding this last aspect, despite a not perfect agreement between PIV numerical and experimental trends under high fan speed velocities, the results could be considered rather satisfactory at all tested conditions.

Afterwards, combustion simulations were carried out. Computed results were compared consistently with the experimental data and rather satisfactory results were achieved for all tested conditions. In agreement with previous works on such topic, it was found that flame stretch mainly influences combustion development during its early propagation stage, while its effects vanish afterwards.

Finally, a comparison between numerical-only mixture burnt masses was carried out. As expected, when a self-sustained flame was developed, an increase of turbulence intensity corresponded to a faster flame front propagation, while a reduction of equivalence ratio produced a slower flame speed. This demonstrated the model capability to predict consistently the effects of fundamental parameters on the combustion development.

Future developments

- From achieved results, it is possible to conclude that the proposed model can be applied with success also when turbulence and velocity conditions at the spark gap are highly inhomogeneous. Moreover, thanks to modifications of the ignition system model, also innovative ignition strategies could be tested and developed.

As a consequence, the model is ready to be tested on actual SI engines to simulate:

1. advanced combustion modes (e.g. ultra-lean, high-EGR conditions);
2. innovative ignition strategies (e.g. high-current, constant-current discharges).

- Despite the performed validation concerned only the average combustion cycle, because of the adopted RANS turbulence modelling, the applied numerical approach is general. Therefore, the stochastic nature of large scale eddies inside the in-cylinder flow can be considered by the use of an LES strategy for turbulence description. This would consequently provide the possibility to simulate and predict the Cyclic Combustion Variability (CCV), a major issue in IC engines.

- However, in order to further assess the Comprehensive CFD model behavior, proposed in this thesis work, and to consider possible improvements for its submodels, additional simplified experimental configurations have to be analyzed.

  The Orleans vessel represents the ideal experimental rig to deepen the assessment of proposed model, thanks to its very simple configuration. In fact, it is characterized by a spherical constant volume with a central ignition and the capability to generate and control a nearly isotropic turbulence intensity at the ignition zone. This allows to isolate and study several phenomena affecting premixed SI combustion by minimizing the uncertainties and the complexities introduced by classical configurations, as optical engines.

- As a first step towards a future numerical analysis, the complete experimental characterization of the Orleans vessel was carried out in this thesis work. First, its cold-flow characterization was performed thanks to a brief description of the experimental results already available in literature. Then, an experimental combustion investigation was carried out to clarify the influence on flame propagation not only of the basic combustion parameters (equivalence ratio, turbulence intensity and pressure) but also of Lewis number, which takes into account the laminar premixed flames intrinsic instabilities (called thermal-diffusional effects). Therefore, a future numerical investigation will clarify the Comprehensive CFD model capabilities in predicting:

1. the influence of basic combustion parameters on a flame propagating under highly controlled conditions (namely, almost zero flow velocity and nearly isotropic turbulence intensity at the ignition zone),
2. the effects of a Lewis number variation on the early flame kernel development.

The Artificially Thickened Flame Model

- In the context of an LES turbulence description, numerical simulations of turbulent premixed reacting flows are not able to resolve the inner structure of the flame front on common computational grids. To overcome this difficulty the Artificially Thickened Flame Model (ATFM) can be adopted: it increases artificially the flame thickness to allow the reaction layer resolution on usual computational grids, solving the aforementioned difficulty.
- The proposed ATFM version is characterized by the following features:
  - The thickening factor F definition is based on the local mesh resolution (*grid adaptive*), in order to minimize the modelling effort (thicker flame fronts result in more modified *flame-turbulence* interactions).
  - Several formulation of the efficiency function E are available to increase the flame speed with no additional modification to its thickness. This is necessary in order to compensate the lost *flame-turbulence* interaction in terms of total flame surface reduction (namely, the lost wrinkling effect), when the reaction layer is artificially thickened. In particular, also a dynamic formulation for E computation is available, where some resolved flame wrinkling is analyzed in order to match the modelled sub-grid scale wrinkling trend with the computed one.
  - The thickening concept is coupled with a tabulation strategy to include detailed chemistry effects without prohibitive flame thickening.
  - A flame sensor Ω is used to modify the diffusion terms of conservation equations only at the reacting region, to ensure a correct pure mixing simulation in case of a generic stratified mixture. In particular, the *Flame sensor based*

on Progress Variable Gradient and Source Term is here proposed because it represents the best solution between the flame sensors available in literature.

- In case a small scale stratification is present and the reaction layer is overlapped to a not negligible mixing layer (with a generic orientation), to correctly follow the ATF concept the thickening procedure should be applied not only on the progress variable gradient (flame thickening) but also on the mixture fraction gradient component parallel to the flame normal direction. This approach can be called *directional thickening* of the $\vec{\nabla}\widetilde{Z}$ and a strategy to apply this concept with a fully-implicit numerical formulation is here proposed.

- As a supplement for the ATFM application, information on numerical strategies for:

  1. the filtering procedure of LES fields,
  2. the evaluation of the sub-grid scale turbulence intensity u'_{Δ},

  are also reported.

Validation

- The experimental configuration of the Darmstadt Turbulent Stratified Flame (TSF) burner was selected to assess the ATFM behaviour. The experimental rig is characterized by three concentric pipes: a central *Pilot*, whose aim is to release a flow of burnt products, and two outer concentric tubes ejecting fresh mixture, called *Slot 1* and *Slot 2*. During this first investigation, a *lean-lean* charge stratification was analyzed and adiabatic conditions were assumed.

- First, the proposed *Flame sensor based on Progress Variable Gradient and Source Term* was successfully tested on a 1D flame configuration. Here are reported its observed features:

  1. It allows to avoid the "cascade" thickening effect, namely an uncontrolled thickening of the flame.
  2. Although it slightly deforms the flame front, the capability to predict correctly the laminar flame velocity is not affected.

3. It is easy to tabulate and considers all relevant characteristics of a premixed flame, independently from the composition and progress variable definition.

- Then, a qualitative model behaviour was analyzed in terms of:
  - characteristic ATFM fields distributions (F, E and Ω),
  - evaluation of the $\vec{\nabla}\widetilde{Z}$ directional thickening.

  As observed, all ATFM fields distributions follow with a reasonable accuracy the experimental flame shape detected by photographs of the investigated working condition. For what concerns the $\vec{\nabla}\widetilde{Z}$ directional thickening, a comparison was carried out with Kuenne's strategy to simply thicken the $\vec{\nabla}\widetilde{Z}$ without considering the flame orientation. As shown by numerical results, the directional thickening approach allows to consistently extend the ATF concept also to Z field, because along the flame tangential direction the $\vec{\nabla}\widetilde{Z}$ is not affected by the thickening procedure. Conversely, with Kuenne's strategy the mixing layer is thickened according to its own direction, as expected.

- Afterwards, the ATFM assessment was finally completed by a quantitative comparison between experimental findings collected on TSF burner and the computed numerical results. Here below are listed the drawn conclusions for each investigated magnitude:

  1. *Reacting axial velocity*
     - No significant differences were observed by comparing numerical results obtained with the different thickening solutions of the mixture fraction gradient, in particular: $\vec{\nabla}\widetilde{Z}$ thickened according to its own direction (Kuenne's strategy, called *ZoldCorr*), thickened along the flame normal direction (*Zcorr*, also called directional thickening) and not thickened (*ZnoCorr*).

       The lack of difference between *ZoldCorr* and *Zcorr* could be explained by a parallel alignment of scalar gradients defined by the intersection angle α of the mixing layer ($\vec{\nabla}\widetilde{Z}$) and the reaction layer ($\vec{\nabla}\widetilde{Y}_c$), as observed by Kuenne. On the other hand, the similarity between thickening (*ZoldCorr*,

Zcorr) and not (*ZnoCorr*) the mixture fraction gradient, especially at high axial positions, could be explained by the Z diffusion effect.

- At all investigated numerical conditions, the mean axial velocity values above the Pilot region were significantly overestimated with respect to experimental findings. This could be a consequence of the adiabatic conditions adopted during this first ATFM assessment. However, also a possible recalibration of the imposed axial velocity value for the Pilot burnt gases can be considered.
- An increase of the flame thickening generates a flow field modification. In particular, the axial velocity values increase nearby the region where the flame is positioned.
- Close to burner exit section the experimental velocity trend seemed rather well captured. On the other hand, at higher axial positions the velocity distribution was not perfectly matched, also if the transition from the initial bump structure (due to the tripartite flow) to smoother conditions detected downstream seemed predicted.

2. *Reacting temperature*

- No significant differences were observed by comparing numerical results obtained with the different thickening solutions of the mixture fraction gradient (*ZoldCorr*, *Zcorr* and *ZnoCorr*). The physical explanation of this phenomenon is similar to what concluded for the reacting axial velocity.
- The experimental burnt mixture temperature close to the centerline is always lower than computed one at the investigated axial positions. This numerical overestimation can be explained by the neglect of heat losses at Pilot walls, because adiabatic conditions were assumed.
- The agreement between numerical and experimental mean temperature profiles was rather satisfactory, especially with the 10 cells thickening.
- At high radial and axial positions, the experimental mean temperature profile shows a second peak that numerical simulations were not able to detect (in this region the temperature is under predicted). This phenomenon is coupled with an increased standard deviation and the same

inability to numerically predict the experimental measurement. Form a previous work (Kuenne), it was concluded that a large scale phenomenon is taking place, but the physical mechanism requires further experimental investigations. From the numerical point of view, the lean flammability limit choice concerning the tabulated chemistry could be a possible cause of this prediction inability, because the analyzed position is characterized by rather lean conditions.

- Since the resolved fluctuations decrease with the decreasing ratio *turbulent flame brush thickness/flame thickness*, the ATF concept generates a numerical underestimation of temperature fluctuating part. This explains the main difference observed between experimental findings and computed results. However, the experimental tendency of larger fluctuations at higher axial positions was numerically predicted.

3. *Reacting mixture fraction*

   - The comparison between numerical results obtained with the different thickening solutions of the mixture fraction gradient (*ZoldCorr*, *Zcorr* and *ZnoCorr*) did not highlighted significant differences at low axial positions, because in this region the mixing layer ($\vec{\nabla}\widetilde{Z}$) and the reaction layer ($\vec{\nabla}\widetilde{Y}_c$) are not yet overlapped.
   - Instead, when at higher axial positions the flame starts to experience the mixture stratification, a difference between thickening (*ZoldCorr*, *Zcorr*) and not (*ZnoCorr*) the mixture fraction gradient is appreciated. In particular, the Z gradient is smoothed only in the overlapping region. This demonstrates how the flame sensor application allow to limit the ATF concept only in the flame thickness region, without affecting pure mixing zones.
   - The lack of difference between *ZoldCorr* and *Zcorr* could be explained similarly to what concluded for mean reacting axial velocity trends.
   - Finally, the general agreement between numerical computations and experimental measurements could be considered satisfactory.

Future developments

- In this thesis work, a novel strategy to apply the thickening procedure not only on the progress variable gradient (flame thickening) but also on the mixture fraction gradient component parallel to the flame normal direction (as required by the ATF concept) is proposed and tested with a fully-implicit numerical formulation. This is called *directional thickening* and allows the ATFM application to generic industrial applications (e.g. direct-injection IC engines) with a robust numerical stability.

  However, the TSF burner configuration does not seem the best choice to fully assess the directional thickening behaviour, because of a parallel alignment between $\vec{\nabla}\widetilde{Z}$ and $\vec{\nabla}\widetilde{Y}_c$ at their overlapping region, as also observed by Kuenne. Therefore, a better experimental configuration should be selected to analyze in deep the proposed improvement, before applying the ATFM on actual engines simulations.

- The ATFM general assessment could be still carried out on the TSF burner configuration. However, as shown by the performed CHT investigation, heat-losses at Pilot tube exit can no more be neglected during future investigations. In fact, as already assessed by previous works (Fiorina and Kuenne), under adiabatic assumptions a flame anchored to the burner lip was predicted, while non-adiabatic simulations evidenced a flame lift-off and a better agreement with experimental findings of temperature and species concentrations.

- Therefore, as a first step towards non-adiabatic investigations of the TSF burner with the proposed ATFM version, *Conjugated Heat Transfer* (CHT) simulations were carried out in the aforementioned heat-losses region.

  First, a calibration procedure of:

  1. the flame brush extension, positioned where the flame front approaches the inner Pilot wall,
  2. the ceramic thermal conductivity $k_{ceramic}$ of Pilot pipe wall

  was carried out. From a comparison between available experimental findings and numerical results, it was concluded that $k_{ceramic} = 3.1\ [W/(m\ K)]$ combined to

a flame brush value of $0.3\ mm$ represent the optimal setup.

Then, CHT simulations were carried out with different strategies to compute the properties of Pilot burnt products. In the light of achieved results, the following conclusions can be drawn:

1. The radial heat-losses experienced by the burnt products nearby the Pilot exit section are not negligible and should be considered in a future detailed TSF burner investigation.
2. The heat conduction phenomenon along ceramic wall towards colder mixture regions (located upstream the flame attachment position) is not negligible and reduces the "nearly constant" temperature region.
3. In case simplified boundary conditions would be used for Pilot wall surfaces, constant values of temperature can be imposed, in particular $T_{pilot\ side} \approx 837\ K$ and $T_{slot1\ side} \approx 827\ K$. This can be performed according to the "nearly constant" value assumed by the temperature along both wall sides from the burner exit section until $\approx 15\ mm$ inside the pipe.
4. If detailed temperature boundary conditions would be used for Pilot wall surfaces, the temperature distributions computed by CHT simulations have to be imposed.

Bibliography

[1] Nitrogen - national institute of standards and technology. http://webbook.nist.gov/cgi/cbook.cgi?ID=C7727379&Mask=20. Accessed: 2018-03-21.

[2] R. G. Abdel-Gayed, D. Bradley, and M. Lawes. Turbulent burning velocities: a general correlation in terms of straining rates. *Proceedings of the Royal Society of London A: Mathematical, Physical and Engineering Sciences*, 414(1847):389–413, 1987.

[3] R. J. Adrian. Twenty years of particle image velocimetry. *Exp. Fluids*, 39(2):159–169, 2005.

[4] C. Angelberger, D. Veynante, and F. Egolfopoulos. Les of chemical and acoustic forcing of a premixed dump combustor. *Flow, Turbulence and Combustion*, 65(2):205–222, 2000.

[5] C. Angelberger, D. Veynante, F. Egolfopoulos, and T. Poinsot. Large eddy simulations of combustion instabilities in premixed flames. In *Proceedings of the Summer Program 1998*, pages 61–82, 1998.

[6] R.S. Barlow and J.H. Frank. Effects of turbulence on species mass fractions in methane/air jet flames. *Symposium (International) on Combustion*, 27(1):1087 – 1095, 1998. Twenty-Seventh Sysposium (International) on Combustion Volume One.

[7] G. K. Batchelor. The effect of homogeneous turbulence on material lines and surfaces. *Proceedings of the Royal Society of London A*, 213(1114), 1952.

[8] M. Boileau, G. Staffelbach, B. Cuenot, T. Poinsot, and C. Bérat. Les of an ignition sequence in a gas turbine engine. *Combustion and Flame*, 154(1):2 – 22, 2008.

[9] R. Borghi. *On the Structure and Morphology of Turbulent Premixed Flames*, pages 117–138. Springer US, 1985.

[10] N. Bouvet, F. Halter, C. Chauveau, and Y. Yoon. On the effective lewis number formulations for lean hydrogen/hydrocarbon/air mixtures. *International Journal of Hydrogen Energy*, 38(14):5949 – 5960, 2013.

[11] D. Bradley. How fast can we burn? *Symposium (International) on Combustion*, 24(1):247 – 262, 1992. Twenty-Fourth Symposium on Combustion.

[12] D. Bradley, M. Z. Haq, R. A. Hicks, T. Kitagawa, M. Lawes, C. G. W. Sheppard, and R. Woolley. Turbulent burning velocity, burned gas distribution, and associated flame surface definition. *Combustion and Flame*, 133(4):415 – 430, 2003.

[13] D. Bradley, A. K. C. Lau, M. Lawes, and F. T. Smith. Flame stretch rate as a determinant of turbulent burning velocity. *Philosophical Transactions of the Royal Society of London A: Mathematical, Physical and Engineering Sciences*, 338(1650):359–387, 1992.

[14] D. Bradley, M. Lawes, and C. G. W. Sheppard. Study of turbulence and combustion interaction: measurement and prediction of the rate of turbulent burning. Technical report, Leeds University, 1995. Periodic report: 01.01.1995 - 30.06.1995.

[15] K. N. C. Bray and R. S. Cant. Some applications of kolmogorov's turbulence research in the field of combustion. *Proceedings: Mathematical and Physical Sciences*, 434(1890):217–240, 1991.

[16] H. Brenner. Fluid mechanics in fluids at rest. *Phys. Rev. E*, 86(1), 2012.

[17] P. Brequigny. *Fuel influence on combustion in Spark-Ignition Engine - Flame Stretch Impact*. phdthesis, Université d'Orléans, December 2014.

[18] P. Brequigny, C. Endouard, C. Mounaïm-Rousselle, and F. Foucher. An experimental study on turbulent premixed expanding flames using simultaneously schlieren and tomography techniques. *Exp. Therm Fluid Sci.*, December 2017.

[19] V. Brinzea, D. Razus, M. Mitu, and D. Oancea. Overall activation energy of propane-air combustion in laminar flames. *Ars Docendi Publishing House*, 1:35–41, 2009.

[20] J. Brübach, J. Janicka, and A. Dreizler. An algorithm for the characterisation of multi-exponential decay curves. *Optics and Lasers in Engineering*, 47(1):75–79, 2009.

[21] J. Brübach, C. Pflitsch, A. Dreizler, and B. Atakan. On surface temperature measurements with thermographic phosphors: A review. *Progress in Energy and Combustion Science*, 39(1):37 – 60, 2013.

[22] T. D. Butler and P. J. O'Rourke. A numerical method for two dimensional unsteady reacting flows. *Symposium (International) on Combustion*, 16(1):1503 – 1515, 1977.

[23] B. Bédat and R. K. Cheng. Experimental study of premixed flames in intense isotropic turbulence. *Combustion and Flame*, 100(3):485 – 494, 1995. 25th Symposium (International) on Combustion Papers.

[24] S. Candel, C. Huynh, and T. Poinsot. Some modeling methods of combustion instabilities. In *Unsteady Combustion*, volume 306 of *NATO ASI Series E*, pages 83–112. Kluwer Academic Publishers, 1996.

[25] S. Candel and T. Poinsot. Flame stretch and the balance equation for the flame area. *Combust. Sci. Technol.*, 70(1-3):1–15, 1990.

[26] F. Charlette, C. Meneveau, and D. Veynante. A power-law flame wrinkling model for les of premixed turbulent combustion part i: non-dynamic formulation and initial tests. *Combustion and Flame*, 131(1):159 – 180, 2002.

[27] F. Charlette, C. Meneveau, and D. Veynante. A power-law flame wrinkling model for les of premixed turbulent combustion part ii: dynamic formulation. *Combustion and Flame*, 131(1):181 – 197, 2002.

[28] C. R. Choi and K. Y. Huh. Development of a coherent flamelet model for a spark-ignited turbulent premixed flame in a closed vessel. *Combustion and Flame*, 114(3):336 – 348, 1998.

[29] J. D. Cobine. *Gaseous Conductors: Theory and Engineering Applications*. Dover Publications, 1958.

[30] O. Colin and A. Benkenida. The 3-zones extended coherent flame model (ecfm3z) for computing premixed/diffusion combustion. *Oil & Gas Science and Technology*, 59(6):593–609, 2004.

[31] O. Colin, F. Ducros, D. Veynante, and T. Poinsot. A thickened flame model for large eddy simulations of turbulent premixed combustion. *Phys. Fluids*, 12(7), 2000.

[32] R. Dahms, M. C. Drake, T. D. Fansler, T. W. Kuo, and N. Peters. Understanding ignition processes in spray-guided gasoline engines using high-speed imaging and the extended spark-ignition model sparkcimm. part a: Spark channel processes and the turbulent flame front propagation. *Combustion and Flame*, 158(11):2229 – 2244, 2011.

[33] R. Dahms, M. C. Drake, T. D. Fansler, T. W. Kuo, and N. Peters. Understanding ignition processes in spray-guided gasoline engines using high-speed imaging and the extended spark-ignition model sparkcimm: Part b: Importance of molecular fuel properties in early flame front propagation. *Combustion and Flame*, 158(11):2245 – 2260, 2011.

[34] R. Dahms, T. D. Fansler, M. C. Drake, T. W. Kuo, A. M. Lippert, and N. Peters. Modeling ignition phenomena in spray-guided spark-ignited engines. *Proceedings of the Combustion Institute*, 32(2):2743 – 2750, 2009.

[35] G. Damköhler. Der einfluss der turbulenz auf die flammengeschwindigkeit in gasgemischen (the effect of turbulence on the flame velocity in gas mixtures). *Zeitschrift fuer Elektrochemie und Angewandte Physikalische Chemiw*, 46(11):601–626, 1940. (translation: NACA-TM-1112, 1947).

[36] A. D'Angola, G. Colonna, C. Gorse, and M. Capitelli. Thermodynamic and transport propertiesin equilibrium air plasmas in a wide pressure and temperature range. *The European Physical Journal D*, 46(1):129–150, Jan 2008.

[37] J. M. Duclos and O. Colin. Arc and kernel tracking ignition model for 3d spark-ignition engine calculations. In *Proceedings of COMODIA*, pages 343–350, 2001.

[38] L. Durand and W. Polifke. Implementation of the thickened flame model for large eddy simulation of turbulent premixed combustion in a commercial solver. In *ASME Turbo Expo 2007*, volume 2, pages 869–878, 2007.

[39] S. Falfari and G. M. Bianchi. Development of an ignition model for s.i. engines simulation. In *SAE Technical Paper*, number 2007-01-0148, 2007.

[40] T. D. Fansler, D. L. Reuss, V. Sick, and R. Dahms. Combustion instability in spray-guided stratified-charge engines: A review. *International Journal of Engine Research*, 16(3):260–305, feb 2015.

[41] B. Fiorina, O. Gicquel, L. Vervisch, S. Carpentier, and N. Darabiha. Approximating the chemical structure of partially premixed and diffusion counterflow flames using fpi flamelet tabulation. *Combustion and Flame*, 140(3):147 – 160, 2005.

[42] B. Fiorina, R. Mercier, G. Kuenne, A. Ketelheun, A. Avdić, J. Janicka, D. Geyer, A. Dreizler, E. Alenius, C. Duwig, P. Trisjono, K. Kleinheinz, S. Kang, H. Pitsch, F. Proch, F. Cavallo Marincola, and A. Kempf.

Challenging modeling strategies for les of non-adiabatic turbulent stratified combustion. *Combustion and Flame*, 162(11):4264 – 4282, 2015.

[43] F. Fuest. *1D Raman/Rayleigh-scattering and CO-LIF measurements in laminar and turbulent jet flames of dimethyl ether using a hybrid data reduction strategy*. PhD thesis, TU-Darmstadt, 2011.

[44] F. Fuest, R. S. Barlow, J. Y. Chen, and A. Dreizler. Raman/rayleigh scattering and co-lif measurements in laminar and turbulent jet flames of dimethyl ether. *Combustion and Flame*, 159(8):2533 – 2562, 2012. Special Issue on Turbulent Combustion.

[45] F. Fuest, R. S. Barlow, D. Geyer, F. Seffrin, and A. Dreizler. A hybrid method for data evaluation in 1-d raman spectroscopy. *Proceedings of the Combustion Institute*, 33(1):815 – 822, 2011.

[46] N. Fuhrmann, J. Brübach, and A. Dreizler. On the mono-exponential fitting of phosphorescence decays. *Appl. Phys. B*, 116(2):359–369, 2013.

[47] B. Galmiche. *Caractérisation expérimentale des flammes laminaires et turbulentes en expansion*. phdthesis, Université d'Orléans, 2014.

[48] B. Galmiche, N. Mazellier, F. Halter, and F. Foucher. Turbulence characterization of a high-pressure high-temperature fan-stirred combustion vessel using ldv, piv and tr-piv measurements. *Exp. Fluids*, 55(1636), 2014.

[49] M. Germano, U. Piomelli, P. Moin, and W. H. Cabot. A dynamic subgrid-scale eddy viscosity model. *Phys. Fluids A*, 3(7):1760–1765, 1991.

[50] G. K. Giannakopoulos, A. Gatzoulis, C. E. Frouzakis, M. Matalon, and A. G. Tomboulides. Consistent definitions of "flame displacement speed" and "markstein length" for premixed flame propagation. *Combustion and Flame*, 162(4):1249 – 1264, 2015.

[51] O. Gicquel, N. Darabiha, and D. Thévenin. Liminar premixed hydrogen/air counterflow flame simulations using flame prolongation of ildm with differential diffusion. *Proceedings of the Combustion Institute*, 28(2):1901 – 1908, 2000.

[52] Ö. L. Gülder. Correlations of laminar combustion data for alternative s.i. engine fuels. In *SAE Technical Paper*, number 841000, 1984.

[53] C. Hasse, M. Bollig, N. Peters, and H.A. Dwyer. Quenching of laminar iso-octane flames at cold walls. *Combust. Flame*, 122(1):117 – 129, 2000.

[54] R. Herweg and R. R. Maly. A fundamental model for flame kernel formation in s. i. engines. In *SAE Technical Paper*, number 922243, 1992.

[55] J. B. Heywood. *Internal Combustion Engine Fundamentals*. 1988.

[56] R. A. Hicks, M. Lawes, C. G. W. Sheppard, and B. J. Whitaker. Multiple laser sheet imaging investigation of turbulent flame structure in a spark ignition engine. In *SAE Technical Paper Series*. SAE International, oct 1994.

[57] A. Hosseinzadeh, A. Sadiki, and J. Janicka. Assessment of the dynamic sgs wrinkling combustion modeling using the thickened flame approach coupled with fgm tabulated detailed chemistry. *Flow, Turbulence and Combustion*, 96(4):939–964, Jun 2016.

[58] G. Joulin and T. Mitani. Linear stability analysis of two-reactant flames. *Combustion and Flame*, 40:235 – 246, 1981.

[59] B. Karlovitz, D.W. Denniston, D.H. Knapschaefer, and F.E. Wells. Studies on turbulent flames: A. flame propagation across velocity gradients b. turbulence measurement in flames. *Symposium (International) on Combustion*, 4(1):613 – 620, 1953. Fourth Symposium (International) on Combustion.

[60] A. R. Kerstein, W. T. Ashurst, and F. A. Williams. Field equation for interface propagation in an unsteady homogeneous flow field. *Phys. Rev. A*, 37:2728–2731, Apr 1988.

[61] J. Kim and R. W. Anderson. Spark anemometry of bulk gas velocity at the plug gap of a firing engine. In *SAE Technical Paper*, number 952459, 1995.

[62] T. Kissel, E. Baum, A. Dreizler, and J. Brübach. Two-dimensional thermographic phosphor thermometry using a cmos high speed camera system. *Applied Physics B*, 96(4):731–734, Sep 2009.

[63] A. Kolmogorov. Dissipation of energy in locally isotropic turbulence. *Doklady Akademiia Nauk SSSR*, 32:16–18, 1941.

[64] A. Kolmogorov. The local structure of turbulence in incompressible viscous fluid for very large reynolds' numbers. *Doklady Akademiia Nauk SSSR*, 30:301–305, 1941.

[65] G. Kuenne, M. Euler, A. Ketelheun, A. Avdic, A. Dreizler, and J. Janicka. A numerical study of the flame stabilization mechanism being determined by chemical reaction rates submitted to heat transfer processes. *Zeitschrift für Physikalische Chemie*, 229(5), jan 2015.

[66] G. Kuenne, A. Ketelheun, and J. Janicka. Les modeling of premixed combustion using a thickened flame approach coupled with fgm tabulated chemistry. *Combustion and Flame*, 158(9):1750 – 1767, 2011.

[67] G. Kuenne, F. Seffrin, F. Fuest, T. Stahler, A. Ketelheun, D. Geyer, J. Janicka, and A. Dreizler. Experimental and numerical analysis of a lean premixed stratified burner using 1d raman/rayleigh scattering and large eddy simulation. *Combustion and Flame*, 159(8):2669 – 2689, 2012. Special Issue on Turbulent Combustion.

[68] K. K. Kuo. *Principles of Combustion*. Wiley, 1986.

[69] C. Kähler, B. Sammler, and J. Kompenhans. Generation and control of tracer particles for optical flow investigations in air. *Exp. Fluids*, 33(6):736–742, 2002.

[70] J. P. Legier, T. Poinsot, and D. Veynante. Dynamically thickened flame les model for premixed and non-premixed turbulent combustion. In *Proceedings of the Summer Program 2000*, pages 157–168, 2000.

[71] D. K. Lilly. A proposed modification of the germano subgrid-scale closure method. *Phys. Fluids A*, 4(3):633–635, 1992.

[72] T. Lucchini, L. Cornolti, G. Montenegro, G. D'Errico, M. Fiocco, A. Teraji, and T. Shiraishi. A comprehensive model to predict the initial stage of combustion in si engines. In *SAE Technical Paper*, number 2013-01-1087, 2013.

[73] U. Maas and S. B. Pope. Simplifying chemical kinetics: Intrinsic low-dimensional manifolds in composition space. *Combustion and Flame*, 88(3):239 – 264, 1992.

[74] E. Mallard and H. Le Chatelier. Recherches expérimentales et théorétiques sur la combustion des mélanges gazeux explosifs. *Ann. Mines*, 1883.

[75] K. R. McManus, T. Poinsot, and S.M. Candel. A review of active control of combustion instabilities. *Progress in Energy and Combustion Science*, 19(1):1 – 29, 1993.

[76] A. Melling. Tracer particles and seeding for particle image velocimetry. *Meas. Sci. Technol.*, 8(12):1406, 1997.

[77] C. Meneveau and T. Poinsot. Stretching and quenching of flamelets in premixed turbulent combustion. *Combustion and Flame*, 86(4):311 – 332, 1991.

[78] M. Metghalchi and J. C. Keck. Laminar burning velocity of propane-air mixtures at high temperature and pressure. *Combustion and Flame*, 38:143 – 154, 1980.

[79] M. Metghalchi and J. C. Keck. Burning velocities of mixtures of air with methanol, isooctane, and indolene at high pressure and temperature. *Combustion and Flame*, 48:191 – 210, 1982.

[80] H. B. Michaelson. The work function of the elements and its periodicity. *J. Appl. Phys.*, 48(11), 1977.

[81] V. Moureau, P. Domingo, and L. Vervisch. From large-eddy simulation to direct numerical simulation of a lean premixed swirl flame: Filtered laminar flame-pdf modeling. *Combustion and Flame*, 158(7):1340 – 1357, 2011.

[82] N. Nordin. *Complex Chemistry Modeling of Diesel Spray Combustion*. phdthesis, Chalmers University of Technology, 2001.

[83] M. O'Connaire, H. J. Curran, J. M. Simmie, W. J. Pitz, and C. K. Westbrook. A comprehensive modeling study of hydrogen oxidation. *Int. J. Chem. Kinet.*, 36:603 – 622, 2004.

[84] P. J. O'Rourke and F. V. Bracco. Two scaling transformations for the numerical computation of multidimensional unsteady laminar flames. *Journal of Computational Physics*, 33(2):185 – 203, 1979.

[85] N. Pashley, R. Stone, and G. Roberts. Ignition system measurement techniques and correlations for breakdown and arc voltages and currents. In *SAE Technical Paper*, number 2000-01-0245, 2000.

[86] N. Peters. Laminar flamelet concepts in turbulent combustion. In *Twenty-first Symposium (International) on Combustion*, pages 1231 – 1250, 1986.

[87] N. Peters. The turbulent burning velocity for large-scale and small-scale turbulence. *J. Fluid Mech.*, 384:107–132, 1999.

[88] N. Peters. *Turbulent Combustion*. Cambridge Monographs on Mechanics. Cambridge University Press, 2000.

[89] T. Poinsot and S. M. Candel. A nonlinear model for ducted flame combustion instabilities. *Combustion Science and Technology*, 61(4-6):121–153, 1988.

[90] T. Poinsot, A. C. Trouve, D. Veynante, S. Candel, and E. J. Esposito. Vortex-driven acoustically coupled combustion instabilities. *J. Fluid Mech.*, 177:265–292, 1987.

[91] T. Poinsot and D. Veynante. *Theoretical and Numerical Combustion*. R.T. Edwards, Inc., second edition, 2005.

[92] T. Poinsot, D. Veynante, and S. Candel. Diagrams of premixed turbulent combustion based on direct simulation. *Symposium (International) on Combustion*, 23(1):613 – 619, 1991. Twenty-Third Symposium (International) on Combustion.

[93] T. Poinsot, D. Veynante, and S. Candel. Quenching processes and premixed turbulent combustion diagrams. *J. Fluid Mech.*, 228:561–606, 1991.

[94] F. Proch and A. M. Kempf. Numerical analysis of the cambridge stratified flame series using artificial thickened flame les with tabulated premixed flame chemistry. *Combustion and Flame*, 161(10):2627 – 2646, 2014.

[95] S. Refael and E. Sher. A theoretical study of the ignition of a reactive medium by means of an electrical discharge. *Combustion and Flame*, 59(1):17 – 30, 1985.

[96] W. L. Roberts, J. F. Driscoll, M. C. Drake, and L. P. Goss. Images of the quenching of a flame by a vortex—to quantify regimes of turbulent combustion. *Combustion and Flame*, 94(1):58 – 69, 1993.

[97] R. Saïd and R. Borghi. A simulation with a "cellular automaton" for turbulent combustion modelling. *Symposium (International) on Combustion*, 22(1):569 – 577, 1989.

[98] F. Seffrin. *Geschwindigkeits- und Skalarfeld-Charakterisierung turbulenter stratifizierter Vormischflammen*. PhD thesis, TU-Darmstadt, 2011.

[99] F. Seffrin, F. Fuest, D. Geyer, and A. Dreizler. Flow field studies of a new series of turbulent premixed stratified flames. *Combustion and Flame*, 157(2):384 – 396, 2010.

[100] L. Selle, G. Lartigue, T. Poinsot, R. Koch, K. U. Schildmacher, W. Krebs, B. Prade, P. Kaufmann, and D. Veynante. Compressible large eddy simulation of turbulent combustion in complex geometry on unstructured meshes. *Combustion and Flame*, 137(4):489 – 505, 2004.

[101] G. S. Settles. *Schlieren and Shadowgraph Techniques: Visualizing Phenomena in Transparent Media (Experimental Fluid Mechanics)*. Springer, 2001.

[102] L. Sforza, T. Lucchini, and A. Onorati. Cfd modelling of flame stretch in si engines. *Energy Procedia*, 82:59 – 66, 2015. 70th Conference of the Italian Thermal Machines Engineering Association, ATI2015.

[103] K. I. Shelkin. On combustion in a turbulent flow. Technical Report NACA-TM-1110, NACA, 1947.

[104] J. Smagorinsky. General circulation experiments with the primitive equations. *Mon. Weather Rev.*, 91(3):99–164, 1963.

[105] J. Song and M. Sunwoo. A modeling and experimental study of initial flame kernel development and propagation in si engines. In *SAE Technical Paper*, number 2000-01-0960, 2000.

[106] Y. Takagi. A new era in spark-ignition engines featuring high-pressure direct injection. *Symposium (International) on Combustion*, 27(2):2055 – 2068, 1998.

[107] Z. Tan and R. D. Reitz. Modeling ignition and combustion in spark-ignition engines using a level set method. In *SAE Technical Paper*. SAE International, mar 2003.

[108] A. Trouve and T. Poinsot. The evolution equation for the flame surface density in turbulent premixed combustion. *J. Fluid Mech.*, 278:1–31, 1994.

[109] J. A. van Oijen and L. P. H. de Goey. Modelling of premixed laminar flames using flamelet-generated manifolds. *Combustion Science and Technology*, 161(1):113–137, 2000.

[110] J. A. van Oijen, F. A. Lammers, and L. P. H. de Goey. Modeling of complex premixed burner systems by using flamelet-generated manifolds. *Combustion and Flame*, 127(3):2124 – 2134, 2001.

[111] L. Vervisch and E. Bidaux. Surface density function in premixed turbulent combustion modeling, similarities between probability density function and flame surface approaches. *Phys. Fluids*, 7(10), 1995.

[112] V. Weber, J. Brübach, R. L. Gordon, and A. Dreizler. Pixel-based characterisation of cmos high-speed camera systems. *Appl. Phys. B*, 103(2):421–433, 2011.

[113] H. Willems and R. Sierens. Modeling the initial growth of the plasma and flame kernel in si engines. *J. Eng. Gas Turbines Power*, 125(2):479–484, 2003.

[114] F. A. Williams. *Combustion Theory*. Taylor & Francis Group, 1994.

[115] P. K. Yeung, S. S. Girimaji, and S. B. Pope. Straining and scalar dissipation on material surfaces in turbulence: Implications for flamelets. *Combustion and Flame*, 79(3):340 – 365, 1990.

[116] A. Zhang, A. Montanaro, L. Allocca, J. Naber, and S. Y. Lee. Measurement of diesel spray formation and combustion upon different nozzle geometry using hybrid imaging technique. *SAE Int. J. Engines*, 7(2):1034–1043, 2014.

[117] A. Zhang, J. D. Naber, and S. Y. Lee. An experimental study of flame kernel evolution in lean and diluted methane-air mixtures at engine-like conditions. *Combust. Sci. Technol.*, 186(8):988–1004, 2014.

[118] X. Zhu, L. Sforza, T. Ranadive, A. Zhang, S. Y. Lee, J. Naber, T. Lucchini, A. Onorati, M. Anbarasu, and Y. Zeng. Experimental and numerical study of flame kernel formation processes of propane-air mixture in a pressurized combustion vessel. *SAE Int. J. Engines*, 9(3):1494–1511, 2016.

Appendices

APPENDIX $\mathcal{A}$

Modelling of the Inter-Electrode Voltage Fall

A particular attention was employed to model the inter-electrode voltage fall V_{IE} (defined in (1.17)), because different modelling approaches should be adopted during arc and glow stages. As described in [61, 85], the arc mode is usually characterized by a low voltage ($V_{IE} < 100\ V$) while, conversely, the glow phase presents higher voltages ($V_{IE} > 200\ V$) to allow an increase of electron emission. Consequently, the voltage falls of (1.17) were modelled as explained in the next two subsections, assuming:

- *Air* as the gaseous conductor between the electrodes. This assumption was performed in absence of detailed experiments regarding spark discharge into fuel/air mixtures, but in the near future, a more suitable approach will be investigated.
- *Nichel* as the electrodes metal, considered a quite common used material.

Table A.1: *Electrons emitted from metals per impacting positive ion γ $[electron/ion]$. Part of the table reported in [29] including some commonly used metals and gaseous conductors.*

Metal	Air	Argon - Ar	Hydrogen - H_2
Aluminium - Al	0.035	0.12	0.095
Copper - Cu	0.025	0.058	0.05
Nichel - Ni	0.036	0.058	0.053
Platinum - Pt	0.017	0.058	0.02

Arc stage

This stage, characterized by a quite low voltage value and a relatively short duration (of the order of μs), required the following modelling strategy.

Cathode voltage fall V_{cf} It is of the order of the primary ionization potential of the gas or vapor in which the arc burns. This is markedly lower than the cathode drop of potential of the glow discharge and for air can be estimated as $V_{cf,arc} = 15.8\ V$, [29]. This value is also confirmed by NIST data about primary ionization potential of N_2, because very close to it [1].

Anode voltage fall V_{af} Estimated by Cobine [29] through the following equation

$$V_{af,arc} = \frac{H_a}{j} - \Phi_0 \tag{A.1}$$

where H_a is the heat received by the anode, j the anode current density and Φ_0 the electrodes metal work function. For Nichel-based electrodes material Kim [61] proposed the ratio $H_a/j = 13.6\ V$, while Michaelson [80] $\Phi_0 = 5.15\ V$.

Gas-column voltage fall V_{gc} Computed according to Kim [61] by using the equation

$$V_{gc,arc}\,(t) = a_{gc}\, l_{spark}\,(t)\ i_S^{b_{gc}}\,(t)\ p^{c_{gc}} \tag{A.2}$$

with l_{spark} being the spark channel length in mm, p the pressure in bar and $a_{gc} = 6.31$, $b_{gc} = -0.75$ and $c_{gc} = 0.51$ the coefficients for the arc stage.

Glow stage

The glow stage is typical of long duration discharges (of the order of ms) and experiences higher voltage values with respect to the arc stage ones, as a consequence of the increased electron emission. Therefore, the implemented modelling strategy of (1.17) parameters is as follows.

Cathode voltage fall V_{cf} Cobine [29] proposed this equation

$$V_{cf,glow} = \frac{3B}{A} \ln\left(1 + \frac{1}{\gamma}\right) \tag{A.3}$$

which predicts a cathode drop of potential significantly higher than the arc stage one. Here, γ represents the electrons emitted from the cathode metal per impacting positive ion and its value, according to Table A.1, can be assumed equal to 0.036. Instead, the parameters A and B are those of the Townsend equation applied with air, where $A = 14.6$ and $B = 365$, as reported in Table A.2.

Anode voltage fall V_{af} According to [29], (A.1) holds also for the glow stage.

Gas-column voltage fall V_{gc} As suggested in [61], (A.2) is valid also for the glow phase but with different coefficients: $a_{gc} = 40.46$, $b_{gc} = -0.32$ and $c_{gc} = 0.51$.

Table A.2: *Constants of the Townsend equation. Part of the table reported in [29] including the constants related to Table A.1 gaseous conductors.*

Gaseous conductor	A	B
Air	14.6	365
Argon - Ar	13.6	235
Hydrogen - H_2	5	130

APPENDIX $\mathcal{B}$

Complements to the ATFM assessment on TSF burner

In addition to the temperature and mixture fraction distributions, investigated in Section 5.2.4, the reacting CO_2 and CH_4 mass fractions are analyzed in the following sections. The final purpose is to provide additional support to the performed ATFM assessment.

Mean CO_2 mass fraction

Figure B.1 shows the experimental and numerical radial profiles of the mean CO_2 mass fraction, which is one of the main products of the reaction.

A comparison between numerical results only points out similar conclusions drawn for mean axial velocity and mean temperature trends (Section 5.2.4).

By focusing, instead, on the similarity between experimental findings and numerical results, the CO_2 mass fraction behaviour is very similar to mean temperature one (Figure 5.30). Therefore, a rather satisfactory agreement between measured and predicted trends is achieved, especially with a flame thickened over 10 cells (right images of Figure B.1). It is worth also to notice that at low axial positions (especially in Figures B.1a and B.1b), the CO_2 mass fraction reaches its equilibrium value and an almost perfect *experimental-numerical* agreement is achieved above

Pilot tube. This confirms that chemical reactions inside the Pilot are completed after the flame holder position and hot gases cool down afterwards, namely in the last portion of the ceramic pipe. More details are available in Chapter 6.

Mean CH_4 mass fraction

The experimental and numerical radial profiles of the mean CH_4 mass fraction, which is the fuel consumed by the reaction process, are plotted in Figure B.2.

Concerning numerical results only, the conclusions drawn for the mean axial velocity and mean temperature trends (Section 5.2.4) are still valid.

About the agreement between experiments and simulations, again, almost satisfactory results were achieved. Numerical predictions obtained with a 10 cells thickening confirm to better fit experimental trends than the ones with a 5 cells thickening. As it is possible to observe:

- at low axial positions ($Y < 35\ mm$) the initial stratification between Slot 1 and 2 is sharpened;
- by increasing Y values (starting form $Y = 35\ mm$) the CH_4 gradients becomes smoother and the peak value above Slot 1 pipe starts to reduce.

This last phenomenon is rather well predicted by performed simulations.

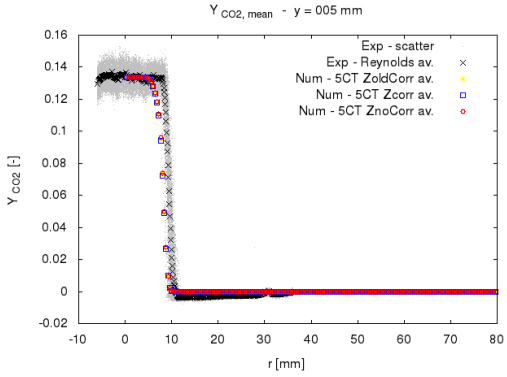
Y CO2, mean - y = 005 mm
Exp - scatter
Exp - Reynolds av.
Num - 5CT ZoldCorr av.
Num - 5CT Zcorr av.
Num - 5CT ZnoCorr av.
Y CO2 [-]
r [mm]

(a)

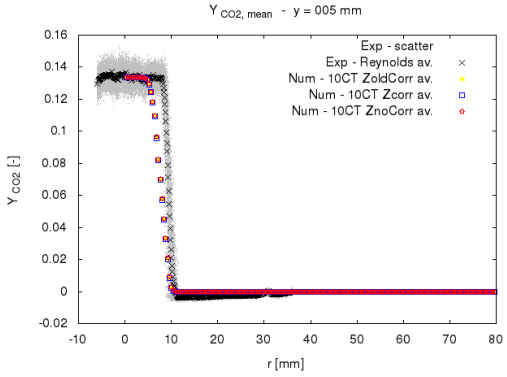
Y CO2, mean - y = 005 mm
Exp - scatter
Exp - Reynolds av.
Num - 10CT ZoldCorr av.
Num - 10CT Zcorr av.
Num - 10CT ZnoCorr av.
Y CO2 [-]
r [mm]

(b)

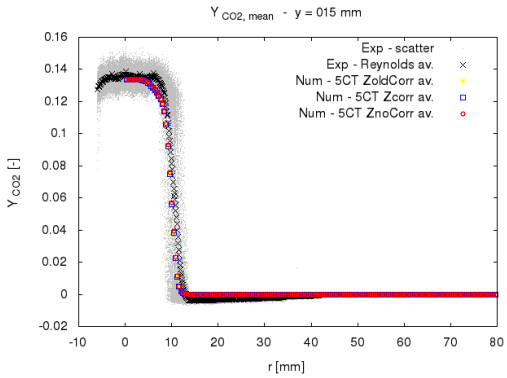
Y CO2, mean - y = 015 mm
Exp - scatter
Exp - Reynolds av.
Num - 5CT ZoldCorr av.
Num - 5CT Zcorr av.
Num - 5CT ZnoCorr av.
Y CO2 [-]
r [mm]

(c)

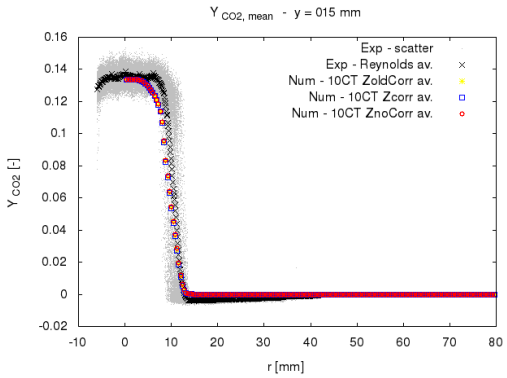
Y CO2, mean - y = 015 mm
Exp - scatter
Exp - Reynolds av.
Num - 10CT ZoldCorr av.
Num - 10CT Zcorr av.
Num - 10CT ZnoCorr av.
Y CO2 [-]
r [mm]

(d)

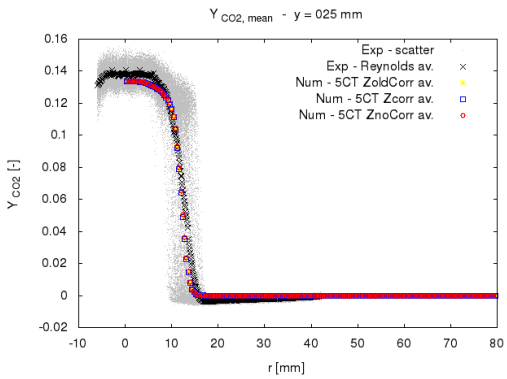
Y CO2, mean - y = 025 mm
Exp - scatter
Exp - Reynolds av.
Num - 5CT ZoldCorr av.
Num - 5CT Zcorr av.
Num - 5CT ZnoCorr av.
Y CO2 [-]
r [mm]

(e)

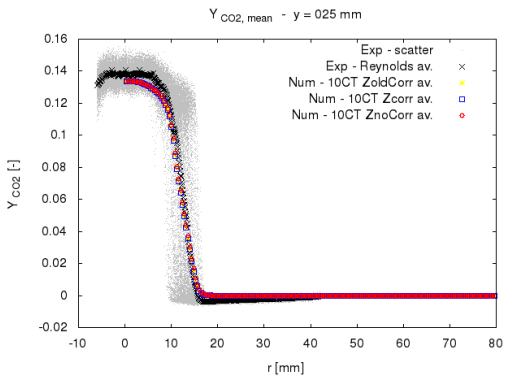
Y CO2, mean - y = 025 mm
Exp - scatter
Exp - Reynolds av.
Num - 10CT ZoldCorr av.
Num - 10CT Zcorr av.
Num - 10CT ZnoCorr av.
Y CO2 [-]
r [mm]

(f)

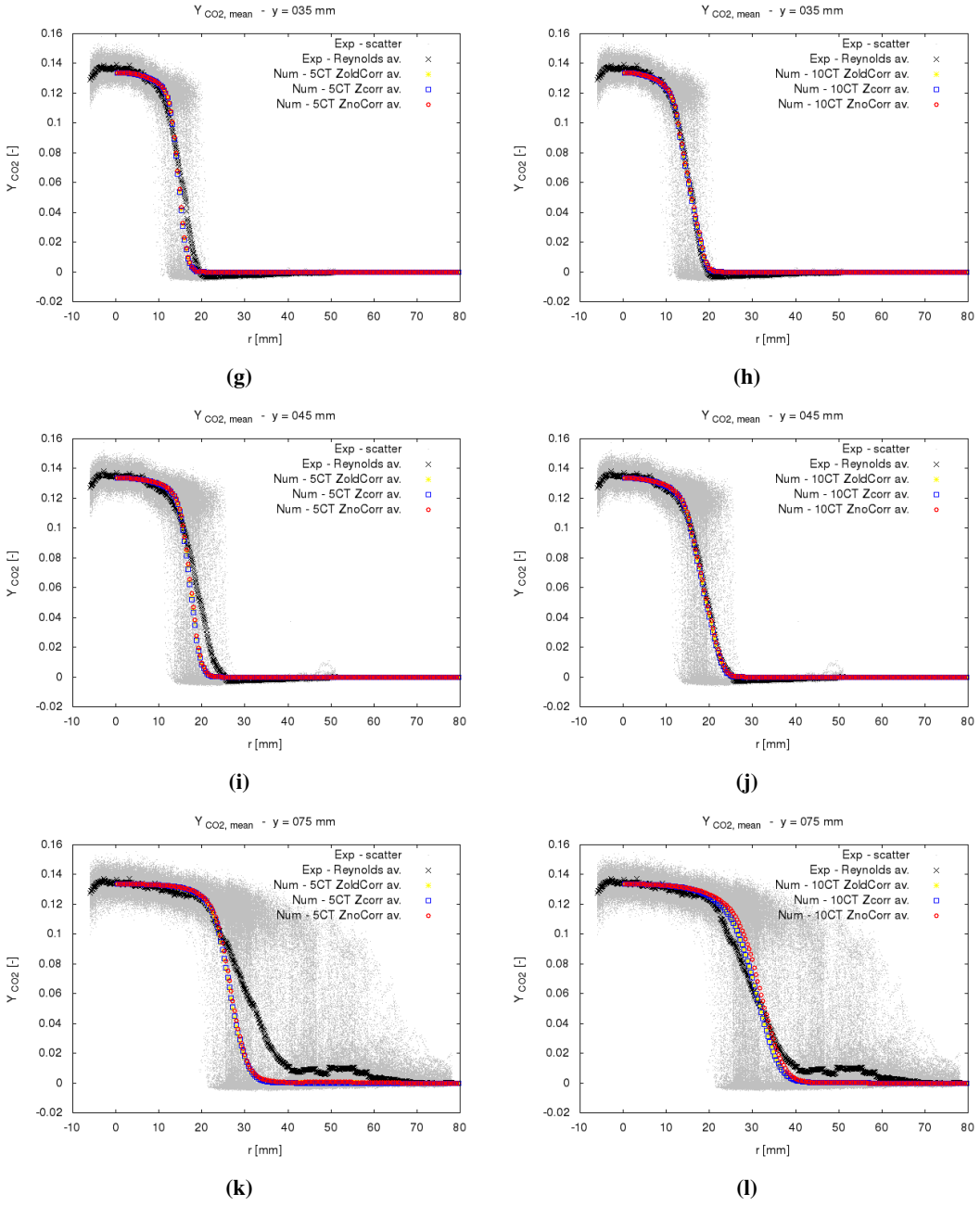

Figure B.1: *Radial profiles of the mean CO_2 mass fraction ($Y_{CO2,\ mean}$). Comparison between experimental findings and numerical results at six different axial positions (see Figure 5.6): $Y = 5\ mm$ (a) and (b), $Y = 15\ mm$ (c) and (d), $Y = 25\ mm$ (e) and (f), $Y = 35\ mm$ (g) and (h), $Y = 45\ mm$ (i) and (j), $Y = 75\ mm$ (k) and (l). Numerical results come from ATFM 3D reacting LES simulations with: a flame thickened over 5 cells (*5CT*, left side images) and over 10 cells (*10CT*, right side images). In ATFM application, the mixture fraction gradient $\vec{\nabla}\widetilde{Z}$ is: thickened according to Kuenne [67] (*ZoldCorr*), thickened only along the flame normal direction (*Zcorr*, as proposed in Section 2.5.2) and not thickened (*ZnoCorr*).*

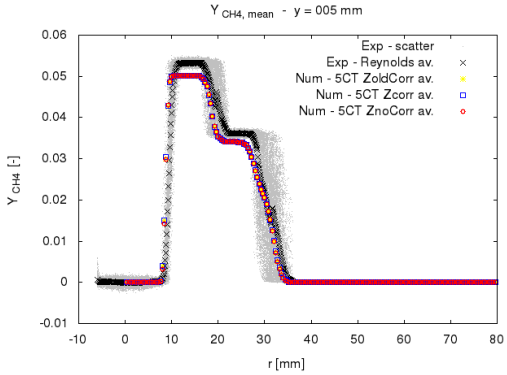
Y CH4, mean - y = 005 mm
Exp - scatter
Exp - Reynolds av.
Num - 5CT ZoldCorr av.
Num - 5CT Zcorr av.
Num - 5CT ZnoCorr av.
Y CH4 [-]
r [mm]

(a)

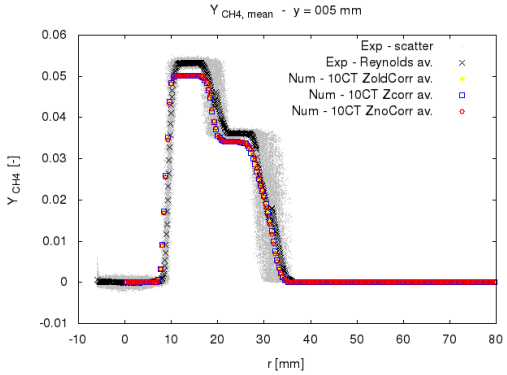
Y CH4, mean - y = 005 mm
Exp - scatter
Exp - Reynolds av.
Num - 10CT ZoldCorr av.
Num - 10CT Zcorr av.
Num - 10CT ZnoCorr av.
Y CH4 [-]
r [mm]

(b)

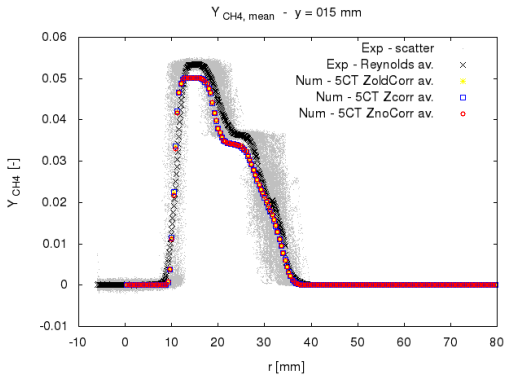
Y CH4, mean - y = 015 mm
Exp - scatter
Exp - Reynolds av.
Num - 5CT ZoldCorr av.
Num - 5CT Zcorr av.
Num - 5CT ZnoCorr av.
Y CH4 [-]
r [mm]

(c)

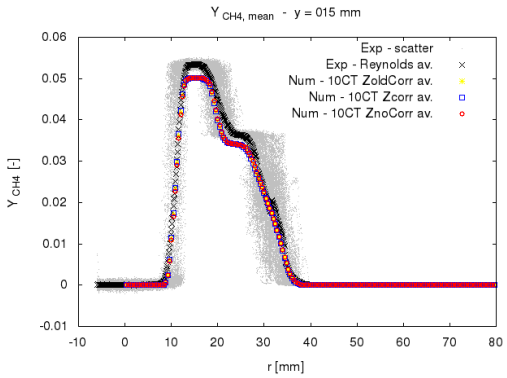
Y CH4, mean - y = 015 mm
Exp - scatter
Exp - Reynolds av.
Num - 10CT ZoldCorr av.
Num - 10CT Zcorr av.
Num - 10CT ZnoCorr av.
Y CH4 [-]
r [mm]

(d)

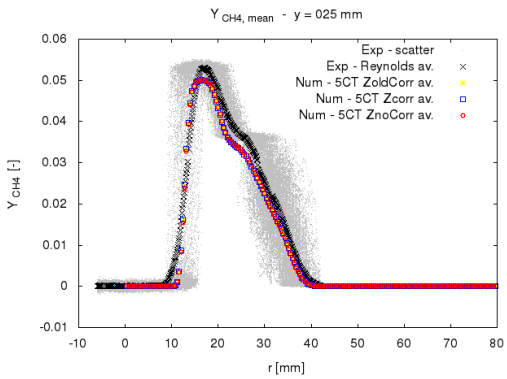
Y CH4, mean - y = 025 mm
Exp - scatter
Exp - Reynolds av.
Num - 5CT ZoldCorr av.
Num - 5CT Zcorr av.
Num - 5CT ZnoCorr av.
Y CH4 [-]
r [mm]

(e)

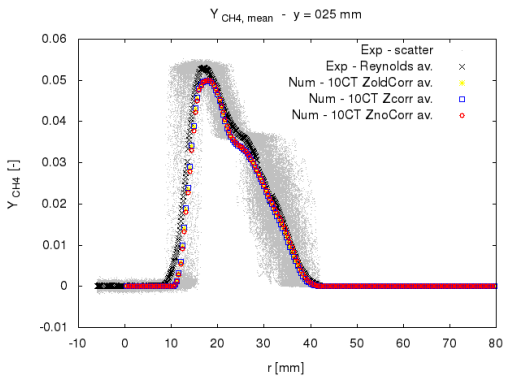
Y CH4, mean - y = 025 mm
Exp - scatter
Exp - Reynolds av.
Num - 10CT ZoldCorr av.
Num - 10CT Zcorr av.
Num - 10CT ZnoCorr av.
Y CH4 [-]
r [mm]

(f)

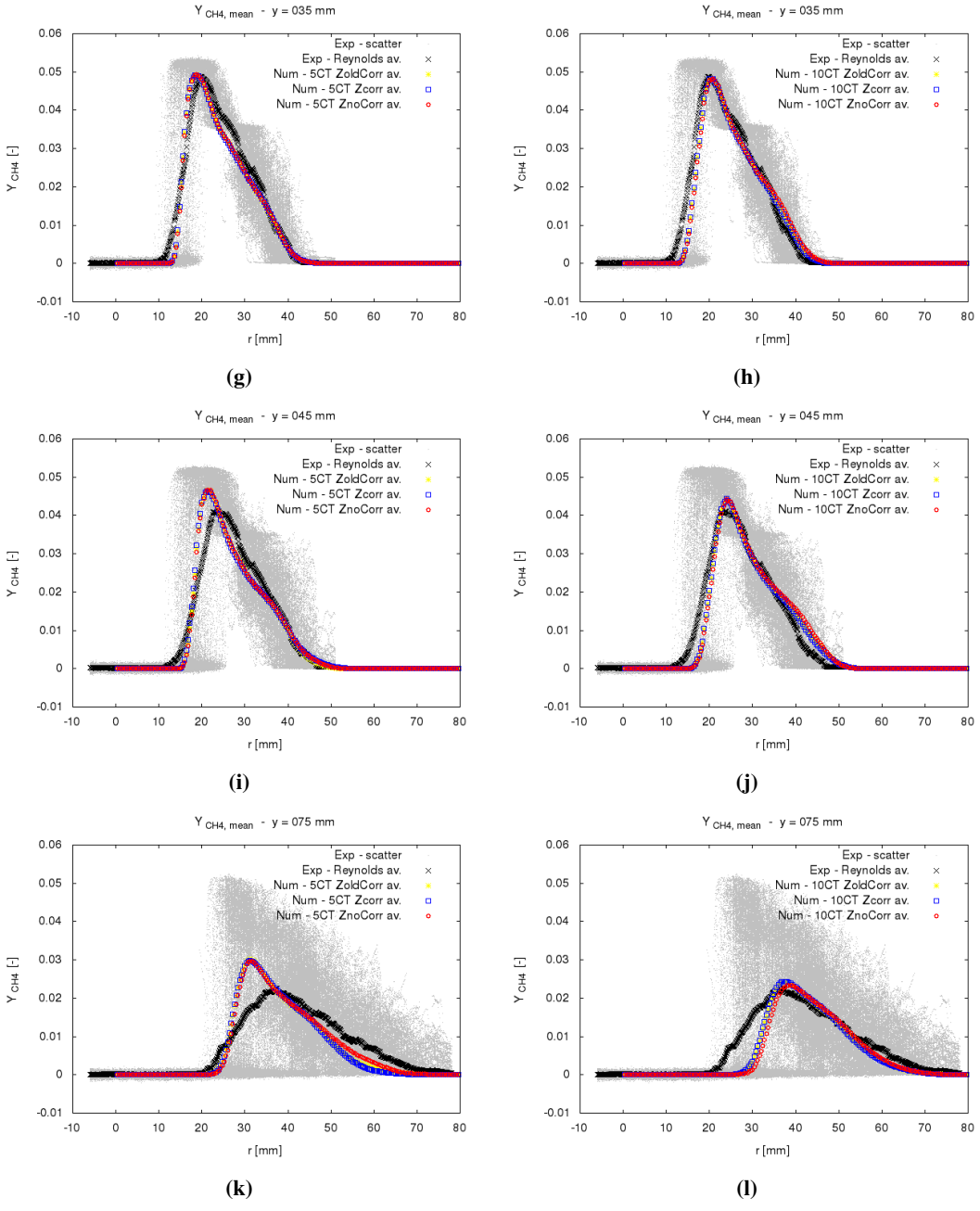

Figure B.2: *Radial profiles of the mean CH_4 mass fraction ($Y_{CH4,\ mean}$). Comparison between experimental findings and numerical results at six different axial positions (see Figure 5.6): $Y = 5\ mm$ (a) and (b), $Y = 15\ mm$ (c) and (d), $Y = 25\ mm$ (e) and (f), $Y = 35\ mm$ (g) and (h), $Y = 45\ mm$ (i) and (j), $Y = 75\ mm$ (k) and (l). Numerical results come from ATFM 3D reacting LES simulations with: a flame thickened over 5 cells (*5CT*, left side images) and over 10 cells (*10CT*, right side images). In ATFM application, the mixture fraction gradient $\vec{\nabla}\widetilde{Z}$ is: thickened according to Kuenne [67] (*ZoldCorr*), thickened only along the flame normal direction (*Zcorr*, as proposed in Section 2.5.2) and not thickened (*ZnoCorr*).*